Modeling of Strain-Hardening Cement-based Composites (SHCC): A Finite Element Method using the Strong Discontinuity Approach (SDA) with Explicit Representation of Fibers

Modellierung von zementgebundenen Kompositmaterialien mit Verfestigung (SHCC): Eine Finite-Elemente-Methode mit Diskontinuitäten („Strong Discontinuity Approach“ SDA) und expliziter Darstellung von Fasern

Dissertation

vorgelegt an der Fakultät Bauingenieurwesen
der Technischen Universität Dresden
zur Erlangung der Würde eines
Doktors der Ingenieurwissenschaften
- Dr.-Ing. -

von
Alaleh Shehni
aus Ahvaz (Iran)

Gutachter
Univ.-Prof. Dr.-Ing. habil. Ulrich Häussler-Combe
Univ.-Prof. Dr.-Ing. Marco di Prisco
Dr.-Ing. Christina Scheffler

Dresden 2020

Abstract

Concrete is a predominant construction material due to several advantages; however, the pure cementitious composites have shown quasi-brittle behavior with undesirable typical large cracks under tensile loading conditions. Thus, the addition of a small volume of short fibers is a well-known strategy to increase the ductility and toughness of cementitious matrices besides optimization of the crack opening. Strain-hardening cement-based composites (SHCCs) is a particular class of fiber-reinforced concretes (FRCC) that can develop controlled multiple cracks while subjected to incremental tensile loading conditions. However, a proper composition design, especially concerning fiber and bond properties, still follows a trial and error approach.

This work presents a newly developed model to simulate SHCC at the meso-scale level. This model is based on Finite-Element-Method and allows for nonlinear behavior for cement matrix, fiber material, and bond laws. Concerning three complexities of target FRCC, i.e., crack formation in the cement matrix, a large number of explicit fibers with arbitrary random distribution, and fibers' interaction with the cement matrix via the bond, extra features are added to standard FE consist of:

- Further development of the Strong Discontinuity Approach (SDA) to model discrete cracking of continuum elements on the element level
- Discretization of single fibers by truss elements with truss nodes independently placed of continuum nodes
- Connecting SDA elements to explicit truss elements by particular bond elements.

In this research study, first, theoretical basics and special implementation issues were described. Later, this newly developed model was calibrated with several simple configurations. The bond law utilized in the simulation was derived from single fiber pullout test and calibrated with several analyses. In the next step, 2D SHCC dumbbell specimens under tensile loading condition were simulated, and a series of numerical case studies were performed to assess the quality, credibility, and limitations of the numerical model. It should be noted

that cracking patterns could not be directly compared to experimental cracking patterns as the simulation model's current state is deterministic by random material properties that influence the experimental specimen behavior. Taking the effect of random field and other simplifying assumptions into account, the simulation model seems to describe enumerated SHCC behavior at an acceptable level.

In summary, a further base is given for the target-oriented design of FRCC material composition to reach the given objectives of material properties. The concepts and methods presented in this study can simulate short and thin polymer fibers in a random position and steel fibers and structures with long reinforcement in a regular arrangement.

Kurzfassung

Beton ist aufgrund mehrerer Vorteile ein vorherrschender Baustoff. Die reinen zementhaltigen Verbundwerkstoffe zeigten jedoch ein quasi sprödes Verhalten mit unerwünschten typischen großen Rissen unter Zugbelastungsbedingungen. Daher ist, neben der Optimierung der Rissöffung, die Zugabe eines kleinen Volumens von kurzen Fasern eine bekannte Strategie, um die Duktilität und Zähigkeit von zementhaltigen Matrizen zu erhöhen. Verbundwerkstoffe auf Zementbasis mit Verfestigungseigenschaften (SHCCs) sind eine besondere Klasse von faserverstärkten Betonen (FRCC), die unter inkrementellen Zugbelastungsbedingungen kontrollierte Mehrfachrisse entwickeln können. Ein geeignetes Zusammensetzungsdesign, insbesondere in Bezug auf Faser- und Verbundeigenschaften, folgt jedoch immer noch der Versuch-und-Irrtum-Methode.

Diese Arbeit präsentiert ein neu entwickeltes Modell zur Simulation von SHCC auf mesoskaliger Ebene. Dieses Modell basiert auf der Finite-Elemente-Methode und ermöglicht nichtlineares Verhalten für Zementmatrix-, Fasermaterial- und Verbundgesetze. In Bezug auf drei Komplexitäten des Ziel-FRCC, d.h. die Rissbildung in der Zementmatrix, eine große Anzahl expliziter Fasern mit zufälliger Verteilung und die Wechselwirkung der Fasern mit der Zementmatrix über den Verbund, werden der Standard-Finite-Elemente-Methode zusätzliche Merkmale hinzugefügt:

- Weiterentwicklung des Strong Discontinuity Approach (SDA) zur Modellierung der diskreten Rissbildung von Kontinuumselementen auf Elementebene
- Diskretisierung einzelner Fasern durch Stabelemente mit Knoten, die unabhängig von Kontinuumsknoten angeordnet sind
- Verbinden von SDA-Elementen mit beliebig angeordneten Stabelementen durch neu entwickelte Verbundelemente

In dieser Forschungsstudie wurden zunächst theoretische Grundlagen und spezielle Implementierungsprobleme beschrieben. Später wurde dieses neu entwickelte Modell mit mehreren einfachen Konfigurationen kalibriert. Das in der Simulation verwendete Verbundgesetz wurde

aus einem Einzelfaser-Ausziehtest abgeleitet und mit mehreren Analysen kalibriert. Im nächsten Schritt wurden 2D-SHCC-Hantelproben unter Zugbelastungsbedingungen simuliert und eine Reihe numerischer Fallstudien durchgeführt, um die Qualität, die Anwendungsmöglichkeiten und Einschränkungen des numerischen Modells zu bewerten. Es ist zu beachten, dass Rissmuster nicht direkt mit experimentellen Rissmustern verglichen werden konnten, da der aktuelle Zustand des Simulationsmodells durch zufällige Materialeigenschaften bestimmt wird, die das Verhalten der experimentellen Probe beeinflussen. Unter Berücksichtigung des Effekts des Zufallsfelds und anderer vereinfachender Annahmen scheint das Simulationsmodell das aufgezählte SHCC-Verhalten auf einem akzeptablen Niveau zu beschreiben.

Zusammenfassend wird eine weitere Grundlage für das zielgerichtete Design der FRCC-Materialzusammensetzung angegeben, um die vorgegebenen Ziele der Materialeigenschaften zu erreichen. Die in dieser Studie vorgestellten Konzepte und Methoden können kurze und dünne Polymerfasern in zufälliger Position und Stahlfasern und -strukturen mit langer Verstärkung in regelmäßiger Anordnung simulieren.

ACKNOWLEDGMENTS

I want to express my gratitude to Prof. Ulrich Häussler-Combe, for the outstanding guidance and the support I received along my Ph.D. journey.

The research described in this thesis was developed within the GRK-2250 project: "Mineral-bonded composites for enhanced structural impact safety", and financed by the German Research Foundation, DFG (Deutsche Forschungsgemeinschaft). I thank all the people involved in this program for creating the structured and synergistic group in which it was a pleasure to work.

I would like to acknowledge Prof. Marco di Prisco and Dr. Christina Scheffler, for their helpful comments and the inspiring discussions, which contributed to the final version of my dissertation.

My acknowledgments are also addressed to Dr. Iurie Curosu and Dr. Ting Gong from the Institute of Construction Materials of the Dresden University of Technology, for their support with performing experimental tests used as reference experiments in this research study.

I would like to thank all the colleagues and friends of the Institute of Concrete Structure. Special thanks to Dr. Silke Scheerer, Dr. Birgit Beckmann, and Angela Heller for their constant support and positive energy. I am also indebted to Tilo and Olga for sharing work, trouble, cakes, and chatting.

Many other people walked with me on this adventure: my deepest gratitude goes to the old Iranian friends and beloved Dutch fellow colleagues from abt, who never let me go, and all the new fellow-travelers, who have been great source of support and kindness. Special thought is dedicated to Maziar, Fatemeh, Andy, Eva, Ramona, Sandra, Franzi, Maryam, Najmeh, Tahereh, Margriet, and Johan.

Last but not least, I would like to thank my parents, my sister Azadeh and my brother Amir for their pure support and unconditional love. This work is dedicated to them.

CONTENTS

1 INTRODUCTION **1**

1.1 BACKGROUND 1

1.2 AIM AND OBJECTIVE 3

1.3 OUTLINE 5

2 MATERIAL MODELS **7**

2.1 CONCRETE 7

2.1.1 Structure of concrete as a multi-level system 7

2.2 STRAIN HARDENING CEMENT-BASED COMPOSITIES(SHCCs) 10

2.2.1 Historical background 10

2.2.2 Strain-hardening behavior 14

2.2.3 Micromechanics of SHCC 16

2.2.4 Fiber inclination angle 18

2.2.5 Bond Behavior of Single Fibers 20

3 DISCRETIZATION APPROACHES **29**

3.1 INTRODUCTION TO MESOSCOPIC SCALE 29

3.1.1 3D Random mesoscopic model 30

3.1.2 2D Sections random mesoscopic model 31

3.2 INTRODUCTION TO IRREGULAR AND REGULAR METHODS 31

3.3 NUMERICAL SIMULATIONS 32

3.3.1 Model specification 32

3.3.2 Analysis results and parameter studies 34

3.3.3 Conclusion 39

4 NUMERICAL MODELING **41**

4.1 INTRODUCTION TO FINITE ELEMENT METHOD 41

4.2 INTRODUCTION TO THE STRONG DISCONTINUTY APPROACH . . . 44
4.2.1 Virtual work principles for SDA . . . 45
4.2.2 Explicit crack modeling with SDA . . . 49
4.2.3 Coupling of continuum to discontinuity . . . 54
4.2.4 Loading time discretization and equilibrium iteration . . . 56
4.2.5 Crack initiation, geometry and tractions . . . 58
4.2.6 Viscous regularization . . . 62
4.3 NEW APPROACH FOR DEFINITION OF EMBEDDED FIBERS WITH FLIXIBLE BOND . . . 64
4.4 NUMERICAL SIMULATIONS . . . 68
4.4.1 Introduction . . . 68
4.4.2 Mesh sensitivity of models with SDA continuum elements . . . 70
4.4.3 Parameter study of fully embedded fiber model . . . 74
4.4.4 Parameter study of model within single fiber passing a small gap . . . 79
4.4.5 Simple model with fibers and aggregates . . . 84

5 SIMULATION AND NUMERICAL PARAMETRIC STUDIES OF TENSION TEST ON DUMBBELL SPECIMEN UNDER QUASI-STATIC LOADING CONDITIONS 89

5.1 EXPRIMENTAL SET-UP . . . 89
5.1.1 Materials . . . 89
5.1.2 Specimen production and testing . . . 91
5.2 FINITE ELEMENT SIMULATIONS . . . 93
5.2.1 Numerical reference model . . . 102
5.3 MATERIAL AND MECHANICAL PARAMETRIC STUDIES . . . 107
5.3.1 Studies on effect of different parameters in bond stress - slip relationship(Maximum bond strength, ultimate bond stress, initial stiffness) . 107
5.3.2 Mesh sensitivity in matrix elements . . . 114
5.3.3 The effect of concrete tensile strength . . . 118
5.3.4 The effect of concrete fracture energy . . . 119
5.3.5 The effect of Young's modulus of concrete . . . 123
5.3.6 The effect of tensile strength of fiber . . . 124
5.3.7 The effect of fiber volume fraction . . . 125

5.3.8 The effect of considering second crack in matrix elements 131
5.4 CONCLUSION 134

6 CONCLUSION **137**
6.1 RETROSPECTIVE VIEW AND FINDINGS 137
6.2 RECOMMENDATIONS 138

BIBLIOGRAPHY **141**

1 INTRODUCTION

1.1 BACKGROUND

Concrete can be considered as a sophisticated stone consist of aggregates cemented by hydraulic cement paste. However, the pure cementitious composites have shown quasi-brittle behavior with undesirable typical large cracks under tensile loading conditions. Thus, the addition of a small volume of short fibers is a well-known strategy to increase the ductility and toughness of cementitious matrices besides optimization of crack opening[20, 72, 122, 83]. An extensive range of composite material properties can be obtained with wide ranges of properties of fibers and cement matrix. This leads to challenges regarding material design.

The composition of constituents still follows an experimental trial and error process when objectives for composite material properties are given. Even with known characteristics of fibers and cement matrix, their interaction due to bond, random fiber orientation, and matrix cracking is complex. Hence, the behavior of the composite is generally not predictable with ordinary material models. Thus, several material models explicitly regarding fibers, cement matrix, and bond have been developed. A respective mesoscopic scale treats a composite as a structure and puts complex composite material behavior down to constituents' structural behavior with each component's known behavior. Numerous studies have indicated that Finite-Element-Method (FEM) has proven to provide extremely high adaptability to model all types of structures [9, 17]. In the present research study, specific approaches are discussed besides the standard finite elements regarding the mesoscopic modeling of FRCC. This concluded crack formation in the cement matrix, a large number of fibers with arbitrary random distribution, and the interaction of fibers with cement matrix via the bond. In previous studies, two approaches are introduced to model the cracking. i.e., smeared crack approaches and discrete crack approaches. The Smeared crack techniques need regularization techniques to avoid mesh sensitivity and to reproduce crack energies[13, 12, 51, 100]. These approaches can be sophisticated if the element sizes are much larger or smaller than the thickness of so-called crack bands developing due to the quasi-brittle behavior of concrete. In the latter

approach, discrete cracks can be modeled by using interface elements located along continuum elements boundaries [75]. However, this approach requires a remeshing technique to capture crack paths[23]. As alternative methods for modeling the discrete cracks as interface elements requires remeshing are Extended-Finite-Element (XFEM) [81, 39, 117] and the Strong-Discontinuity-Approach (SDA) [35, 52, 97, 4, 5]

Both approaches provide an explicit evaluation of crack width to imply crack tractions and need no further regularization for mesh objectivity and fracture energy reproduction. XFEM introduces additional degrees of freedom on the system level, which makes this approach inconvenient for structures with a large number of cracks. SDA condenses discontinuity degrees of freedom on the element level leading to enhanced element formulations that do not explicitly carry additional degrees of freedom to the system level. This makes SDA more appropriate in case of a large number of cracks.

Three different classes are introduced in the formulation of SDA: Statically Optimal Symmetric (SOS), Kinematically Optimal Symmetric (KOS), and Statically and Kinematically Optimal Nonsymmetric (SKON) [52, 127]. The SDA formulation discussed in the present research is similar to the KOS; both follow the same way in constructing the matrix of the strain functions in discontinuity. Two alternative approaches are suggested to treat the discontinuity or the crack path across neighboring elements. i.e., continuous path and discontinuous path. Crack path continuity may be enforced by tracking algorithms [98], but this stimulates locking effects, specifically in the SOS formulation [127]. The extension of crack path discontinuities can be reduced by minimizing element sizes whereby the crack path is clearly indicated. A control of implausible multiple crack path courses is proposed with adaption methods[110]. Relations for crack tractions depending on crack width are derived from experimental investigations about concrete tensile failure behavior [110, 34, 58]. They generally introduce nonlinearities, e.g., in case non-monotonic behavior with un- and reloading of cracks in inhomogeneous structures during a loading history.

In modeling of FRCC, fibers have to be treated in addition to the cracked continuum. Models suggested in previous studies are based on FEM using (1) a smeared crack approach and stress-strain curves obtained from experiments[60, 116, 42, 119]. These models can be used just for specific structural elements under the same conditions as applied for experimental specimen [99]. (2) Discrete crack approaches with crack-width determination, as discussed above, are used with concerning advanced mechanical property determination due to fiber

bridging [37, 76]. (3) Bond stress-slip based models where the fibers are discretely modeled in the cement matrix at the meso-level [22]. In this approach, a wide range of FRCC regardless of fiber lengths and fiber types can be analyzed. Discrete or smeared approaches can be applied depending on the crack traction-crack width law or stress-strain softening law whereby the material properties are assumed as homogenized, finally yielding a macroscopic approach suitable for the analysis of whole structures.

Mesoscopic models explicitly distinguishing cement matrix, fibers, and fiber-matrix bond are summarized by [3]. Fibers are treated as embedded elements, whereas the mesh of a fiber cloud is generated independently from the cement matrix mesh. Moreover, a coupling procedure is used to connect these two independent meshes. These models can also investigate the effect of production techniques and conditions[120]. Some proposals modify the constitutive law to consider the effect of fiber-matrix interaction, whereas bond is considered as rigid [104, 26, 27]. Fibers are modeled as embedded elements. Discrete forces are applied to the continuum mesh near the fiber ends position to consider fibers' effect in the analysis[105]. Furthermore, this effect is described using closing loads to replace the interaction between fiber, crossing a cohesive crack, and the matrix [109]. Various approaches for the fiber-matrix interaction use analytical relations derived from pullout tests, e.g. [63] basing on experimental investigations [64, 65], or [105] concluding from the model by [44]. Lattice models as alternatives to FEM are proposed, e.g., by [55].

1.2 AIM AND OBJECTIVE

Strain-hardening cement-based composite (SHCC) is a particular class of fiber-reinforced cement composites (FRCC), which offers a high potential to improve structural behavior regarding tensile strength and ductility [68, 67, 90]. Thus, a large number of thin, short polymer fibers are mixed within a matrix of fine-grained concrete. The presented study's target composite is a high-strength SHCC made with ultra-high molecular weight polyethylene (UHMWPE or shortly PE). These fibers have a length of 6 mm and a diameter of 20 μm [29], which nominal strength is 2 500 N/mm^2 with a brittle failure mode. The volume fraction of fibers is 2 % of the volume regarding the cement matrix. The particular cementitious matrix used in SHCC has high cement content, a low water-to-binder ratio, a small amount of fine sand, and no coarse sand or aggregates. This matrix should guarantee a proper interaction with the hydrophobic PE fibers. Thus, this has to provide a high packing density

and strength [30, 31]. The mechanical response of FRCC significantly influenced the cement matrix, shape, and distribution of fibers in the composite, the mechanical properties of the interface between the cement matrix and individual fibers[20]. Low tensile strength and fracture energy are beneficial regarding the development of multiple steady-state cracks and strain-hardening in the FRCC composite. The strength of the bond between fibers and matrix should be adjusted to let the fibers be active in load-bearing in the crack bridging stage while ensuring adequate free length for fiber deformation with crack opening and preventing premature fiber failure.

The work presented herein provides a numerical method that aims to simulate the fiber-reinforced cementitious composite behavior. It uses the mesoscopic approach combining models for discrete matrix cracking, explicit fibers, and flexible bond for every single fiber explicitly.

The model discretization is described by finite elements whereby small displacements and strains are assumed. The discretized model differentiates continuous and discontinuous contributions to the cement matrix continuum's displacement field, whereby the discontinuous contributions are treated on the element level with SDA. In this study, discontinuous displacement contributions are also synonymously referred to as cracks. The extension of an uncracked continuum element to a cracked SDA element is commanded regarding the Rankine criteria to be defined and depends on the loading history. Thus, a single element can experience multiple cracking in different orientations. Cracking is combined with crack tractions transferred over cracks within the fictitious or cohesive crack concept to dissipate fracture energy. The loading history can treat different loading conditions, i.e., monotonic crack loading, unloading, crack closure, and reloading.

Furthermore, truss elements with their nodes independent from continuum element nodes are arbitrarily embedded in the continuum to model single fibers. Unique bond elements are utilized to model the interaction between continuum elements and single truss elements. These elements connect truss nodes and neighbor continuum nodes like a spring for both uncracked and cracked elements in a like manner whereby different mechanical characteristics can be assigned as the bond law, e.g., nonlinear material behavior whereas in a local system aligned to the truss direction, the longitudinal slip reproduces a given bond behavior and the lateral slip or intersection is basically avoided by a penalty term.

1.3 OUTLINE

The entire work is structured in six chapters overall. After a general introduction to the study in chapter 1, the background history and different classification of FRCC and its components are discussed in chapter 2. Later, the simulation of the fiber pullout test, for the specific type of fiber used in the enumerated SHCC, is performed within DIANA software to validate and calibrate the bond-slip relationship, which will be assigned as the bond law in further simulations.

Different discretization approaches are explained briefly in chapter 3. Three different 2D sections derived from a random 3D meso-model contain aggregates and mortar are analyzed to study the differences between these methods. The aggregates are randomly distributed in the 3D reference model. Several numerical parametric studies are performed to see the mesh sensitivity of each discretization approach besides studying the influence of random field on total response.

In chapter 4, the newly developed model is described based on other existing similar approaches. This model utilizes a discrete matrix cracking approach, and randomly distributed fibers are modeled explicitly and independently from matrix discretization points. Select types of elements are introduced, connecting the fiber nodes to neighboring matrix nodes like a spring. Various types of material behavior can be assigned as bond law to these bond elements. Later, other numerical aspects required for further numerical simulations are discussed in detail. Furthermore, numerical case studies are conducted to calibrate and validate the enumerated numerical method. With the use of these benchmarks, first, the mesh objectivity of the model is investigated, then different scenarios for the position of fiber concerning to continuum are considered.

Following this, in chapter 5, a numerical model to simulate a total response of 2D SHCC dumbbell specimen under tensile loading condition is discussed. The experiment set-up, loading condition, mechanical properties of specimens are explained, and several numerical parametric studies are conducted to validate the developed numerical model. The study is extended in sections of this chapter by further, more in-depth search for influences associated with mechanical properties of each component of FRCC and model characteristics. In the end, based on the finding of the study, weaknesses are identified, and enhancements are proposed.

2 MATERIAL MODELS

Nowadays, the addition of a small volume of short fibers is a well-known strategy to increase the ductility and toughness of cementitious matrices besides optimizing the crack opening. In contrast, the pure cementitious composites have shown quasi-brittle behavior with undesirable typical large cracks under tensile loading condition[20, 72, 122, 83]. This chapter aims to provide a historical perspective of different components in fiber-reinforced composites with particular focus on SHCC, which is the target FRC in this research.

2.1 CONCRETE

2.1.1 Structure of concrete as a multi-level system

Concrete can be considered as a sophisticated stone consist of aggregates cemented by hydraulic cement paste. The typical response of aggregates can be considered linearly elastic within the service load range while the mortar is described as a viscoelastic material. The heterogeneous structure of concrete is explained in terms of a multi-level hierarchy-system. Concrete is a composite material with a variety of inhomogeneities and structural defects of different sizes. By simplifying the real structure, scientists have suggested various classifications for different characteristic levels in order to consider different effects of crack propagation and crack arresting in concrete.

In research published by Zaitsev and Wittmann in 1981, four different levels of the system are introduced to classify the concrete based on the inhomogeneities and structural imperfections of various sizes[126]. The first level is the macro-level which the main inhomogeneities are given by "big"' inclusions such as aggregates[118]. The typical linear dimensions of representative volume element (RVE) are in order of magnitude of 100 mm, and the minimum dimensions are at least four times the maximum size of aggregate. The average stress and strain of this RVE are called macro-stress and macro-strain, and the relationship between

these two parameters is highly nonlinear, which can be caused by the propagation of imperfections. These values are used for the characterization of plain concrete and reinforced composite structures. The cracks in the interfaces between mortar and aggregates are the main structural failures at this level. Stress and strain values computed from the meso-level are used to understand the behavior of these shrinkage cracks.

The second level is the meso-level, which mortar volume between "big" inclusions is considered, and "little" inclusions define the main inhomogeneity represents the fine aggregates. Since there is a low chance of occurrence of shrinkage cracks compare to macro-level systems, they are neglected in this level. Consequently, the effect of "little" inclusions is represented by some modification factors. The linear dimensions of RVE are in typical order of magnitude of 10 mm. The average stress and strain of this RVE are called meso-stress and meso-strain, and the relationship between these two parameters is assumed to be quasi-linear.

Micro-level is the third level in which the hardened matrix between "little" inclusions is considered in the model, and "big" pores demonstrate the main inhomogeneities. The linear dimensions of RVE are in almost 0. 5 mm, whereas the maximum size of pores can be in the order of magnitude of 10^{-1} mm. The micro-stress and micro-strain are the average stress and strain of this RVE, and their relationship is assumed nearly linear. Pores can be distributed randomly with a high range of various sizes and random shapes.

The complicated pore system's recommended shape is "hole-with-notch" shape for pores, leading to cracks due to stress concentration. There can be so-called priori cracks due to shrinkage stresses in the unloaded specimen. In Fig. 2.1, all cracks are assumed coplanar and oriented in the direction of applied compressive stress to make the worse scenario. The cracks will propagate gradually by increasing the load. The related crack length λ, which is crack length divided by the pore's radius, depends on the applied load as shown in Eq. (2.1).

$$q_{po} = \sqrt{\frac{\pi \cdot E_{\lambda}}{2 \cdot r_{po}}} \sqrt{\frac{(1+\lambda)^7}{(1+\lambda)^2 - 1}} \tag{2.1}$$

where q_{po} is the applied load, E_{λ} is the modulus of elasticity of the material, l_{po} is crack length, r_{po} is the radius of the pore.

The last level in this classification of cement composite is Nano-level, in which the hardened cement paste between "big" pores is assumed with the main inhomogeneities shown by

"little" pores named capillary pores. The typical dimension of this "little" pores is in the range of 10^{-4} mm, whereas the linear dimension of RVE in this level is approximately $5e^{-4}$ mm. Some modifications in the mechanical properties of materials represent the effect of "little" pores in the model, and they will be geometrically neglected, same as in the meso-level[126].

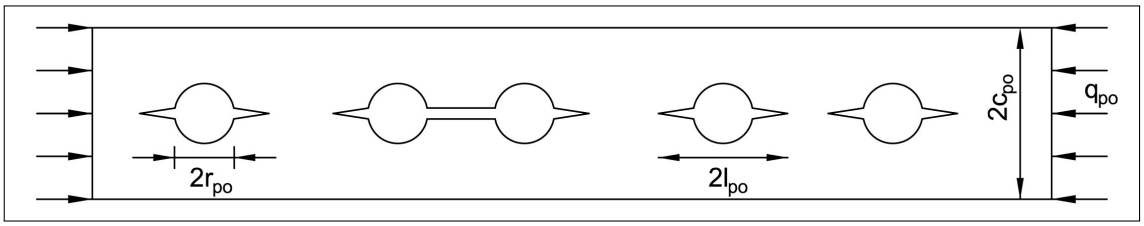

Figure 2.1: simplified model of micro-level of concrete(hardened cement paste)[126]

Further studies have argued that the macro scale's fracture behavior can be indicated within characteristic material structure and processes on meso- and micro-levels with no significant need for study in the nano-level. Thus, concrete is considered a homogeneous material on the macro level, and corresponding mechanical properties are utilized in the analysis of concrete structures in civil engineering. In the meso-scale level, air voids, cracks, inclusions, and interfaces are considered. Thus, in fracture meso-models, concrete is assumed to be a three-phase system consist of mortar matrix, aggregates, and interfacial transition zone(ITN), see Fig. 2.2(b). On the other hand, on the micro-level, each component of the concrete structure, i.e., the cement matrix, aggregates, and ITN, are considered highly heterogeneous with complex structure, see Fig. 2.2(a)[8].

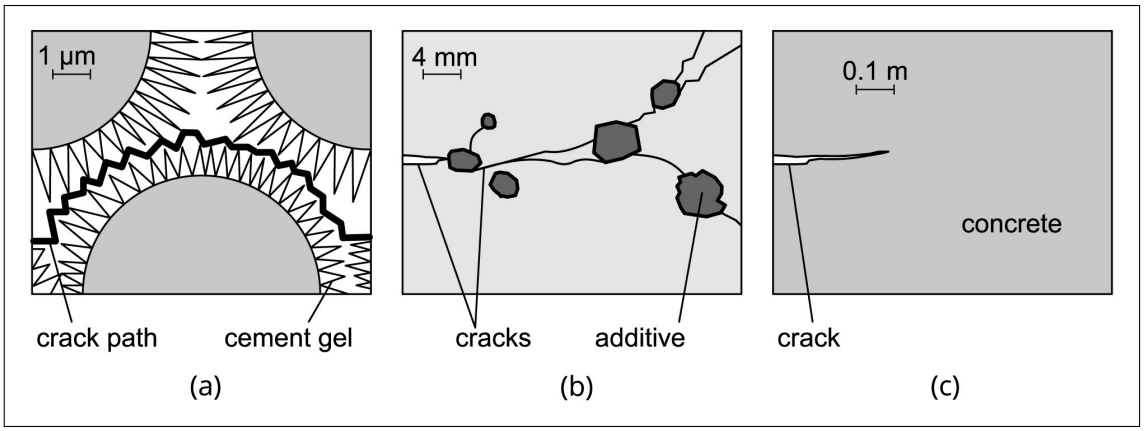

Figure 2.2: Multi-level system a)micro, b)meso-, c)macro-level[79]

It has been proven that the classification of concrete structure in different levels helps describe the real behavior in a simplified and approximate way. A hierarchic system of three different

levels shows that these different models are connected systematically. It means that models on a given level depend on the previous model results, see Table 2.1[123].

Structural Level	Characteristic features	Type of models
Micro-level	Structure of hardened	Material sciencemodels
Meso-level	Pores, Cracks, Inclusions, Interfaces	Material engineering models, Mechanical and numerical models
Macro-level	Geometry of structural elements	Structural engineering models, Material laws

Table 2.1: Characteristic structural features of hardened cement paste and concrete[123]

2.2 STRAIN HARDENING CEMENT-BASED COMPOSITIES(SHCCs)

2.2.1 Historical background

The idea of using fibers in concrete became universal in the 1960's following studies on the use of steel fibers in concrete, while it had been noted back in 19874 by Berard[21, 107, 108]. Krenchel published a fundamental study on FRC in 1964 in Denmark[59], while scientists in the U.K. tested the usage of glass fibers to strengthen the cement matrix[77, 32]. After that, numerous studies were carried out with a focus on brittle matrix composites such as cement-based composites[6, 57, 56]. There was a lack of information on the tensile stress-strain response of composite since the fracture mechanic approach was used for dealing with the tensile strength of FRC by [108]. The first time, the tensile stress elongation curve was published in papers by Naaman in 1972[84, 82, 92]. Naaman used straight smooth steel fibers within aspect ratio less than 100 and a relatively high volume fraction of fibers(from 1. 5 to 3%). However, no multiple cracking was reported due to relatively weak bond properties. After first cracking, all the mentioned experiments on composites showed strain-softening behavior with localization at that crack section, typical strain-softening tension response is shown in Fig. 2.3[84, 89].

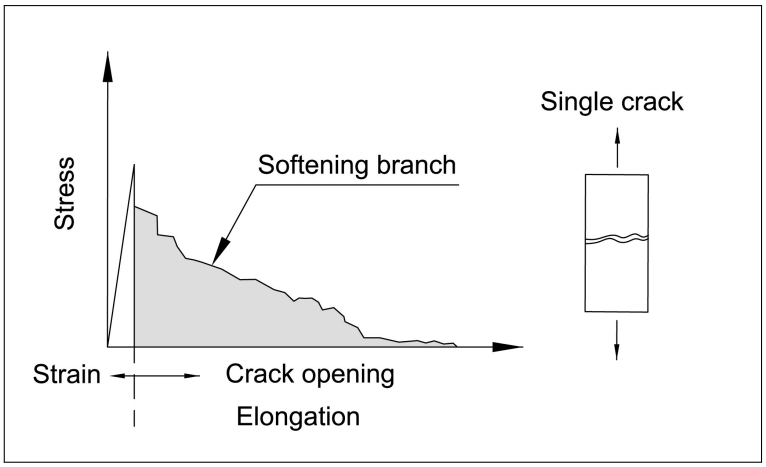

Figure 2.3: Multi-level systems For concrete

Plenty of studies were published in the 1970s with a focus on fiber-reinforced cement composites [43, 56, 95, 112, 111]. The desired performance was described in terms of high strength and ductility. For the first time in the RILEM Symposium in 1978, the strain-hardening term was used by Kasparkiewicsz, who reported on evidencing of multiple cracking and strain hardening behavior on several tensile tests. The specimens were paddle-shaped and contained 2% by volume hooked-ends steel fibers[1, 89]. Naaman and Shah published their research, where they reported a particular response of tensile specimens consist of 2. 5% steel fibers by volume. The enumerated specimens showed a ductile response with the so-called "inelastic multiple cracking range". They demonstrated the qualitative response of FRC composites in strain-softening and strain-hardening stages. These load-elongation curves concluded all fiber-reinforced composites, similar to what is shown in Fig. 2.4[85].

Slurry infiltrated fiber concrete(SIFCON) was introduced in the early 1980s. To produce this composite, first, the mold was filled by fibers, then the cement-based slurry was added to the fiber network. This production method result in comparatively high range of fiber content from 5% to 12%[61, 62]. Numerous studies illustrated that SIFCON as an FRCC could show relatively high ductile behavior besides high strength in tension, which fulfilled both features as a desirable composite and belongs to strain-hardening composites [87, 89, 91, 86].

After that, Naaman suggested using a new classification to characterize this cement composite behavior named "High-Performance Fiber Reinforced Cement Composites"(HPFRCC). This new term used for composites with high strength and toughness-ductility[87, 86]. Namman had used conventional fiber reinforced concrete and "high performance". Two terms represent the later, i.e., "strain-softening", "strain-hardening" in further researches[87].

Afterward, in the 1995 workshop, three different models were discussed to describe fibers' critical volume fraction to achieve multiple cracking and strain-hardening behavior. These three models are discussed in detail in [93].

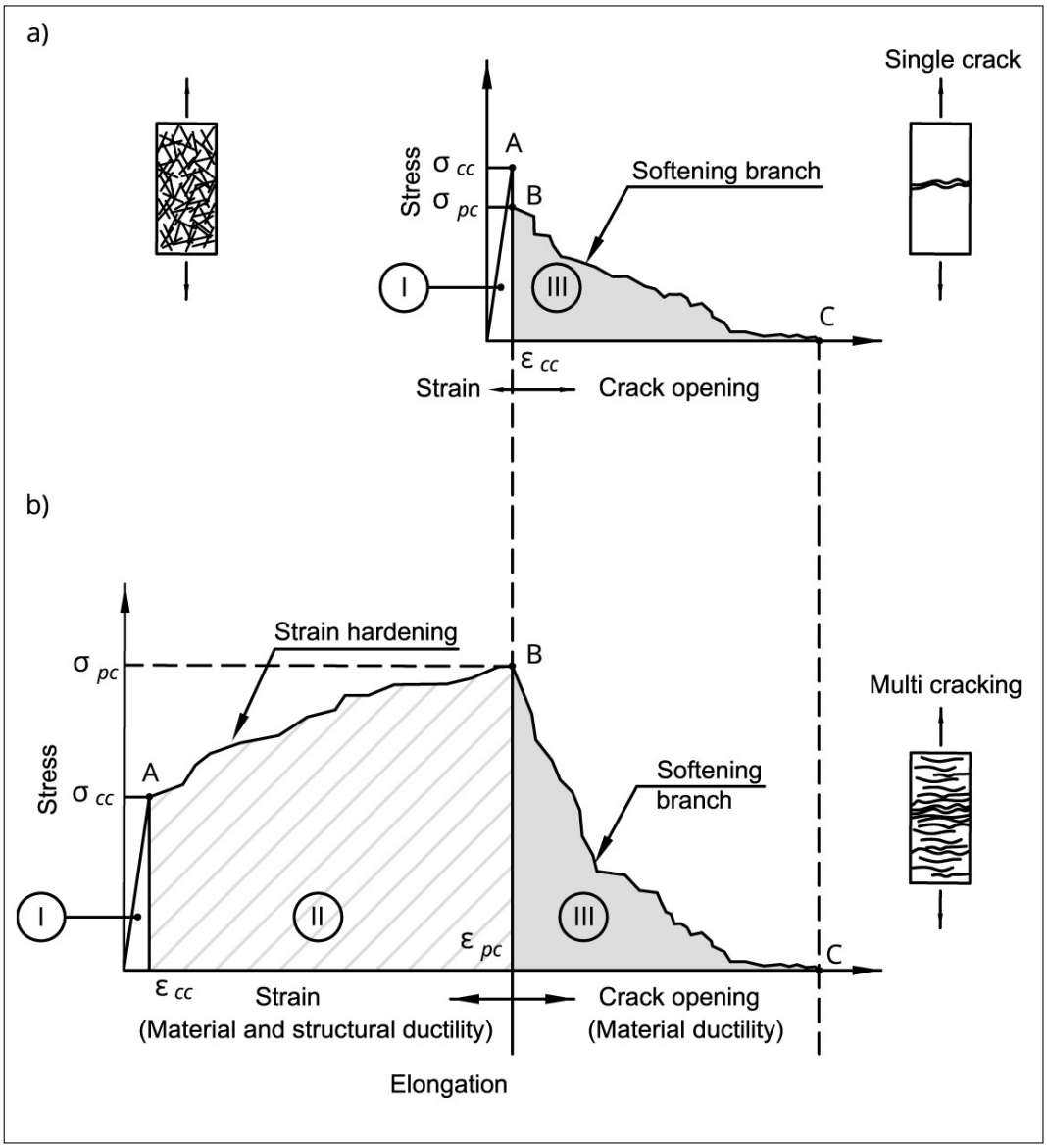

Figure 2.4: Stress-strain response under tensile loading a)Conventional strain-softening FRCC b)Strain-hardening FRCC (HPFRCC) [89]

Fiber-reinforced cement composites have been used in numerous applications. It should be pointed out that the particular presence of fibers caused changes in the matrix's fundamental properties, e.g., tensile strength, strain capacity, and crack tip toughness[111]. This presence can be as stand-alone or in combination with reinforcing bars and prestressing tendons; besides, they can be utilized as a strengthener in the existing structure in repair and rehabilitation work. An extensive range of properties of the composite material can be obtained

with wide ranges of fibers and cement matrix properties, the main fiber characteristics of interest in fiber-reinforced cementitious composites are shown in Table 2.2.

Fiber characteristics			
Material			**Physio-chemical**
Natural organic	**Natural mineral**	**Man-made**	
Wood Jute Bamboo Straw Horse hair	Asbestos Rock wool	Steel Polymers(synthetic) Glass Carbon Metallic	Density Surface roughness Chemical stability Fire resistance Non-reactivity with cement

Mechanical	**Geometrical**		
	Dimensions	**Section**	**Shape**
Strength Elastic modulus Transverse modulus Stiffness Ductility Elongation to failure	Length Diameter	Circular Elliptical Square Rectangular Flat	Smooth Deformed Indented Etched Crimped Coiled with end paddles End hooks 2D, 3D

Table 2.2: Main fiber characteristics of interest in fiber reinforced cement composites[88]

Stand-alone applications include mostly thin products such as cladding, cement boards, pipes, electrical poles, and slabs on grades and pavements. Fibers are also utilized in hybrid applications to support other structural materials such as reinforced and prestressed concrete, and structural steel. e.g., impact and seismic resistant structures, jacketing for repair and strengthening of beams and columns, and, in the case of steel, encased beams and trusses to improve ductility and fire resistance. Unique applications of high-performance fiber-reinforced cement composites, e.g., bridge decks and unique structures. e.g., offshore platforms, spacecraft launching platforms, super high-rise structures, blast-resistant structures, bank vaults, and other high-end structures, see Table 2.3[88].

Strain-Hardening FRC composites		
Hybrid application with reinforced-concrete and/or prestressed concrete		
Energy/Thoughness	**Mechanical properties**	**Cracking control**
Impact, Ductility, Seismic, etc.	Tension, Shear, Bending, etc.	Seviceability, Corrosion resistance, Durability, etc.

Stand-alone applications		**Hybrid applications with steel members**
Thin sheets, Pipes, boards, shells	Repair, retrofit, rehabilitaion	Encased trusses and beams, Fire resistance

Table 2.3: Advantages of using SHCCs in structural applications[88]

2.2.2 Strain-hardening behavior

Strain-hardening cement-based composites(SHCCs), a particular class of fiber-reinforced concretes, can develop controlled multiple cracks while subjected to incremental tensile loading conditions [73, 67, 90]. The addition of a small volume of short fibers can improve structural behavior regarding tensile strength and ductility. In previous studies, the contribution of short fibers in overall behavior and specifically in the post-cracking phase is considered with smeared crack formulation or crack bands within the finite element method [24, 80, 7].

Numerous test methods have been developed to study the behavior of Cement-based composites under tensile loading. Concerning their tensile response, FRCC can be classified into two categories, namely, strain-softening composites and strain-hardening(HPFRCC), see Fig. 2.4.

Strain-softening FRC composites tensile response, see Fig. 2.4(a), started with the crack-free state and followed by strain-softening branch and immediate crack localization after the first crack. On the other hand, the tensile response of HPFRCC, shown in Fig. 2.4(b), starts with a sharp initial slope till reaching to first cracking, part (I), and continues with the strain-hardening branch (part II) where the micro-cracks form and propagate. The slope in the crack-free state depends on the stiffness of the cement matrix and fibers, while Young's modulus of the concrete is affected by Young's modulus of the composite. The extension amount pertains to fiber stiffness and fiber volume fraction. The first stage is characterized by its stress and strain coordinates (σ_{cc},ϵ_{cc}), where the first structural cracking forms and the strain-hardening branch ends in the peak point (shown with point(B) in Fig. 2.4(b))

and characterized with its stress and strain (σ_{pc},ϵ_{pc}). In this stage, micro/Macro cracks propagate, and multiple cracking develops until one crack becomes critical and specify the crack localization, and part III starts. The critical crack will open under increased straining while crack propagation is stopped, and other cracks become narrower slightly[89]. Three stages of tensile behavior of SHCCs consist of elastic phase, strain-hardening and multiple cracking phase and softening phase are shown in Fig. 2.5

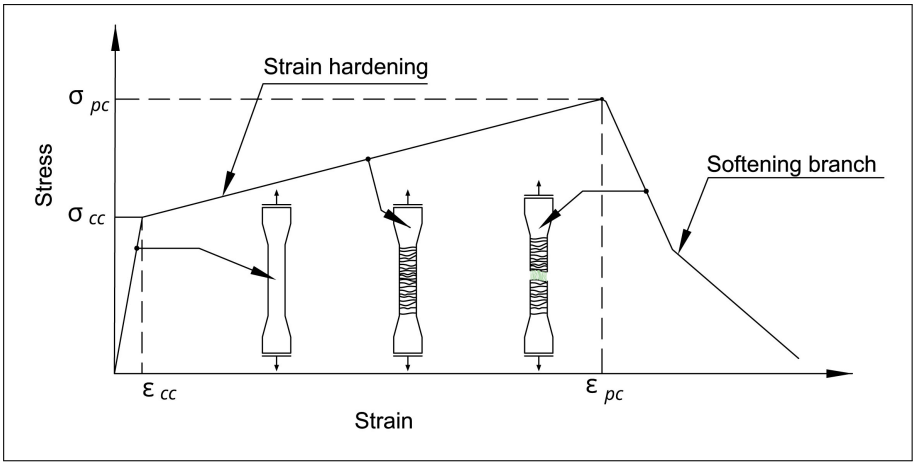

Figure 2.5: Tensile behavior of SHCC(elastic phase, strain-hardening and multiple cracking phase and softening phase)[28]

The desired strain-hardening behavior usually reached through a high number of thin, short polymer fibers mixed with the fine-grained concrete matrix. The modeled composite is a high-strength SHCC made with ultra-high molecular weight polyethylene (UHMWPE or shortly PE). The fibers have a length of 6 - 10 mm and a diameter of 20 μm [29]. Nominal strength is 2 500 N/mm^2 with a brittle failure mode. Fibers are mixed up to 2 % of volume with the cement matrix.

The enumerated high strength mixture has a very high cement content and a significant low water-to-binder ratio of 0. 18, which leads to high homogeneity and satisfactory workability. The cement paste consists of cement and silica fume with no fly ash and a small amount of fine sand. The silica fume makes the nature of the mixture highly cohesive. This cementitious matrix has high packing density in fresh states and a dense microstructure on the hardened stage in order to make a proper interaction with the hydrophobic PE fibers. The average spread diameters are 120 mm after cone lifting and 145 mm after 15 jolts in flow test[30, 31, 28].

Parameter	Unit	Value
CEM I 52.5 R-SR3/NA	[kg/mm^3]	1 460
Fly ash Steament H4	[kg/mm^3]	–
Silica fume Elkem 971	[kg/mm^3]	292
Quartz sand 0.06 - 0.2 mm	[kg/mm^3]	145
HRWRA Glenium ACE 460 (BASF)*	[kg/mm^3]	35
Water	[kg/mm^3]	315

HEWRA - high range water reducing agent(superplasticizer)

Table 2.4: Mixture composition of concrete[28]

2.2.3 Micromechanics of SHCC

The distribution and orientation of fibers are of crucial importance to the mechanical properties of composites. The angle of inclination and position of short fibers can be randomly selected in SHCC, while these two parameters are computed precisely in the design of continuous fibers. Since these short fibers are added to the cement paste during the mixture stage, this leads to random distribution and fiber orientation in the cementitious matrix.

Marshal and Cox describe steady-state cracking in fiber with an analytical formulation, which is based on energy balance, see Fig. 2.6[78]. In this figure, the gray area between the stress-displacement relation for bridging fibers and the constant stress line represents the applied stress and should be less than complimentary energy, is equal to $J_C/2$ where J_C is the crack tip toughness and the critical condition for the matrix is determined by the applied stress (σ_a). This area is constant for specific matrix and volume fraction of fiber[78]. Further studies adapted this formulation for randomly distributed fiber reinforce cementitious with short fibers and a particular focus on crack bridging mechanisms [68, 71]. In these studies, it is assumed that the fiber will experience a complete pullout with a frictional bond, which is weak enough to prevent fiber's rupture.

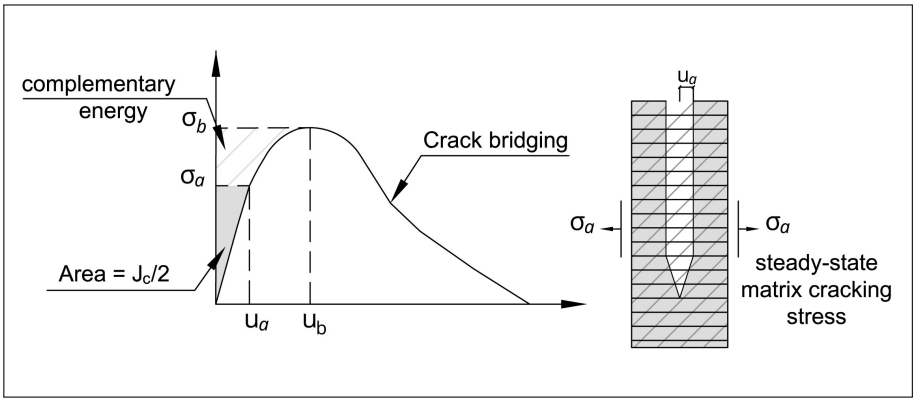

Figure 2.6: Steady-state matrix cracking stress[78],[28]

The crack bridging is defined based on force equilibrium for a single fiber embedded in the matrix with an embedded length l whereby the load is applied on its free end. In Fig. 2.7, the load-displacement relation for the frictional pullout of a single fiber is shown. The debonding occurs when the applied load (P) is increasing incrementally. The fiber is stretching along the debonded zone, which leads to an increase of displacement (δ) in the free end. Linear stress distribution along the debonded zone assumes that the displacement caused by elastic deformation of the bond is not considered[28].

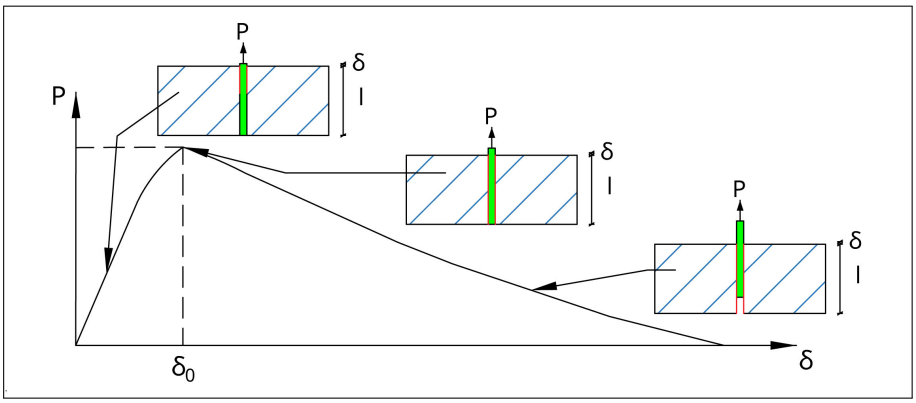

Figure 2.7: Load-displacement relation for the frictional pullout of a single fiber[28]

The resulting force-displacement relation up to the peak pullout load is

$$P(\delta) = \frac{\pi}{2}\sqrt{(1+\eta)E_f d_f^3 \tau \delta e^{f\phi}}, \quad \delta \leq \delta_0 \tag{2.2}$$

where E_f is modulus of elasticity, d_f is fiber diameter, τ is the frictional bond strength and δ_0 is a critical displacements at which fiber is fully debonded along the entire embedded length of l and is computed by Eq. (2.3)[28].

$$\delta_0 = (4l^2\tau)/[(1-\eta)E_f d_f] \tag{2.3}$$

with

$$\eta = (V_f E_f)/(V_m E_m) \tag{2.4}$$

where V_f and V_m are the fiber and matrix volume fractions, respectively. When debonding is completed, fiber pullout starts and the pullout load decreased. While $\delta_0 < \delta \leq l$ this force is related to the displacement and computed by Eq. (2.5) whereby frictional bond is assumed

to be constant and the elastic stretching of the fiber is neglected

$$P(\delta) = \pi\tau l d_f(1 - \frac{\delta}{l})e^{f\phi}, \quad \delta_0 < \delta \leq l \tag{2.5}$$

2.2.4 Fiber inclination angle

Positive effect of fiber inclination on the pullout resistance can be seen with the exponential term in Eq. (2.2)[70],[69]. Considering the contribution of individual fibers in a composite with randomly distributed and oriented fibers, a relation is proposed in [70] for crack bridging, see Eqs. (2.6). In this formula, the embedded length for a fiber with length (L_f) is between 0 and $L_f/2$ on either side of the crack shown in Fig. 2.8.

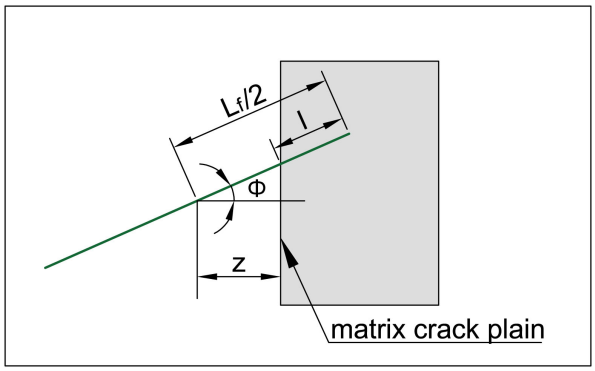

Figure 2.8: A fiber crossing a matrix crack[70]

$$\sigma_B(\delta) = \frac{4V_f}{\pi d_f^2} \int_{\phi=0}^{\frac{\pi}{2}} \int_{z=0}^{(L_f/2)cos\phi} P(\delta)p(\phi)p(z)\,\mathrm{d}z\,\mathrm{d}\phi \tag{2.6}$$

where ϕ is orientation of fiber with respect to tensile loading direction, d_f is fiber diameter, V_f is fiber volume fraction, $p(\phi)$ and $p(z)$ are the probability density function of the orientation angle and centroidal distance of fibers from crack plane[28]. A uniformly random location and orientation of fiber is assumed whereby

$$p(\phi) = sin(\phi), \quad 0 \leq \phi \leq \frac{\pi}{2} \quad \text{and} \quad p(z) = \frac{2}{L_f}, \quad 0 \leq z \leq (\frac{L_f}{2}) \cdot cos(\phi) \tag{2.7}$$

and the energy absorption for a single fiber of embedded length l which is pulled out within angle ϕ is computed as following

$$G_s = \frac{\pi}{2} d_f \tau l^2 e^{f\phi} \tag{2.8}$$

where τ is bond strength of fiber-matrix interface and f is snubbing friction coefficient[70].

From previous studies, it is observed that the increase in local friction due to high compression at the matrix region near the fiber exiting point has caused the increase in pull-out forces. Thus, for specimens in pull-out test with the same end-slippage and embedded length l, the bridging force will be increased with increase of the inclination angle (ϕ) [70]. This effect is called "snubbing effect", shown in Fig. 2.9, and has been studied for cementitious composite with synthetic fibers in [69]. The relation between bridging force for angle pull-out ($P|_\phi$) and ($P|_\phi = 0$) for $\phi = 0$ is explained by:

$$P|_\phi = e^{f\phi} \cdot P|_{\phi=0} \tag{2.9}$$

where snubbing friction coefficient f is an interface material parameter, depends on each fiber/matrix combination[70] and different values in the range of 0 and 1 are recommended in literature[125], [124].

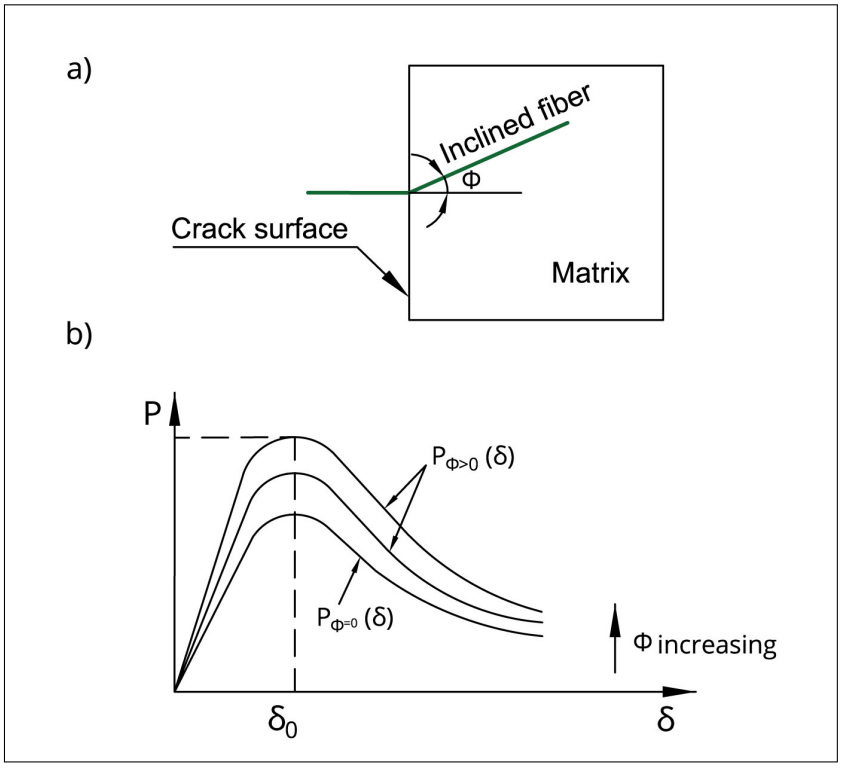

(a)

Figure 2.9: a)Frictional pulley model b)load-displacement relation for the frictional pullout of the inclined single fiber [125]

2.2.5 Bond Behavior of Single Fibers

Experimental references for the following simulations are explained in detail in [31, 28]. Test set up is shown in Fig. 2.10(a) and Fig. 2.10(b) shows the force-displacement graphs of PE fibers out of the high-strength matrix obtained at different displacement rates of 0.005 mm/s with embedment length $2mm$. As they are characterized by relatively large scatter, mean data are used as an experiment reference for the following simulations, see Fig. 2.11(a,b).

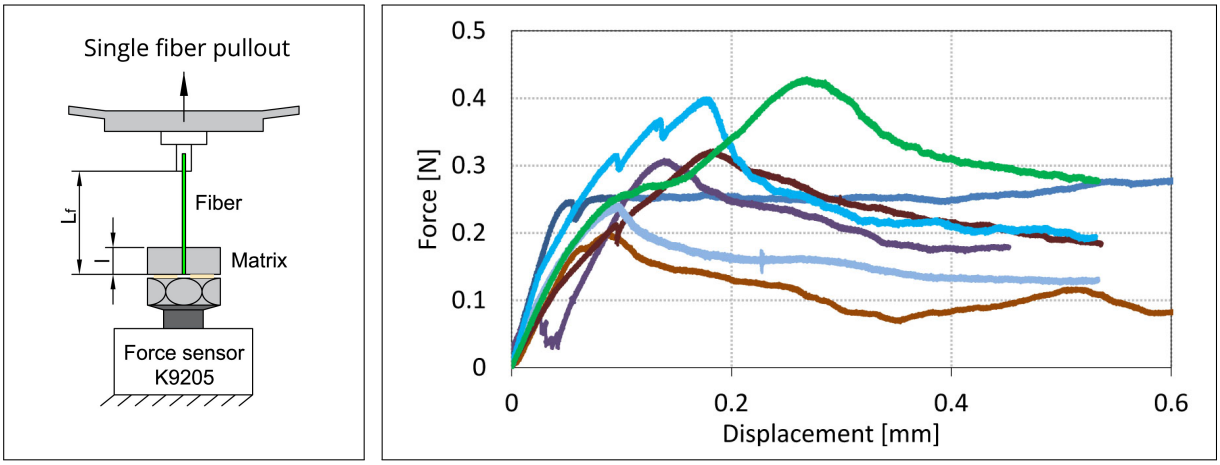

(a) (b)

Figure 2.10: a)Testing setup for single fiber pullout b)pullout curves of HDPE fibers out of the high-strength matrix M2 obtained at different displacement rates of 0.005 mm/s; embedment length 2 mm[31, 28]

Bond stress τ has a unit [N/mm^2]. It is advantageously transformed into a stress flow T with a unit [N/mm] by multiplying it by fiber circumference U_f

$$T = U_f \tau = 2\sqrt{\pi A_f}\,\tau \tag{2.10}$$

derived from, e.g., the fiber cross sectional area A_f. The mean value for bond stresses, shown in Fig. 2.11(b), is defined based on force equilibrium for single fiber and with the use of mean values obtained from force-displacements curves, shown in Fig. 2.11(a)[31, 28]. It should be pointed out that the deformation related to the free length part of the fiber is neglected in the first approach, and its effect will be considered and adjusted later in the simulation of a single fiber pullout test. A typical course formulated as multi-linear is used for bond slip behavior and shown in Fig. 2.11(b). The same is used for the negative range with a reversal

of signs of slip and bond stress. It is characterized by an initial elasticity, maximum bond stress at a prescribed slip, and constant residual bond stress from another prescribed slip.

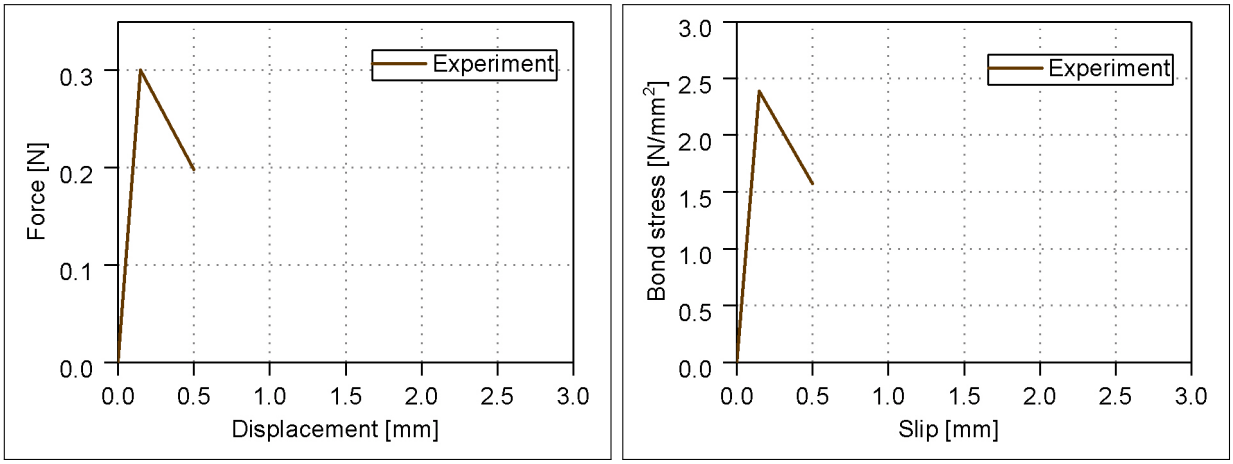

(a) (b)

Figure 2.11: Mean data computed based on single fiber pullout tests result; a)force-displacement and b)bond law (these two graphs will be used as experiment references for further simulations and reffered as "Experiment" curves

DIANA software version 10.3 is used for modeling this experiment and its setup. Single fiber is modeled as embedded truss elements and divided into eight elements. The embedded reinforcements used in simulations within have several main characteristics, i.e., a)Reinforcements are embedded in structural elements, the so-called mother elements, whereas Diana ignores the space occupied by an embedded reinforcement. The mother element neither diminishes in stiffness, nor weight. The embedded reinforcement does not contribute to the weight (mass) of the element, b)Embedded reinforcements do not have degrees of freedom of their own and c)in embedded reinforcements the strains in the reinforcements are computed from the displacement field of the mother elements, which implies perfect bond between the reinforcement and the surrounding material.[33].

A bi-linear material model, derived from mean data of pullout curves, is assigned to the bond element, see Fig. 2.12. The residual stress is assumed with nearly zero to cover fiber pullout at least approximately. Precise modeling of fiber pullout would require a large displacement approach that exceeds the current small displacement assumption's scope. The softening part of bond law $B-1$ is an extrapolation of the softening path of the experiment curve until the bond stress reaches zero value.

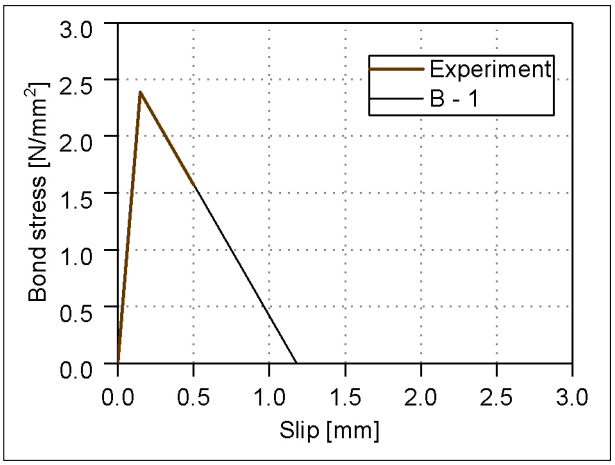

Figure 2.12: Bond law - B - 1 (derived from mean data)

Typical property values for fiber which later will be used for the following numerical simulations are given in Table 2.6.

Parameter	**Unit**	**Value**
Young's modulus E	[N/mm^2]	29 000
Poisson's ratio ν	-	0.2
Tensile strength f_{ct}	[N/mm^2]	3.8
Fracture energy G_f	[N/mm]	$100 \cdot 10^{-3}$
Critical crack width w_{cr}	[mm]	0.079

Table 2.5: Fine grained concrete property values

Parameter	**Unit**	**Value**
Young's modulus E_f	[N/mm^2]	80 000
Embedded length L_{emb}	[mm]	2
Free length L_{fr}	[mm]	5
Diameter $\oslash$	[mm]	0. 02
Cross sectional area A_f	[mm^2]	$3.14 \cdot 10^{-4}$

Table 2.6: Fiber property values

For modeling the experimental set-up in DIANA, the load will be applied in displacement control conditions on a dummy mass representing the upper support. This dummy mass is connected to the single fiber tip within a translation spring, representing the free length of the fiber. The stiffness of this spring is computed from Eq. 2.11.

$$K_{spring} = E_{fiber} \cdot A / L_{fr} = 5.03 N/mm \tag{2.11}$$

where E_{fiber} is fiber's Young's modulus, A is fiber's section area and L_{fr} is free length of fiber.

Matrix is modeled with eight-node isoparametric solid brick elements. This element is based on linear interpolation and Gauss integration nodes. The matrix elements located at the bottom support surface are entirely tied in all degrees of freedom to a corner node. This node is called a master node, and it is enough to fix this node as point support. Thus, the total force-displacement graph can be obtained easily by reading the total response in the master node directly, see Fig. 2.13.

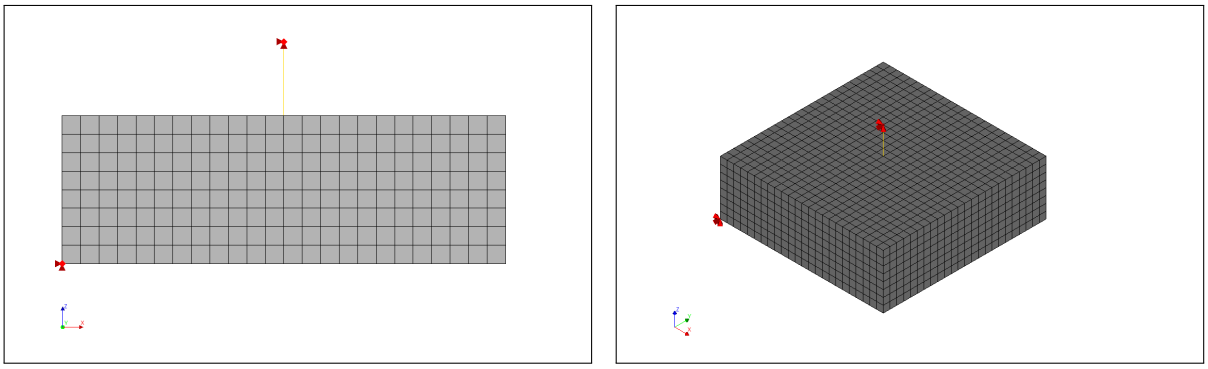

(a) 2D view (b) 3D view

Figure 2.13: Finite element model of single fiber Pullout test in DIANA; a)2D view, b)3D view

The bond behavior is modeled with a bond-slip mechanism where the relative slip of the reinforcement and the concrete is described in a phenomenological sense. The mechanical behavior of the slip zone is then characterized by the interface element with a zero thickness. The constitutive laws for bond-slip defined based on a total deformation theory, which expresses the tractions as a function of the total relative displacements. In Diana, the relation between the normal traction and the normal relative displacement is assumed to be linear elastic whereas, in nonlinear simulation, the elastic shear stiffness will be replaced by computed stiffness derived from predefined bond law in calculations[33].

Several parameters are needed as input for defining a bond material in DIANA, i.e., shear stiffness modulus, normal stiffness modulus, and nonlinear bond law curve. Diana offers four predefined curves and the user-defined multilinear diagram for the relations between shear traction and slip. Below are some guidelines on how to assess the interface elastic stiffness

parameters in DIANA to compute normal and shear elastic stiffness modulus, see Eq. 2.12.

$$K_n = 100 \cdot n_f \cdot E_{bulk}/L_{emb} = 1.18e7 N/mm \quad \text{and} \quad K_t = K_n/100 = 1.18e5 N/mm \quad (2.12)$$

where K_n is elastic stiffness of interface in the normal direction, n_f is number of fiber divisions, E_{bulk} is bulk's Young's modulus and the factor 100 defines the ratio between displacements in interface (which should be small) and continuum elements. K_t is elastic stiffness of interfaces in tangential direction.

As mentioned before, the bond-slip models for bond-slip reinforcement bars include a non-linear relation between shear traction and shear slip, whereas the relations between normal tractions and normal relative displacements are kept linear. A multilinear bond-slip curve is specified with two values for each point, i.e., shear slip values and corresponding shear traction values, see $B-1$ curve in Fig. 2.14(a). The first point must be the origin (0,0), and the diagram may also contain descending parts (softening). If the initial shear modulus does not correspond to the diagram's initial slope, the modulus is replaced by the initial slope of the diagram during the initialization phase of the nonlinear analysis[33].

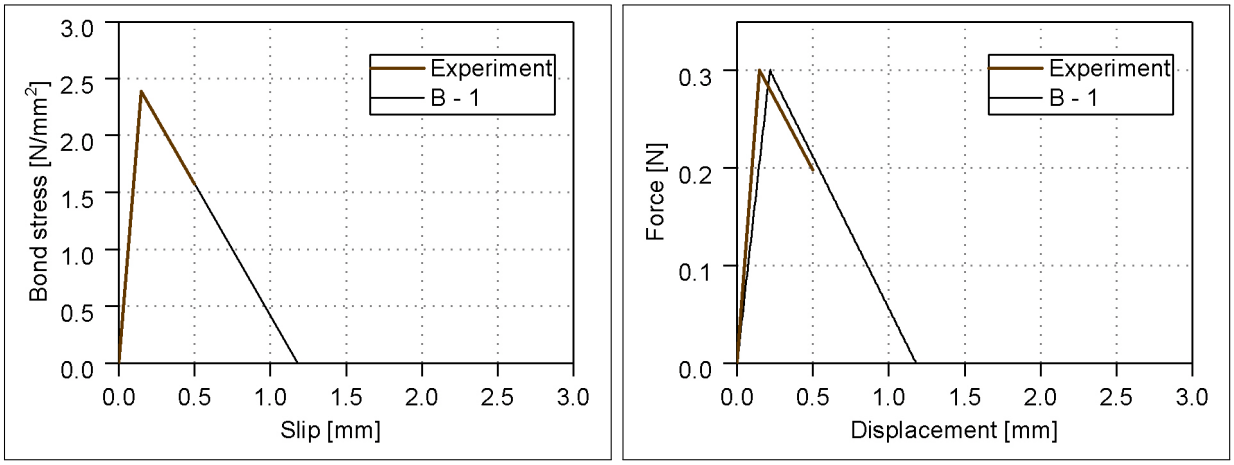

(a) (b)

Figure 2.14: Single fiber pullout simulation - B - 1 bond law a)Bond law graph b)Force-displacement result

In the second step, the Hordijk material model is used for the softening part of the bond curve. Within the Hordijk material model, the bond stress is decreasing gradually in softening, whereas the area under the softening path, which is related to dissipation energy, is mostly the same as the corresponding area in bond law $B-1$. As it is mentioned before, the bond laws are defined by multilinear curves in DIANA. Thus, the points for the bond

law $B-2$ are computed manually concerning the Hordijk formulation explained in [33], see Fig. 2.15(a). In Fig. 2.15(b), the force-displacement curve related to pullout simulation using $B-2$ as bond-slip relation of bond elements is shown, and more modifications are needed to achieve better agreement with experiment result.

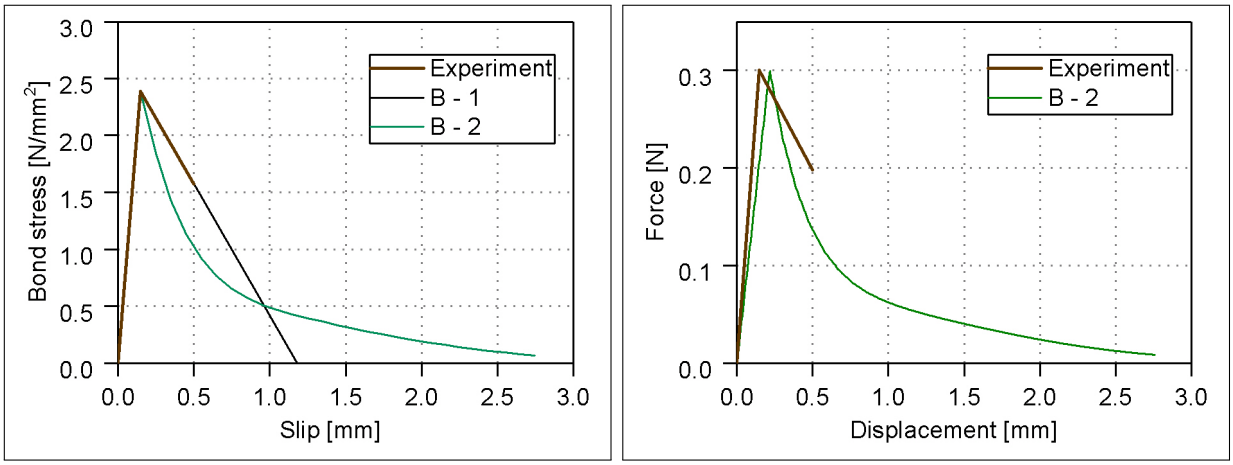

(a) (b)

Figure 2.15: Single fiber pullout simulation - B - 2 bond law a)Bond law graph b)Force-displacement result

There is a slight difference between force-displacement result curve of experiment and simulation curve for $B-1$ bond law, see Fig. 2.14(b). This difference is due to the first assumption of neglecting the effect of the fiber free length. To consider this effect and adjust the bond behavior, the bond peak will be shifted to the lower slip with the value has been computed as a difference between experiment result and $B-1$ force-displacement curve, see Fig. 2.14(b), while the slope in softening part of new bond law is kept the same as the slope in $B-1$ bond law. This bond law is called: $B-3$ and shown in Fig. 2.16(a). In Fig. 2.16(b), the force-displacement curve related to pullout simulation using $B-3$ as bond-slip relation of bond elements is shown.

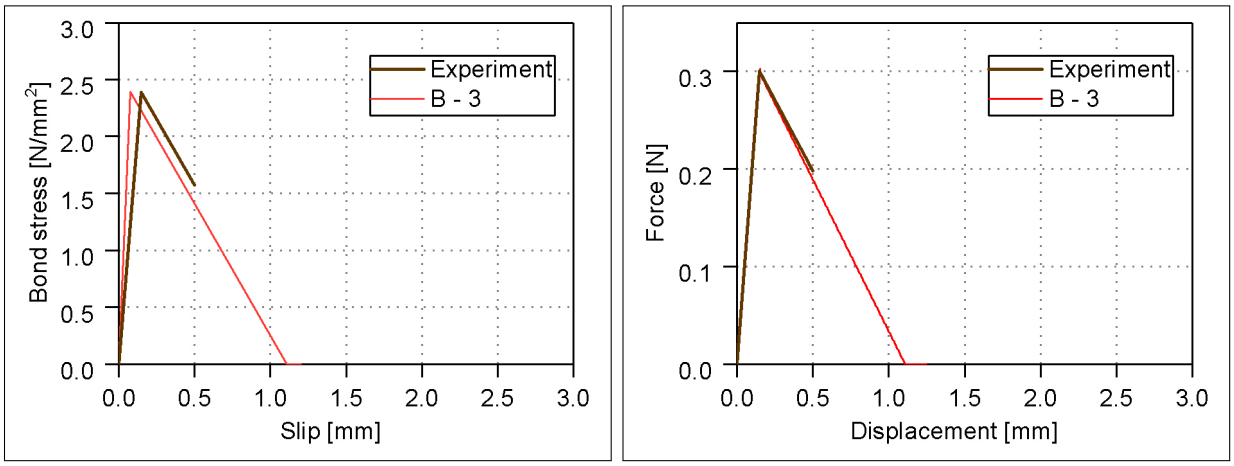

(a) (b)

Figure 2.16: Single fiber pullout simulation - B - 3 bond law a)Bond law graph b)Force-displacement result

The results related to $B-3$ bond model had good agreement with experimental result, see Fig. 2.16(b). As it is mentioned before, the residual stress is assumed with nearly zero to cover fiber pullout at least approximately. However, the area under bond-slip graph, which is related to the dissipation energy, is considered higher in bond law $B-3$ than the values derived from mean data, see Fig. 2.16(a). In final step, the bond law is modified with several trail and error in a way to have the same area for result curve equal and the experiment curve. This modified curve is called $B-4$ and shown in Fig. 2.17(a). Results related to this material model assigned to bond elements is shown in Fig. 2.17(b). The area under softening phase of pullout is the same for graph derived from mean values of experiment and simulation within bond law $B-4$.

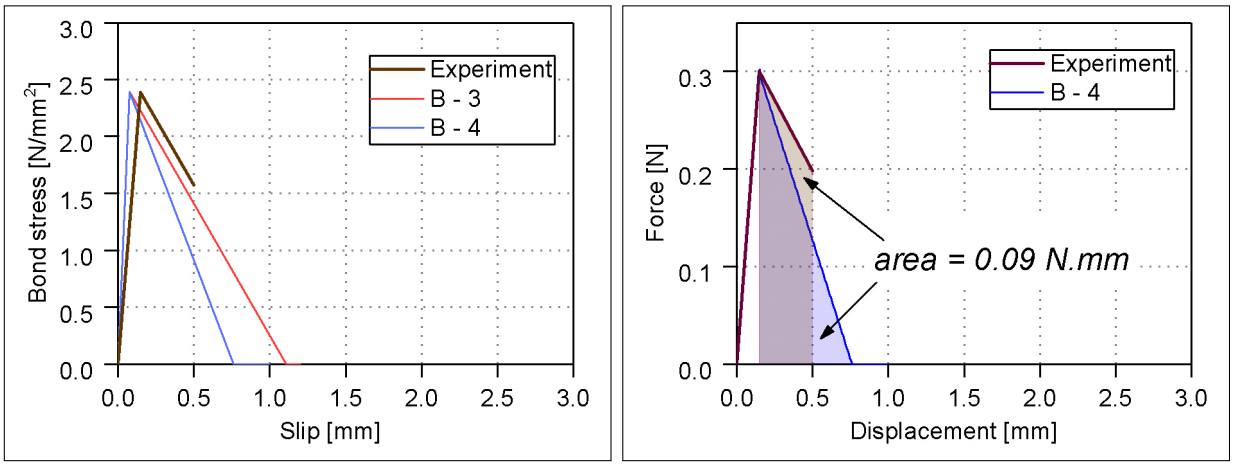

(a) (b)

Figure 2.17: Single fiber pullout simulation - bond law - B - 4 a)Bond law graph b)Force-displacement result

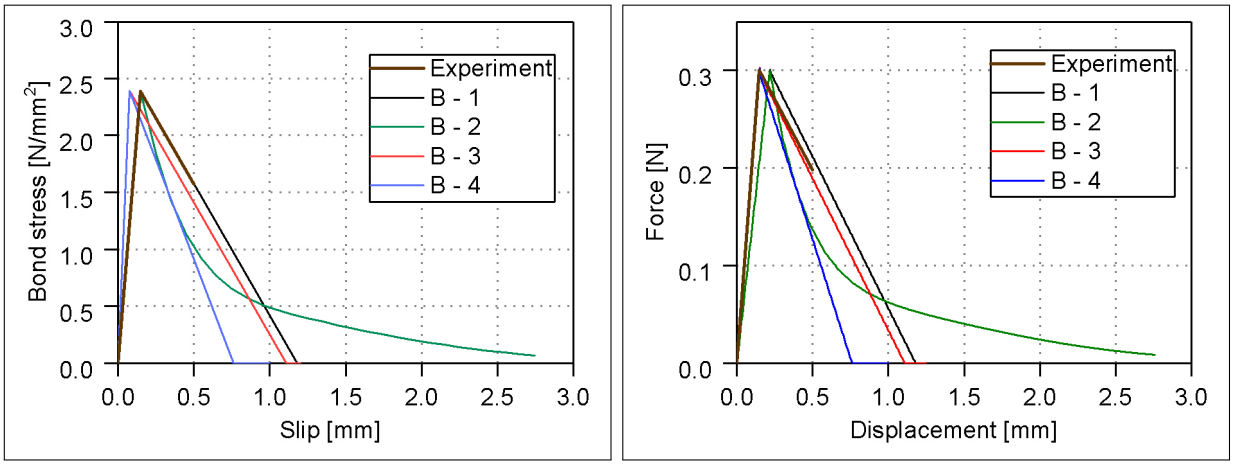

(a) (b)

Figure 2.18: Single fiber pullout simulation - bond laws B - 1,2,3 and 4 a)Bond law graph b)Force-displacement result

To give a better overview of the performed adjustments, all assigned bond laws and corresponding pullout simulation curves are shown together in Fig. 2.18(a,b). The final comparison between the simulation for $B-4$ bond law and experiment result has proven that with this bond law, the initial slope, maximum pullout force, and the dissipation energy analyzed by the simulation are in good agreement with corresponding values in experimental reference. This bond law will be used later in chapter 5 as a first assumption in the simulation of the 2D-dumbbell specimen.

3 DISCRETIZATION APPROACHES

The Finite Element Method(FEM) has prevailed upon other numerical methods in the calculation of mechanical behavior of components and structural mechanics for many years [129, 10, 15], about applications in the reinforced concrete structure, see [45]. However, dependency on the geometry of materials will bring lots of limitations, especially when aggregates are considered in the model in different ranges of sizes and locations. Thus, an unstructured irregular mesh is needed to cover all the edges adequately. Hence, several discretization methods have been introduced, regardless of geometry and topology of inclusions. As an alternative to FEM, new functions have been formulated which are no longer restricted to finite elements, e.g., Element Free Galerkin(EFG) method[16, 18, 38, 66, 19]. In EFG method, the omission of elements allows excellent flexibility in the arrangement of nodes, facilitating adaptive mesh refinement, and large deformation will appear further. Another method which allows high geometric adaptability with advantages for solving problems of structural mechanics is Isogeometric Analysis(IGA) method. IGA method used the "Non-Uniform Rational B-Splines"(NURBS) approach. NURBS are standard approaches in CAD for the description of free form surfaces, see [25, 36, 14, 96, 48].

The mesh free methods are highly recommended for complex simulation, e.g., large material distortion, impact loading condition, moving boundaries, the special interaction between elements moving discontinuities, and widespread crack propagation. In this chapter, several random 2D sections will be analyzed within regular and irregular mesh methods, and the results will be discussed briefly, whereas the formulations are discussed in detail in[49], and presented results are published in[113].

3.1 INTRODUCTION TO MESOSCOPIC SCALE

Based on the heterogeneous concrete structure, different levels are considered to investigate different effects of crack propagation and crack arresting. In the meso-scale level, air voids,

cracks, inclusions, and interfaces are considered. Thus, in fracture meso-models, concrete is assumed to be a three-phase system consist of mortar matrix, aggregates, and interfacial transition zone(ITN)[8]. In the following simulations, the matrix and aggregates are modeled and the ITN is neglected in the model. Different scale of modeling for concrete is discussed in detail in Section 2.1.

3.1.1 3D Random mesoscopic model

A 3D random mesoscopic model has been generated by a program written in MATLAB software. This model consists of aggregates and mortar, while coarse aggregates are presented as spheres with randomly distributed size and location. The random distribution of aggregate is based on Fuller's curve. This curve can be described by a simple equation given below and presented in Fig. 3.1.

$$P(d) = (\frac{d_i}{D})^n \tag{3.1}$$

Where as: $P(d)$ is Cumulative percentage passing a sieve with the diameter d_i. d_i is diameter of aggregate, D is Maximum aggregate grain size and n is Exponent with a typical value between 0.45 and 0.70 (assumed as 0.5). In this study, the minimum and the maximum size of aggregate's diameter are considered to be 2 and 16 mm respectively and n as 0.5 with 19 sieves. Fig. 3.2(a) shows aggregate distribution in a 3D mesoscopic model which is calculated with Eq. (3.1) and based on Fuller's curve shown in Fig. 3.1. In this model each of three dimensions of the model is equal to 60 mm.

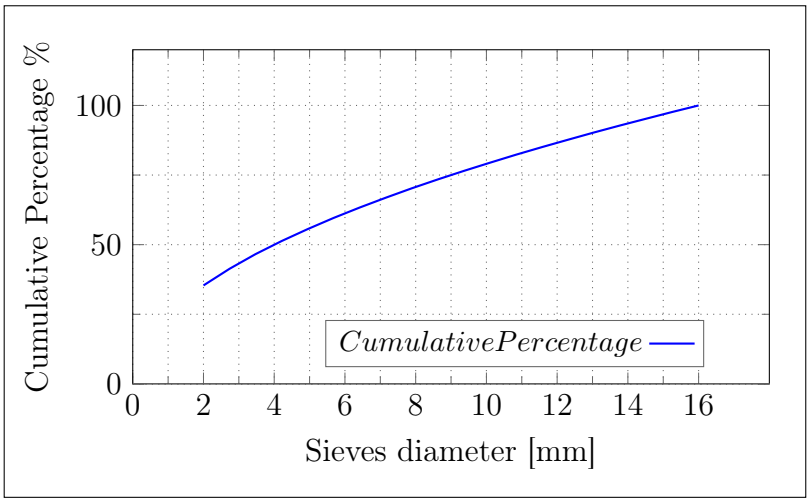

Figure 3.1: Grading of aggregate based on Fuller's curve gradation

3.1.2 2D Sections random mesoscopic model

As mentioned earlier, the 2D simulation will provide reliable results with fewer complications in modeling. An example of the 2D section, made out of the 3D random mesoscopic model, is shown in Fig. 3.2(b). This 3D random mesoscopic model is generated with MATLAB code written by Tino Kühn [94], and the aggregates are randomly distributed whereas their sizes are following the fuller cure as mentioned in Section 3.1.1. Several 2D sections have been created out of this 3D model and analyzed within different discretization approaches which will be discussed in the following sections.

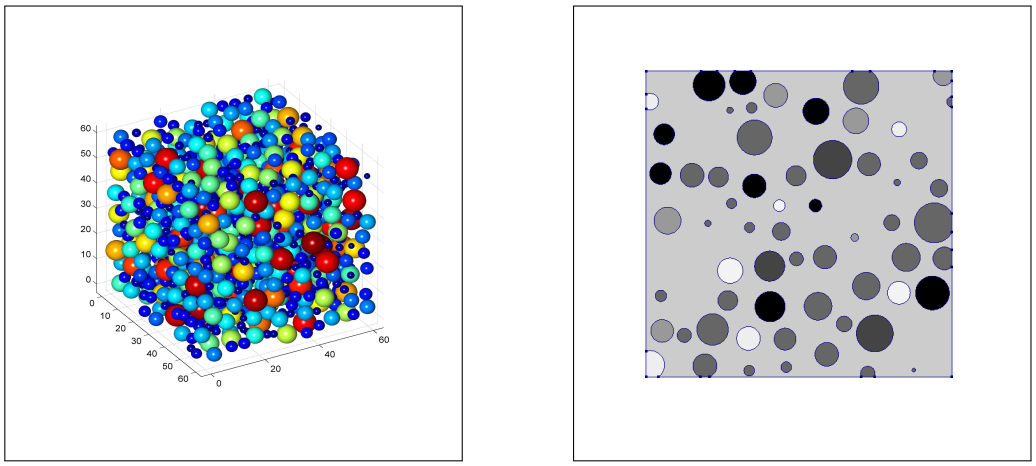

(a) 3D random mesoscopic model (b) 2D cross section

Figure 3.2: a) 3D random mesoscopic model, and b) 2D section - random mesoscopic model consist of mortar and aggregates

3.2 INTRODUCTION TO IRREGULAR AND REGULAR METHODS

Discretization methods are classified into two different categories. The first approach is irregular mesh, which follows the geometry of different materials, and properties are presented by the whole element. FEM is the most common method among numerical approaches, which is used by most commercial software and using an irregular mesh approach as a discretization method, see Fig. 3.3(a), shows irregular mesh model used for analysis with DIANA. Another approach is conventional mesh methods, whereby material properties are considered at the integration point level, see Fig. 3.3(b), which shows the regular mesh model used with in-house program CaeFem. In the developed model within mesh-free approaches, the material

is assigned individually to each node (integration point or node, depends on the discretization approach). The code will investigate the node's position, and if the node belongs to the matrix area or aggregates. Thus, it will assign the corresponding material based on the geometry of components. In this chapter, models are analyzed with three different regular mesh methods, i.e., Finite element methods with regular mesh, Element Free Galerkin method, and Isogeometric analysis method and compared with FEM irregular mesh method results from two programs, i.e., DIANA and CaeFem.

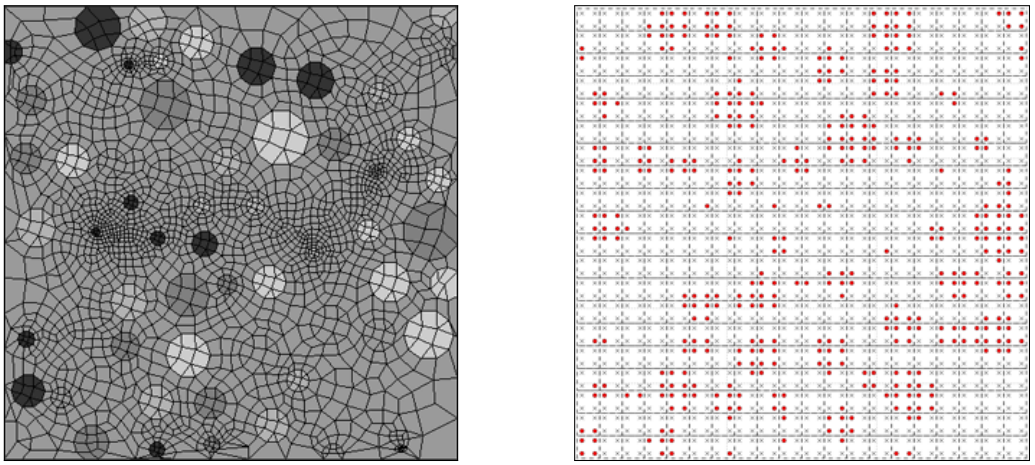

(a) Irregular mesh - DIANA model

(b) Regular mesh -CaeFem model

Figure 3.3: Discretized models

3.3 NUMERICAL SIMULATIONS

3.3.1 Model specification

In this section, three 2D sections have been selected to investigate the effect of different discretization methods, mesh objectivity, and the area fraction of aggregates on the total reaction of models under tensile loading conditions. Fig. 3.4 shows the 2D sections used for the simulation.

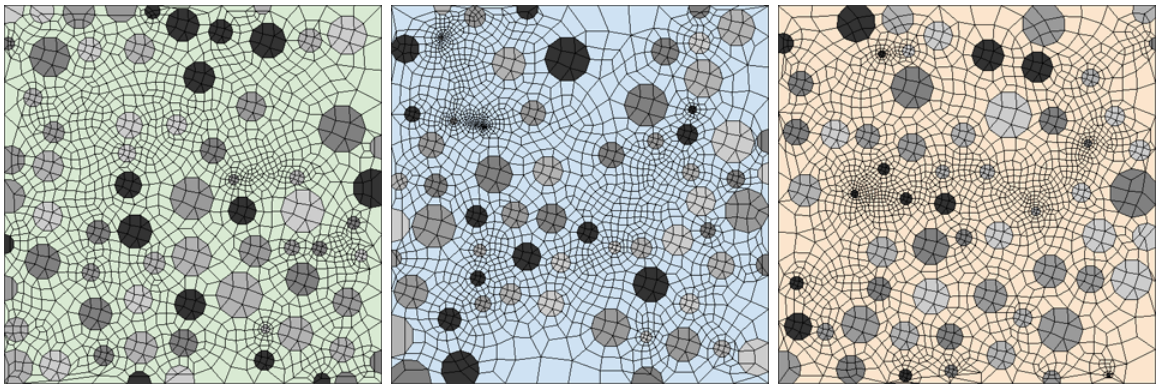

(a) Model 1 - z=0 mm (b) Model 2 - z=15 mm (c) Model 3 - z=30 mm

Figure 3.4: 2D sections generated from 3D-Random mesoscopic model

The mentioned three models, shown in Fig. 3.4, are subjected to the same loading, boundary conditions and the same material properties are assigned to the components. Table 3.1, shows the reference material properties and Fig. 3.5(a,b) show loading and boundary condition assigned to the 2D models. Plane stress material model is used and all materials are assumed to behave linearly. Model is fixed on bottom edge and tension load is applied gradually on top edge of model as prescribed deformation in vertical direction. The results for final stage of loading equal to 0.01 mm will be discussed in next section.

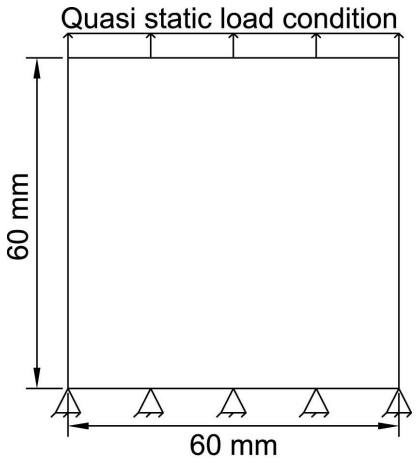

(a) Geometry, boundary condition

Figure 3.5: Schematic representation of 2D model, subjected to the prescribed displacement and static boundary conditions

Table 3.1: Material properties

	Aggregates	Mortar
Young's modulus	60000 MPa	20000 MPa
Poisson ratio	0.15	0.2

3.3.2 Analysis results and parameter studies

Three different range of mesh sizes are studied for each of the mentioned 2D sections, Fig. 3.6 shows nine models used for the parameter study. DIANA is a well-known commercial FEM software and is used to validate results obtained from simulation within the in-house program CaeFem[33]. The parameter used for results comparison is the total reaction force in the vertical direction and in the last stage of loading equal to 0. 01 mm. Tables 3.2, 3.3, and3.4 show results of each analysis in detail. Each table discussed results obtained for one of the 2D sections, which is analyzed with four discretization methods within in-house program CaeFem, i.e., FE-regular mesh method, FE-Irregular mesh method, EFG method and IGA method besides results from simulations performed by DIANA. These simulations are repeated for three different mesh sizes to investigate the mesh objectivity of the methods. Results comparisons for models with different numerical discretization approaches and with different numbers of degrees of freedom are shown in Figs. 3.7, 3.8, and3.9.

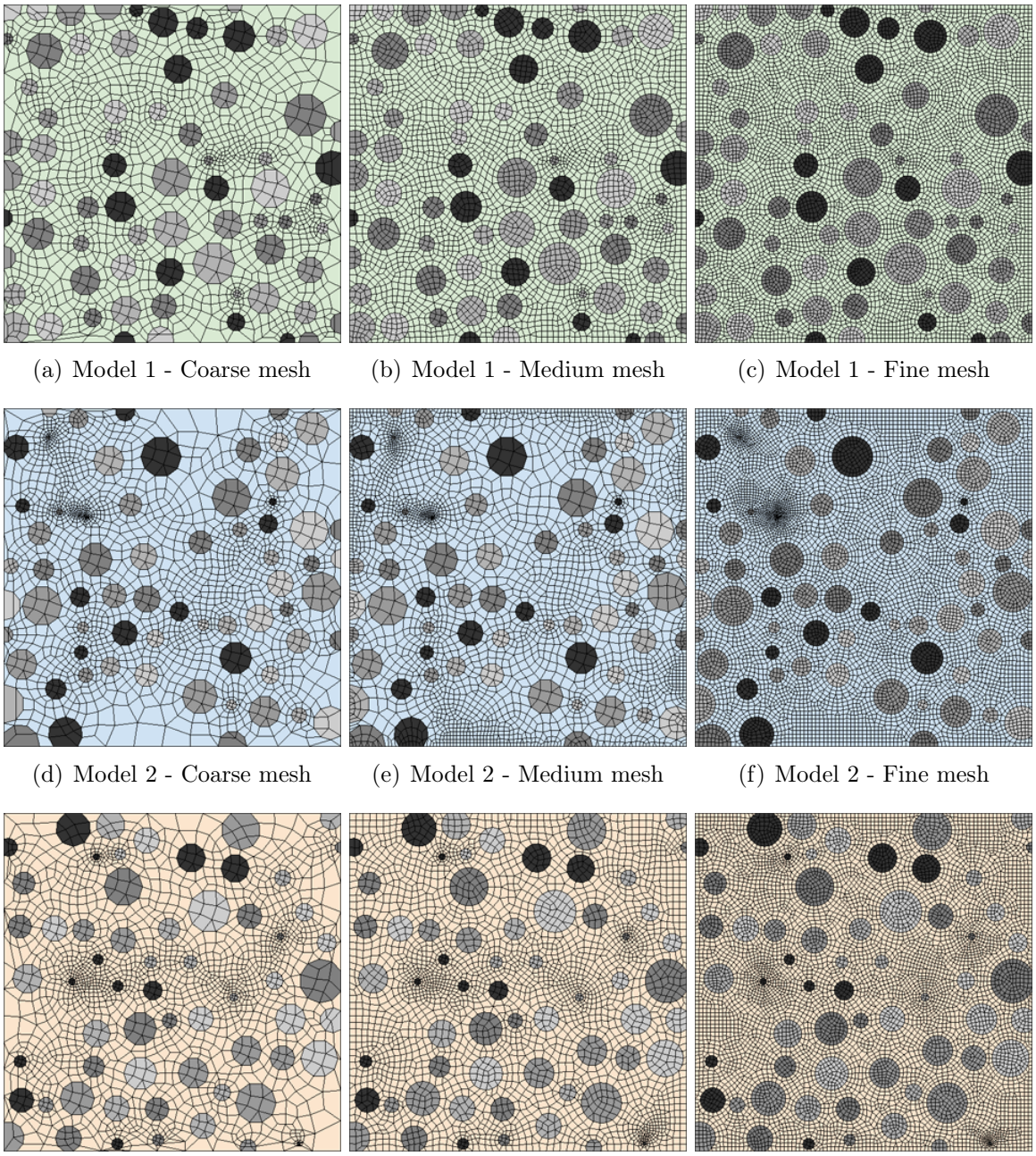

(a) Model 1 - Coarse mesh (b) Model 1 - Medium mesh (c) Model 1 - Fine mesh

(d) Model 2 - Coarse mesh (e) Model 2 - Medium mesh (f) Model 2 - Fine mesh

(g) Model 3 - Coarse mesh (h) Model 3 - Medium mesh (i) Model 3 - Fine mesh

Figure 3.6: 2D section models used for sensitivity analysis

The total reaction forces are shown on vertical axes in Figs. 3.7,3.8,and3.9. These axes are adjusted in a way to focus more on the differences between the various discretization approaches results. It is observed that different discretization methods are converging to the same results by increasing the number of degrees of freedom using in the simulation. As the mesh is getting finer, there is a good agreement in the results obtained from different discretization methods. However, increasing the number of degrees of freedom will increase

the time of calculation exponentially. Since the results are not changing significantly for different mesh sizes, even the model with coarse mesh has provided reliable results.

Table 3.2: Results comparison / Model 1 - $z = 0$ mm

	Model 1 Z = 0 mm	Number of Dof	Total reactions $F_x[N]$	Total reactions $F_y[N]$	Erorr Percentage
Coarse mesh	DIANA(Irregular mesh/FEM)	3660	-0.81	-380.89	-
	CaeFem(Irregular mesh/FEM)	3660	-0.84	-381.44	0.14%
	CaeFem(Regular mesh/FEM)	3872	-0.59	-397.93	4.47%
	CaeFem(Regular mesh/EFG method)	3872	-0.60	-397.95	4.48%
	CaeFem(Regular mesh/IGA method)	3872	-0.72	-432.47	13.54%
Medium mesh	DIANA(Irregular mesh/FEM)	7774	-0.88	-383.22	-
	CaeFem(Irregular mesh/FEM)	7774	-0.87	-383.51	0.08%
	CaeFem(Regular mesh/FEM)	7442	-1.06	-395.19	3.13%
	CaeFem(Regular mesh/EFG method)	7442	-1.06	-395.18	3.12%
	CaeFem(Regular mesh/IGA method)	7442	-1.00	-431.01	12.47%
Fine mesh	DIANA(Irregular mesh/FEM)	14692	-0.85	-384.17	-
	CaeFem(Irregular mesh/FEM)	14692	-0.85	-384.34	0.04%
	CaeFem(Regular mesh/FEM)	15138	-0.65	-392.00	2.04%
	CaeFem(Regular mesh/EFG method)	15138	-0.74	-392.47	2.16%
	CaeFem(Regular mesh/IGA method)	15138	-0.83	-427.99	11.41%

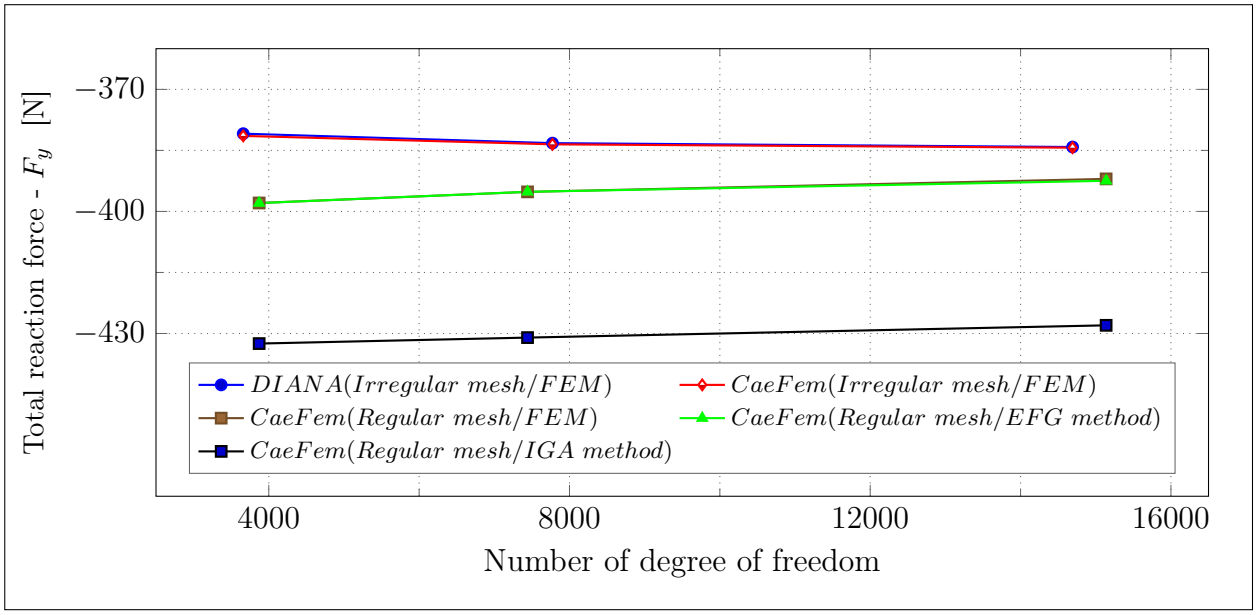

Figure 3.7: Results comparison / Model 1 - $z = 0$ mm

Table 3.3: Results comparison / Model 2 - $z = 15$ mm

	Model 2 Z = 15 mm	Number of Dof	Total reactions $F_x[N]$	Total reactions $F_y[N]$	Erorr Percentage
Coarse mesh	DIANA(Irregular mesh/FEM)	4310	-4.37	-369.52	-
	CaeFem(Irregular mesh/FEM)	4310	-4.41	-370.02	0.13%
	CaeFem(Regular mesh/FEM)	3872	-5.82	-385.18	4.24%
	CaeFem(Regular mesh/EFG method)	3872	-5.84	-385.25	4.26%
	CaeFem(Regular mesh/IGA method)	3872	-6.03	-419.04	13.40%
Medium mesh	DIANA(Irregular mesh/FEM)	6776	-4.54	-368.92	-
	CaeFem(Irregular mesh/FEM)	6776	-4.56	-369.34	0.11%
	CaeFem(Regular mesh/FEM)	7442	-5.36	-381.63	3.45%
	CaeFem(Regular mesh/EFG method)	7442	-5.36	-381.62	3.44%
	CaeFem(Regular mesh/IGA method)	7442	-5.42	-415.89	12.73%
Fine mesh	DIANA(Irregular mesh/FEM)	15922	-4.80	-372.08	-
	CaeFem(Irregular mesh/FEM)	15922	-4.80	-372.24	0.04%
	CaeFem(Regular mesh/FEM)	15138	-5.03	-378.70	1.78%
	CaeFem(Regular mesh/EFG method)	15138	-5.03	-378.72	1.78%
	CaeFem(Regular mesh/IGA method)	15138	-5.53	-414.32	11.35%

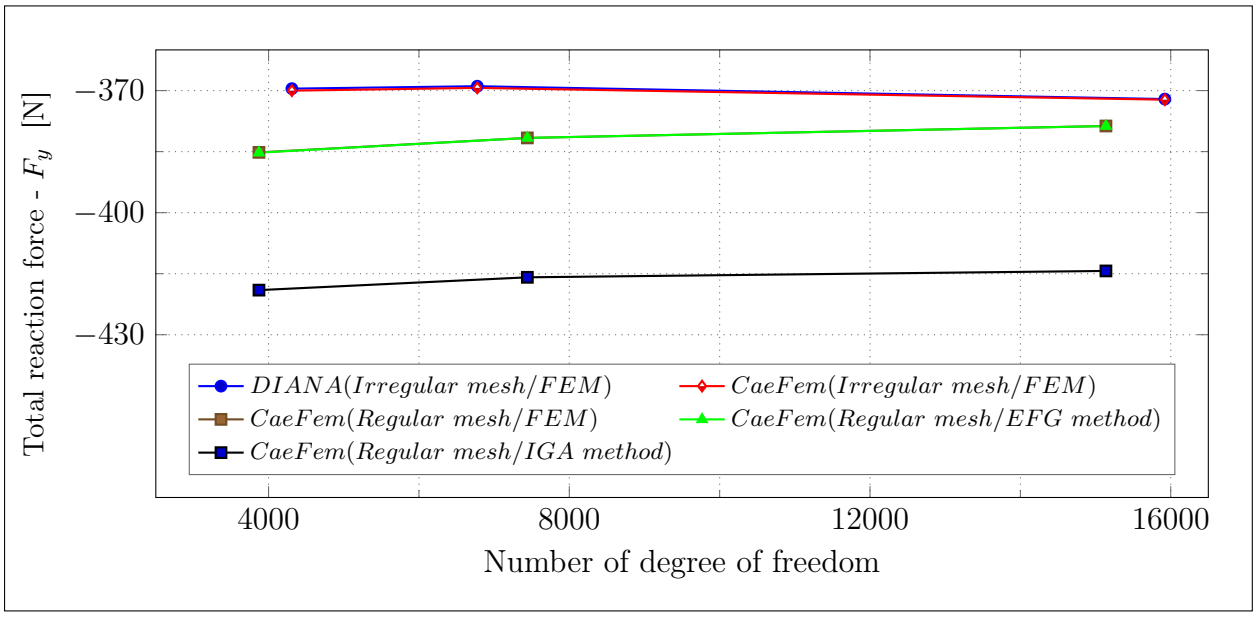

Figure 3.8: Results comparison / Model 2 - $z = 15$ mm

Table 3.4: Results comparison / Model 3 - $z = 30$ mm

	Model 3 Z = 30 mm	Number of Dof	Total reactions $F_x[N]$	Total reactions $F_y[N]$	Erorr Percentage
Coarse mesh	DIANA(Irregular mesh/FEM)	4348	-1.98	-367.49	-
	CaeFem(Irregular mesh/FEM)	4348	-1.97	-368.00	0.14%
	CaeFem(Regular mesh/FEM)	3872	-2.21	-380.91	3.65%
	CaeFem(Regular mesh/EFG method)	3872	-2.23	-380.96	3.66%
	CaeFem(Regular mesh/IGA method)	3872	-2.64	-414.98	12.92%
Medium mesh	DIANA(Irregular mesh/FEM)	6918	-1.99	-368.74	-
	CaeFem(Irregular mesh/FEM)	6918	-1.99	-369.03	0.08%
	CaeFem(Regular mesh/FEM)	7442	-1.93	-378.46	2.64%
	CaeFem(Regular mesh/EFG method)	7442	-1.93	-378.45	2.64%
	CaeFem(Regular mesh/IGA method)	7442	-2.36	-413.35	12.10%
Fine mesh	DIANA(Irregular mesh/FEM)	15576	-2.02	-369.96	-
	CaeFem(Irregular mesh/FEM)	15576	-2.02	-370.10	0.04%
	CaeFem(Regular mesh/FEM)	15138	-2.25	-376.73	1.83%
	CaeFem(Regular mesh/EFG method)	15138	-2.25	-376.75	1.84%
	CaeFem(Regular mesh/IGA method)	15138	-2.29	-411.43	11.21%

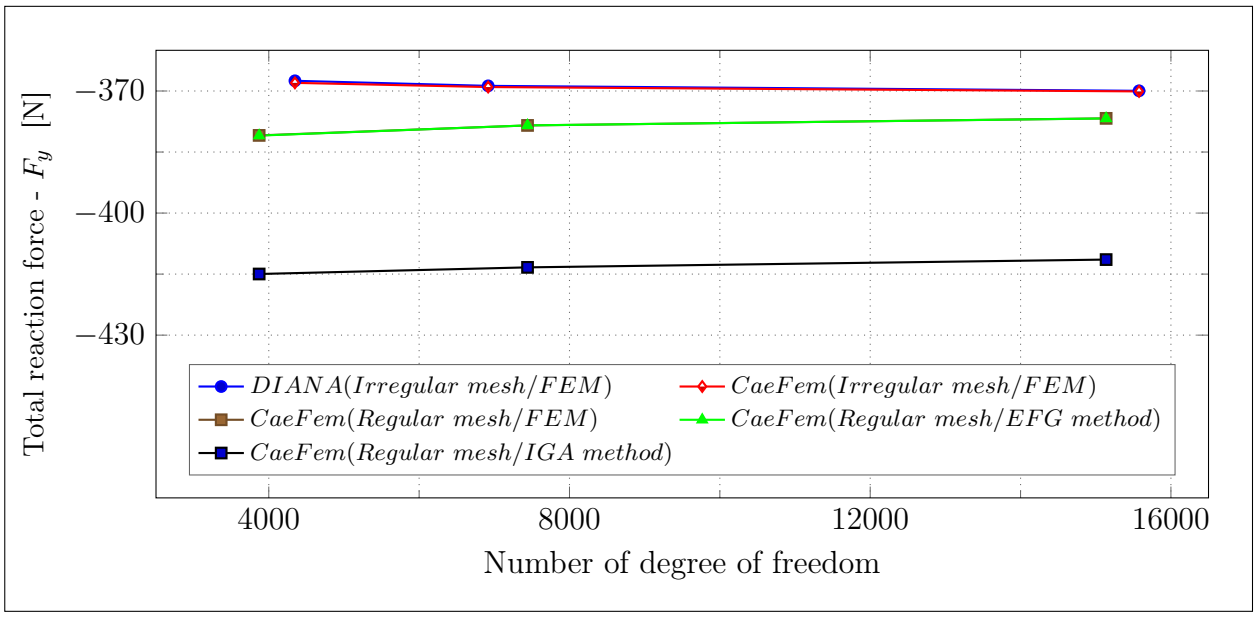

Figure 3.9: Results comparison / Model 3 - $z = 30$ mm

From Figs. 3.7,3.8,and 3.9, it is observed that IGA is the most conservative method among different discretization methods. The general differences between each 2D model's total reactions, see Figs. 3.7,3.8,and3.9, represent the effect of the random field of aggregates and area fraction of aggregate. The area fraction of aggregates in 2D models, i.e., model 1, model 2, and model 3, is 0.32, 0.28, and 0.26, respectively. It is observed that the total reaction

forces are decreasing as the area fraction of aggregates is decreasing, which can be explained by elastic material models assigned to structural components in these three reference cases.

3.3.3 Conclusion

Three 2D models derived from the 3D mesoscopic random model are used to investigate each discretization method's capability and weakness. Total reaction forces in the horizontal direction(perpendicular to the loading direction) are small since deformation is applied in the vertical direction. These results do not follow a particular pattern concerning discretization methods, mesh sizes, and area fraction of aggregate. Total reaction forces in loading direction are the parameter used for parameter study. DIANA and CaeFem provide the same result with the FE-Irregular mesh discretization method, which proves the developed program's accuracy. EFG method has almost the same result as FEM with regular mesh; however, EFG needs more time to perform the analysis. While the mesh becomes finer, results are converging, and less error percentage is observed when the number of degrees of freedom is higher. This error is computed based on result differences of each discretization method compare to reference simulation performed within DIANA. The focus will be on introducing fibers in 2D models as truss elements and coupling them with discrete discontinuities in the next phase of this research. Moreover, the newly developed model's formulations and parameter study will be discussed in the following chapters.

4 NUMERICAL MODELING

The present chapter starts with a short introduction to the Finite element method. Later, different numerical approaches are introduced, and the ones used in the newly developed model are briefly explained. In the following, the formulations utilized in the numerical model are discussed in detail and several numerical studies are performed to calibrate and validate the enumerated numerical method. The presented formulations and results are partly published in[50].

4.1 INTRODUCTION TO FINITE ELEMENT METHOD

The finite element method is a numerical technique applied for solving problems in different fields, including mathematical physics and engineering, e.g., structural analysis, heat transfer, fluid flow, mass transport, and electromagnetic potential [74]. FEM uses mathematics to understand and measure any physical phenomena thoroughly.

The solving problem is performed in four different phases. First, it starts with the specification of geometry, material, and mechanical properties of the system. The second step is mathematical modeling, including the formulation of equations for presenting the overall system's response by considering the boundary condition and loading. Numerical modeling is the third phase of the whole procedure, including subdividing the infinite continuum in reality into a discrete number of points concerning space and time, which is called discretization. Finally, in computational modeling, the problem will be solved by processing and implementing algorithms with the help of computers.

During the modeling and analysis, because of the technique's numerical nature, errors can occur due to the simplification of models, rounding, and discretization [101]. A system of a physical problem under specific loading and condition can be marked out mathematically by equations conducting the response. Regarding FEM, the structural analysis is based on three aspects, i.e., equilibrium, constitutive laws, and kinematic formulation.

In the finite element method, instead of solving the problem for the entire body, the system of interest will be divided into small elements by discretization techniques and formulate the equations for each element and combine the individual result to estimate the overall response of the complete system. Discretization means interpolation, i.e., displacements within an element are interpolated using the values at nodes belonging to a specific element. Adjacent elements share common nodes in a way that the continuum will be formed. Generally, polynomial functions are used to compute variables at any point within an element by interpolation of the values of the nodes which they belongs. First, the displacements are computed, and then further results like strain and stress can be calculated.

In the standard finite element method, kinematic compatibility is implied with the discretization of a continuous displacement field [45], components of nodal displacements $\bar{\boldsymbol{u}}_I$ have to be chosen such that the kinematic boundary conditions are fulfilled [46].

$$\bar{\boldsymbol{u}}(\boldsymbol{x}) = \boldsymbol{N}(\boldsymbol{x}) \cdot \bar{\boldsymbol{u}}_I \tag{4.1}$$

with a local coordinate $\boldsymbol{x}$, a matrix of shape functions $\boldsymbol{N}$ and a vector of nodal displacements $\bar{\boldsymbol{u}}_I$. This leads to strains

$$\boldsymbol{\epsilon}(\boldsymbol{x}) = \frac{\partial \bar{\boldsymbol{u}}}{\partial \boldsymbol{x}} = \boldsymbol{B}(\boldsymbol{x}) \cdot \bar{\boldsymbol{u}}_I \tag{4.2}$$

with the matrix of shape function derivatives $\boldsymbol{B}$ [10]. Constitutive laws are used for describing the relation between stress and strain for deriving the equations for each finite element. These material laws can be summarized with

$$\boldsymbol{\sigma} = \boldsymbol{\sigma}(\boldsymbol{\epsilon}) \tag{4.3}$$

The small changes of strain and stress in physical or loading time t should be computed from their total values are defined as following:

$$\dot{\boldsymbol{\epsilon}} = \frac{\partial \boldsymbol{\epsilon}}{\partial \boldsymbol{t}} \quad \text{and} \quad \dot{\boldsymbol{\sigma}} = \frac{\partial \boldsymbol{\sigma}}{\partial \boldsymbol{t}} \tag{4.4}$$

The incremental form of Eq. (4.3) will be as following:

$$\dot{\boldsymbol{\sigma}} = \boldsymbol{C}_T(\boldsymbol{\epsilon}) \cdot \dot{\boldsymbol{\epsilon}} \tag{4.5}$$

with time derivatives $\dot{\boldsymbol{\sigma}}$,$\dot{\boldsymbol{\epsilon}}$ of stress and strain with respect to a loading time t and a tangential material stiffness $\boldsymbol{C}_T$. An equilibrium condition is one of the basic components of structural analysis besides kinematic compatibility and material laws. An advantageous formulation based on the principle of virtual works is extensively used for structural analysis. It states, for any solid body in static equilibrium subjected to small virtual displacement, the virtual strain energy $\delta\boldsymbol{U}$ of internal stresses is equal to the virtual work of $\delta\boldsymbol{W}$ the external forces acting on it.

$$\delta\boldsymbol{W} = \delta\boldsymbol{U} \tag{4.6}$$

This equilibrium condition is formulated as integral form

$$\int_V \delta\boldsymbol{\epsilon}^T \cdot \boldsymbol{\sigma}\,\mathrm{d}V = \int_V \delta\bar{\boldsymbol{u}}^T \cdot \boldsymbol{b}\,\mathrm{d}V + \int_{A_t} \delta\bar{\boldsymbol{u}}^T \cdot \boldsymbol{t}\,\mathrm{d}A \tag{4.7}$$

where V is the volume of solid body, $\boldsymbol{b}$ is its body forces, A is its surface and $\boldsymbol{t}$ is surface traction prescribed at all or part of A. Virtual displacements $\delta\bar{\boldsymbol{u}}$ and derived virtual strains $\delta\boldsymbol{\epsilon}$, both are introduced as vectors and transposed and multiplied by the vectors $\boldsymbol{u}$, $\boldsymbol{t}$ and $\boldsymbol{\sigma}$, where $\boldsymbol{\sigma}$ is the field of stress. Applying the displacement interpolation Eqs. (4.1) to virtual displacement leads to

$$\delta\bar{\boldsymbol{u}} = \boldsymbol{N} \cdot \delta\bar{\boldsymbol{u}}_I \quad \text{and} \quad \delta\bar{\boldsymbol{\epsilon}} = \boldsymbol{B} \cdot \delta\bar{\boldsymbol{u}}_I \tag{4.8}$$

Using Eqs. (4.8), with Eq. (4.7) leads to the discretized equilibrium conditions

$$\delta\bar{\boldsymbol{u}}^T \cdot [\int_V \boldsymbol{B}^T \cdot \boldsymbol{\sigma}\,\mathrm{d}V] = \delta\bar{\boldsymbol{u}}^T \cdot [\int_V \boldsymbol{N}^T \cdot \boldsymbol{b}\,\mathrm{d}V + \int_{A_t} \boldsymbol{N}^T \cdot \boldsymbol{t}\,\mathrm{d}A] \tag{4.9}$$

This could be summarized as following

$$\delta\bar{\boldsymbol{u}}^T \cdot (\boldsymbol{p}_I - \boldsymbol{f}_I) = 0 \tag{4.10}$$

where internal nodal forces

$$\boldsymbol{f}_I = \int_V \boldsymbol{B}^T \cdot \boldsymbol{\sigma}\,\mathrm{d}V \tag{4.11}$$

and external nodal forces

$$\boldsymbol{p}_I = \int_V \boldsymbol{N}^T \cdot \boldsymbol{b}\,\mathrm{d}V + \int_{A_t} \boldsymbol{N}^T \cdot \boldsymbol{t}\,\mathrm{d}A \tag{4.12}$$

Virtual displacements $\delta\bar{\boldsymbol{u}}$ are kept in this formulation for a later combination with the equilibrium condition covering a discontinuous displacement field. A linearization is performed with

$$\dot{\boldsymbol{f}}_I = \int_V \boldsymbol{B}^T \cdot \dot{\boldsymbol{\sigma}}\,\mathrm{d}V = \int_V \boldsymbol{B}^T \cdot \boldsymbol{C}_T \cdot \boldsymbol{B}\,\mathrm{d}V \cdot \dot{\bar{\boldsymbol{u}}}_I = \boldsymbol{K}_T \cdot \dot{\bar{\boldsymbol{u}}}_I \tag{4.13}$$

with the tangential stiffness matrix $\boldsymbol{K}_T$.

4.2 INTRODUCTION TO THE STRONG DISCONTINUTY APPROACH

In previous studies, two approaches have been used for modeling the crack formation in concrete structures, i.e., smeared crack formulation and discrete crack approach within finite element method [11]. Smeared crack approaches need regularization techniques to consider mesh sensitivity and reproduce fracture energy [12, 51, 100]. These techniques are generally complicated and expensive, depending on the ratio of element size to the crack bands, which are creating and propagating due to the quasi-brittle behavior of concrete.

In contrast, in discrete crack approaches, the crack width can be computed explicitly for crack traction and naturally solves the problem of mesh sensitivity and reproduction of crack energy due to strain-softening behavior. Discrete crack approaches are classified in two groups: a)Extended-Finite-Element (XFEM) [81, 39, 117] and b)the Strong-Discontinuity-Approach (SDA)[35, 53, 97, 4, 5].

XFEM is practically expensive for structures with a large number of cracks, since propagating displacement discontinuities are carried to the system level with considering the additional degree of freedom and requires corresponding crack propagation criteria for crack propagation continuation and propagation direction and length. However, SDA treats discontinuity degrees of freedom on the element level, which simplifies crack propagation criteria and is the utmost advantage in modeling the structures with a large number of cracks.

Three different classes are introduced for the formulation of SDA, i.e., Statically Optimal Symmetric (SOS), Kinematically Optimal Symmetric (KOS), and Statically and Kinematically Optimal Nonsymmetric (SKON) [52, 127]. The SDA formulation used in this research, is similar to the KOS; both have the same approach in constructing the matrix of the strain functions in the discontinuity. The classes mentioned above have the Hu-Washizu principle as a basis for developing the formulation. While the presented SDA formulation in this research starts from the well-known principle of virtual work, then couples continuum to the discontinuity by relating the total displacement based on continuous and discontinuous displacement parts. The mentioned formulation will be discussed in detail in Section 4.2.1.

Two approaches are introduced to treat the discontinuity or the crack path across neighboring elements: continuous path and discontinuous path. Crack path continuity can be enforced by tracking algorithms [98]. However, this may lead to stimulation locking effects, specifically in the SOS formulation [127]. The extension of crack path discontinuities can relatively be reduced by reducing element sizes whereby the crack path is indicated. A control of implausible multiple crack path courses is proposed with adaption methods [110]. Relations for crack tractions depending on crack width are derived from experimental investigations about concrete tensile failure behavior [110, 34, 58]. They generally introduce nonlinearities, e.g., in case non-monotonic behavior with un- and reloading of cracks in inhomogeneous structures during a loading history.

4.2.1 Virtual work principles for SDA

The general Hu-Washizu variational principle describes independent fields for displacements, strains and stresses. A displacement field is assumed as

$$\boldsymbol{u} = \bar{\boldsymbol{u}} + \widehat{\boldsymbol{u}} \tag{4.14}$$

with a part $\bar{\boldsymbol{u}}$ which is continuous over the whole domain under consideration and an enhancement $\widehat{\boldsymbol{u}}$ which, e.g., allows for discontinuities. Strain is assumed as

$$\boldsymbol{\epsilon} = \nabla^{sym}\bar{\boldsymbol{u}} + \widehat{\boldsymbol{\epsilon}} \tag{4.15}$$

with an assumed enhancement $\widehat{\boldsymbol{\epsilon}}$ which is not subject to any interelement continuity requirements. The corresponding four-field Hu-Washizu principle can be written as

$$\begin{aligned}
\int_V \nabla^{sym}\delta\bar{\boldsymbol{u}}^T \cdot \boldsymbol{\sigma}(\boldsymbol{\epsilon})\,\mathrm{d}V &= \int_V \delta\bar{\boldsymbol{u}}^T \cdot \boldsymbol{b}\,\mathrm{d}V + \int_{A_t} \delta\bar{\boldsymbol{u}}^T \cdot \boldsymbol{t}\,\mathrm{d}A \\
\int_V \delta\widehat{\boldsymbol{\epsilon}}^T \cdot [\boldsymbol{\sigma}(\boldsymbol{\epsilon}) - \widehat{\boldsymbol{\sigma}}]\,\mathrm{d}V &= 0 \\
\int_V \delta\widehat{\boldsymbol{\sigma}}^T \cdot [\nabla^{sym}\widehat{\boldsymbol{u}} - \widehat{\boldsymbol{\epsilon}}]\,\mathrm{d}V &= 0 \\
\int_V \nabla^{sym}\delta\widehat{\boldsymbol{u}}^T \cdot \widehat{\boldsymbol{\sigma}}\,\mathrm{d}V &= \int_V \delta\widehat{\boldsymbol{u}}^T \cdot \boldsymbol{b}\,\mathrm{d}V + \int_{A_t} \delta\widehat{\boldsymbol{u}}^T \cdot \boldsymbol{t}\,\mathrm{d}A
\end{aligned} \tag{4.16}$$

with variations δ, the symmetric nabla operator ∇^{sym}, assumed stress $\widehat{\boldsymbol{\sigma}}$ and stress $\boldsymbol{\sigma}(\boldsymbol{\epsilon})$ from a material law[52]. With $\widehat{\boldsymbol{u}} = 0$,$\boldsymbol{u} = \bar{\boldsymbol{u}}$ this corresponds to the basics explained in [115]. Finite element interpolations for stresses and strains are assumed with

$$\begin{aligned}
\widehat{\boldsymbol{\sigma}} &= \boldsymbol{S} \cdot \boldsymbol{s} \\
\widehat{\boldsymbol{\epsilon}} &= \boldsymbol{G} \cdot \boldsymbol{e}
\end{aligned} \tag{4.17}$$

Standard interpolation functions $\boldsymbol{N}$ and enhancing functions $\boldsymbol{N}_c$

$$\begin{aligned}
\bar{\boldsymbol{u}} &= \boldsymbol{N} \cdot \boldsymbol{d} \\
\widehat{\boldsymbol{u}} &= \boldsymbol{N}_c \cdot \boldsymbol{d}_c
\end{aligned} \tag{4.18}$$

are used for displacements. Displacement gradients are derived with

$$\begin{aligned}
\nabla^{sym}\bar{\boldsymbol{u}} &= \boldsymbol{B} \cdot \boldsymbol{d} \\
\nabla^{sym}\widehat{\boldsymbol{u}} &= \boldsymbol{B}_c \cdot \boldsymbol{d}_c
\end{aligned} \tag{4.19}$$

Thus, using a Galerkin approach the interpolations yield from Eq. (4.16)

$$\begin{aligned}
\delta\boldsymbol{d}^T \cdot \textstyle\int_V \boldsymbol{B}^T \cdot \boldsymbol{\sigma}(\boldsymbol{\epsilon})\,\mathrm{d}V &= \delta\boldsymbol{d}^T \cdot \boldsymbol{f}^{ext} \\
\delta\boldsymbol{e}^T \cdot \left[\textstyle\int_V \boldsymbol{G}^T \cdot \boldsymbol{\sigma}(\boldsymbol{\epsilon})\,\mathrm{d}V - \int_V \boldsymbol{G}^T \cdot \boldsymbol{S}\,\mathrm{d}V \cdot \boldsymbol{s}\right] &= 0 \\
\delta\boldsymbol{s}^T \cdot \left[\textstyle\int_V \boldsymbol{S}^T \cdot \boldsymbol{B}_c\,\mathrm{d}V \cdot \boldsymbol{d}_c - \int_V \boldsymbol{S}^T \cdot \boldsymbol{G}\,\mathrm{d}V \cdot \boldsymbol{e}\right] &= 0 \\
\delta\boldsymbol{d}_c^T \cdot \textstyle\int_V \boldsymbol{B}_c^T \cdot \boldsymbol{S}\,\mathrm{d}V \cdot \boldsymbol{s} &= \delta\boldsymbol{d}_c^T \cdot \boldsymbol{f}_c^{ext}
\end{aligned} \tag{4.20}$$

with

$$\begin{aligned}
\boldsymbol{f}^{ext} &= \textstyle\int_V \boldsymbol{N}^T \cdot \boldsymbol{b}\,\mathrm{d}V + \int_{A_t} \boldsymbol{N}^T \cdot \boldsymbol{t}\,\mathrm{d}A \\
\boldsymbol{f}_c^{ext} &= \textstyle\int_V \boldsymbol{N}_c^T \cdot \boldsymbol{b}\,\mathrm{d}V + \int_{A_t} \boldsymbol{N}_c^T \cdot \boldsymbol{t}\,\mathrm{d}A
\end{aligned} \tag{4.21}$$

Different types of enhancement will be discussed in the following.

1) Displacements are not enhanced, i.e. $\boldsymbol{d}_c = 0, \boldsymbol{u} = \bar{\boldsymbol{u}}$. This makes Eqs. (4.16, 4.20)$_4$ obsolete. Eqs. (4.20)$_{1,2}$ reduce to

$$\begin{aligned} \int_V \boldsymbol{B}^T \cdot \boldsymbol{\sigma}(\boldsymbol{\epsilon}) \, \mathrm{d}V &= \boldsymbol{f}^{ext} \\ \int_V \boldsymbol{G}^T \cdot \boldsymbol{\sigma}(\boldsymbol{\epsilon}) \, \mathrm{d}V &= 0 \end{aligned} \tag{4.22}$$

The second equation corresponds to the orthogonality condition set by [115]. Together with a linear elastic material law

$$\boldsymbol{\sigma}(\boldsymbol{\epsilon}) = \boldsymbol{C} \cdot [\nabla^{sym} \bar{\boldsymbol{u}} + \widehat{\boldsymbol{\epsilon}}] = \boldsymbol{C} \cdot [\boldsymbol{B} \cdot \bar{\boldsymbol{u}} + \boldsymbol{G} \cdot \boldsymbol{e}] \tag{4.23}$$

the well-known form is obtained as following:

$$\int_v \begin{bmatrix} \boldsymbol{B}^T \cdot \boldsymbol{C} \cdot \boldsymbol{B} & \boldsymbol{B}^T \cdot \boldsymbol{C} \cdot \boldsymbol{G} \\ \boldsymbol{G}^T \cdot \boldsymbol{C} \cdot \boldsymbol{B} & \boldsymbol{G}^T \cdot \boldsymbol{C} \cdot \boldsymbol{G} \end{bmatrix} \mathrm{d}V \cdot \begin{pmatrix} \boldsymbol{d} \\ \boldsymbol{e} \end{pmatrix} = \begin{pmatrix} \boldsymbol{f}^{ext} \\ 0 \end{pmatrix} \tag{4.24}$$

This is the "statically optimal symmetric formulation" (**SOS**). Regarding kinematic discontinuities SOS ensures natural traction continuity ($\boldsymbol{t} = \boldsymbol{n} \cdot \boldsymbol{\sigma}$) but might introduce spurious stress transfer [52].

2) Stresses and strains are not enhanced independently, i.e. $\widehat{\boldsymbol{\sigma}} = \boldsymbol{\sigma}(\boldsymbol{\epsilon}) = \boldsymbol{\sigma}$ and $\boldsymbol{e} = 0$. Strains are derived from enhanced displacements instead

$$\boldsymbol{\epsilon} = \nabla^{sym} \bar{\boldsymbol{u}} + \widehat{\boldsymbol{\epsilon}}, \qquad \widehat{\boldsymbol{\epsilon}} = \nabla^{sym} \widehat{\boldsymbol{u}} \tag{4.25}$$

and we obtain $\widehat{\boldsymbol{\sigma}} - \boldsymbol{\sigma}(\boldsymbol{\epsilon}) = 0$ and $\widehat{\boldsymbol{\epsilon}} - \nabla^{sym} \widehat{\boldsymbol{u}} = 0$ and from Eq. (4.16)

$$\begin{aligned} \int_V \nabla^{sym} \delta \bar{\boldsymbol{u}}^T \cdot \boldsymbol{\sigma} \, \mathrm{d}V &= \int_V \delta \bar{\boldsymbol{u}}^T \cdot \boldsymbol{b} \, \mathrm{d}V + \int_{A_t} \delta \bar{\boldsymbol{u}}^T \cdot \boldsymbol{t} \, \mathrm{d}A \\ \int_V \nabla^{sym} \delta \widehat{\boldsymbol{u}}^T \cdot \boldsymbol{\sigma} \, \mathrm{d}V &= \int_V \delta \widehat{\boldsymbol{u}}^T \cdot \boldsymbol{b} \, \mathrm{d}V + \int_{A_t} \delta \widehat{\boldsymbol{u}}^T \cdot \boldsymbol{t} \, \mathrm{d}A \end{aligned} \tag{4.26}$$

Interpolation of strains according to Eqs. (4.19) yields

$$\boldsymbol{\epsilon} = \boldsymbol{B} \cdot \boldsymbol{d} + \boldsymbol{B}_c \cdot \boldsymbol{d}_c \tag{4.27}$$

and further regarding Eq. (4.26) to

$$\begin{aligned} \delta \boldsymbol{d}^T \cdot \int_V \boldsymbol{B}^T \cdot \boldsymbol{\sigma} \, \mathrm{d}V &= \delta \boldsymbol{d}^T \cdot \boldsymbol{f}^{ext} \\ \delta \boldsymbol{d}_c^T \cdot \int_V \boldsymbol{B}_c^T \cdot \boldsymbol{\sigma} \, \mathrm{d}V &= \delta \boldsymbol{d}_c^T \cdot \boldsymbol{f}_c^{ext} \end{aligned} \tag{4.28}$$

With the linear elastic material law Eq. (4.23) the well known form

$$\int_V \begin{bmatrix} \boldsymbol{B}^T \cdot \boldsymbol{C} \cdot \boldsymbol{B} & \boldsymbol{B}^T \cdot \boldsymbol{C} \cdot \boldsymbol{B}_c \\ \boldsymbol{B}_c^T \cdot \boldsymbol{C} \cdot \boldsymbol{B} & \boldsymbol{B}_c^T \cdot \boldsymbol{C} \cdot \boldsymbol{B}_c \end{bmatrix} \mathrm{d}V \cdot \begin{pmatrix} \boldsymbol{d} \\ \boldsymbol{d}_c \end{pmatrix} = \begin{pmatrix} \boldsymbol{f}^{ext} \\ \boldsymbol{f}_c^{ext} \end{pmatrix} \tag{4.29}$$

is obtained. This is the "kinematically optimal symmetric formulation" (**KOS**). It avoids spurious stress transfer with kinematic discontinuities but might violate natural traction continuity [52].

3) The "statically and kinematically optimal nonsymmetric formulation" (**SKON**) avoids the former deficiencies using a Petrov-Galerkin approach. But this leads to unsymmetric systems it is not treated with its details. For its discussion and comparison with SOS and KOS see [54, 40].

A variant of KOS will be further discussed in the following. The displacement enhancement

$$\widehat{\boldsymbol{u}} = H_d \breve{\boldsymbol{u}} = H_d \, \boldsymbol{N}_c \cdot \boldsymbol{d}_c \tag{4.30}$$

with a continuous field $\breve{\boldsymbol{u}}$ and a Heaviside function H_d defining a line of discontinuity within the domain V. Displacement gradients is computed as

$$\begin{aligned} \nabla^{sym} \widehat{\boldsymbol{u}} &= [\delta_d \, \boldsymbol{n} \otimes \boldsymbol{N}_c + H_d \, \nabla^{sym} \boldsymbol{N}_c] \cdot \boldsymbol{d}_c \\ &= \boldsymbol{B}_c \cdot \boldsymbol{d}_c \end{aligned} \tag{4.31}$$

whereas δ_d is the Dirac-delta function, the normal $\boldsymbol{n}$ along the line of discontinuity and the tensor product operator $\otimes$ connecting the $\boldsymbol{n}$-index with the first $\boldsymbol{N}_c$-index. Applying the enhancement strain operator $\boldsymbol{B}_c$ to Eq. $(4.28)_2$ yields

$$\delta \boldsymbol{d}_c^T \cdot \int_V \delta_d \, (\boldsymbol{n} \otimes \boldsymbol{N}_c)^T \cdot \boldsymbol{\sigma} \, \mathrm{d}V + \delta \boldsymbol{d}_c^T \cdot \int_V H_d \, \nabla^{sym} \boldsymbol{N}_c^T \cdot \boldsymbol{\sigma} \, \mathrm{d}V = \delta \boldsymbol{d}_c^T \cdot \boldsymbol{f}_c^{ext} \tag{4.32}$$

and with the discontinuity traction $\boldsymbol{t} = \boldsymbol{n}^T \cdot \boldsymbol{\sigma}$

$$\delta \boldsymbol{d}_c^T \cdot \int_{A_d} \boldsymbol{N}_c^T \cdot \boldsymbol{t} \, \mathrm{d}V + \delta \boldsymbol{d}_c^T \cdot \int_V H_d \, \nabla^{sym} \boldsymbol{N}_c^T \cdot \boldsymbol{\sigma} \, \mathrm{d}V = \delta \boldsymbol{d}_c^T \cdot \boldsymbol{f}_c^{ext} \tag{4.33}$$

with the discomtinuity surface A_d due to the Dirac-delta integration property. This corresponds to a virtual work principle

$$\int_{A_d} \delta \breve{\boldsymbol{u}}^T \cdot \boldsymbol{t} \, \mathrm{d}V + \int_V H_d \, \nabla^{sym} \delta \breve{\boldsymbol{u}}^T \cdot \boldsymbol{\sigma} \, \mathrm{d}V = \int_V H_d \, \delta \breve{\boldsymbol{u}}^T \cdot \boldsymbol{b} \, \mathrm{d}V + \int_{A_t} H_d \, \delta \breve{\boldsymbol{u}}^T \cdot \boldsymbol{t} \, \mathrm{d}A \tag{4.34}$$

Equations (4.34), $(4.16)_1$ are used for weak equilibrium conditions Eqs. (4.7). The fulfillment of Eqs. (4.34), $(4.16)_1$ should also yield variational consistency regarding the two-field Eqs. (4.26) derived from the four-field Hu-Washizu variational principles Eq. (4.16).

4.2.2 Explicit crack modeling with SDA

The following discussion to a large extent follows the research work published in[4]. A displacement discontinuity is regarded on the element level. A 2D continuum element with four nodes with a single discontinuity is shown in Fig. 4.1. The displacement field is assumed

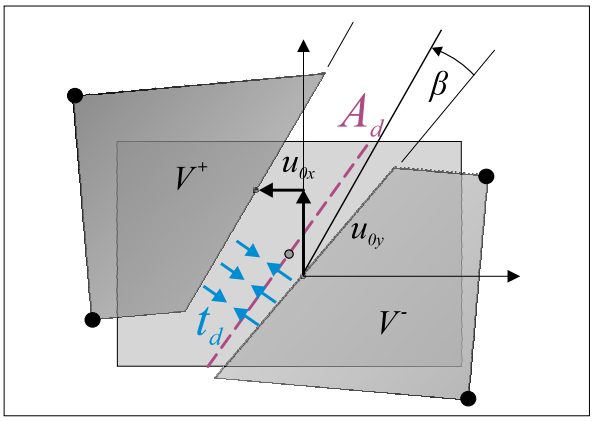

Figure 4.1: Kinematics of strong discontinuity approach[50]

to consist of a continuous part $\bar{\boldsymbol{u}}$ and an enhancing part $\widehat{\boldsymbol{u}}$ which might include discontinuous contributions

$$\boldsymbol{u}(\boldsymbol{x}) = \bar{\boldsymbol{u}}(\boldsymbol{x}) + \widehat{\boldsymbol{u}}(\boldsymbol{x}) \tag{4.35}$$

with a local coordinate $\boldsymbol{x}$. This corresponds to the KOS approach.

Following the rules for kinematics, equilibrium and material behavior are again utilized within this setup. Regarding kinematics the total displacement is decomposed according to Eq. (4.35) with an enhanced discontinuous part

$$\widehat{\boldsymbol{u}}(\boldsymbol{x}) = \mathcal{H}\ \|\boldsymbol{u}(\boldsymbol{x})\| \tag{4.36}$$

composed of a discontinuity splitting term

$$\mathcal{H} = \begin{cases} r, & \boldsymbol{x} \in V^+ \\ r-1, & else \end{cases} \tag{4.37}$$

with a constant splitting parameter $0 \leq r \leq 1$ to be chosen and a rigid body displacement term

$$\|\boldsymbol{u}(\boldsymbol{x})\| = \begin{bmatrix} 1 & 0 & -y+y_0 \\ 0 & 1 & x-x_0 \end{bmatrix} \cdot \begin{pmatrix} u_{0,x} \\ u_{0,y} \\ \beta \end{pmatrix} = \boldsymbol{N}_w(\boldsymbol{x}) \cdot \boldsymbol{w} \tag{4.38}$$

where β is the rotational degree of freedom, $u_{0,x}$,$u_{0,y}$ are translational degrees of freedom and $r = 0.5$ is generally used in the following. Here $\boldsymbol{w}$ and $\boldsymbol{N}_w$ are introduced as discontinuity degree of freedom and the discontinuity shape function, respectively, which lead to a fixed crack with center $\boldsymbol{x}_0$. The element's splitting into domains V^-,V^+ with respect to the crack orientation. Eq. (4.38) leads to a rigid body displacement of nodes as following where $\boldsymbol{M}_w$ collects the values of $\boldsymbol{N}_w$ at the element nodes

$$\hat{\boldsymbol{u}}_I = \begin{bmatrix} \boldsymbol{N}_w(\boldsymbol{x}_1) \\ \boldsymbol{N}_w(\boldsymbol{x}_2) \\ \boldsymbol{N}_w(\boldsymbol{x}_3) \\ \boldsymbol{N}_w(\boldsymbol{x}_4) \end{bmatrix} \cdot \boldsymbol{w} = \boldsymbol{M}_w \cdot \boldsymbol{w} \tag{4.39}$$

with nodal coordinates $\boldsymbol{x}_I$,$I = 1 \dots 4$. This is split into domains V^+,V^- by $\boldsymbol{\mathcal{H}} \cdot \hat{\boldsymbol{u}}_I$ with a diagonal

$$\boldsymbol{\mathcal{H}} = \begin{bmatrix} \mathcal{H}_1 & & & & \\ & \mathcal{H}_1 & & & \\ & & \ddots & & \\ & & & \mathcal{H}_4 & \\ & & & & \mathcal{H}_4 \end{bmatrix} \tag{4.40}$$

with $\mathcal{H}_I$ from Eq. (4.37) according to nodal mappings into V^+ or V^-, see Fig. 4.1.

Nodal displacements $\bar{\boldsymbol{u}}_I$ describe the continuous displacement field, see Eq. (4.1), and nodal displacements $\boldsymbol{\mathcal{H}} \cdot \hat{\boldsymbol{u}}_I$ represent the discontinuous displacement field together form the nodal displacements for the total displacement.

$$\boldsymbol{u}_I = \bar{\boldsymbol{u}}_I + \boldsymbol{\mathcal{H}} \cdot \hat{\boldsymbol{u}}_I \tag{4.41}$$

The interpolation of the total displacement field is determined with

$$\boldsymbol{u}(\boldsymbol{x}) = \boldsymbol{N}(\boldsymbol{x}) \cdot \boldsymbol{u}_I = \boldsymbol{N}(\boldsymbol{x}) \cdot \bar{\boldsymbol{u}}_I + \boldsymbol{N}(\boldsymbol{x}) \cdot \boldsymbol{\mathcal{H}} \cdot \hat{\boldsymbol{u}}_I \tag{4.42}$$

i.e., the interpolation operator is applied after superposing continuous and enhanced nodal contributions which is characteristic for KOS [52], this includes a continuous mapping of the discontinuous displacement field. With total nodal displacements $\boldsymbol{u}$ given from a computation on the system level and the discontinuity degrees of freedom $\boldsymbol{w}$ determined on element level, see following Section 4.2.4, the actual continuous field $\bar{\boldsymbol{u}}$ is recovered with

$$\bar{\boldsymbol{u}}(\boldsymbol{x}) \;\; = \;\; \boldsymbol{N}(\boldsymbol{x}) \cdot \boldsymbol{u}_I - \boldsymbol{N}(\boldsymbol{x}) \cdot \boldsymbol{\mathcal{H}} \cdot \boldsymbol{M}_w \cdot \boldsymbol{w} \tag{4.43}$$

using Eqs. (4.42,4.39). Continuum strains are derived from the actual continuous field with

$$\boldsymbol{\epsilon} = \frac{\partial \bar{\boldsymbol{u}}}{\partial \boldsymbol{x}} = \frac{\partial \boldsymbol{u}}{\partial \boldsymbol{x}} - \mathcal{H} \frac{\partial \left\| \boldsymbol{u}(\boldsymbol{x}) \right\|}{\partial \boldsymbol{x}} = \boldsymbol{B}(\boldsymbol{x}) \cdot \boldsymbol{u}_I - \boldsymbol{B}(\boldsymbol{x}) \cdot \boldsymbol{\mathcal{H}} \cdot \hat{\boldsymbol{u}}_I = \boldsymbol{B}(\boldsymbol{x}) \cdot \boldsymbol{u}_I - \boldsymbol{B}_w(\boldsymbol{x}) \cdot \boldsymbol{w} \tag{4.44}$$

with $\boldsymbol{B}$ according to Eq. (4.2) and

$$\boldsymbol{B}_w(\boldsymbol{x}) = \boldsymbol{B}(\boldsymbol{x}) \cdot \boldsymbol{\mathcal{H}} \cdot \boldsymbol{M}_w \tag{4.45}$$

This leads to zero strains in case $\boldsymbol{u}_I = \boldsymbol{\mathcal{H}} \cdot \hat{\boldsymbol{u}}_I$, i.e. when the total nodal displacements reproduce the discontinuous displacement field $\mathcal{H}\ \|\boldsymbol{u}(\boldsymbol{x})\|$.

The approach may be extended to multiple fields of displacement discontinuities. A secondary discontinuity, e.g., is introduced with the extension of Eq. (4.36)

$$\begin{aligned}
\boldsymbol{u}(\boldsymbol{x}) &= \bar{\boldsymbol{u}}(\boldsymbol{x}) + \mathcal{H}_1\ \|\boldsymbol{u}(\boldsymbol{x})\|_1 + \mathcal{H}_2\ \|\boldsymbol{u}(\boldsymbol{x})\|_2 \\
&= \bar{\boldsymbol{u}}(\boldsymbol{x}) + \mathcal{H}_1\, \boldsymbol{N}_{w,1} \cdot \boldsymbol{w}_1 + \mathcal{H}_2\, \boldsymbol{N}_{w,2} \cdot \boldsymbol{w}_2 \\
&= \bar{\boldsymbol{u}}(\boldsymbol{x}) + \begin{bmatrix} \mathcal{H}_1 \boldsymbol{N}_{w1} & \mathcal{H}_2 \boldsymbol{N}_{w,2} \end{bmatrix} \cdot \begin{pmatrix} \boldsymbol{w}_1 \\ \boldsymbol{w}_2 \end{pmatrix} \\
&= \bar{\boldsymbol{u}}(\boldsymbol{x}) + \boldsymbol{N}_w^{II} \cdot \boldsymbol{w}^{II}
\end{aligned} \tag{4.46}$$

The extensions to $\boldsymbol{M}_w^{II}$, see Eq. (4.39), and $\boldsymbol{B}_w^{II}$, see Eq. (4.45), are straightforward with the number of discontinuity degrees of freedom doubled on the element level whereby $\boldsymbol{\mathcal{H}}$ remains unchanged. The application of SDA to other than four-node 2D elements, in particular triangular elements and 3D elements, is also straightforward. The latter introduces six discontinuity degrees of freedom for each discontinuity according to spatial rigid body movements and has a plane-convex polygon separating an element. Further, the discontinuity contour can be changed with modifications of $\boldsymbol{\mathcal{H}}$ to consider the rotating crack approach during a loading history. Earlier, the kinematics is discussed, and discontinuity equilibrium will be formulated in the next step. A weak form

$$\begin{aligned}
\int_V \mathcal{H}\, \delta \nabla^{sym} \|\boldsymbol{u}\|^T \cdot \boldsymbol{\sigma}\, \mathrm{d}V + \int_{A_d} \delta \|\boldsymbol{u}\|^T \cdot \boldsymbol{t}_d\, \mathrm{d}A \\
= \int_V \mathcal{H}\, \delta \|\boldsymbol{u}\|^T \cdot \boldsymbol{b}\, \mathrm{d}V + \int_{A_t} \mathcal{H}\, \delta \|\boldsymbol{u}\|^T \cdot \boldsymbol{t}\, \mathrm{d}A
\end{aligned} \tag{4.47}$$

in analogy to Eq. (4.7) is used with the symmetric Nabla operator ∇^{sym}, the path A_d along the discontinuity and the traction t_d along the discontinuity, see Fig. 4.1, differ from Eq. (4.34) with a derivation in a general context.. The discontinuity interpolation Eq. (4.38) yields

$$\begin{aligned}
\nabla^{sym} \|\boldsymbol{u}\| &= 0 \\
\delta \|\boldsymbol{u}\| &= \boldsymbol{N}_w \cdot \delta \boldsymbol{w}
\end{aligned} \tag{4.48}$$

which in analogy to Eq. (4.10) leads to a discretized discontinuity equilibrium

$$\delta \boldsymbol{w}^T \cdot (\boldsymbol{p}_w - \boldsymbol{f}_w) = 0 \tag{4.49}$$

with

$$\boldsymbol{f}_w = \int_{A_d} \boldsymbol{N}_w^T \cdot \boldsymbol{t}_d \, \mathrm{d}A \tag{4.50}$$

and

$$\boldsymbol{p}_w = \int_V \mathcal{H} \, \boldsymbol{N}_w^T \cdot \boldsymbol{b} \, \mathrm{d}V + \int_{A_t} \mathcal{H} \, \boldsymbol{N}_w^T \cdot \boldsymbol{t} \, \mathrm{d}A \tag{4.51}$$

Compare to Eqs. (4.11,4.12), $\boldsymbol{f}_w$,$\boldsymbol{p}_w$ are not nodal forces assigned to nodal degrees of freedom but generalized 'discontinuity' forces assigned to the discontinuity degrees of freedom whereby $\boldsymbol{f}_w$ can be considered as internal due its dependence on generalized internal 'stresses' $\boldsymbol{t}_d$ and $\boldsymbol{p}_w$ as external due to its dependence on given loading terms $\boldsymbol{b}$,$\boldsymbol{t}$.

Finally, a generalized type of material behavior has to be regarded. In analogy to Eq. (4.3), a general form is given by

$$\boldsymbol{t}_d = \boldsymbol{t}_d(\boldsymbol{w}) \tag{4.52}$$

which follows the fictitious or cohesive crack model [47]. In analogy to Eq. (4.5) it should be specified in an incremental form

$$\dot{\boldsymbol{t}}_d = \boldsymbol{C}_{Tw}(\boldsymbol{w}) \cdot \dot{\boldsymbol{w}} \tag{4.53}$$

This leads to a linearization of the internal discontinuity forces

$$\dot{\boldsymbol{f}}_w = \int_{A_d} \boldsymbol{N}_w^T \cdot \boldsymbol{C}_{Tw} \cdot \boldsymbol{N}_w \, \mathrm{d}A \cdot \dot{\boldsymbol{w}} = \boldsymbol{K}_{T,nn} \cdot \dot{\boldsymbol{w}} \tag{4.54}$$

with a tangential discontinuity stiffness matrix $\boldsymbol{K}_{T,nn}$ in analogy to Eq. (4.13).

4.2.3 Coupling of continuum to discontinuity

The discretized continuous part described by Eq. (4.10) and the part including a discontinuity only described by Eq. (4.49) has to be coupled. This is started by deriving the virtual continuous displacement from the total displacement and the discontinuous part as given with Eqs. (4.35,4.36)

$$\delta\bar{\boldsymbol{u}} = \delta\boldsymbol{u} - \mathcal{H}\,\delta\,\|\boldsymbol{u}\| \tag{4.55}$$

and applying the interpolations Eqs. (4.42,4.38)

$$\delta\bar{\boldsymbol{u}} = \boldsymbol{N}\cdot\delta\boldsymbol{u}_I - \mathcal{H}\boldsymbol{N}_w\cdot\delta\boldsymbol{w} \tag{4.56}$$

Later, the virtual strains are given by Eq. (4.44)

$$\delta\boldsymbol{\epsilon} = \boldsymbol{B}(\boldsymbol{x})\cdot\delta\boldsymbol{u}_I - \boldsymbol{B}_w(\boldsymbol{x})\cdot\delta\boldsymbol{w} \tag{4.57}$$

Eq. (4.7) is still applicable due to continuity of $\bar{}$ and $\delta\bar{}$. Thus the application to the weak equilibrium form for the continuous field Eq. (4.7)

$$\begin{aligned}
&\delta\boldsymbol{u}_I^T\cdot\int_V\boldsymbol{B}^T\cdot\boldsymbol{\sigma}\,\mathrm{d}V - \delta\boldsymbol{w}^T\cdot\int_V\boldsymbol{B}_w^T\cdot\boldsymbol{\sigma}\,\mathrm{d}V\\
&\quad=\delta\boldsymbol{u}_I^T\cdot\int_V\boldsymbol{N}^T\cdot\boldsymbol{b}\,\mathrm{d}V - \delta\boldsymbol{w}^T\cdot\int_V\mathcal{H}\boldsymbol{N}_w^T\cdot\boldsymbol{b}\,\mathrm{d}V\\
&\qquad+\delta\boldsymbol{u}_I^T\cdot\int_{A_t}\boldsymbol{N}^T\cdot\boldsymbol{t}\,\mathrm{d}A - \delta\boldsymbol{w}^T\cdot\int_{A_t}\mathcal{H}\boldsymbol{N}_w^T\cdot\boldsymbol{t}\,\mathrm{d}A
\end{aligned} \tag{4.58}$$

leads to an extended form of Eq. (4.10)

$$\delta\boldsymbol{u}^T\left(\boldsymbol{p}_I - \boldsymbol{f}_I\right) - \delta\boldsymbol{w}^T\cdot\left(\boldsymbol{p}_w - \boldsymbol{f}_c\right) = 0 \tag{4.59}$$

with $\boldsymbol{p}_I$ from Eq. (4.12), $\boldsymbol{f}_I$ from Eq. (4.11), $\boldsymbol{p}_w$ from Eq. (4.51) and coupling discontinuity forces

$$\boldsymbol{f}_c = \int_V\boldsymbol{B}_w^T\cdot\boldsymbol{\sigma}\,\mathrm{d}V \tag{4.60}$$

with $\boldsymbol{B}_w$ from Eq. (4.45). Adding the conditions for the extended discretized equilibrium for the continuous field Eq. (4.59) and the discretized equilibrium for the discontinuous field

Eq. (4.49) yields two sets of combined discretized equilibrium conditions for a particular element

$$\begin{aligned} \boldsymbol{r}_I &= \boldsymbol{p}_I - \boldsymbol{f}_I = 0 \\ \boldsymbol{r}_w &= \boldsymbol{f}_c - \boldsymbol{f}_w = 0 \end{aligned} \tag{4.61}$$

with residuals $\boldsymbol{r}_I$,$\boldsymbol{r}_w$ as $\delta\boldsymbol{u}_I$,$\delta\boldsymbol{w}$ are independent and arbitrary.

Terms of Eq. (4.61) remain to be linearized with their derivations with respect to the loading time t. The internal nodal forces time derivative $\dot{\boldsymbol{f}}_I$ from Eq. (4.13) has to be extended to imply the total displacement time derivative by Eq. (4.44)

$$\begin{aligned} \dot{\boldsymbol{f}}_I &= \int_V \boldsymbol{B}^T \cdot \dot{\boldsymbol{\sigma}} \, \mathrm{d}V = \int_V \boldsymbol{B}^T \cdot \boldsymbol{C}_T \cdot \dot{\boldsymbol{\epsilon}} \, \mathrm{d}V \\ &= \int_V \boldsymbol{B}^T \cdot \boldsymbol{C}_T \cdot \boldsymbol{B} \, \mathrm{d}V \cdot \dot{\boldsymbol{u}}_I - \int_V \boldsymbol{B}^T \cdot \boldsymbol{C}_T \cdot \boldsymbol{B}_w \, \mathrm{d}V \cdot \dot{\boldsymbol{w}} \\ &= \boldsymbol{K}_{T,uu} \cdot \dot{\boldsymbol{u}}_I - \boldsymbol{K}_{T,uw} \cdot \dot{\boldsymbol{w}} \end{aligned} \tag{4.62}$$

with the tangential stiffness matrices $\boldsymbol{K}_{T,uu}$,$\boldsymbol{K}_{T,uw}$. The time derivative of the coupling discontinuity forces, see Eq. (4.60), is derived in an analogous way

$$\begin{aligned} \dot{\boldsymbol{f}}_c = &= \int_V \boldsymbol{B}_w^T \cdot \boldsymbol{C}_T \cdot \boldsymbol{B} \, \mathrm{d}V \cdot \dot{\boldsymbol{u}}_I - \int_V \boldsymbol{B}_w^T \cdot \boldsymbol{C}_T \cdot \boldsymbol{B}_w \, \mathrm{d}V \cdot \dot{\boldsymbol{w}} \\ &= \boldsymbol{K}_{T,wu} \cdot \dot{\boldsymbol{u}}_I - \boldsymbol{K}_{T,ww} \cdot \dot{\boldsymbol{w}} \end{aligned} \tag{4.63}$$

with further tangential stiffness matrices $\boldsymbol{K}_{T,wu}$,$\boldsymbol{K}_{T,ww}$. The time derivative of the internal discontinuity forces $\boldsymbol{f}_w$ is given by Eq. (4.54) and $\dot{\boldsymbol{p}}_I$, see Eq. (4.12), is ruled by prescribed $\dot{\boldsymbol{b}}$,$\dot{\boldsymbol{t}}$.

Thus, incremental equilibrium conditions $\dot{\boldsymbol{p}}_I - \dot{\boldsymbol{f}}_I = 0$,$\dot{\boldsymbol{f}}_c - \dot{\boldsymbol{f}}_w = 0$ corresponding to Eq. (4.61) are given with

$$\begin{bmatrix} \boldsymbol{K}_{T,uu} & -\boldsymbol{K}_{T,uw} \\ -\boldsymbol{K}_{T,wu} & \boldsymbol{K}_{T,ww} + \boldsymbol{K}_{Tnn} \end{bmatrix} \cdot \begin{pmatrix} \dot{\boldsymbol{u}}_I \\ \dot{\boldsymbol{w}} \end{pmatrix} = \begin{pmatrix} \dot{\boldsymbol{p}} \\ 0 \end{pmatrix} \tag{4.64}$$

This is decoupled with the second row to be solved firstly on the element level

$$\dot{\boldsymbol{w}} = \boldsymbol{\mathcal{D}}_{T,w} \cdot \dot{\boldsymbol{u}}_I \tag{4.65}$$

with

$$\boldsymbol{\mathcal{D}}_{T,w} = [\boldsymbol{K}_{T,ww} + \boldsymbol{K}_{Tnn}]^{-1} \cdot \boldsymbol{K}_{T,wu} \tag{4.66}$$

and the solution $\dot{\boldsymbol{w}}$ to be used for the first row

$$\boldsymbol{\mathcal{K}}_{T,u} \cdot \dot{\boldsymbol{u}}_I = \dot{\boldsymbol{p}} \tag{4.67}$$

with

$$\boldsymbol{\mathcal{K}}_{T,u} = \boldsymbol{K}_{T,uu} - \boldsymbol{K}_{T,uw} \cdot [\boldsymbol{K}_{T,ww} + \boldsymbol{K}_{Tnn}]^{-1} \cdot \boldsymbol{K}_{T,wu} \tag{4.68}$$

whereby the latter is assembled on the system level and solved for the nodal displacement increments of the whole system.

4.2.4 Loading time discretization and equilibrium iteration

The Euler backward approach with a constant time step $t^i = \Delta t \cdot i, i = 1 \dots n$ is used for loading time discretization. It is performed with

$$\begin{aligned} \dot{\boldsymbol{w}}^i &\approx \frac{\Delta \boldsymbol{w}}{\Delta t} = \frac{\boldsymbol{w}^i - \boldsymbol{w}^{i-1}}{\Delta t} \\ \dot{\boldsymbol{u}}_I^i &\approx \frac{\Delta \boldsymbol{u}_I}{\Delta t} = \frac{\boldsymbol{u}_I^i - \boldsymbol{u}_I^{i-1}}{\Delta t} \\ \dot{\boldsymbol{p}}^i &\approx \frac{\Delta \boldsymbol{p}}{\Delta t} = \frac{\boldsymbol{p}^i - \boldsymbol{p}^{i-1}}{\Delta t} \end{aligned} \tag{4.69}$$

Equilibrium $\boldsymbol{p}_I^{i-1} - \boldsymbol{f}_I^{i-1} = 0, \boldsymbol{f}_c^{i-1} - \boldsymbol{f}_w^{i-1} = 0$ is assumed for the preceding time t^{i-1}. The loading $\boldsymbol{p}^i$ is basically prescribed for all time steps. This yields a nonlinear set of algebraic equations

$$\boldsymbol{\mathcal{K}}_{T,u}(\boldsymbol{u}_I, \boldsymbol{w}) \cdot \Delta \boldsymbol{u}_I = \Delta \boldsymbol{p} \tag{4.70}$$

according to Eq. (4.67) to gain a solution $\boldsymbol{u}_I^i = \boldsymbol{u}_I^{i-1} + \Delta \boldsymbol{u}_I$ on the system level with a potential residuum

$$\boldsymbol{r}_I = \boldsymbol{p}_I - \boldsymbol{f}_I \tag{4.71}$$

see Eq. $(4.61)_1$. Iterated values of $\boldsymbol{u}_I^i$,$\Delta\boldsymbol{u}_I$ are indicated with ${}^{\nu}\boldsymbol{u}_I^i$,$\Delta^{\nu}\boldsymbol{u}_I$. A first starter for Eq. (4.70) is given with

$$\boldsymbol{\mathcal{K}}_{T,u}(\boldsymbol{u}_I^{i-1},\boldsymbol{w}^{i-1}) \cdot \delta^1\boldsymbol{u}_I = \Delta\boldsymbol{p} \tag{4.72}$$

and $\Delta^1\boldsymbol{u}_I = \delta^1\boldsymbol{u}_I$ and ${}^1\boldsymbol{u}_I^i = \boldsymbol{u}_I^{i-1} + \Delta^1\boldsymbol{u}$.

The displacements derived on the system level can be used for each element to iterate for its discontinuity degrees of freedom using the generally nonlinear set of equations

$$\Delta\boldsymbol{w} = \boldsymbol{\mathcal{D}}_{T,w}(\boldsymbol{u}_I,\boldsymbol{w}) \cdot \Delta\boldsymbol{u}_I \tag{4.73}$$

according to Eq. (4.65) with a potential residuum

$$\boldsymbol{r}_w = \boldsymbol{f}_c - \boldsymbol{f}_w \tag{4.74}$$

see Eq. $(4.61)_2$. A first starter for Eq. (4.73) is given with

$$\delta^1\boldsymbol{w} = \boldsymbol{\mathcal{D}}_{T,w}\left({}^1\boldsymbol{u}_I^i,\boldsymbol{w}^{i-1}\right) \cdot \Delta^1\boldsymbol{u}_I \tag{4.75}$$

and $\Delta^1\boldsymbol{w} = \delta^1\boldsymbol{w}$ and ${}^1\boldsymbol{w}^i = \boldsymbol{w}^{i-1} + \Delta^1\boldsymbol{w}$ and a residuum

$${}^1\boldsymbol{r}_w = \boldsymbol{f}_c\left({}^1\boldsymbol{u}_I^i,{}^1\boldsymbol{w}^i\right) - \boldsymbol{f}_w\left({}^1\boldsymbol{w}^i\right) \tag{4.76}$$

For $|{}^1\boldsymbol{r}_w| > tol_w$ this is iteratively solved with the Newton-Raphson method in the general form

$$\begin{aligned} \delta^{\mu+1}\boldsymbol{w} &= -\left.\frac{\partial\boldsymbol{r}_w(\boldsymbol{w})}{\partial\boldsymbol{w}}\right|_{\boldsymbol{w}={}^{\mu}\boldsymbol{w}^i} \cdot {}^{\mu}\boldsymbol{r}_w \\ \Delta^{\mu+1}\boldsymbol{w} &= \Delta^{\mu}\boldsymbol{w} + \delta^{\mu+1}\boldsymbol{w} \\ {}^{\mu+1}\boldsymbol{w}^i &= \boldsymbol{w}^{i-1} + \Delta^{\mu+1}\boldsymbol{w} \end{aligned} \tag{4.77}$$

The Jacobian is given with

$$\frac{\partial\boldsymbol{r}_w(\boldsymbol{w})}{\partial\boldsymbol{w}} = \frac{\boldsymbol{f}_c\left({}^1\boldsymbol{u}_I^i,\boldsymbol{w}\right)}{\partial\boldsymbol{w}} - \frac{\boldsymbol{f}_w\left(\boldsymbol{w}\right)}{\partial\boldsymbol{w}} = -\left(\boldsymbol{K}_{T,ww} + \boldsymbol{K}_{T,nn}\right) \tag{4.78}$$

see Eqs. (4.63,4.54).

With $|^{\mu}\boldsymbol{r}_w| \approx 0$ and discontinuity equilibrium and $\boldsymbol{w}^i$ given on the element level the computation continues for an improved $\boldsymbol{u}^i$ on the system level. From Eq. (4.71) the current residual is given with

$$^{1}\boldsymbol{r}_I = \boldsymbol{p}_I^i - \boldsymbol{f}_I\left(^{1}\boldsymbol{u}_I^i, \boldsymbol{w}^i\right) \tag{4.79}$$

and for $|^{1}\boldsymbol{r}_I| > 0$ the general Newton-Raphson iteration is performed with

$$\begin{aligned} \delta^{\nu+1}\boldsymbol{u}_I &= -\left.\frac{\partial \boldsymbol{r}_I(\boldsymbol{u}_I)}{\partial \boldsymbol{u}_I}\right|_{\boldsymbol{u}_I = {}^{\nu}\boldsymbol{u}_I^i} \cdot {}^{\nu}\boldsymbol{r}_I \\ \Delta^{\nu+1}\boldsymbol{u}_I &= \Delta^{\nu}\boldsymbol{u}_I + \delta^{\nu+1}\boldsymbol{u}_I \\ {}^{\nu+1}\boldsymbol{u}_I^i &= \boldsymbol{u}_I^{i-1} + \Delta^{\nu+1}\boldsymbol{u}_I \end{aligned} \tag{4.80}$$

which is nested with $\boldsymbol{w}$-iterations on the element level. The Jacobian is determined as

$$\begin{aligned} \frac{\partial \boldsymbol{r}_I(\boldsymbol{u}_I)}{\partial \boldsymbol{u}_I} &= -\frac{\partial \boldsymbol{f}_I(\boldsymbol{u}_I, \boldsymbol{w})}{\partial \boldsymbol{u}_I} - \frac{\partial \boldsymbol{f}_I(\boldsymbol{u}_I, \boldsymbol{w})}{\partial \boldsymbol{w}} \cdot \frac{\partial \boldsymbol{w}}{\partial \boldsymbol{u}_I} \\ &= -\boldsymbol{K}_{T,uu} + \boldsymbol{K}_{T,uw} \cdot \boldsymbol{\mathcal{D}}_{T,w} \\ &= -\boldsymbol{\mathcal{K}}_{T,u} \end{aligned} \tag{4.81}$$

see Eqs. (4.62, 4.65,4.68). System equilibrium is reached with $|^{\nu}\boldsymbol{r}_u| \approx 0$ and yields the solutions for the total displacements $\Delta\boldsymbol{u}_I$,$\boldsymbol{u}_I^i$ of all nodes and for the discontinuity degrees of freedom $\Delta\boldsymbol{w}$,$\boldsymbol{w}^i$ for all elements. This leads to strains and strain increments with Eq. (4.44) and finally to bulk stresses at time t^i with a constitutive law. The solutions for the following time steps are derived in the same way whereby following the prescribed loading history.

4.2.5 Crack initiation, geometry and tractions

Crack initiation depends on predefined criteria, whereas the crack formation pertain with the loading history. A Rankine criterion is used in the following, i.e. a crack initiates when principal tensile stress exceeds the uniaxial tensile strength of the bulk material. The normal to the crack surface coincides with the direction of the respective principal stress.

Phenomena become complex from a phenomenological point of view after crack initiation. Mesoscopic crack development is characterized by (1) micro-crack alignment, (2) micro-crack enlargement, (3) crack bridging by aggregates, (4) macro cracking, cracking evolves within the so-called process band with a width of 2-3 times the largest aggregate size, see Fig. 4.2.

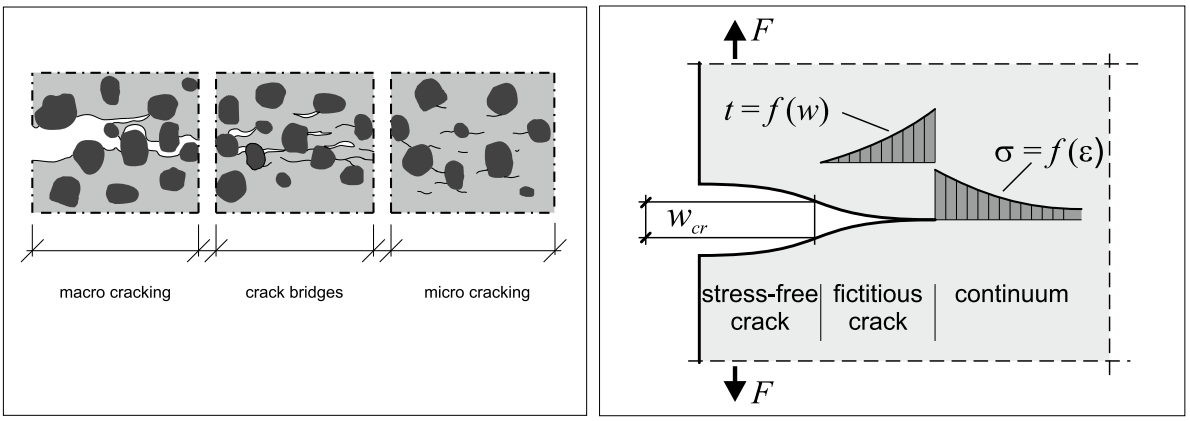

Figure 4.2: a) Scheme of mesoscopic crack formation b) Fictitious crack model[50]

This is simplified with the fictitious or cohesive crack model [47] in order to remain within the framework of continuum mechanics.

This model has to be related to finite elements. Element stresses are computed in element integration points. Numerical integration is performed with the Gaussian scheme with four sampling points for the 2D quad element currently under consideration. As the element size is chosen to be relatively small for FRCC specimen subject to the investigation, the mesh size is in the magnitude of [mm] and generally smaller than the crack bandwidth. Cracks are not allowed concerning every integration point; however, they are placed in an element's geometric center. Thus, a crack initiates when the center projection of the integration point's largest principal stresses exceeds the uniaxial tensile strength whereby the normal to the crack surface coincides with the direction of centered principal stress. This yields the data x_0,y_0 and V^+,V^- for $\boldsymbol{\mathcal{H}}$, see Eqs. (4.38,4.40) and Fig. 4.1, utilized for the SDA extension of an element fulfilling the criteria during a loading history.

Cracked neighbor elements do not constrain crack directions, i.e., a crack contour extending over a series of elements is not enforced to be continuous. On the one hand, the principal stress directions generally will not deviate too much within neighbored elements, on the other hand, the computed crack contour indicates an extended band without sharp bounds in vast areas and not a distinct macro crack. The criteria for crack initiation are checked after each time step for each element, i.e., an explicit check is performed. This might lead to an overestimation of concrete tensile strength, controlled by the time step size. These assumptions about position, direction, and checkpoints simplify the procedure to a large extent. They also easily allow for the initiation of multiple cracks with the same center but different orientations.

Furthermore, tractions transmitted depending upon crack width have to be defined for the fictitious crack model. The general form has already been given with Eqs. (4.52,4.53). Regarding 2D, this includes a normal component and a shear component. The behavior of the normal component has been investigated to a large extent allowing for a softening course as shown in Fig. 4.3 for normal crack tractions t_n depending on normal crack width w_n [102, 41, 106]. This is constrained by the maximum normal stress t_{ct} on crack initiation,

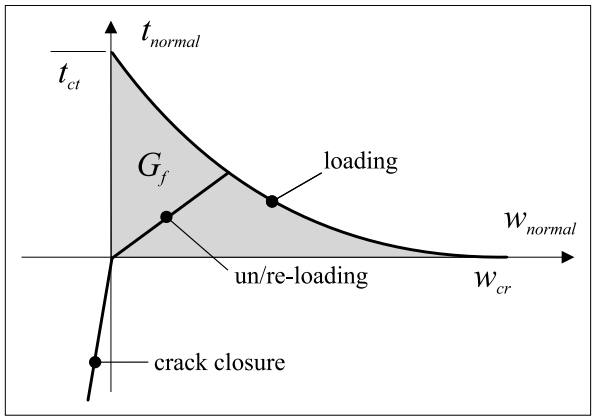

Figure 4.3: Relation between normal components of crack traction - crack width[50]

which is the concrete uniaxial tensile strength, the so-called critical crack w_{cr} width where crack tractions come to zero and further the fracture energy

$$G_f = \int_0^{w_{cr}} t_n \, \mathrm{d}w_n \tag{4.82}$$

These values are generally assumed as material parameters to be determined from experiments. This approach is modified insofar as t_{ct},G_f are used as input parameters and a parabolic $t_n - w_n$-relation

$$t_n = t_{ct} \left(\delta_n^2 - 2\delta_n + 1\right), \quad 0 \leq \delta_n = \frac{w_n}{w_{cr}} \leq 1 \tag{4.83}$$

is assumed with an extremal minimum in w_{cr}. Thus, the fracture energy is given with $G_f = \frac{1}{3} t_{ct} w_{cr}$. This yields a value w_{cr} for prescribed values G_f,t_{ct} generally conforming to experimental data which for w_{cr} anyway are hard to estimate regarding the background given in Fig. 4.2. The tangential stiffness is given with

$$\frac{\mathrm{d}t_n}{\mathrm{d}w_n} = \frac{t_{ct}}{w_{cr}} \left(2\delta_n - 2\right) \tag{4.84}$$

This describes the state of loading. Unloading is possible from all points of the loading path and follows a branch indicated in Fig. 4.3 with the point of initial unloading ($w_{n,u}$,$t_{n,u}$) connected to the origin. The pair ($w_{n,u}$,$t_{n,u}$) is a state variable comprising the preceding load history. The ratio ($t_{n,u}/w_{n,u}$) indicates the unloading stiffness and ($t_{n,u}/w_{n,u}$) w_n the crack traction with the current w_n on the unloading path. Crack closure is modeled with a penalty approach with a high constant positive stiffness in the range $w_n \leq 0$. Reloading elastically retraces crack closure and unloading up to the current ($w_{n,u}$,$t_{n,u}$) and continues along the loading path.

In contrast to the normal component, much less knowledge is available for the shear component t_s depending on the crack sliding w_s. A simple shear retention

$$t_s = \alpha_s \, (1 - \delta_n)^2 \, E_{bulk} \;\; w_s \tag{4.85}$$

is assumed for this purpose with Young's modulus E_{bulk} of the bulk material and a shear retention factor α_s. The inclusion of the related normal crack width δ_n, see Eq. (4.83), scales the shear traction down with increasing normal crack width. The shear retention factor is assumed in a range $0 \leq \alpha_s \leq 0.01$ and subject to parameter sensitivity studies. The tangential stiffness is assumed with

$$\frac{\mathrm{d}t_s}{\mathrm{d}w_s} = \alpha_s \, (1 - \delta_n)^2 \, E_{bulk} \tag{4.86}$$

The contribution $\mathrm{d}t_s/\,\mathrm{d}w_n$ is neglected in order to preserve general symmetry. A value $\alpha_s > 0$ generally proves to be necessary regarding convergence and stability of numerical computations. The relations of t_n,t_s depending on w_n,w_s and their tangential stiffness are originally formulated in a local coordinate system aligned to the crack orientation. Regarding Eqs. (4.52,4.53) they remain, specifically for each cracked element, to be transformed into the global coordinate system to which the derivations of Sections 4.2.2 to 4.2.4 refer to.

A final point pertains to the order of Gaussian numerical integration is to determine quantities like $\boldsymbol{f}_I \ldots$ and $\boldsymbol{K}_{T,uu} \ldots$. It is performed on the element level whereby results are assembled on the system level if required. This primarily concerns integrations over domains V of elements extended with SDA to describe cracks or a discontinuity of displacements. Such discontinuities generally also lead to discontinuities of stresses, which might impair the precision of the Gaussian integration scheme. Bulk stress discontinuities should be attenuated

due to equilibrating crack tractions upon the fulfillment of Eq. (4.47). Thus, the ordinary 2×2 integration for 2D quad elements is retained for SDA quad elements. This is used as a reference for parameter studies with varying integration orders in later investigations.

Furthermore, regarding $\boldsymbol{f}_w$, see Eq. (4.50), and $\boldsymbol{K}_{T,nn}$, see Eq. (4.54), numerical integrations have to be performed along the discontinuity contour A_d, see Fig. 4.1. With the linear discontinuity approach Eq. (4.38) and the at most quadratic approach for tractions, see Fig. 4.3(a) 2-point Gaussian integration generally proves to be sufficient for the 2D setup.

4.2.6 Viscous regularization

Switches between loading and unloading branch of crack tractions are typical for minimal normal crack width values w_n or spatially non-homogeneous structures during a loading history whereby a crack initiation in a particular element often leads to internal stress redistributions and unloading in neighbored cracked elements. As the tangential stiffness differs in sign, see Fig. 4.3, the Newton-Raphson iteration for the equilibrium on the element level, see Eqs. (4.74) – (4.77), tends to yield an oscillating behavior consecutively switching between the loading and unloading branches.

Two cases can be observed: a stationary residual oscillation with an upper bounded $|\boldsymbol{r}_w|$, see Eq. (4.74), and an unstable oscillation with strongly increasing and unbounded $|\boldsymbol{r}_w|$. While the first one generally is followed by convergence in later steps, the latter destabilizes the whole simulation and leads to a computation exit. This is typical for large systems. A stabilization may practically be reached by introducing a regularizing additional viscous contribution to the crack traction, crack width relation Eq. (4.52)

$$\begin{aligned} \boldsymbol{t}_d &= \boldsymbol{f}(\boldsymbol{w}) + \boldsymbol{t}_{d,vis} \\ \boldsymbol{t}_{d,vis} &= \eta_w \, \dot{\boldsymbol{w}} \\ \dot{\boldsymbol{t}}_{d,vis} &= \eta_w \, \ddot{\boldsymbol{w}} \end{aligned} \tag{4.87}$$

with a parameter η_w to reach a damping effect [17]. The function $\boldsymbol{f}$ marks the quasi-static contribution according to Eqs (4.83,4.85) transferred to the global system. Time derivatives of $\boldsymbol{w}$ are discretized in time with the one step Newmark-method [9] with time integration

parameters γ,β

$$\begin{aligned}
\dot{\boldsymbol{w}}^i &\approx \frac{\gamma}{\beta\Delta t}\left[\boldsymbol{w}^i - \boldsymbol{w}^{i-1}\right] + \left(1 - \frac{\gamma}{\beta}\right)\dot{\boldsymbol{w}}^{i-1} + \Delta t\left(1 - \frac{\gamma}{2\beta}\right)\ddot{\boldsymbol{w}}^{i-1} \\
&= \frac{\gamma}{\beta\Delta t}\Delta\boldsymbol{w} + \left(1 - \frac{\gamma}{\beta}\right)\dot{\boldsymbol{w}}^{i-1} + \Delta t\left(1 - \frac{\gamma}{2\beta}\right)\ddot{\boldsymbol{w}}^{i-1} \\
\ddot{\boldsymbol{w}}^i &\approx \frac{1}{\beta\Delta t^2}\left[\boldsymbol{w}^i - \boldsymbol{w}^{i-1}\right] - \frac{1}{\beta\Delta t}\dot{\boldsymbol{w}}^{i-1} - \left(\frac{1}{2\beta} - 1\right)\ddot{\boldsymbol{w}}^{i-1} \\
&= \frac{1}{\beta\Delta t^2}\Delta\boldsymbol{w} - \frac{1}{\beta\Delta t}\dot{\boldsymbol{w}}^{i-1} - \left(\frac{1}{2\beta} - 1\right)\ddot{\boldsymbol{w}}^{i-1}
\end{aligned} \tag{4.88}$$

as second order derivatives occur. The time integration parameters are generally chosen with $\gamma = 1/2, \beta = 1/4$ to have unconditional stability independent of Δt. This leads to

$$\begin{aligned}
\dot{\boldsymbol{w}}^i &= \frac{2}{\Delta t}\Delta\boldsymbol{w} - \dot{\boldsymbol{w}}^{i-1} \\
\ddot{\boldsymbol{w}}^i &= \frac{4}{\Delta t^2}\Delta\boldsymbol{w} - \frac{4}{\Delta t}\dot{\boldsymbol{w}}^{i-1} - \ddot{\boldsymbol{w}}^{i-1}
\end{aligned} \tag{4.89}$$

and firstly

$$\boldsymbol{t}_{d,vis} = \frac{2\eta_w}{\Delta t}\Delta\boldsymbol{w} - \eta_w\,\dot{\boldsymbol{w}}^{i-1} \tag{4.90}$$

The rate of the viscous crack traction is approximated in analogy to Eq. $(4.89)_1$

$$\dot{\boldsymbol{t}}^i_{d,vis} = \frac{2}{\Delta t}\Delta\boldsymbol{t}_{d,vis} - \dot{\boldsymbol{t}}^{i-1}_{d,vis} \tag{4.91}$$

Using Eqs. $(4.89)_2$, (4.91) for Eq. $(4.87)_3$ yields

$$\Delta\boldsymbol{t}_{d,vis} = \frac{2\eta_w}{\Delta t}\Delta\boldsymbol{w} - 2\eta_w\dot{\boldsymbol{w}}^{i-1} - \frac{\Delta t}{2}\eta_w\,\ddot{\boldsymbol{w}}^{i-1} + \frac{\Delta t}{2}\dot{\boldsymbol{t}}^{i-1}_{d,vis} \tag{4.92}$$

As $\dot{\boldsymbol{w}}^{i-1}$,$\ddot{\boldsymbol{w}}^{i-1}$,$\dot{\boldsymbol{t}}^{i-1}_{d,vis}$ are given and constant in the current setup an algorithmic tangential stiffness is derived with

$$\frac{\partial\Delta\boldsymbol{t}_{d,vis}}{\partial\Delta\boldsymbol{w}} = \frac{2\eta_w}{\Delta t}\,\boldsymbol{I} \tag{4.93}$$

with the identity matrix $\boldsymbol{I}$. The integration of this approach into the Newton-Raphson iteration on the element level, see Eqs. (4.74) – (4.78), is straightforward by adding $\boldsymbol{t}_{d,vis}$ from Eq. (4.90) to $\boldsymbol{t}_d$ in Eq. (4.50) and the tangential stiffness Eq. (4.93) to $\boldsymbol{C}_{Tw}$ in Eq. (4.53).

Summing up, the final tangential discontinuity material stiffness $\boldsymbol{C}_{Tw}$ from Eq. (4.53) has two additive contributions: the quasi-static part from Eqs. (4.84,4.86) translated into the global system and the viscous part from Eq. (4.93). The first one potentially is negative definite due to the negative stiffness $\mathrm{d}t_n/\,\mathrm{d}w_n$, the second one is always positive definite. A negative definite sum generally impairs the Newton-Raphson equilibrium iteration. But the sum can always be made positive definite, i.e., regularized, by an appropriate selection of $\eta_w/\Delta t$. On the other hand, the selection of a viscosity η_w for this viscous regularization approach is somehow arbitrary as no experimental evidence is currently available. It should be chosen such that it facilitates convergence behavior but has no significant impact on simulation results. Based on simulation experiences, considering the viscous regularization is necessary for large systems; otherwise, the solutions cannot be obtained.

4.3 NEW APPROACH FOR DEFINITION OF EMBEDDED FIBERS WITH FLIXIBLE BOND

The mechanical properties of fibers have been described in Section 2.2. 2D truss elements are used to model the fibers, which act uni-axially and ignore the bending effect. These truss elements are arbitrarily distributed and freely embedded in continuum whereby the fiber nodes are independent of continuum nodes, and they do not have to share positions, see Fig. 4.4 Truss elements and continuum elements are coupled by unique bond elements which

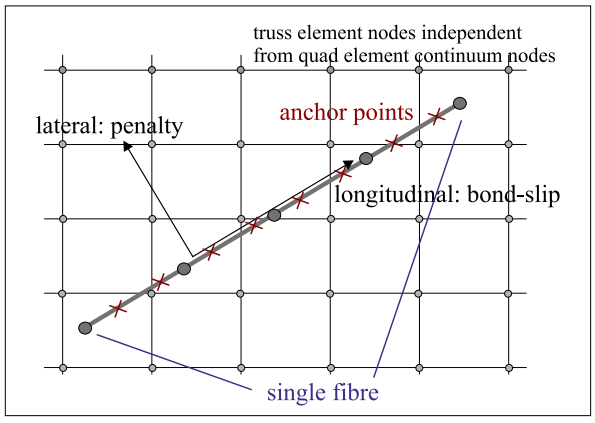

Figure 4.4: Truss elements arbitrarily embedded in continuum[50]

are developed in the following. Displacements of truss elements are interpolated, defined by a relationship as following

$$\boldsymbol{u}_t(\boldsymbol{x}) = \boldsymbol{N}_t(\boldsymbol{x}) \cdot \boldsymbol{u}_{tI} \tag{4.94}$$

which is similar to Eq. (4.1) but with their specific shape functions $\boldsymbol{N}_t$. Furthermore, displacements of continuum elements are interpolated according to Eq. (4.42)

$$\boldsymbol{u}(\boldsymbol{x}) = \boldsymbol{N}(\boldsymbol{x}) \cdot \boldsymbol{u}_I \tag{4.95}$$

in its full form for SDA or restricting to $\bar{\boldsymbol{u}}_I$ for others.

The difference of displacement or slip is computed as following utilized several anchors points $\boldsymbol{x}_{a,i}$ placed along with the truss elements, see Fig. (4.4).

$$\begin{aligned} \boldsymbol{s} &= \boldsymbol{u}_t\left(\boldsymbol{x}_{a,i}\right) - \boldsymbol{u}\left(\boldsymbol{x}_{a,i}\right) \\ &= \left[\begin{array}{cc} \boldsymbol{N}_t(\boldsymbol{x}_{a,i}) & -\boldsymbol{N}(\boldsymbol{x}_{a,i}) \end{array}\right] \cdot \begin{pmatrix} \boldsymbol{u}_{tI} \\ \boldsymbol{u}_I \end{pmatrix} \\ &= \boldsymbol{B}_b(\boldsymbol{x}_{a,i}) \cdot \begin{pmatrix} \boldsymbol{u}_{tI} \\ \boldsymbol{u}_I \end{pmatrix} \end{aligned} \tag{4.96}$$

for a particular anchor point derived from the corresponding truss element's nodal displacements and the nodal displacements of neighboring continuum elements. This also constitutes the kinematic variable of the bond element assigned to the anchor point $\boldsymbol{x}_{a,i}$. The slip induces bond forces

$$\boldsymbol{t}_b = \boldsymbol{t}_b(\boldsymbol{s}) \tag{4.97}$$

as a counteracting couple for the truss element on the one hand, and the underlying continuum, on the other hand. The relation is generally nonlinear. It may be considered as further material relation in analogy to Eqs. (4.3,4.52) and is also assumed to be known. An incremental form

$$\dot{\boldsymbol{t}}_b = \boldsymbol{C}_{Tb}(\boldsymbol{s}) \cdot \dot{\boldsymbol{s}} \tag{4.98}$$

is used in the following in analogy to Eqs. (4.11,4.53) and is related to the global coordinate system. Regarding a local system aligned to the truss direction, the bond-slip relation is assumed in a way to avoid a lateral slip or intersection by a penalty term, and the longitudinal slip reproduces a given bond behavior. This is generally connected with an upper limit for the longitudinal bond force, i.e., a bond strength.

Regarding the discretization a bond force couple, one part applied to a truss element, the other part applied to a continuum element, is introduced as point load at $\boldsymbol{x}_{a,i}$ leading to a couple of nodal forces

$$\boldsymbol{f}_b = \begin{pmatrix} \boldsymbol{f}_{bt} \\ \boldsymbol{f}_{bc} \end{pmatrix} = \boldsymbol{B}_b^T \cdot \boldsymbol{t}_b \tag{4.99}$$

for the truss element $\boldsymbol{f}_{bt}$ on the one hand, and for the neighbor continuum element $\boldsymbol{f}_{bc}$, on the other hand. This is in analogy to Eqs. (4.11,4.60) whereby the integration over a domain is not required as bond is implemented through single forces. This is linearized with

$$\begin{aligned} \dot{\boldsymbol{f}}_b &= \boldsymbol{B}_b^T \cdot \boldsymbol{C}_{Tb} \cdot \boldsymbol{B}_b \cdot \begin{pmatrix} \dot{\boldsymbol{u}}_{tI} \\ \dot{\boldsymbol{u}}_I \end{pmatrix} \\ &= \boldsymbol{K}_{T,b} \cdot \begin{pmatrix} \dot{\boldsymbol{u}}_{tI} \\ \dot{\boldsymbol{u}}_I \end{pmatrix} \end{aligned} \tag{4.100}$$

for a particular bond element using Eqs. (4.98,4.96). As embedded fibers do not have displacement boundary conditions externally prescribed a minimum number of two anchor points $\boldsymbol{x}_{a,i}$, i.e., a minimum of two bond elements are required per truss element to avoid rigid body movements. They are conveniently placed in truss element integration points.

Nodal forces $\boldsymbol{f}_b$ and the tangential stiffness $\boldsymbol{K}_{T,b}$ can be assembled on the system level for each bond element: $\boldsymbol{f}_b$ is added to the assembled $\boldsymbol{f}_I$, see Eq. (4.11), $\boldsymbol{K}_{T,b}$ is added to the assembled $\boldsymbol{\mathcal{K}}_{T,u}$, see Eq. (4.68), according to the mappings of the underlying truss and continuum elements. Thus, the introduction of bond elements seamlessly fits into the solution procedure described in Section 4.2.4.

A standard 2D truss element is given with the isoparametric two-node element with two degrees of freedom per node, i.e., four degrees of freedom with shape functions, see Eq. (4.94)

$$\begin{aligned} \boldsymbol{N}_t &= \begin{bmatrix} N_{t1}(\xi) & 0 & N_{t2}(\xi) & 0 \\ 0 & N_{t1}(\xi) & 0 & N_{t2}(\xi) \end{bmatrix} \\ N_{t1}(\xi) &= \tfrac{1}{2}(1-\xi) \\ N_{t2}(\xi) &= \tfrac{1}{2}(1+\xi) \end{aligned} \tag{4.101}$$

with the local coordinate $-1 \leq \xi \leq 1$. This implies constant longitudinal strains and stresses. An enhanced approach is chosen for quadratic longitudinal displacements with

$$\begin{aligned} \boldsymbol{N}_t' &= \begin{bmatrix} N_{t3}(\xi) & 0 & N_{t4}(\xi) & 0 & N_{t5}(\xi) \\ 0 & N_{t1}(\xi) & 0 & N_{t2}(\xi) & 0 \end{bmatrix} \\ N_{t3}(\xi) &= \tfrac{1}{2}(1-\xi) - \tfrac{1}{2}(1-\xi^2) \\ N_{t4}(\xi) &= \tfrac{1}{2}(1+\xi) - \tfrac{1}{2}(1-\xi^2) \\ N_{t5}(\xi) &= 1-\xi^2 \end{aligned} \tag{4.102}$$

introducing a fifth nodal degree of freedom for longitudinal displacements. This, at first, is valid in a coordinate system aligned with the first displacement direction u_x' following the truss element axis. This leads to an aligned $\boldsymbol{B}$-matrix, compare Eq. (4.1)

$$\boldsymbol{B}_t' = \frac{1}{L} \begin{bmatrix} 2\xi - 1 & 0 & 2\xi + 1 & 0 & -4\xi \end{bmatrix} \tag{4.103}$$

with an element length L according to well-known rules of isoparametric finite elements. The aligned direction is rotated by an angle φ to the global direction, see Fig. 4.4. As $\boldsymbol{u}' = \boldsymbol{T} \cdot \boldsymbol{u}$ with

$$\boldsymbol{T} = \begin{bmatrix} \cos\varphi & \sin\varphi & 0 & 0 & 0 \\ -\sin\varphi & \cos\varphi & 0 & 0 & 0 \\ 0 & 0 & \cos\varphi & \sin\varphi & 0 \\ 0 & 0 & -\sin\varphi & \cos\varphi & 0 \\ 0 & 0 & 0 & 0 & 1 \end{bmatrix} \tag{4.104}$$

the final $\boldsymbol{B}$-matrix is given with

$$\boldsymbol{B}_t = \boldsymbol{B}_t' \cdot \boldsymbol{T} \tag{4.105}$$

leading to linear strains with an additional degree of freedom not assigned to a node. Regarding embedded truss elements, this enhanced approach yields the same behavior as fully quadratic elements but with fewer degrees of freedom. The linear and quadratic approaches work in both 2d and 3D and can be used with different finite elements approaches, including the SDA approach described in Section 4.2. These cover a wide range of reinforcement types from a large number of short fibers randomly positioned and orientated, whereby discretized

with a small number of elements up to long single rebars distributed regularly in composite whereby each discretized with a large number of elements. In the case of thick fibers, beam elements can be used instead of truss elements with bending stiffness, whereby this will add a rotational degree of freedom into the system beneath translational. A rebar bending, e.g., might become relevant as so-called dowel action upon the crossing of cracks.

4.4 NUMERICAL SIMULATIONS

4.4.1 Introduction

Previous studies stated in Chapter 2, show that it is not still possible to fully understand and predict the behavior of fiber-reinforced concrete structures under different loading conditions. Thus, this leads to further investigations and research in this field. In this chapter, several sensitivity analyses are performed to evaluate the model, which is developed based on numerical methods and explained thoroughly in Chapter 4. The benchmarks in the following sections, are introduced to study the effect of structural and modeling parameters, e.g., mesh sensitivity of matrix and fibers, fiber's angle concerning the loading direction, and capability of the newly developed model to analyze a model contains all component of the mesoscopic model. These parameter studies can show both strength points and the restriction of the developed model. In the following sections, models under small-displacement increments (Quasi-static) conditions are discussed, and the Newton-Raphson method is used to gain equilibrium by iteration for each loading increment. The mechanical properties of aggregates and matrix are given in Table 4.1 and Table 4.2, respectively.

Parameter	**Unit**	**Value**
Young's modulus E	[N/mm^2]	60 000
Poisson's ratio ν	-	0.15

Table 4.1: Mechanical properties of aggregates

Parameter	**Unit**	**Value**
Young's modulus E	[N/mm^2]	29 000
Poisson's ratio ν	-	0.2
Tensile strength f_{ct}	[N/mm^2]	3.8
Fracture energy G_f	[N/mm]	$100 \cdot 10^{-3}$
Critical crack width w_{cr}	[mm]	0.079

Table 4.2: Mechanical properties of fine grained concrete

Basic fiber properties have been described in Section 2.2. Typical property values which later will be used for the following numerical simulations are given in Table 4.3 whereby the fiber's strength is reduced compared to nominal values corresponding to practical experience. The simulation model allows for a wide range of these values. However, the bond law used in the simulation of benchmarks is $B-5$, which is the same bond law used for the reference model in Chapter 5, to keep the constancy between the benchmarks and larger-scale simulations, see Table 4.4. Bond law $B-4$ is derived from simulation of single fiber pullout test and discussed in Section 2.2.5. The transformation from bond law $B-4$ to bond law $B-5$ will be explained in detail in Section 5.2.

Parameter	**Unit**	**Value**
Young's modulus E_f	[N/mm^2]	80 000
Tensile strength f_f	[N/mm^2]	1 600
Length L	[mm]	6
Diameter $\oslash$	[mm]	0. 02
Cross sectional area A_f	[mm^2]	$3.14 \cdot 10^{-4}$
Failure load P_{fu}	[N]	0.5

Table 4.3: Mechanical properties of fibers

Parameter	**Unit**	**Value - B-5**
Bond strength τ_{max}	[N/mm^2]	2.39
Ultimate bond stress τ_f	[N/mm^2]	0.0
Slip$_{\tau_{max}}$ S$_1$	[mm]	0. 022
Slip$_{\tau_f}$ S$_2$	[mm]	0. 706

Table 4.4: Mechanical properties of bond - B - 5 bond law

A setup of loading and boundary conditions is shown in Fig. 4.5, whereby loading is applied as prescribed nodal displacement on the top edge of the model and model is fully supported in bottom edge.

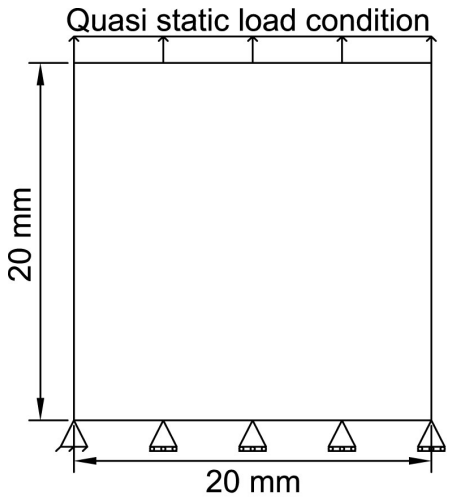

Figure 4.5: Geometry, boundary condition and acting load for simple benchmark

4.4.2 Mesh sensitivity of models with SDA continuum elements

In the first series of parameter studies, the mesh sensitivity of SDA elements in the developed model is investigated within four different discretization qualities and unit dimensions (length and height of $1mm$) shown in Fig. 4.6. In Fig. 4.6, the crack's direction and position are shown with red dash lines, and the location of crack's origin point, which is placed in element center, is displayed with the red circle. Material properties, loading, and boundary condition for all models are the same, as explained in section 4.4.1.

The simulations load-displacement results are shown in Fig. 4.7. It is observed that the model with two vertical matrix elements shows the same response as the model with one matrix element. The contribution of each element in the damage stage is connected to the fracture energy of matrix material. Thus, in model with two vertical elements, the contribution of two elements is twice of one element model; however, the length of cracks is half of the crack's length in one element model so both models will show the same behavior at the end in this specific loading and boundary conditions. The same logic can be used to explain that the response of the model within two horizontal matrix elements is the same as the model with four matrix elements shown in Fig. 4.7.

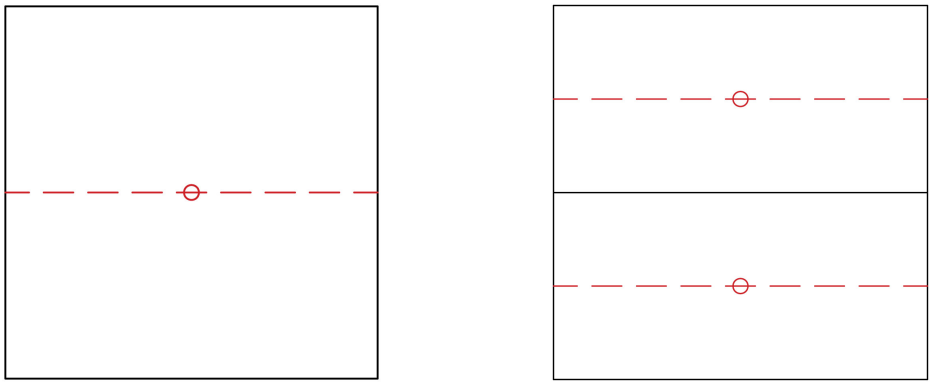

(a) Model within one matrix element

(b) Model within two horizontal matrix elements

(c) Model within two vertical matrix elements

(d) Model within four matrix elements

Figure 4.6: Simple matrix models with their crack patterns and crack's anchor points

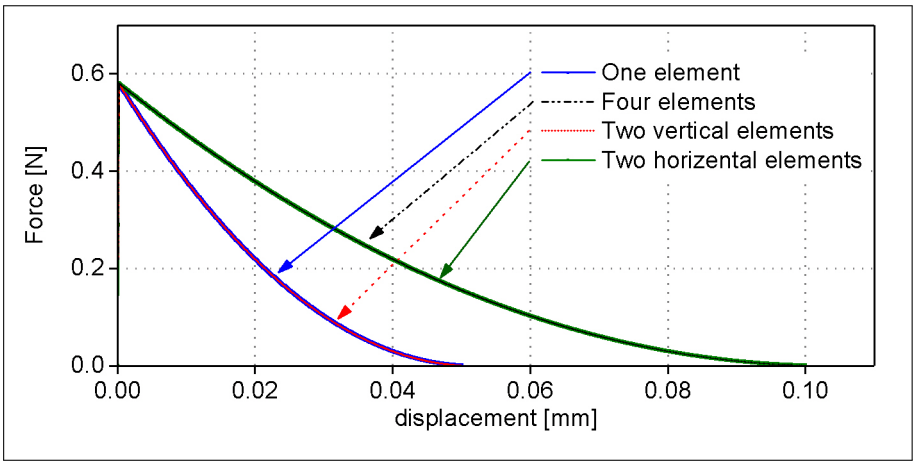

Figure 4.7: Simple matrix models - force vs displacement results

The mesh sensitivity of another four models with different discretization is investigated, models are shown in Fig. 4.8. Material properties, dimensions, loading, and boundary condition for all models are the same, as explained in section 4.4.1 and shown in Fig. 4.5.

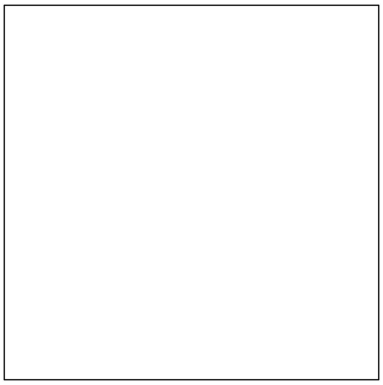

(a) Model within one matrix element-very coarse mesh

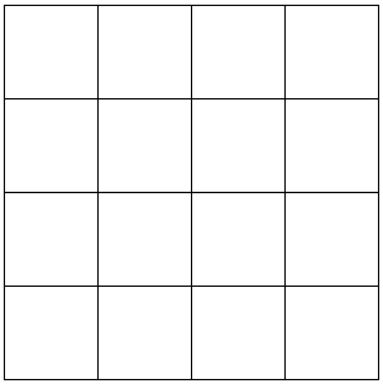

(b) Model within 16 matrix elements-coarse mesh

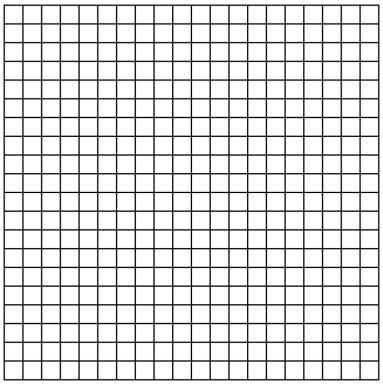

(c) Model within 400 matrix elements-medium mesh

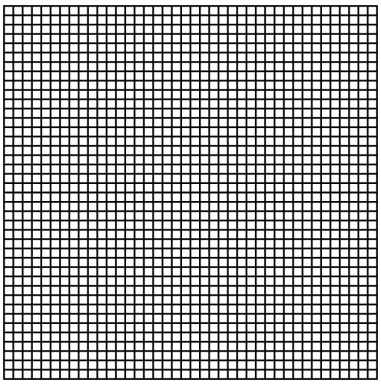

(d) Model within 1600 matrix elements-fine mesh

Figure 4.8: Simple matrix models used for checking the size in-dependency of SDA approach

From the results shown in Fig. 4.9 and based on the mentioned explanation, increasing the number of elements will increase their contribution in the damage phase and increase the area under the curve in softening stage.

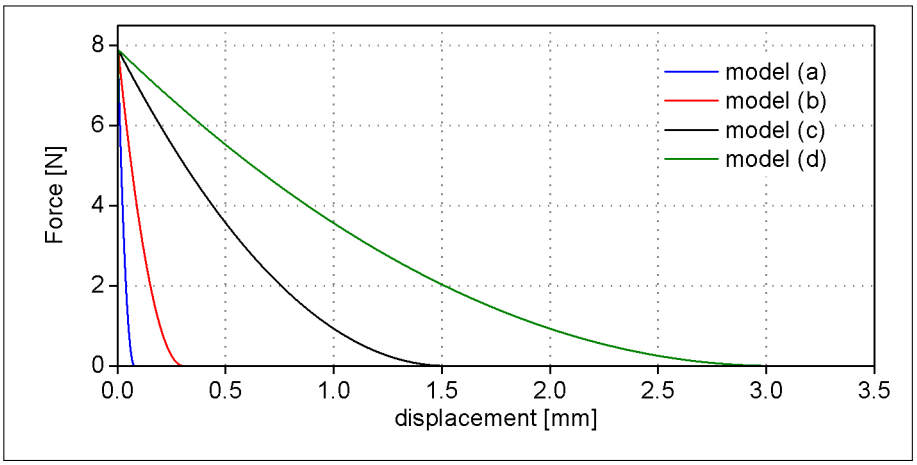

Figure 4.9: Simple matrix models - force vs displacement results

The SDA approach is known as a mesh-independent method which performs a natural regularization in the strain-softening stage. To see this effect, each discretization's fracture energy is modified to present the same softening behavior. Thus, for this specific loading, geometry, and boundary conditions and based on the enumerated explanation, if fracture energy in one element model is equal to A, in model with 16, 400 and 1600 elements, the fracture energy should be equal to A/4, A/20, and A/40, respectively, to represent the same total response. Results are shown in Fig. 4.10.

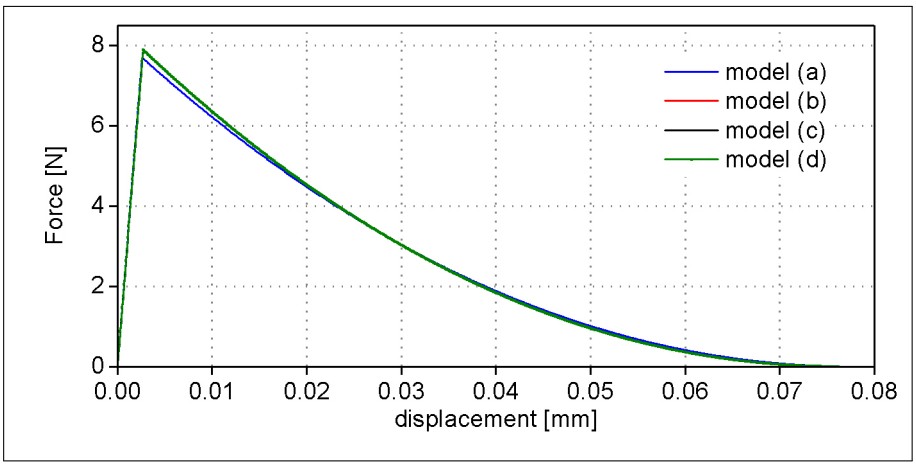

Figure 4.10: Simple matrix models within modified material properties - mean stress vs displacement results

Discretization is one of the four stages of FEM explained in chapter 4. Within the numerical methods, equations are solved for smaller elements to simulate the larger system's overall behavior. From the graph shown in Fig. 4.11, it is observed that computation time for a model with a very fine mesh is almost 400 times of computation time for the model within one element which both will represent the same results shown in Fig. 4.10. This shows the big advantage of using the SDA approach, which is the size in-dependency due to natural regularization, leading to less modeling effort and less time computation.

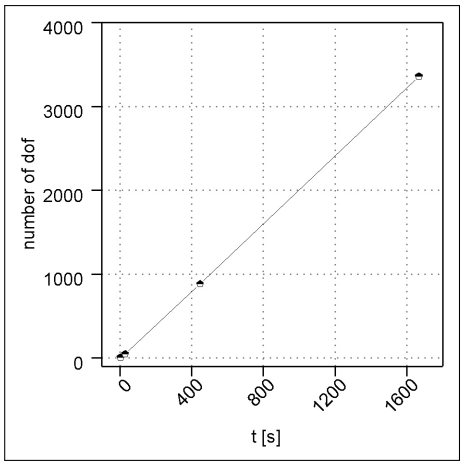

Figure 4.11: Simple matrix models - time vs number of degree of freedom

4.4.3 Parameter study of fully embedded fiber model

Geometry, boundary, and loading conditions for fully embedded models are shown in Figs. 4.12. Uniform prescribed displacement is applied on the top edge of the model to provide longitudinal tension conditions. The discretization of matrix elements follows the model within medium mesh (400 matrix elements) presented in the previous section, it is shown in Fig. 4.8(c) and partly in Fig. 4.12(a). The linear elastic material is assigned to the continuum without limited tensile strength, and small load steps have been chosen to provide the quasi-static loading condition. The result corresponding maximum loading equal to 0. 1 mm will be discussed in the following. The fiber is divided into five elements. The influence of fiber angle is investigated in two conditions, i.e., a)fiber is located in the middle of specimen vertically in the direction of prescribed load, b)fiber is inclined concerning the loading direction with 45-degree inclination angle (ϕ), the position of fibers are shown in details in Fig. 4.12.

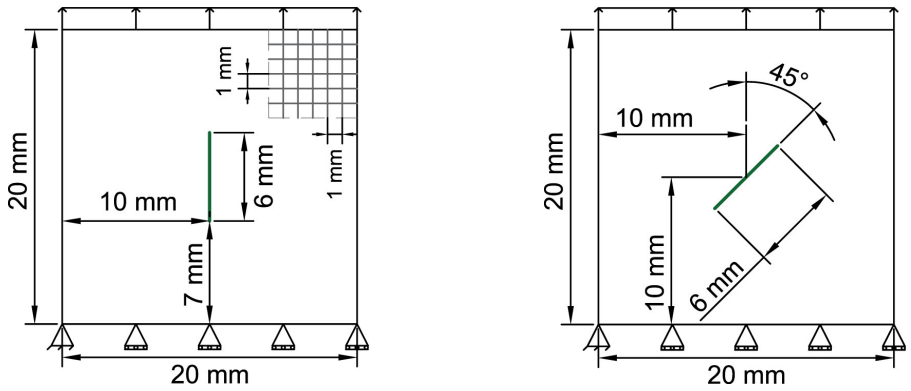

(a) Vertical embedded fiber

(b) Inclined embedded fiber - $\phi = 45°$

Figure 4.12: Geometry, boundary condition and acting load for fully embedded fiber models

From results, shown in Fig. 4.13, the typical behavior of an embedded fiber is observed, such as the bond stresses that have maximum absolute values with different signs at the ends whereby longitudinal stress of fiber is zero at the ends with an intermediate maximum. To fulfill the fiber cutout's equilibrium condition, the spatial derivative of longitudinal stresses, scaled by some constant factors, is equal to the derivative of the bond stresses.

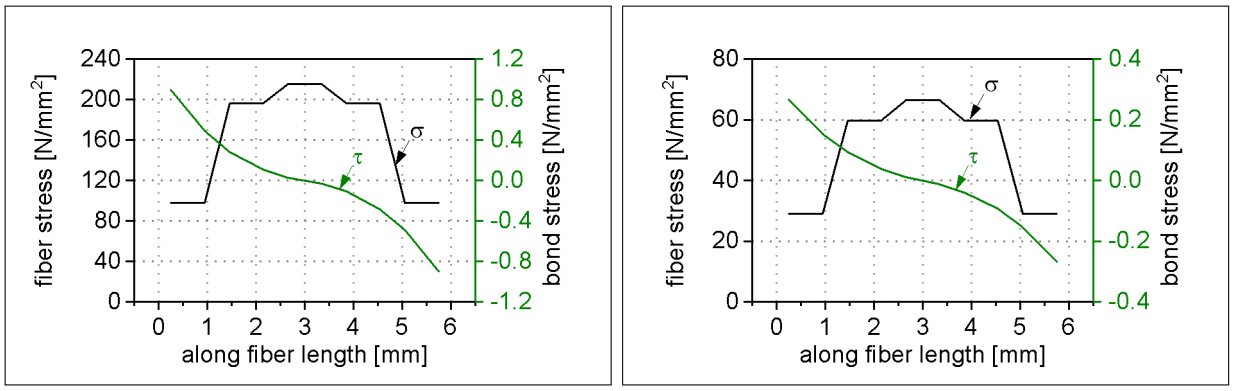

(a) Vertical embedded fiber

(b) Inclined embedded fiber - $\phi = 45°$

Figure 4.13: Fully embedded fiber models - fiber and bond stresses along fiber length - fibers within 5 element divisions

Regarding the influence of fiber's orientation concerning tensile loading direction, it is observed that in model with embedded fiber with a 45-degree inclination angle, the maximum stress in fiber and bond stress is decreased by a factor of 3.12 in comparison to model within fiber align to load direction. The significant effect of the inclination angle is easily seen from these results which leads to further investigations, three new models with different inclination angle (ϕ) are analyzed whereby enhanced truss elements, see Eq. (4.102), are used

for better understanding of longitudinal stresses in fibers in a different condition, shown in Fig. 4.14.

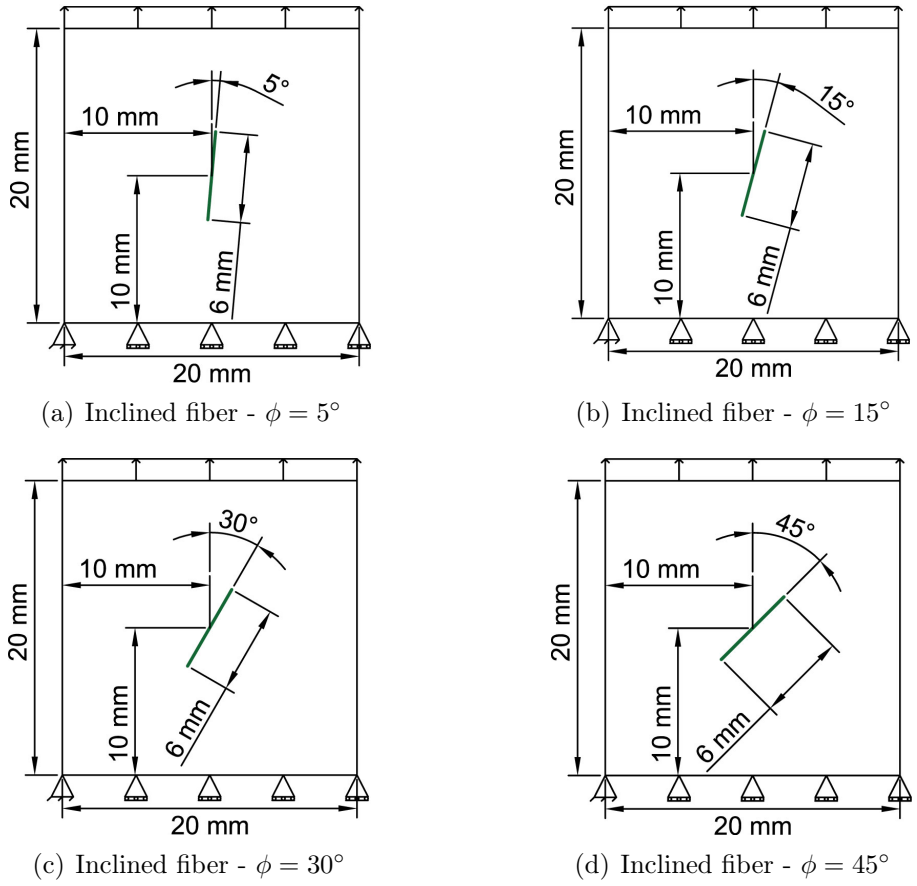

(a) Inclined fiber - $\phi = 5°$

(b) Inclined fiber - $\phi = 15°$

(c) Inclined fiber - $\phi = 30°$

(d) Inclined fiber - $\phi = 45°$

Figure 4.14: Geometry, boundary condition and acting load for fully embedded fiber models within different inclination angles

The effect of fiber's inclination angle on fiber stresses and bond stresses is shown in Fig. 4.15 where the prescribed displacement applied to the model is equal to 0. 1 mm. In Fig. 4.15(d), the results for both linear and enhanced elements are shown for the model with inclined embedded fiber $\phi = 45°$. This shows stresses in model with enhanced elements are changing linearly, which gives a better understanding of the distribution of stresses in fiber.

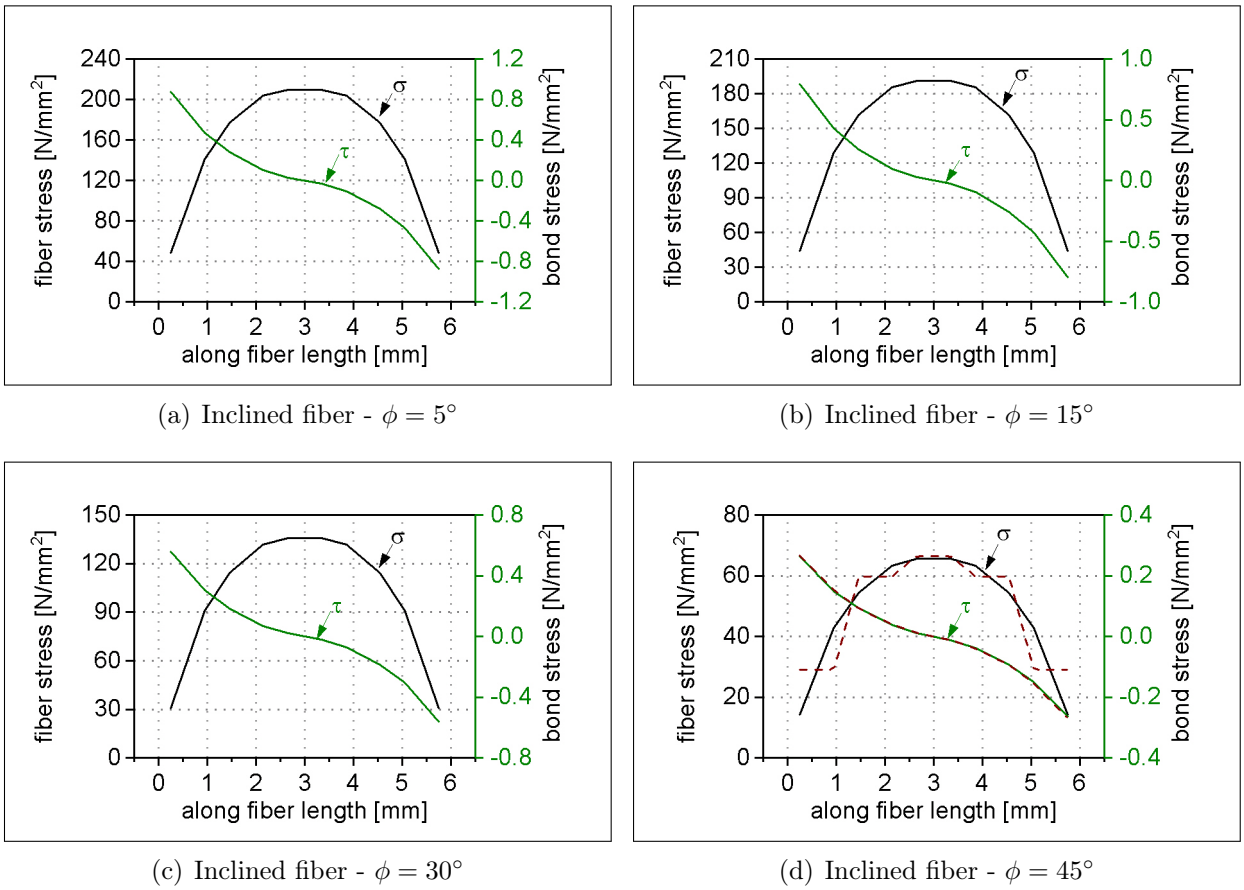

(a) Inclined fiber - $\phi = 5°$

(b) Inclined fiber - $\phi = 15°$

(c) Inclined fiber - $\phi = 30°$

(d) Inclined fiber - $\phi = 45°$

Figure 4.15: Fully embedded fiber models and different inclination angles - fiber and bond stresses along fiber length

In Figs. 4.16(a,b) maximum fiber stresses and bond stresses for different inclination angles are compared. The presented results show that maximum fiber stresses and bond stresses are decreased by a factor of 3.12 from the model with the fiber orientated along tensile loading direction to model with $\phi = 45°$. These results are normalized based on the stresses for the model with vertical fiber and shown in Fig. 4.17, both graphs for bond and fiber stresses are laying on each other to establish the internal equilibrium.

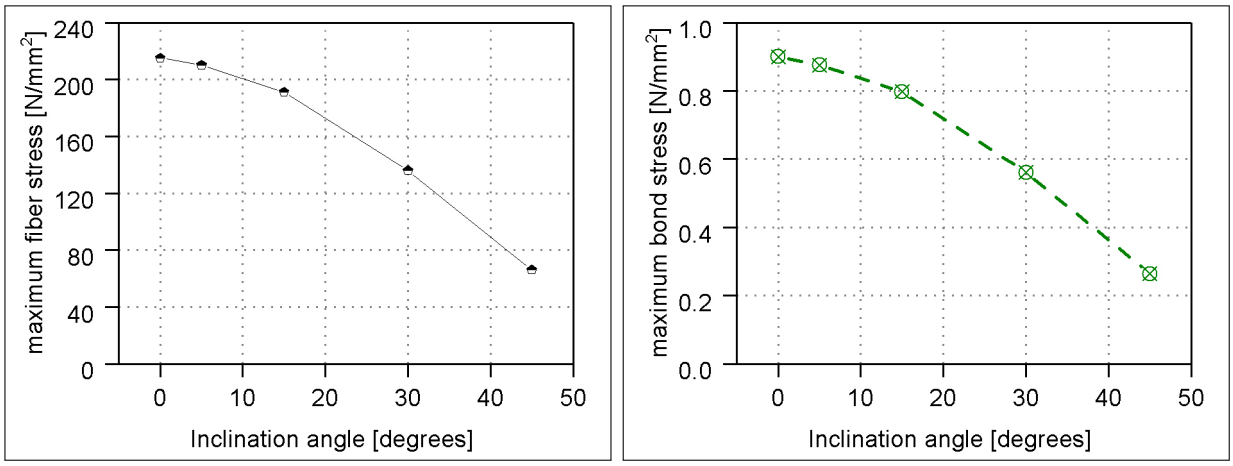

(a) (b)

Figure 4.16: a) Maximum fiber stresses and b)maximum bond stresses in fiber elements in fully embedded fiber models and within different inclination angles

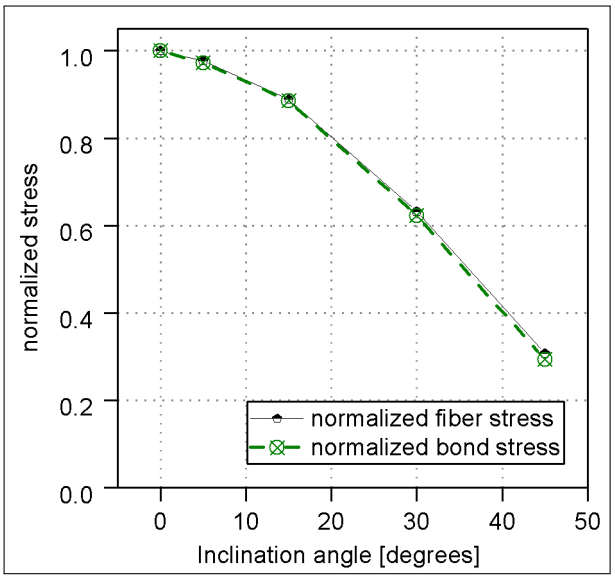

Figure 4.17: Normalized fiber and bond stresses in fully embedded fiber models and different fiber angles

As discussed before, the discretization quality plays a significant role in analyzing the full system's behavior. However, for fiber-reinforced concrete structure, which contains a large number of fibers, ($\approx 10^4$), the required fiber discretization quality is an important topic. In the next step, the influence of the number of fiber's divisions is investigated by increasing the divisions from 5 to 10 divisions whereby a linear approach is used for the longitudinal truss displacements leading to constant longitudinal strains and stresses within a single truss element. In Fig. 4.18, comparative results are shown for two enumerated models, including 5 and 10 divisions for single fiber. Fiber stresses and bond stresses are computed and compared

in both conditions of vertical and inclined embedded fiber. Results for models with five divisions are shown in dash lines. It shows that increasing the number of fiber divisions will not significantly affect the value of maximum fiber stresses and the computed bond stresses along the fiber length. In these results, straight lines connect the stresses on neighbored integration points, and the constant stress approach balances external longitudinal stresses. Thus, the differences between curves are minimal; the coarse approach will be chosen as reference for the following simulations, especially in simulations with a large number of degrees of freedom. This simplification will have a significant effect on modeling effort and time of calculation. Moreover, the size of fiber elements is in good compatibility with mesh size for continuum elements in the medium mesh model (see Fig. 4.8).

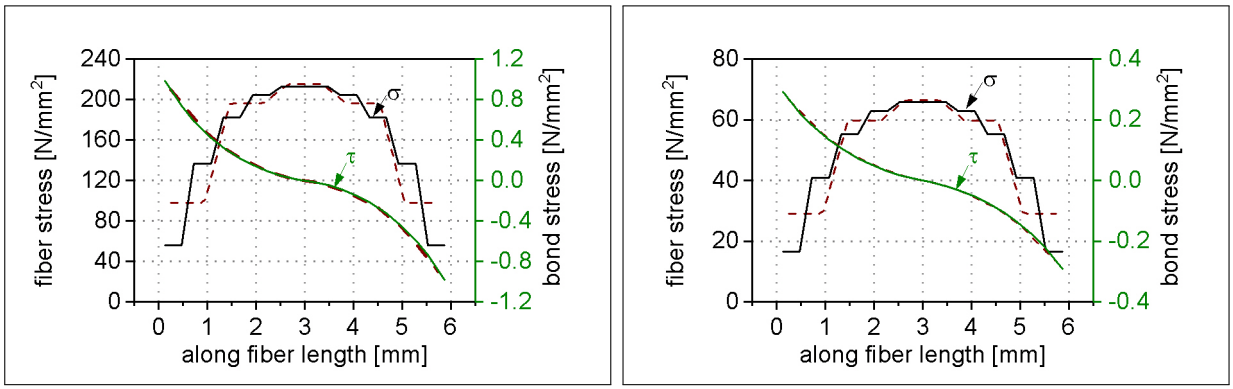

(a) Vertical embedded fiber

(b) Inclined embedded fiber - $\phi = 45°$

Figure 4.18: Fully embedded fiber models - fiber and bond stresses along fiber length - fiber within 5 divisions vs 10 element divisions

4.4.4 Parameter study of model within single fiber passing a small gap

The geometry, boundary condition, loading direction, and fiber positions are shown in Fig. 4.19. The discretization of matrix elements follows the model within medium mesh (400 matrix elements) discussed in section 4.4.2, it is shown in Fig. 4.8(c) and partly in Fig. 4.19(a). A small gap of 0.02 mm divides the continuum into two identical sections. These sections are connected to each other with a single fiber, which passes both sections equally. Uniform prescribed displacement is applied on the top edge of the model to provide longitudinal tension conditions.

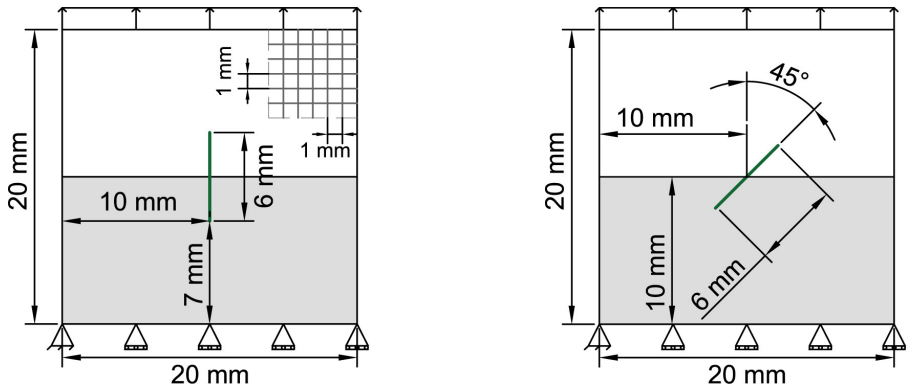

(a) Fiber in load direction (b) Inclined fiber - $\phi = 45°$

Figure 4.19: Geometry, boundary condition and acting load for models within small gap

The linear elastic material is assigned to the continuum without limited tensile strength, and small load steps have been chosen to provide the quasi-static loading condition. From force-displacement results, see Fig. 4.20, it is observed that the fiber reaches the fiber's failure load, see Table 4.3, when the prescribed displacement is equal to 0. 1 mm for the model with $\phi = 0$. This displacement stage is shown as δ_0 in Fig. 4.20 and will be used as a reference for further investigations and parameter studies.

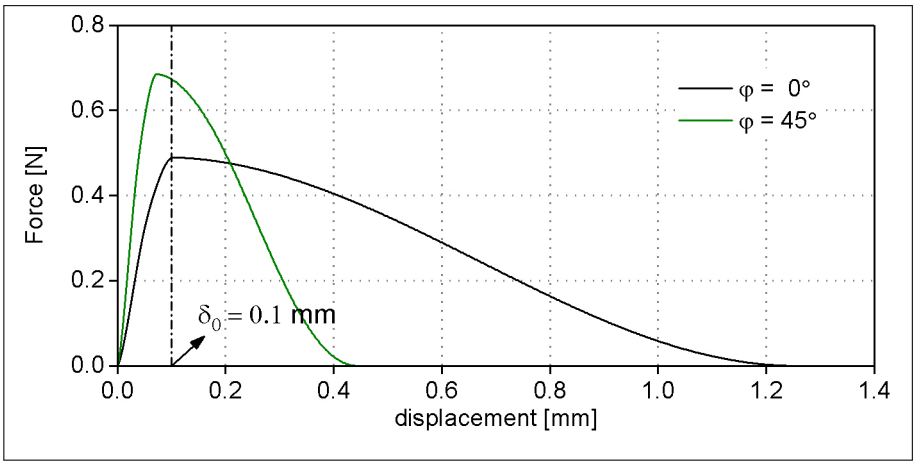

Figure 4.20: Models within small gap - total response vs displacement results

In Fig. 4.21, fiber stresses along the fiber length for $\delta = \delta_{0,\phi=0}$ are shown for two conditions ($\phi = 0°$,45°). From these results, it is observed that bond elements have reached the peak magnitude for bond strength in both cases, corresponding to bond strength discussed in Section 4.3 and stated in Table 4.4). On the other hand, stress in intermediate fiber elements has reached almost the maximum tensile strength of fiber mentioned in Table 4.3 for both conditions.

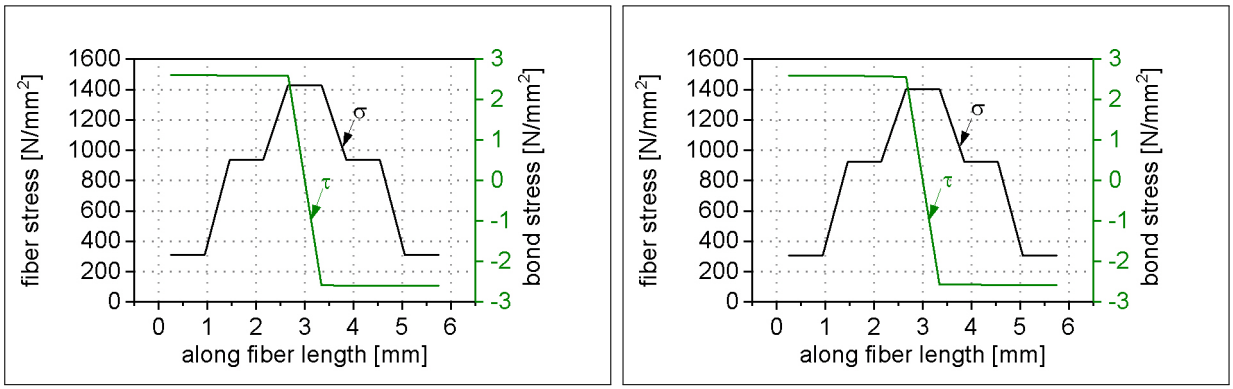

(a) Fiber in load direction

(b) Inclined fiber - $\phi = 45°$

Figure 4.21: Models within small gap - fiber and bond stresses along fiber length

Several sensitivity analyses are performed by the use of the newly developed model to investigate the effect of fiber's inclination angle concerning tensile loading conditions. Three new models with different inclination angles (ϕ) are analyzed whereby enhanced truss elements are used for better understanding of longitudinal stresses in fibers in a different condition; models are shown in Fig. 4.22.

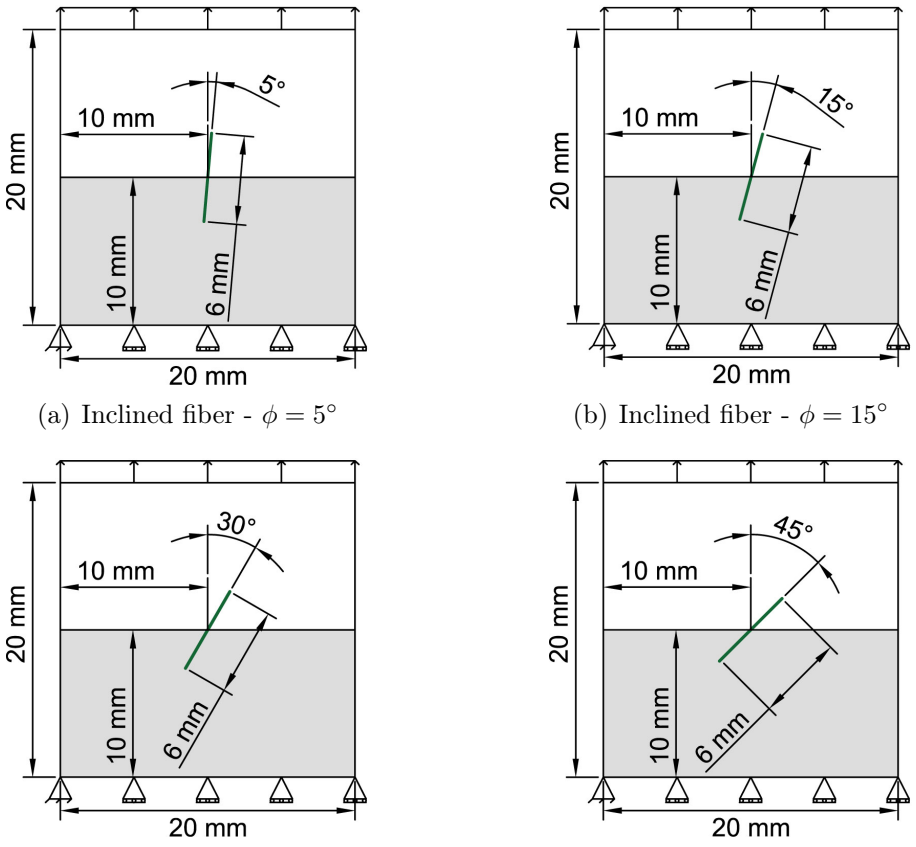

(a) Inclined fiber - $\phi = 5°$

(b) Inclined fiber - $\phi = 15°$

(c) Inclined fiber - $\phi = 30°$

(d) Inclined fiber - $\phi = 45°$

Figure 4.22: Geometry, boundary condition and acting load for models within small gap and different inclination angles

The effect of the inclination angle of fiber on fiber stresses and bond stresses is shown in Fig. 4.23 where the prescribed displacement applied on the model is equal to 0. 1 mm. From these results, it is observed that in all models with different inclination angles, the computed fiber stresses along the fiber length and bond stresses in bond elements are almost equal to fiber's tensile strength and bond strength, respectively. In Fig. 4.23(d), the result for both linear and enhanced elements are shown for the model with $\phi = 45°$, which shows stresses in model with enhanced elements are changing linearly, and this gives a better understanding of the distribution of stresses in fibers.

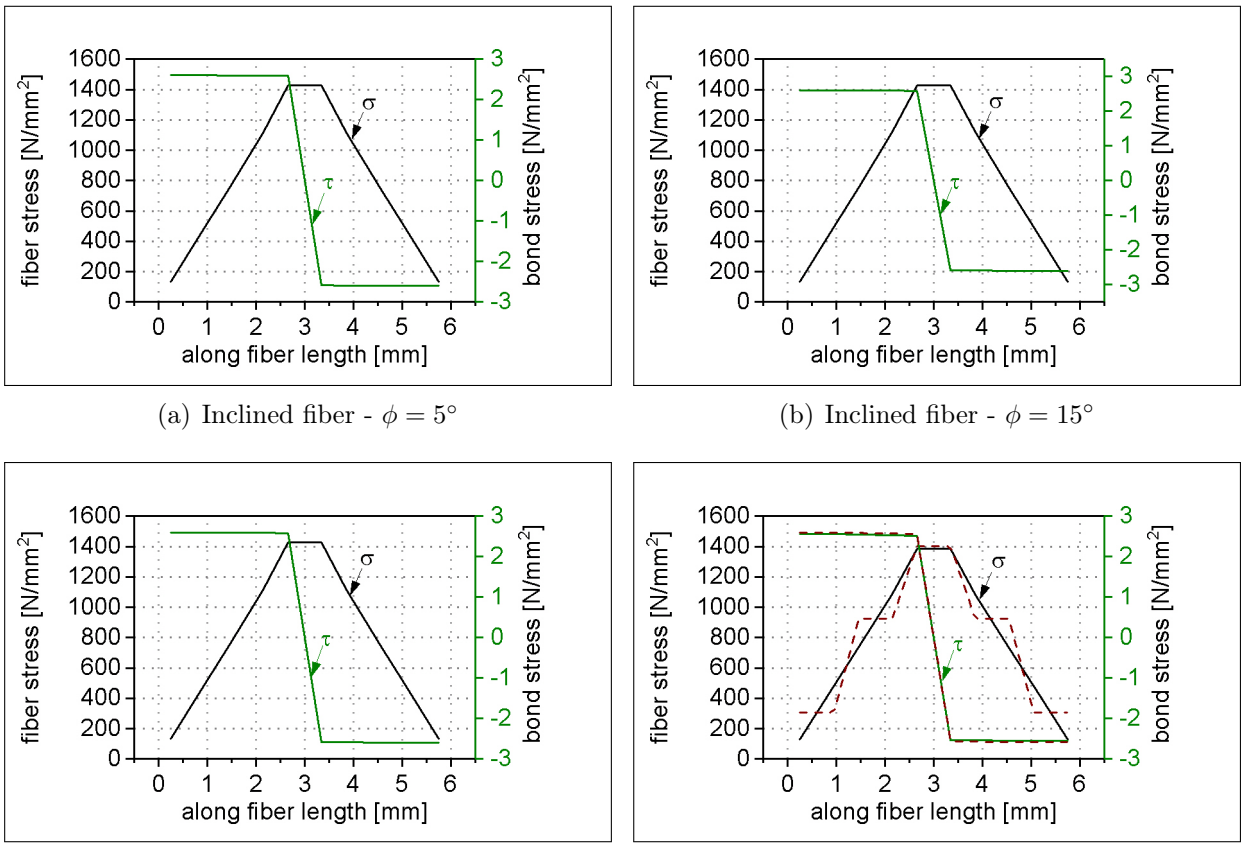

(a) Inclined fiber - $\phi = 5°$

(b) Inclined fiber - $\phi = 15°$

(c) Inclined fiber - $\phi = 30°$

(d) Inclined fiber - $\phi = 45°$

Figure 4.23: Models within small gap and different inclination angles - fiber and bond stresses along fiber length

In Fig. 4.24, the curves show the total response of models with different inclination angles. From these results, it is observed that the total response of model is increasing with the increase in inclination angle.

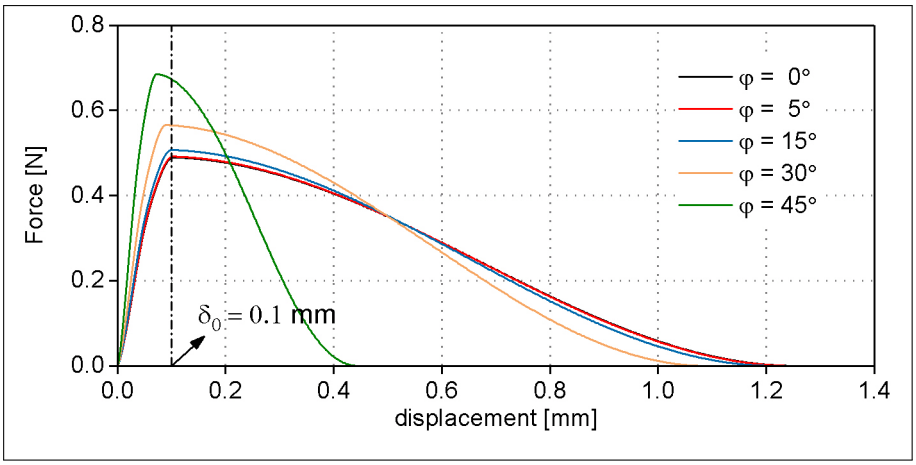

Figure 4.24: Models within small gap - total response vs displacement results

As it is discussed in detail in Section 2.2.5, the effect of the inclination angle is considered with the factor $e^{f\phi}$. Based on Eq. (4.106) for the same end-slippage and embedded length l, the bridging force for the model with inclination angle (ϕ) can be computed as:

$$P|_{\phi} = e^{f\phi} \cdot P|_{\phi=0} \tag{4.106}$$

whereas snubbing friction coefficient f is an interface material parameter, depends on each fiber/matrix combination[70] and different values in the range of 0 and 1 are recommended in literature[125], [124]. The effect of inclination angles for models with inclined fiber is shown in Fig. 4.25. It is observed that the model's total response is increasing with the increase of the inclination angle. Based on Eq. (2.2), the ratio between pull-out force for vertical fiber and inclining fiber models are expected to be equal to a factor of $e^{f\phi}$. Thus, in Fig. 4.25(b), forces are normalized with bridging forces derived from vertical fiber simulation, and it is observed that normalized bridging forces are in good agreement in respect to formula curve where snubbing friction factor is assumed ($f = 0.35$) [124].

In the simulation of 2D dumbbell experiments, which will be discussed in Chapter 5, no extra factor is added to the formulation concerning the effect of fiber's angle since unique production techniques caused the fibers to be mostly aligned longitudinally in the direction of applied tension load. The fiber angles in numerated specimens are assumed to be less than 5° concerning the load direction . Thus, based on the graphs shown in Fig. 4.24, no significant differences are observed between results for $\phi = 0°$ and $\phi = 5°$.

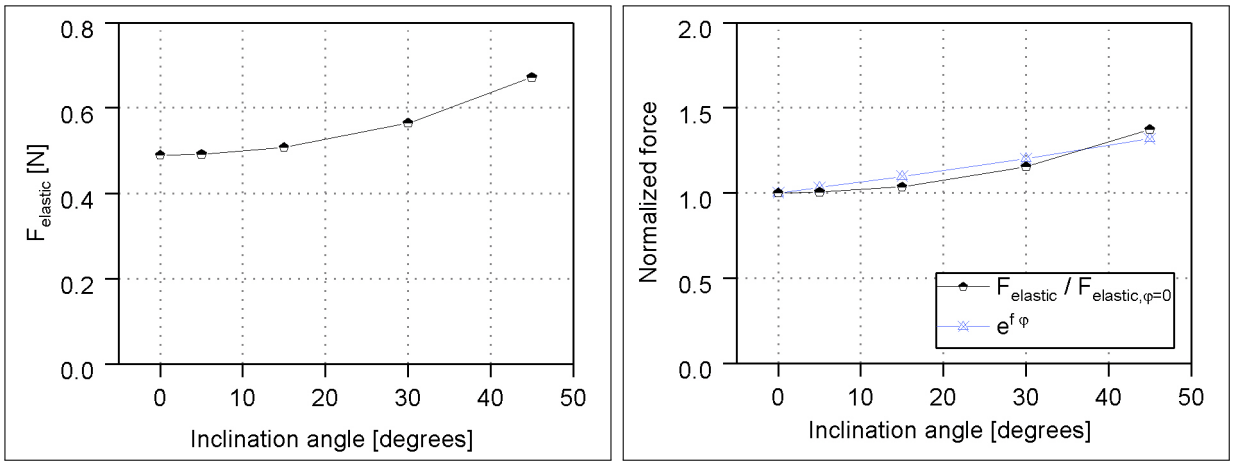

(a) (b)

Figure 4.25: a)Total reaction forces and b)normalized forces for models with gap and different inclination angles fiber angles in $\delta = \delta_{0,\phi=0}$ and $f = 0.35$

4.4.5 Simple model with fibers and aggregates

In this section, four different models are studied, which setup of loading, boundary conditions and geometry assigned to all models are shown in Fig. 4.26. Elastic material model is assigned to fibers modeled with embedded enhanced truss elements and have length of 4 mm whereas each single fiber is divided into five elements. Continuum elements are SDA quad elements whereas secondary cracking is constrained by a minimum deviation of 45 degrees compared to primary cracking orientation The matrix elements have the dimension of 1 mm$x$1 mm, the discretization of matrix elements is shown in Fig. 4.26.

Mechanical properties assigned to aggregates, matrix, fiber and bond elements are stated in Tables 4.5,4.6,4.7,4.8, respectively. Very low crack energy is assigned to the matrix elements to capture softening concerning the small size of the specimen whereas and two weak elements are introduced to add the imperfection to the analysis. Thus, they have a tensile strength of $f_{ct} = 2.7\,\mathrm{N/mm^2}$ and shown with gray elements in Fig. 4.26.

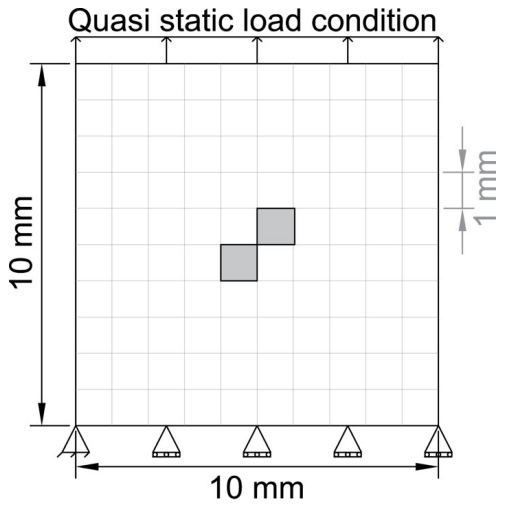

Figure 4.26: Geometry, boundary condition and acting load

Parameter	**Unit**	**Value**
Young's modulus E	[N/mm^2]	60 000
Poisson's ratio ν	-	0.1

Table 4.5: Mechanical properties of aggregates

Parameter	**Unit**	**Value**
Young's modulus E	[N/mm^2]	25 000
Poisson's ratio ν	-	0.2
Tensile strength f_{ct}	[N/mm^2]	3.0
Fracture energy G_f	[N/mm]	$20 \cdot 10^{-3}$

Table 4.6: Mechanical properties of concrete

Parameter	**Unit**	**Value**
Young's modulus E_f	[N/mm^2]	60 000
Poisson's ratio ν	-	0.1
Length L	[mm]	4
Cross sectional area A_f	[mm^2]	$1 \cdot 10^{-6}$

Table 4.7: Mechanical properties of fibers

Parameter	**Unit**	**Value**
Bond strength τ_{max}	[N/mm^2]	4.78
Ultimate bond stress τ_f	[N/mm^2]	0.0
Slip$_{\tau_{max}}$ S$_1$	[mm]	0. 022
Slip$_{\tau_f}$ S$_2$	[mm]	0. 354

Table 4.8: Mechanical properties of bond

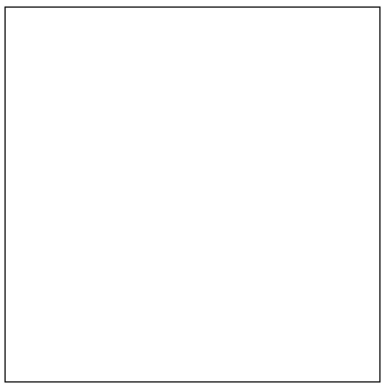

(a) Model within cementitious matrix

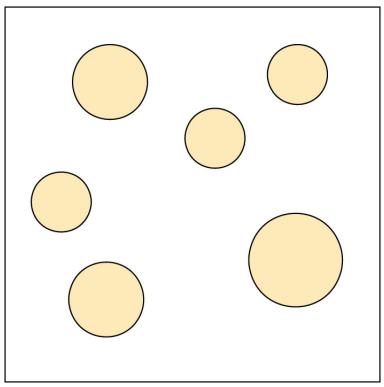

(b) Model within aggregates

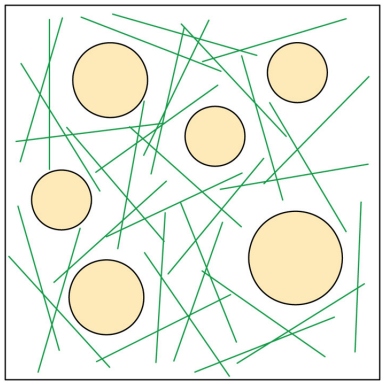

(c) Model within fibers and aggregates

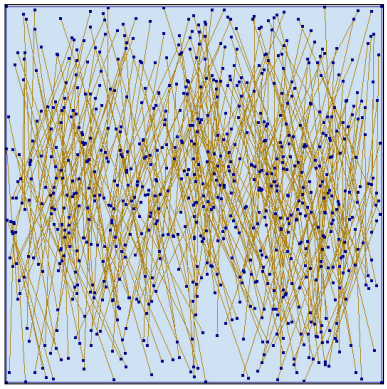

(d) Model within fibers

Figure 4.27: Simple models with fibers and aggregates

Four models are shown in Fig. 4.27, the first model is a model with just matrix elements. The second model includes six aggregates with a random radius and position; the area fraction of these aggregates is 6% of the model's total area. The third model is a model with 33 fibers which randomly distributed in the model. The volume fraction of fibers is much less than the magnitude typically used for strengthening fiber reinforced concrete structures; however, this section aims to generally show the capability of the newly developed model in analyzing models containing different components of mesoscopic model. In the last model, aggregates are removed, and the whole model is filled with fibers randomly. Four hundred fibers are considered in the model, whereas fibers' inclination is restricted within a range of ± 5 degrees to the loading direction. The volume fraction of fiber is still much less than the typical range for SHCCs.

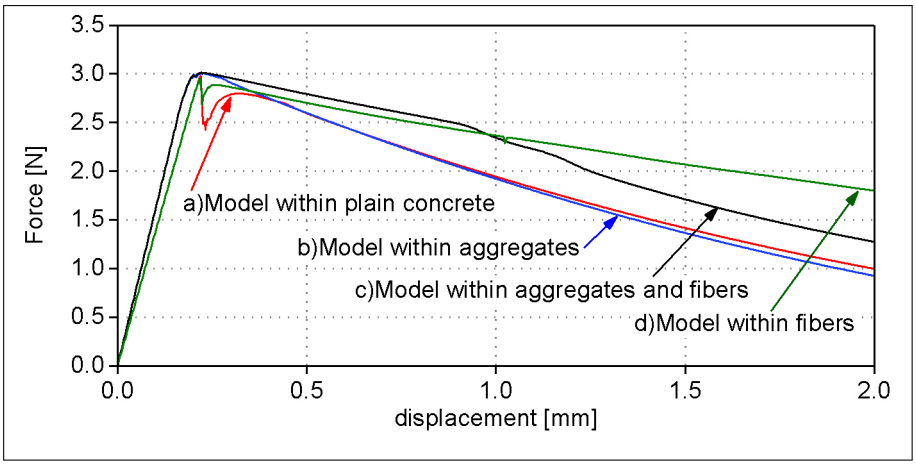

Figure 4.28: Simple models with fibers and aggregates - force vs displacement results

From the results shown in Fig. 4.28, it is observed that two models without aggregates (models a and d) have the same elastic path whereas the softening curve of model a is started with a sudden drop which can be a sign of formation of a critical crack. Later, the model with fibers shows more ductile behavior in softening phase. This can be explained by the fact that the fibers have a significant role in load-bearing in this stage.

Comparing two models without fibers (models a and b), model b has higher initial slope because of aggregates with much higher Young's modulus, but since the area fraction is not that much high, the difference is not too big. On the other hand, the model without aggregates starts softening path with a small drop, but shortly after that, both models follow mostly the same softening path.

Two models contain fibers (models c and d), it is seen that model with aggregate and fibers have a higher initial slope of elastic path, it can be explained with high Young's modulus of aggregate. As mentioned before, fibers have a significant impact on the softening stage; this can be seen with ductile behavior seen in the softening phase. Moreover, if two models with aggregate are compared, it is observed that model without fibers has a steep softening phase.

To sum up, it is observed that the newly developed model is successfully capable in the simulation of models contains different components of mesoscopic models. However, it should be stated that the number of fibers in this simplified case study is much lower than the minimum value needed for achieving the strain-hardening desired as SHCC tensile response. Moreover, the model with aggregates is not pursued further in the current research, since the specimen under consideration is made of fine concrete.

5 SIMULATION AND NUMERICAL PARAMETRIC STUDIES OF TENSION TEST ON DUMBBELL SPECIMEN UNDER QUASI-STATIC LOADING CONDITIONS

In the current chapter, a numerical model is explained to simulate the total response of 2D SHCC dumbbell specimens under tensile loading conditions in order to calibrate and validate the enumerated numerical method introduced in Chapter 4. It starts from the experiment set-up, loading condition, mechanical properties of specimens, and continuous with several numerical parametric studies. The study is extended by further with more in-depth investigations into the influences associated with the mechanical properties of each component of FRCC and model characteristics. These particular experiments have been introduced and partly discussed in published researches in[114, 50].

5.1 EXPRIMENTAL SET-UP

5.1.1 Materials

The composite used for simulation is a high-strength SHCC made with ultra-high molecular weight polyethylene (UHMWPE; or shortly PE) Dyneema SK62 fibers, produced by DSM, the Netherlands[2]. The used Dyneema fibers are gel-spun, multi-filament fibers with high tensile strength, low elongation at their breaking points, and deep longitudinal grooves showing the oriented fibrils, see Table 5.1. They have a cut-length of 6 mm and an average diameter of 20 μm, and mixed up to 2% of volume with the cement matrix. The nominal tensile strength of fibers is 2 500 N/mm^2 with a brittle failure mode.

These hydrophobic PE fibers have a high chemical residence to most chemicals, e.g., acids, alkalis, and water. They show better performance in high-strength SHCC due to their weak

interracial bonds in water-based composites caused by their nonpolar molecular structure. This high-strength matrix is developed to exhibit to provide the proper interaction between PE fibers and hardened cement paste through high packing density and strength[31, 30]. Thus, the developed high-strength matrix should yield a very low fracture toughness to ensure a steady-state cracking in the strain-hardening phase[68].

The matrix has a high cement content, low water-to-binder ratio, a small amount of fine sand, and no coarse sand or aggregates to achieve desired micromechanical conditions,, see Table 5.2. The low tensile strength and evident brittleness are beneficial regarding the formation of multiple steady-state cracks and strain-hardening in the SHCC composite, which is discussed in detail in Section 2.2[30].

The PE fibers' bond properties in the high-strength cementitious matrix have been studied in detail in previous works published in [31, 29]. The bond is described by a bond-slip relation with softening after reaching the bond strength and complete pullout of the fibers with embedment lengths of up to 3 mm. The bond strength should be moderated to let the fibers play their role in crack bridging while ensuring adequate free length for fiber deformation with crack opening and avoiding premature fiber failure. The reference pullout test and the bond law utilized in simulation, are discussed in detail in Section 2.2.5.

Parameter	**Unit**	**Value**
Diameter $\oslash$	[mm]	0.02
Length L	[mm]	6
Aspect ratio	-	300
Tensile strength f_f	[N/mm^2]	1 600
Young's modulus E_f	[N/mm^2]	80 000
Elongation at break%	-	3.5

Table 5.1: Mechanical properties of polymer fibers (Dyneema) used in target SHCC[31]

Parameter	**Unit**	**Value**
CEM I 52.5 R-SR3/NA	[Kg/m^3]	1 460
Silica fume Elkem 971	[Kg/m^3]	292
Quartz sand $(0.06 - 0.2mm)$	[Kg/m^3]	145
Water	[Kg/m^3]	315
HRWRA Glenium ACE 460 (BASF)	[Kg/m^3]	35
HDPE fibers (2.06% by volume)	[Kg/m^3]	20

Table 5.2: Mixture composition of high-strength SHCC[31]

5.1.2 Specimen production and testing

Unique dumbbell-shaped specimens with a very thin cross-section in the gauge portion are designed and produced in order to use as reference experiments of 2D FEM simulations of SHCC with a discrete fiber representation, see Fig. 5.1(a). The molds consist of plastic elements assemble through bolted connections. The small thickness is achieved by pressing profiled elements into the molds filled with fresh SHCC until the purposefully dimensioned spacers impeded any further displacement. The pressed material is squeezed towards the molds' open ends, which is aligning the fibers longitudinally. The predominantly longitudinal orientation of the fibers is also a desired aspect concerning the performed numerical simulations.

The specimens are cured for 27 days in the molds. The curing is done in sealed plastic bags in a climatic chamber with constant temperature (20°C) and humidity (65°C) conditions. This curing procedure allows minimizing the development of shrinkage cracks, which can be promoted by the high cement content in the investigated SHCC as well as large surface area and a small cross-section of the samples[114].

Before testing, the specimens are extracted from the mold assembly together with the profiled mold elements. The latter are connected to each other by long threaded rods at the specimen ends, as shown in Fig. 5.1(b). The extraction is done to apply the speckle pattern necessary for the optical monitoring of the deformations during the test as well as for cutting the notches. Before the test starts, these elements are bolted back to the specimens and confined the samples during the gluing process[114].

The specimens have a cross-section of $3.5\,\text{mm} x 40\,\text{mm}$ in the gauge portion and $40\,\text{mm} x 40\,\text{mm}$ at their ends. The total specimen length is 250 mm with a gauge length of 100 mm. The transition zones between the large cross-sections at samples' ends and the thin gauge portions are 35 mm long. These geometrical proportions ensure proper fixation of the samples in the testing machine on one hand, and failure localization in the gauge portion, on the other[114]. Fig. 5.2(b) shows a specimen fixed in the testing machine and the confining mold elements. Non-rotatable boundaries were ensured by gluing the specimens in thick steel rings, which were bolted to the machine cross-members. The same testing conditions are used as the previous works on common specimen geometries published in [31, 29]. The tests are performed in a hydraulic testing machine Zwick 1200 in a displacement controlled mode with a displacement rate of $0.05\,\text{mm/s}$. Notched and un-notched specimens are tested. The

Figure 5.1: a) Naked un-notched SHCC specimen, b) specimen fixed in the testing machine. The lateral confining elements were removed shortly before load initiation[114, 50]

notches with a length of 5 mm and a height of 4 mm, are cut in the middle on both sides of the samples, the position and dimensions of notches on both sides of the specimen are shown in Fig. 5.5(a). The results on notched specimens with a fiber content of 2% are used as reference experiments and shown in Fig. 5.2.

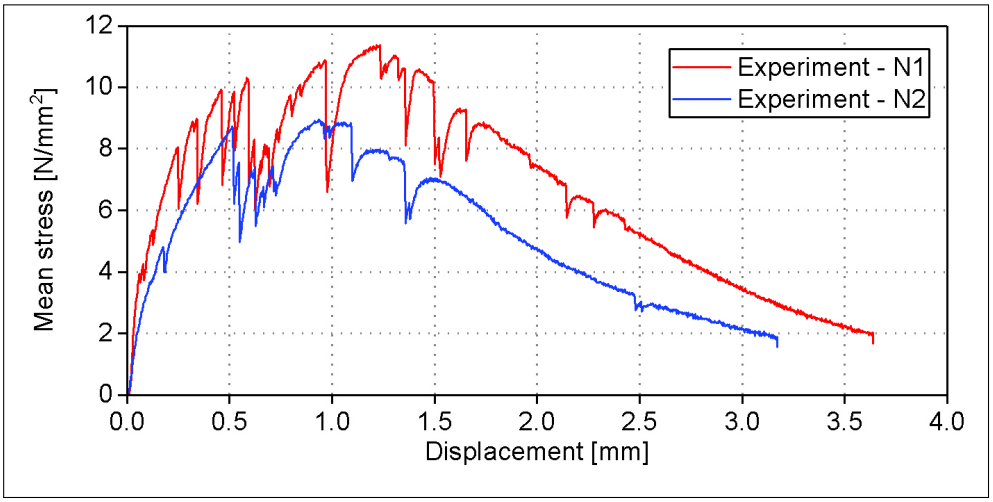

Figure 5.2: Experimental results on notched specimens with a fiber content of 2%

5.2 FINITE ELEMENT SIMULATIONS

The 2D SHCC tensile models are analyzed with in-house program CaeFem used newly developed model introduced in Chapter 4. As it is mentioned before, the specimen is very thin in mid-region with $t = 3.5\,\text{mm}$ to provide 2D conditions. The loading is applied by displacement control condition on the top edge while the specimen is fixed in lower support. The test results related to two nominally the same notched specimens explained in Section 5.1, are used as experimental references. Each component of cement-based composites should be modeled separately on the mesoscopic scale. The model is in the context of plane-stress.The embedded fibers are represented by 2D truss elements[128]. Thus, the matrix elements are 2D four-node continuum elements with linear elastic material behavior and limited tensile strength rolled by Rankine criteria to extend to cracked SDA element and depends on load history. The fixed cracks approach is applied whereas secondary cracking is allowed. The formulation of mentioned material models and methods are discussed in detail in chapter 4.

Due to the localization of cracks in the notched area, special attention will be given to the middle of the dumbbell specimen for numerical simulation, see Figs. 5.3 and 5.4. During the experiments, the deformations are evaluated using Digital Image Correlation in which three virtual calipers were placed longitudinally on specimen edges and in the middle. The deformation axes diagrams shown in Fig. 5.2 represent the average of the elongation of these profiles, which show the whole gauge surface in the mid of the specimen.

In Figs. 5.3 and 5.4, each DIC image represents a specific step of crack development. They show how the cracks are formed, propagated, and localized in the notched area during the experiments. It should be stated that the notches did not impede multiple crack formation in the whole gauge surface, which is typical for SHCC. However, they concentrated the crack formation in the middle of the sample and allowed modeling a smaller region of 40 mm length in the middle of the sample. This way, the modeling effort will be efficient, and the required computational time will be optimized and is schematically shown in Fig. 5.5(a). The notched area is discretized with 1560 quad continuum elements with a thickness of $t = 0.1\,\text{mm}$. A total number of 1698 fibers is computed for the simulation model considering the single fiber volume of $1.88 \cdot 10^{-3}\,\text{mm}^3$, and 2% volume fraction of fiber.

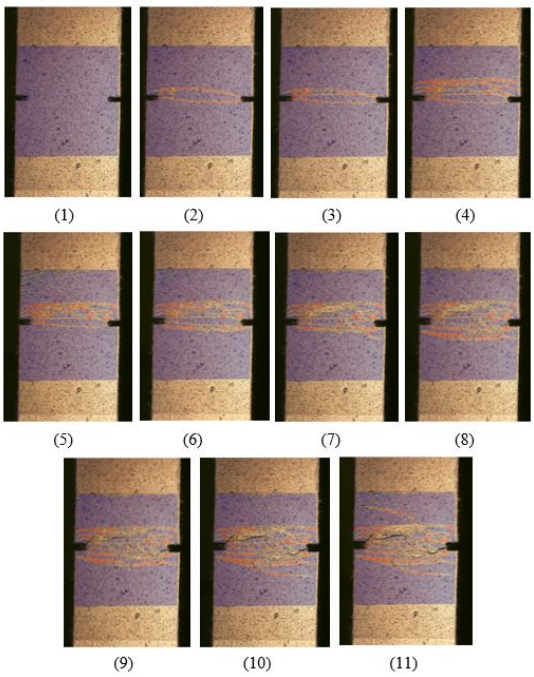

Figure 5.3: DIC images, crack pattern during tensile test at different load steps: $1) u = 0.02\,\text{mm}$, $2) u = 0.3\,\text{mm}$, $3) u = 0.52\,\text{mm}$, $4) u = 0.77\,\text{mm}$, $5) u = 1.02\,\text{mm}$, $6) u = 1.27\,\text{mm}$, $7) u = 1.52\,\text{mm}$, $8) u = 1.77\,\text{mm}$, $9) u = 2.02\,\text{mm}$, $10) u = 2.27\,\text{mm}$, $11) u = 2.52\,\text{mm}$[*Specimen N1*][114]

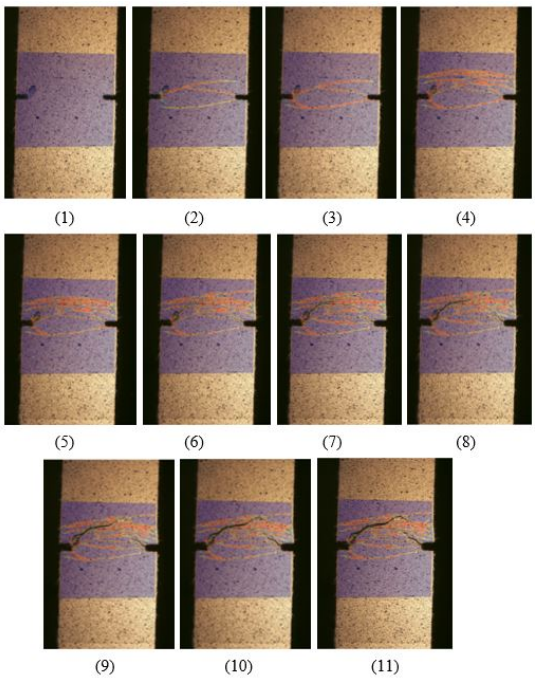

Figure 5.4: DIC images, crack pattern during tensile test at different load steps: $1) u = 0.048\,\text{mm}$, $2) u = 0.3\,\text{mm}$, $3) u = 0.55\,\text{mm}$, $4) u = 0.8\,\text{mm}$, $5) u = 1.05\,\text{mm}$, $6) u = 1.3\,\text{mm}$, $7) u = 1.55\,\text{mm}$, $8) u = 1.8\,\text{mm}$, $9) u = 2.05\,\text{mm}$, $10) u = 2.3\,\text{mm}$, $11) u = 2.55\,\text{mm}$ [*Specimen N2*][114]

Fibers are distributed randomly in the model, whereas the inclination of fibers is restricted within a range of ±5 degrees from the vertical due to special production techniques explained in Section 5.1.2, see Fig. 5.5(b). A single fiber is discretized with five constant stress truss elements. The whole simulation model includes 23 046 degrees of freedom. A viscous regularization is required in order to avoid premature destabilization of the computation, see Section 4.2.6. A viscosity value combined with an initial loading time step is chosen for this purpose; see Eq. (5.1).

$$\eta_w = 10\,\frac{\mathrm{N}}{\mathrm{mm}^2}\,\frac{\mathrm{s}}{\mathrm{mm}}, \qquad \Delta t = 0.001\,\mathrm{s} \tag{5.1}$$

The shear retention factor, see Eq. (4.85), is assumed with $\alpha_s = 0.01$. This is derived from parameter studies on Willam's test discussed in[103, 121, 50].

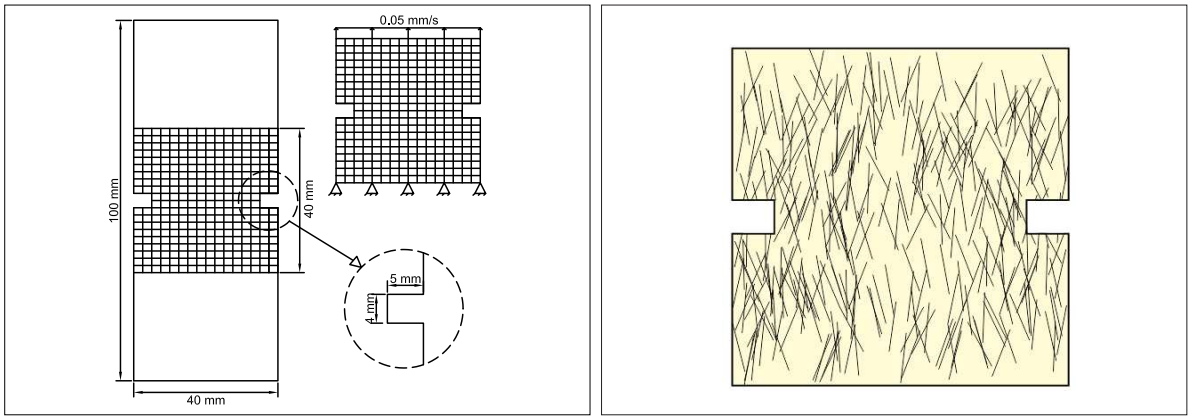

Figure 5.5: Dumbbell specimen simulation a) Geometry of mid region of specimen with scheme of discretized center segment b) scheme of random fiber placement[114, 50]

The fine-grained concrete properties are listed in Table 5.3. Truss nodes and neighboring continuum nodes are coupled by particular bond elements, explained in detail in Section 4.3. The bond-slip relation is defined so that the lateral bond is constrained with an elastic penalty approach in order to avoid mutual intersections and is flexible in a longitudinal direction according to the governing bond-slip law. Linear elastic material models with limited tensile strength are assigned to embedded truss elements; fiber mechanical properties are shown in Table 5.4.

Parameter	**Unit**	**Value**
Young's modulus E	[N/mm^2]	29 000
Poisson's ratio ν	-	0.2
Tensile strength f_{ct}	[N/mm^2]	3.8
Fracture energy G_f	[N/mm]	$100 \cdot 10^{-3}$
Critical crack width w_{cr}	[mm]	0.079

Table 5.3: Mechanical properties of fine grained concrete

Parameter	**Unit**	**Value**
Young's modulus E_f	[N/mm^2]	80 000
Tensile strength f_f	[N/mm^2]	1 600
Length L	[mm]	6
Diameter $\oslash$	[mm]	0. 02
Cross sectional area A_f	[mm^2]	$3.14 \cdot 10^{-4}$
Failure load P_{fu}	[N]	0.5

Table 5.4: Mechanical properties of fiber

Within the current mesoscopic framework, bond properties have to be based on experimental data for pullout of single fibers in fine-grained concrete blocks. Such experiments are explained in detail in Section 2.2.3. As they are characterized by relatively large, scatter mean data are used for the following. A typical course formulated as spline and with considering some modifications, which are explained in Section 2.2.5, is shown in Fig. 5.6. This bond law is derived from the simulation of a single fiber pullout test and used as the first approach and later will be modified to improve the simulation results compared to the reference experiments, the same used for the negative range with a reversal of signs of slip and bond stress. It is characterized by an initial elasticity, maximum bond stress at a prescribed slip, and constant residual bond stress continuous from another prescribed slip on, see Table 5.5.

The residual stress is assumed with nearly zero to cover fiber pullout at least approximately. Precise modeling of fiber pullout would require a large displacement approach that exceeds the current small displacement assumption's scope. In Fig. 5.6, A bi-linear graph is used in pullout simulation within DIANA software and is discussed in detail in Section 2.2.5. The Spline graph in this figure is assigned to bond elements in the in-house program CaeFem. The spline and bi-linear graphs are the same in all the mentioned bond characteristics, i.e., initial elasticity, maximum bond stress at the prescribed slip, and the constant residual bond stress.

Parameter	**Unit**	**Value - B-4**
Bond strength τ_{max}	[N/mm^2]	2.39
Ultimate bond stress τ_f	[N/mm^2]	0.0
Slip$_{\tau_{max}}$ S_1	[mm]	0.076
Slip$_{\tau_f}$ S_2	[mm]	0.760

Table 5.5: Mechanical properties of bond - B - 4

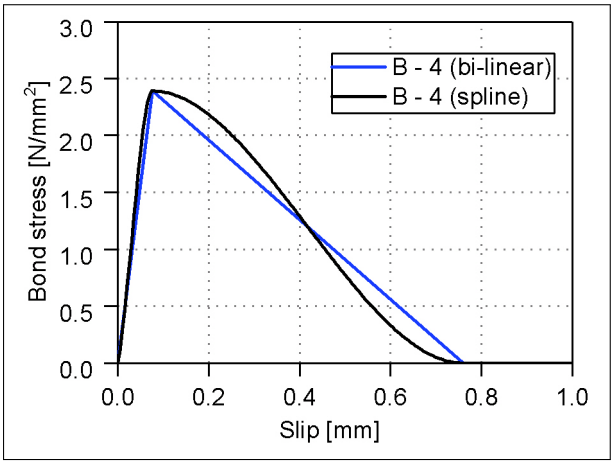

Figure 5.6: Bond law - B - 4 (bi-linear vs spline)

As the loading is applied on top with vertical prescribed displacements, see Fig. 5.5(a), reaction forces come as results and yield a computed load-displacement curve to be compared with experimental results. The experiments' displacement base must be adjusted to reach comparable displacements for the discretized notched center part. Even though there is a different length of the simulation model and the experimental model, based on what is discussed about Figs. 5.3 and 5.4, it can be assumed that the deformation read from DIC images can be determined as notched area deformation due to localization of cracks because of notches. Load-displacement results from simulation and experiments are shown in Fig. 5.7, whereby loading is expressed in terms of mean stress according to a common convention.

This simulation is performed within the in-house program CaeFem, and the bond law assigned to the bond elements is $B-4$, the spline shown in Fig. 5.6. The SHCC behavior is characterized by highly increased tensile strength, a superior ductile behavior with steep hardening phase compared to simulation of plain concrete notched model without fibers, see Fig. 5.7.

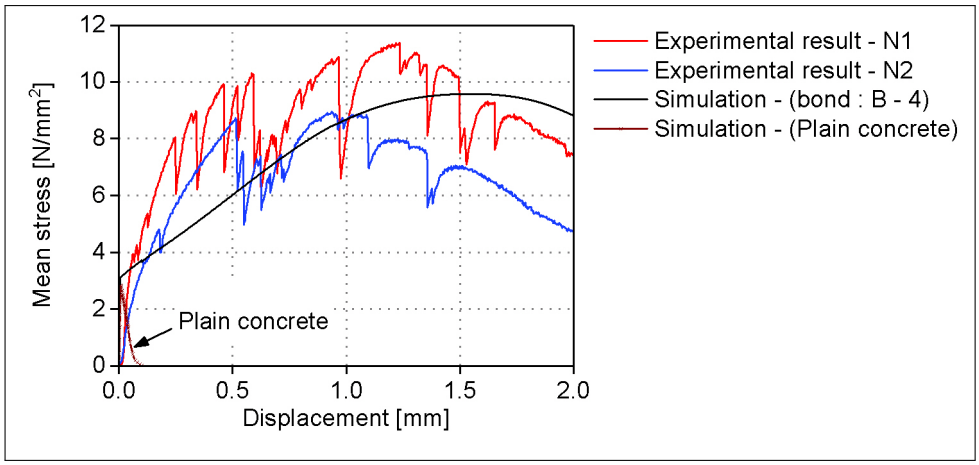

Figure 5.7: Mean stress - displacement results - bond law - B - 4 and plain concrete

Comparing SHCC experiment and simulation characteristic items are commented as follows:

- The initial stiffness of the experimental specimen is significantly lower compared to the simulation. This is attributed to the pre-cracking of the very thin specimen; the micro-cracks are created during handling and fitting the specimen in the experiment setup before the test is started, see Fig. 5.6.

- Experimental curves show a distinct roughness whereby single spikes are hypothetically assigned to particular cracking events. As the number of spikes is much lower than the number of final cracks, these particular events presumably belong to instantaneously larger cracks with localizations arising from the actual scatter of material properties, i.e., matrix tensile strength, bond properties and fracture energy. Dynamic phenomena presumably also come into play with these effects. The current simulation model does not cover random fields and short-time dynamics.

- The experiment has a steep hardening phase compare to a slight increase observed in the simulation result. Since the crack bridging phase is the significant characteristic of SHCCs, several parameter studies are planned to improve the simulation result to have a better agreement with experiments concerning the hardening phase.

- The maximum response of simulation has almost the same value as the experiments concerning the scatter experiment graphs. Thus, the slight increase of the hardening branch in simulation leads to much higher displacement values corresponding to the maximum total response. Accordingly, the crack localization and start point of the softening phase will be started at higher applied displacement load[50].

The load-displacement characteristics demonstrate the global behavior. However, the simulation allows local investigations for whole loading history and results in matrix strains and stresses, cracking patterns, crack width, dissipated energy, fiber and bond stresses, and fiber failure events.

The crack patterns on the deformed mesh geometry for three prescribed displacements are shown in Fig. 5.8. The presented crack pattern in Fig. 5.8c for $u = 1.56\,\text{mm}$, indicates a state in which the bridging stage is ended and crack localization is started. A crack fully intersects an element through its center by definition, see also Section 4.2.5, and is indicated by a thicker dark gray line.

Although outer geometry and boundary conditions are symmetric concerning the vertical and horizontal center lines, symmetry is not preserved in the simulation results due to fibers' random positions. Computed crack contours spreading over neighbored elements are not continuous but slightly deviate in their orientation. The interpretation of this simulation property has also been discussed in Section 4.2.5. Secondary cracking is constrained by a minimum deviation of 45 degrees compared to primary cracking orientation and occurs relatively soon. This introduces some bias into secondary crack orientation. Some overall skewness of fiber orientations presumably triggers the overweight with a counterclockwise orientation.

The simulation crack patterns are deterministic; on the contrary, the experimental specimen behavior is influenced by random material properties. Thus the simulation crack patterns cannot be directly compared to experimental cracking patterns.

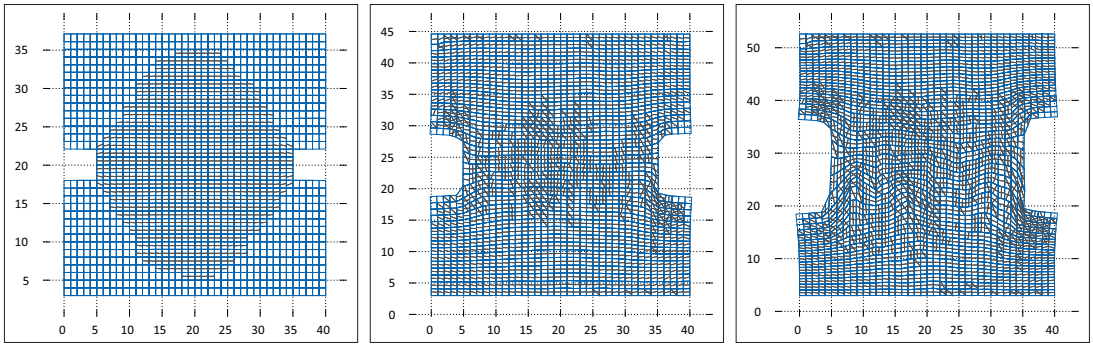

(a) $u = 0.01\,\text{mm}$ (b) $u = 0.76\,\text{mm}$ (c) $u = 1.56\,\text{mm}$

Figure 5.8: Crack pattern results - bond law - B - 4 (displacements scaled by factor 10)

In Fig. 5.9, fiber stresses and bond stresses are shown for the mentioned three prescribed displacements. Figs. 5.9(a,b) show the stage shortly after loading is started; small values are computed for stresses in fiber and bond elements. The highest values of stresses belong to the fibers in the center of the notched model and following the crack pattern shows in Fig. 5.8(a) whereby $u = 0.01\,\text{mm}$. Figs. 5.9(c,d) show the stage corresponding to the halfway of hardening phase whereby $u = 0.76\,\text{mm}$. In this stage, several fibers in the mid part of the specimen experience stress almost equal to the fiber's tensile strength, and the stresses in the bond elements, connected these fibers to the matrix, also experience high values equal to the maximum bond strength. The stress pattern in this stage is also compatible to the crack pattern. Figs. 5.9(e,f) show the stage at the end of hardening phase whereby $u = 1.56\,\text{mm}$. It is observed that more fibers, located in the center of the model, are reaching the limited strength comparing to the previous level. At this stage, the localization of the critical crack and softening phase will be started.

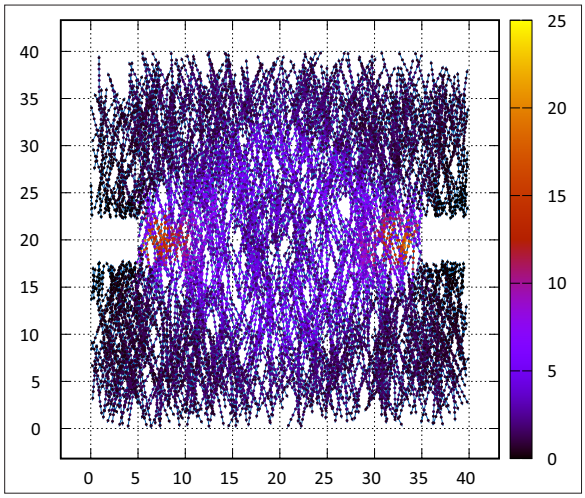

(a) Fiber stress in N/mm^2 , $u = 0.01$ mm

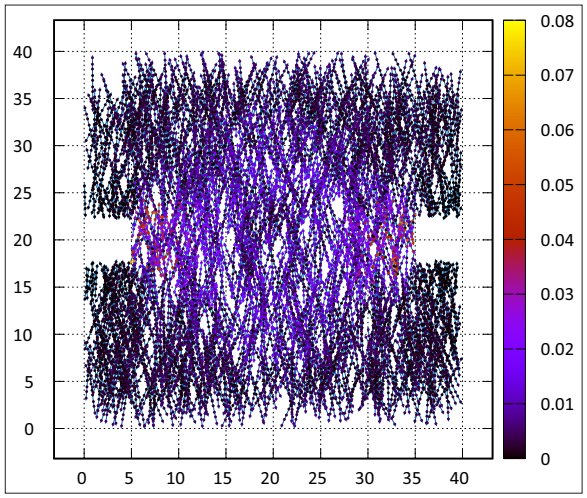

(b) Bond stress in N/mm^2 , $u = 0.01$ mm

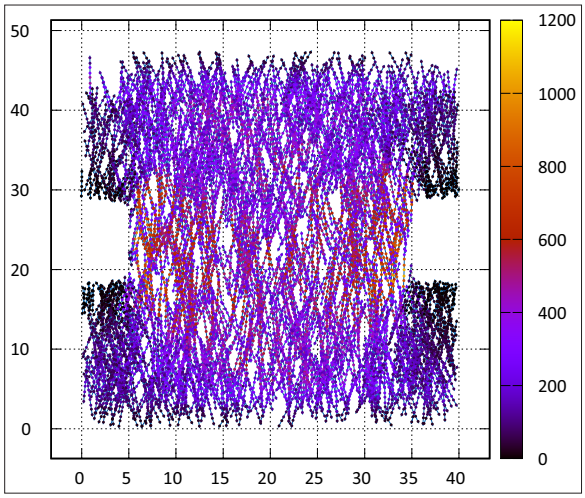

(c) Fiber stress in N/mm^2 , $u = 0.76$ mm

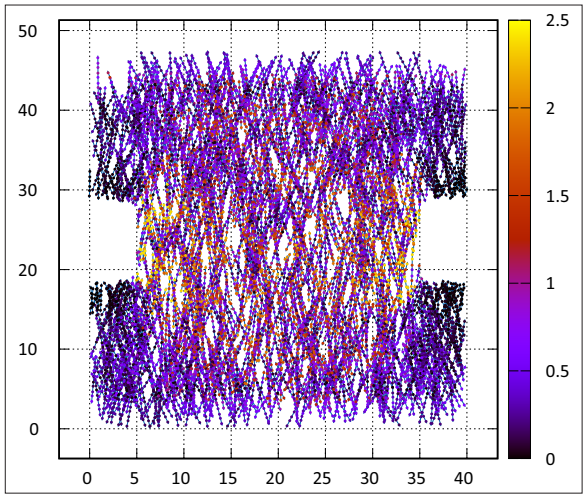

(d) Bond stress in N/mm^2 , $u = 0.76$ mm

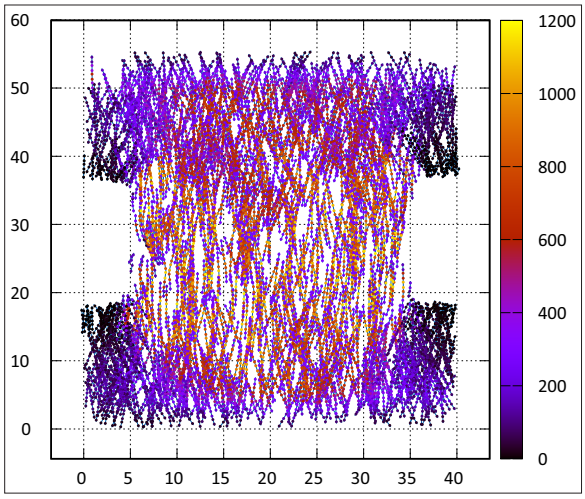

(e) Fiber stress in N/mm^2 , $u = 1.56$ mm

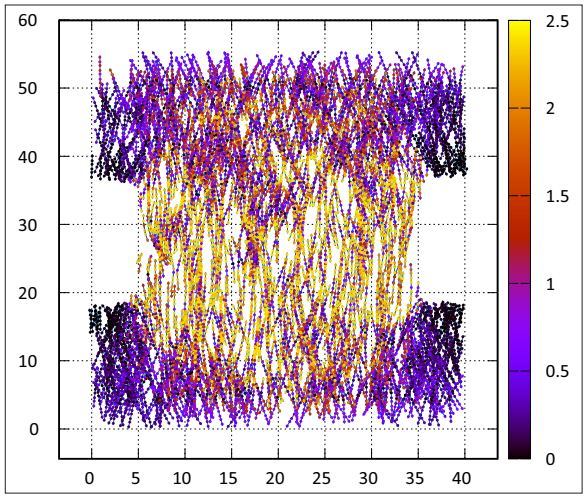

(f) Bond stress in N/mm^2 , $u = 1.56$ mm

Figure 5.9: Fiber stresses and bond stresses - bond law - B - 4 (displacements scaled by factor 10)

5.2.1 Numerical reference model

Previous studies have argued that the aimed strain-hardening can be modeled whereas a bond behavior, assigned to the bonds connecting fibers to the matrix in SHCC simulations, starts with a very high initial slope [116]. It means that the bond elements pass the elastic phase on the pullout curve sharply and the softening phase has begun with much lower slips comparing to corresponding mean values derived from single fiber pullout tests simulations. On the one hand, it can be due to the fibers group effect due to the interactions between fibers or/and fibers and the surrounding matrix at the same time in the composite. This effect becomes significant in the case of composites with the high volume fraction of fibers, which in the present work is 2%. On the other hand, the fibers are connected to the matrix elements with the bond elements, in which one or more surrounded matrix elements can experience the crack initiation at the same time, which may cause a fast drop, and immature softening behavior occurs in much lower slips. Thus, a new bond law is introduced, $B-5$, which is the same as bond law: $B-4$ in most of the bond properties except the initial slope, see Table 5.6. This means that the softening phase of the bond curve begins in a lower prescribed slip based on this bond law compare to the corresponding one in $B-4$.

Parameter	**Unit**	**Value - B-4**	**Value - B-5**
Bond strength τ_{max}	[N/mm^2]	2.39	2.39
Ultimate bond stress τ_f	[N/mm^2]	0.0	0.0
Slip$_{\tau_{max}}$ S_1	[mm]	0.076	0.022
Slip$_{\tau_f}$ S_2	[mm]	0.760	0.706

Table 5.6: Mechanical properties of bonds - B - 4 and 5

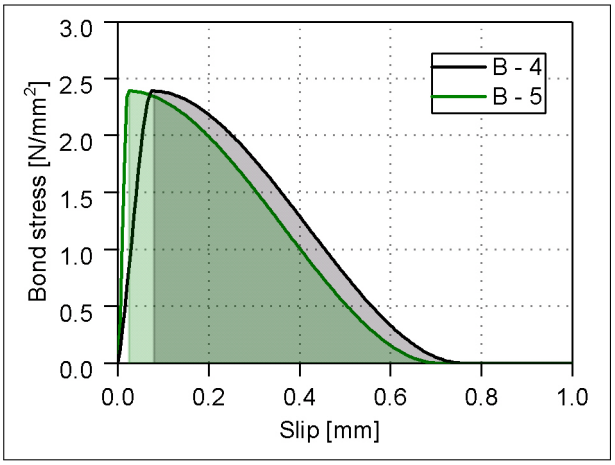

Figure 5.10: Bond law - B - 4 vs B - 5

In Fig. 5.10, two bond laws are shown and compared. The prescribed slip corresponding to the ultimate bond stress in bond law $B-5$ is determined so that the area, under the softening phase of both curves, has the same value.

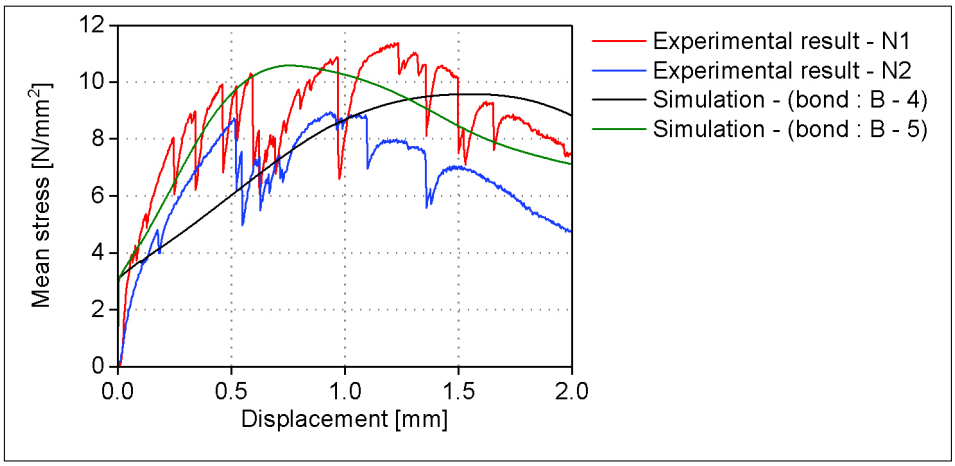

Figure 5.11: Mean stress - displacement results - bond law - B - 4 vs B - 5

In Fig. 5.11, the total responses of both models with different bond laws are presented. It is observed that model with bond law $B-5$ has a very good agreement with experiment references concerning the modeling of stain-hardening and crack bridging stage of target composite, which is the most significant characteristic of SHCCs. On the other hand, the initial slope in experiments is lower than the simulation curve. This can be the effect of microcracks, which are created in the specimens during the production and preparation stage and caused because of the shallow thickness of the specimens.

The crack patterns on the deformed mesh geometry for three prescribed displacements are shown in Fig. 5.12 and following the same arrangements as the ones shown in Fig. 5.8. The presented crack pattern in Fig. 5.12(c) for $u = 0.76\,\text{mm}$, shows a state which softening branch is started, Fig. 5.12(b) shows the results in half way of hardening phase, $u = 0.38\,\text{mm}$ and Fig. 5.12(a) is related to state shortly after loading is started $u = 0.01\,\text{mm}$.

As mentioned before, the simulation crack patterns can not be directly compared to experimental cracking patterns due to the significant influence of the random material properties in experiment. Two crack patterns are shown in Figs. 5.8(b) and 5.12(c), both are occurred at the same loading step ($u = 0.76\,\text{mm}$) and have different assigned bond laws. By comparing these two patterns, it is observed that: the model with bond law $B - 5$ experience more cracks than the model with bond law $B - 4$ under same applied load $u = 0.76\,\text{mm}$.

This can be explained by this fact that model with bond law $B - 5$ has reached the peak of total response at this loading stage, whereas its hardening phase is ended, and the localization of crack will be started. The higher total response compared to the model with bond law $B - 4$ at the same applied load means more cracks are created and propagated in matrix elements, and fibers actively contribute in the load-bearing.

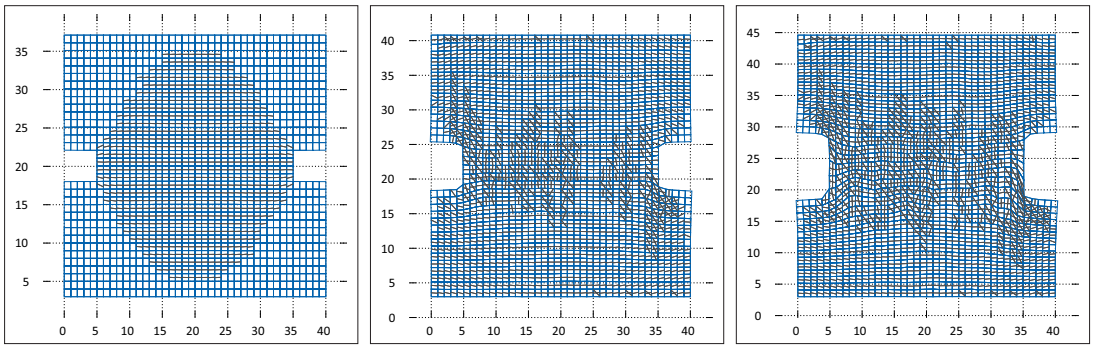

(a) $u = 0.01\,\text{mm}$ (b) $u = 0.38\,\text{mm}$ (c) $u = 0.76\,\text{mm}$

Figure 5.12: Crack pattern results - bond law - B - 5 (displacements scaled by factor 10)

In Fig. 5.13, fiber stresses and bond stresses are shown for the mentioned three prescribed displacements. Figs. 5.13(a,b) show the stage shortly after loading is started, small values are computed for stresses in fiber and bond elements. The highest values of stresses belong to the fibers in the center of the notched model and following the crack pattern shows in Fig. 5.12(a) whereby $u = 0.01\,\text{mm}$. Figs. 5.13(c,d) show the stage corresponding to the halfway of hardening phase whereby $u = 0.38\,\text{mm}$. In this stage, several fibers in the mid part of the specimen experience stress almost equal to the tensile strength of the fiber, and the stresses in the corresponding bond elements also have high values equal to bond strength. The stress pattern in this stage is also comparable to the crack pattern.

Figs. 5.13(e,f) shows the stage at the end of the hardening phase, whereas the crack bridging stage is stopped, and the crack localization and softening phase will be started, $u = 0.76\,\text{mm}$. It is observed that more fibers, which are located in the center of the model, reaching the limited strength compared to the previous level and the model with bond law $B-4$ at the same load step, shown in Figs. 5.13(e,f) and Figs. 5.9(c,d). As it is mentioned before, at this loading step, the model with bond law $B-5$ has a higher total response which means that fibers are playing a significant role in load-bearing, it is shown by higher stresses mostly equal to fiber strength in fibers in mid of specimen Fig. 5.13(e). Thus, higher engagement of fibers in load bearing leads to more cracks observed in the crack pattern shown in Fig.5.12(c) than in Fig. 5.8(b).

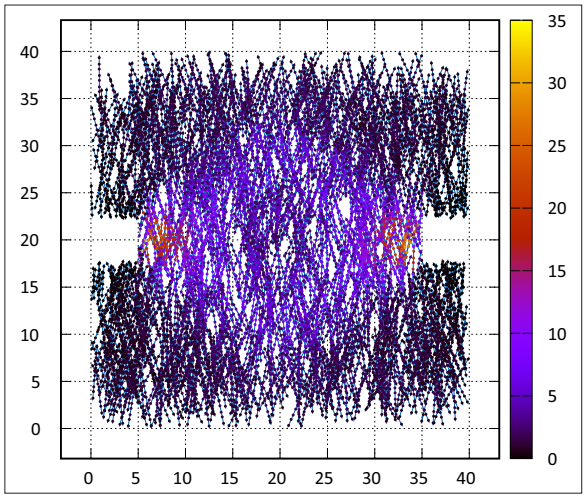

(a) Fiber stress in N/mm^2 , $u = 0.01$ mm

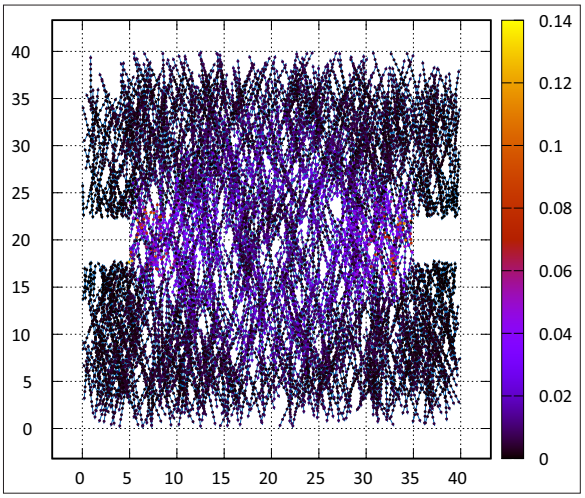

(b) Bond stress in N/mm^2 , $u = 0.01$ mm

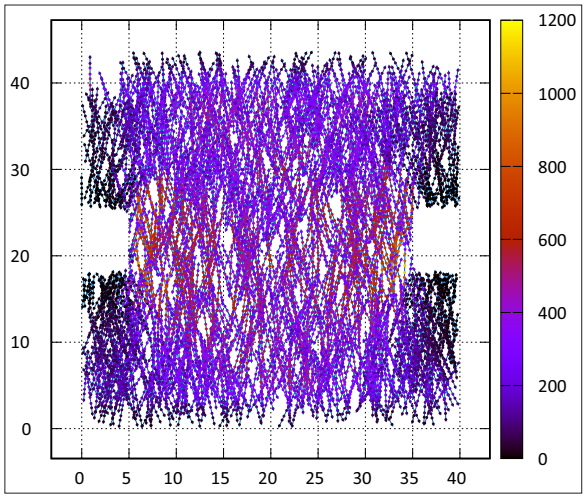

(c) Fiber stress in N/mm^2 , $u = 0.38$ mm

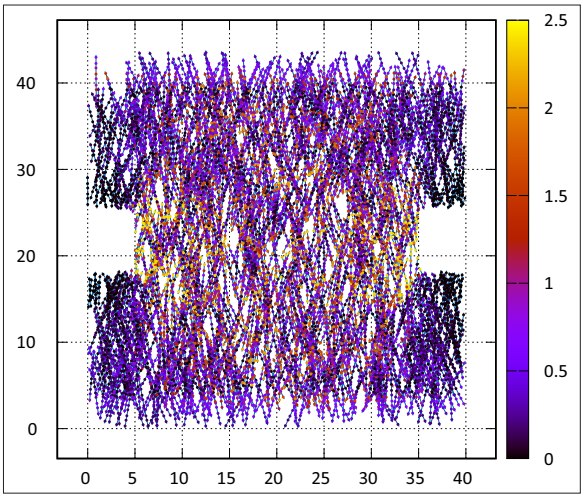

(d) Bond stress in N/mm^2 , $u = 0.38$ mm

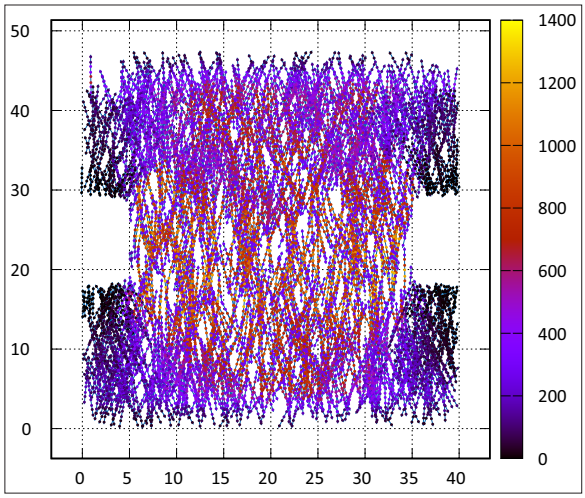

(e) Fiber stress in N/mm^2 , $u = 0.76$ mm

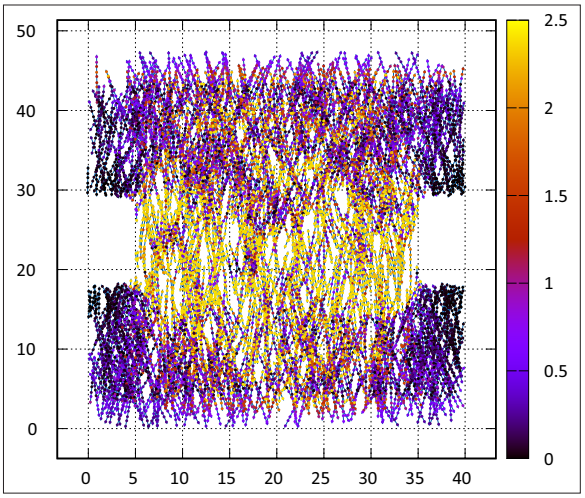

(f) Bond stress in N/mm^2 , $u = 0.76$ mm

Figure 5.13: Fiber stresses and bond stresses - bond law - B - 5 (displacements scaled by factor 10)

5.3 MATERIAL AND MECHANICAL PARAMETRIC STUDIES

5.3.1 Studies on effect of different parameters in bond stress - slip relationship(Maximum bond strength, ultimate bond stress, initial stiffness)

In this section, first, three different bond laws are assigned to bond elements to investigate the effect of maximum bond strength on the specimen's overall response. These three bond laws are different in maximum bond strengths while the area under the curves has been kept the same by shifting the slip corresponding to the ultimate bond stress, see Table 5.7 and Fig. 5.14.

Parameter	Unit	Value - B-5	Value - B-6	Value - B-7
Bond strength τ_{max}	[N/mm^2]	2.39	2.20	2.60
Ultimate bond stress τ_f	[N/mm^2]	0.0	0.0	0.0
Slip$_{\tau_{max}}$ S_1	[mm]	0.022	0.022	0.022
Slip$_{\tau_f}$ S_2	[mm]	0.706	0.765	0.651

Table 5.7: Mechanical properties of bonds - B - 5, 6 and 7

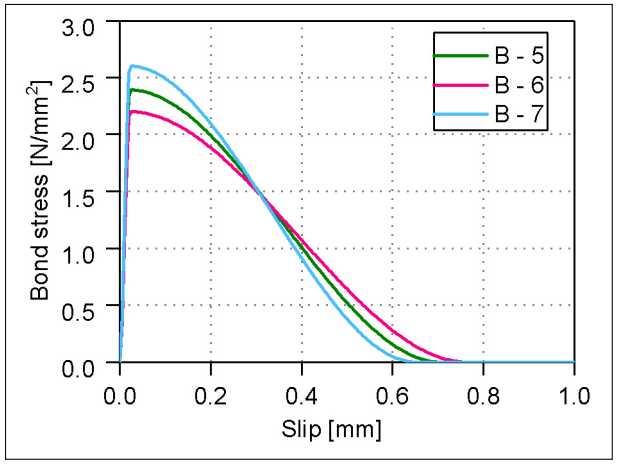

Figure 5.14: Bond laws - B - 5, 6 and 7

From simulation results shown in Fig. 5.15, it is observed that a slight change in the value of maximum bond strength has a direct effect on the value of maximum mean stress. When the reference maximum bond stress is multiplied by the factor of 0.92 and 1.087, the maximum mean stress will be changed with the factor of 0.94 and 1.067 compare to maximum mean stress of reference model, respectively. This shows that the result is mostly subjected to the same ratio matter as bond-slip behavior is varying, and the total response curve is following the bond-slip curve shape.

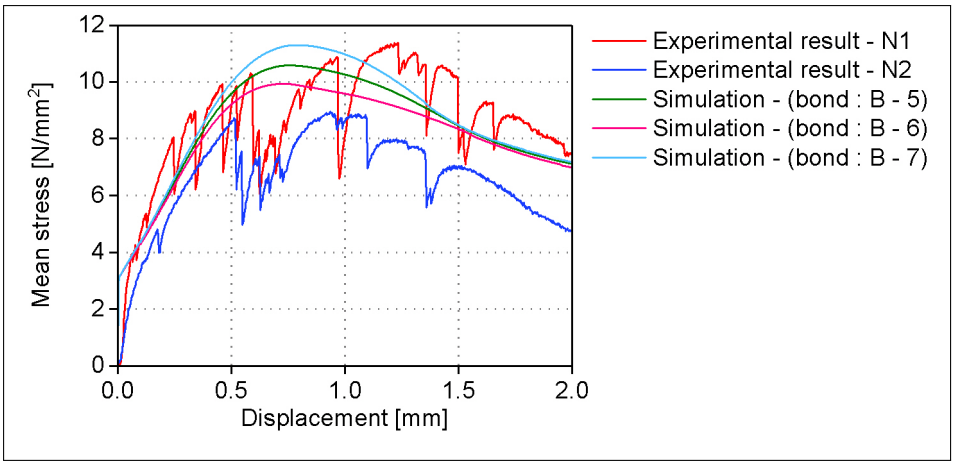

Figure 5.15: Mean stress - displacement results - bond laws - B - 5, 6 and 7

The crack patterns for enumerated simulations within three different bond laws at the same loading step are shown in Fig. 5.16 and following the same arrangements as the ones shown in Fig. 5.9. As mentioned before, the simulation crack patterns can not be directly compared to experimental cracking patterns due to the significant influence of the random fiber field. From crack patterns shown in Fig. 5.16, it is observed that the crack patterns are mostly the same and slightly different in some matrix elements. This can be explained by this fact that based on the total response results shown in Fig. 5.15, all the three simulations reach the peak of response mostly at the same loading step which is used as a reference step for patterns shown in Fig. 5.16 Thus, for enumerated simulations, the shown load step is the beginning of the crack localization stage.

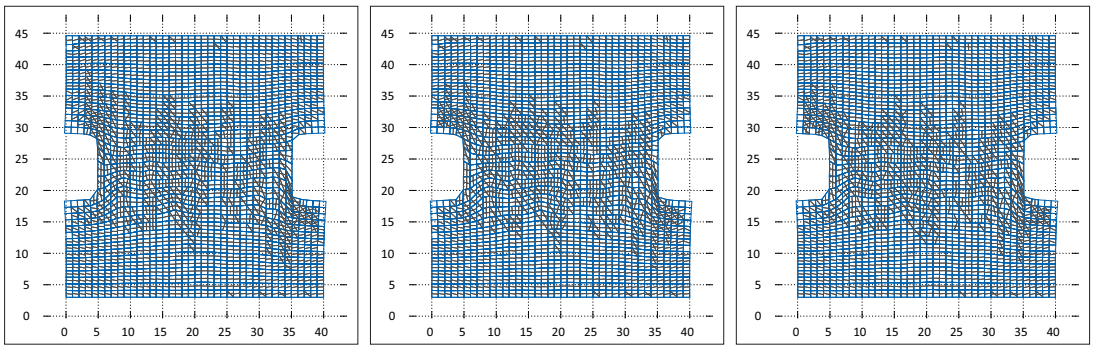

(a) B - 5 (b) B - 6 (c) B - 7

Figure 5.16: Crack pattern results - bond laws - B - 5, 6 and 7 - $u = 0.76\,\text{mm}$ (displacements scaled by factor 10)

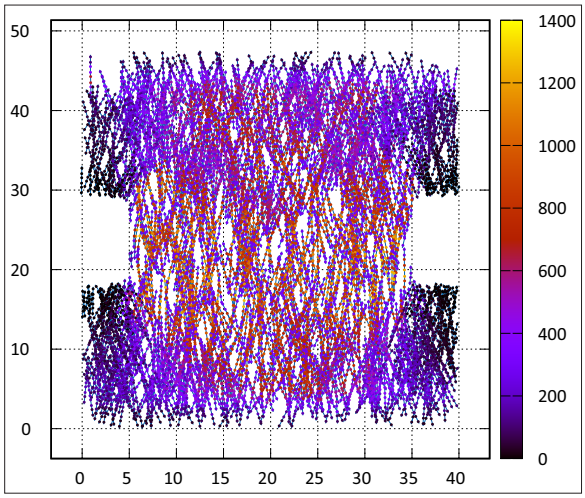

(a) Fiber stress in N/mm^2 , B - 5

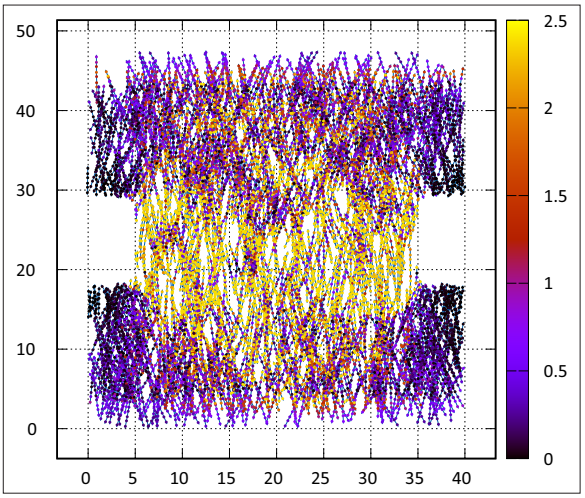

(b) Bond stress in N/mm^2 , B - 5

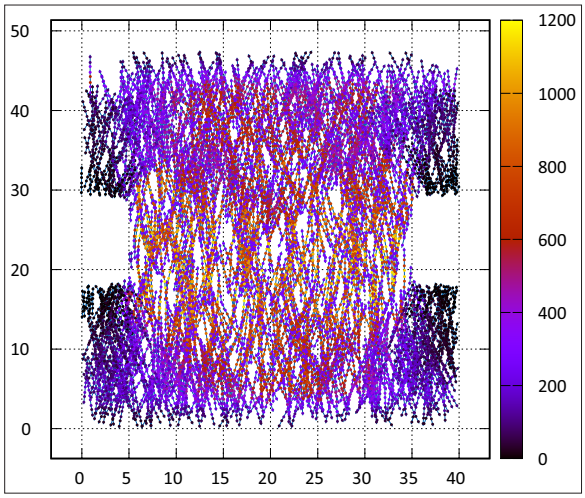

(c) Fiber stress in N/mm^2 , B - 6

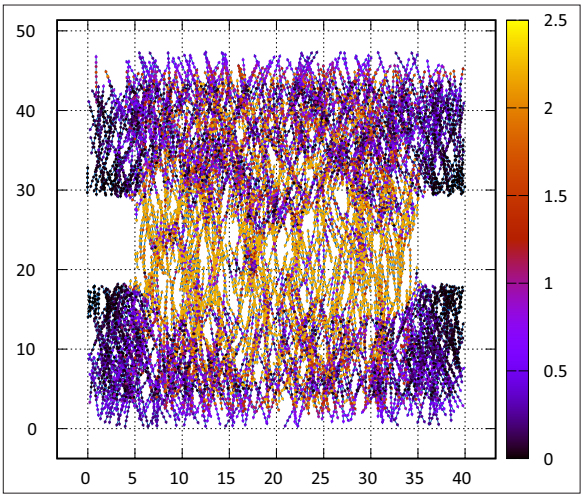

(d) Bond stress in N/mm^2 , B - 6

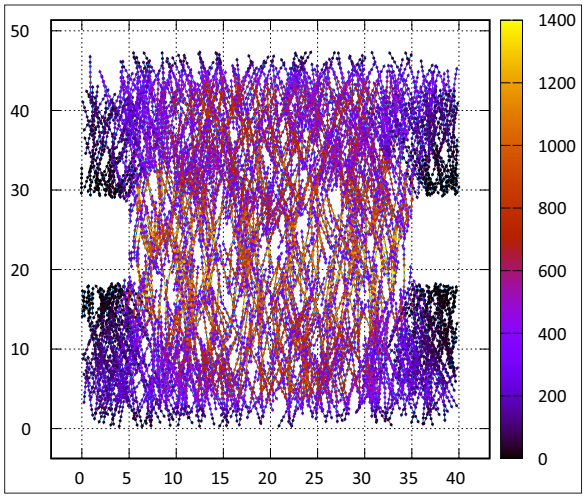

(e) Fiber stress in N/mm^2 , B - 7

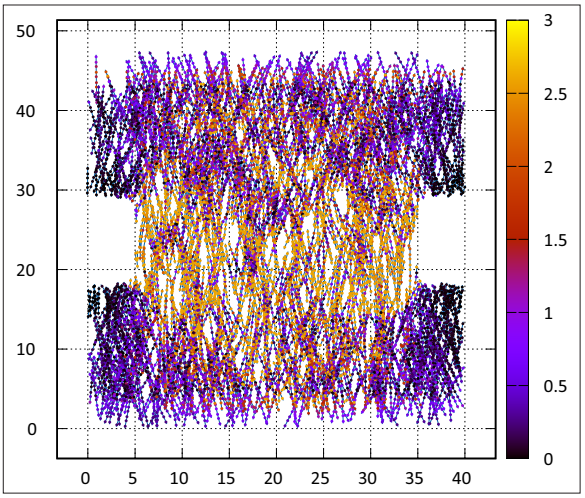

(f) Bond stress in N/mm^2 , B - 7

Figure 5.17: Fiber stresses and bond stresses - bond laws - B - 5, 6 and 7 - $u = 0.76\,\text{mm}$ (displacements scaled by factor 10)

In Fig. 5.17, fiber stresses and bond stresses are shown for each mentioned three simulations within three different bond laws at the same prescribed displacements loading condition. From these contour results, it is observed that the model with a lower bond strength also experienced lower stresses in fibers, it means that with higher bond strength, the bond elements can transfer higher stresses between matrix elements and truss elements. Thus, the fibers have more contribution in load-bearing, and this leads to higher stresses in fibers and increases the total response of the specimen, as shown in Fig. 5.15.

As it is mentioned before the residual stress is assumed with nearly zero to cover fiber pullout at least approximately. To investigate the effect of residual stress(ultimate stress), two new bond laws are introduced, see Table 5.8 and Fig. 5.18. Bond laws $B-8$ and $B-9$, are different from bond law $B-5$ in residual stresses and corresponding slips. In bond law $B-8$, the residual stress is half of the assigned bond strength at the same slip corresponding to the ultimate bond stress in bond law $B-5$. On the other hand, bond law $B-9$ represents a plastic behavior with a plateau, which starts when the stress in bond element reaches the bond strength, and the residual stress remains equal to bond strength for the higher slip.

Parameter	**Unit**	**Value - B-5**	**Value - B-8**	**Value - B-9**
Bond strength τ_{max}	[N/mm^2]	2.39	2.39	2.39
Ultimate bond stress τ_f	[N/mm^2]	0.0	1.2	2.39
Slip$_{\tau_{max}}$ S$_1$	[mm]	0.022	0.022	0.022
Slip$_{\tau_f}$ S$_2$	[mm]	0.706	0.706	0.706

Table 5.8: Mechanical properties of bonds - B - 5, 8 and 9

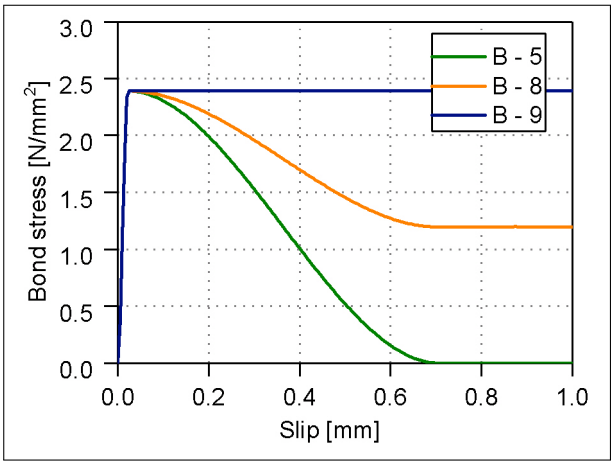

Figure 5.18: Bond laws - B - 5, 8 and 9

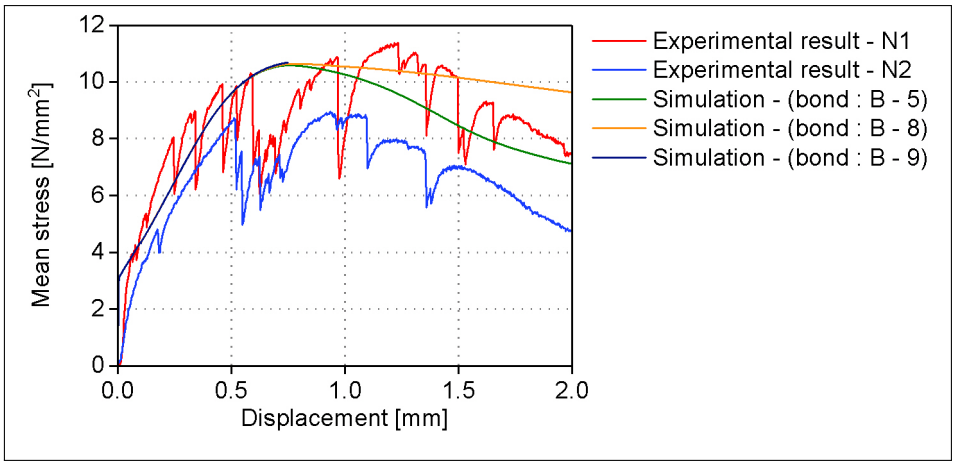

Figure 5.19: Mean stress - displacement results - bond laws - B - 5, 8 and 9

From the results shown in Fig. 5.19, it is observed that the arrangement of total responses of specimens is following the changes applied to the bond laws. These changes in bond laws refer to the softening phase and residual stresses, while the bond strength and initial slopes are kept the same in all three applied bond laws. Thus, the simulations representing dumbbell specimens' responses are also varied from reference simulation in the softening stage. However, all three simulations present the same path for elastic and strain-hardening stages. In the presented results, it is observed that the utilization of bond law with lower residual stress leads to a steep decrease of stresses softening phase compare to model with higher residual stress. The newly developed numerical model stopped the model's analysis with plastic bond laws at the end of the hardening phase and could not reach the convergence even with much lower load steps.

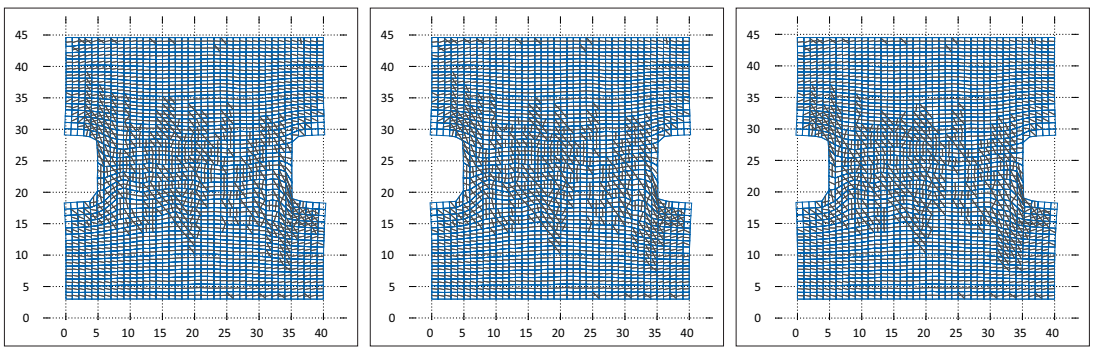

(a) B - 5 (b) B - 8 (c) B - 9

Figure 5.20: Crack pattern results - bond laws - B - 5, 8 and 9 - $u = 0.76\,\text{mm}$ (displacements scaled by factor 10)

Crack patterns for enumerated simulations within three different bond laws at the same loading step, are shown in Fig. 5.20 whereas following the same arrangements as shown in Fig. 5.9. The chosen load step is the hardening phase's endpoint and corresponds to the peak of the response curve. It is observed that the crack patterns are mostly the same and slightly different in a couple of matrix elements. This can be explained by this fact that based on the total response results shown in Fig. 5.19, all the three simulations experience the same paths and values for elastic and hardening phase and basically response the same in these stages. Since the reference load step corresponds to the highest response and they are mostly in the same conditions regarding crack formation and distribution of stresses in elements.

In Fig. 5.21, fiber stresses and bond stresses are shown for each mentioned three simulations within three different bond laws at the same prescribed displacements loading condition. As it is explained for the crack patterns, the models experience the same elastic and hardening phase and have mostly the same crack patterns, see Figs. 5.20and 5.19. Since all the three mentioned models have the same total response and crack patterns at the reference load step, the fiber stresses and bond stresses are expected to be the same.The results are shown in Fig. 5.20 prove this theory. In the result contours for all three conditions, the highest fibers stresses, almost equal to fiber strength, are observed in the fibers located in the notched area. Thus, the highest bond stress, equal to bond strength, are observed in corresponding bond elements.

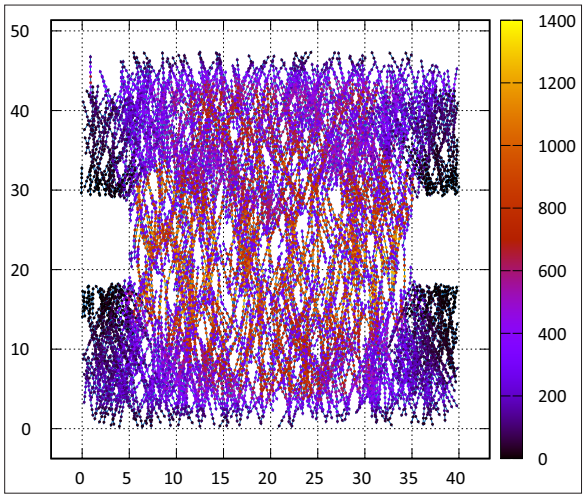

(a) Fiber stress in N/mm^2 , B - 5

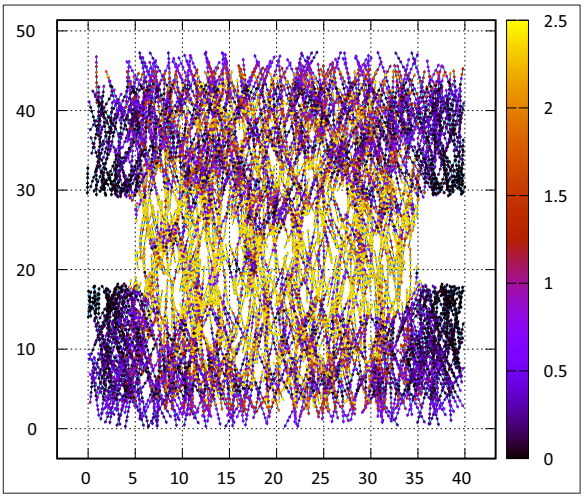

(b) Bond stress in N/mm^2 , B - 5

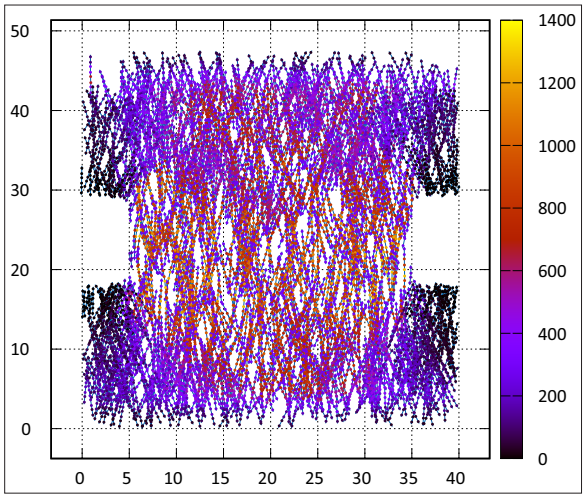

(c) Fiber stress in N/mm^2 , B - 8

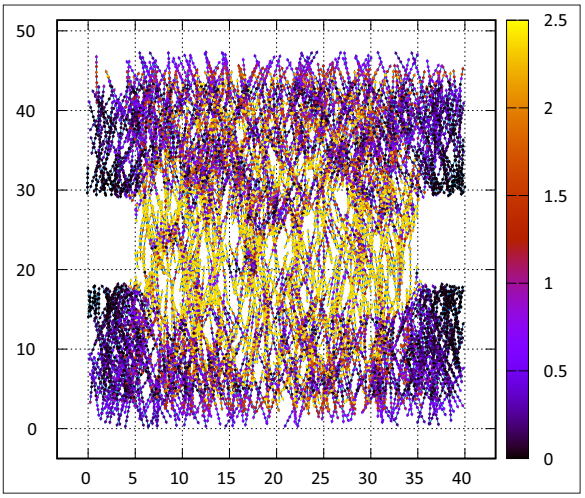

(d) Bond stress in N/mm^2 , B - 8

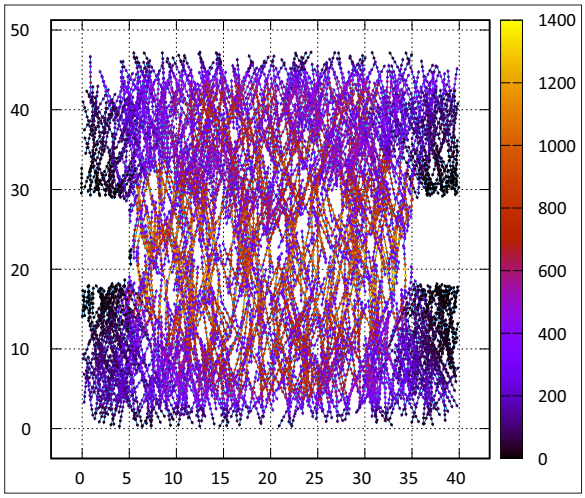

(e) Fiber stress in N/mm^2 , B - 9

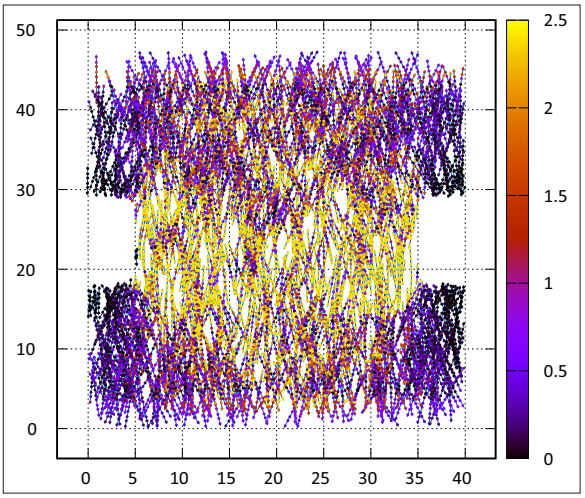

(f) Bond stress in N/mm^2 , B - 9

Figure 5.21: Fiber stresses and bond stresses - bond laws - B - 5, 8 and 9 - $u = 0.76\,\text{mm}$ (displacements scaled by factor 10)

5.3.2 Mesh sensitivity in matrix elements

Continuum elements in the reference model are SDA quad elements with dimension of $1\,\text{mm}x1\,\text{mm}$. In this step of parameter studies, each of these SDA elements are divided to four 2D elements with dimension of $0.5\,\text{mm}x0.5\,\text{mm}$ to study the effect of continuum element size in total response of specimens under tension quasi-static loading condition. It should be mentioned that the decrease of mesh size of matrix elements from $1\,\text{mm}x1\,\text{mm}$ to $0.5\,\text{mm}x0.5\,\text{mm}$ increases the degrees of freedom of simulation from 26 073 to 30 753. Besides, model with smaller matrix mesh size needs smaller load steps for achieving the convergence in analysis. These two changes increase the time of computation from 130 959 second to 359 513 second which is a factor of 2.7.

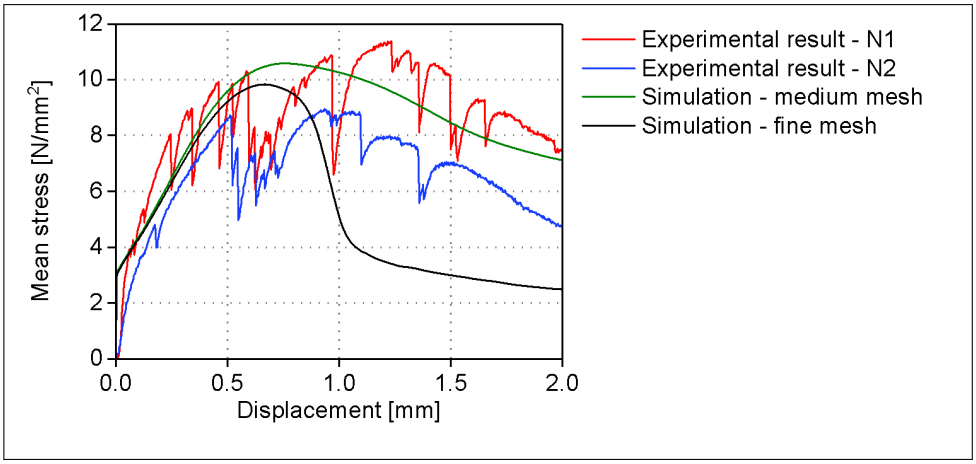

Figure 5.22: Mean stress - displacement results - effect of mesh sensitivity of matrix elements

From the results shown in Fig. 5.22, it is observed that the finer mesh model has less stiffness compare to the coarser mesh model. A sharp decrease of mean stress is seen after the hardening phase's peak in the model with fine mesh. Generally, it is expected that changes in the discretization of matrix elements should not have a significant effect on the softening path. Thus, in the softening path, the propagation of cracks is stopped, and crack localization is started, so SDA elements' contribution is decreased in this stage, and fibers are highly contributing to load-bearing.

Several items concerning the comparison between results related to reference simulation and simulation with finer mesh for matrix element should be considered as follows:

- Dissipated crack energy might have mesh dependency in case all elements are cracked, related case studies are discussed in Section. 4.4.2. On the other hand,

it should be noted that smaller elements have less crack width due to the same specimen elongation.

- The fiber discretization is not refined for model with finer matrix mesh with regards to large computational effort.
- Finer discretization generally leads to softer response, but this is very pronounced in this case and indicates a mesh dependency regarding the strain softening range.

These items need further research which currently exceed the scope of the present work. Respective conclusions are basically assumed to be still valid but maybe subject to more precise specifications.

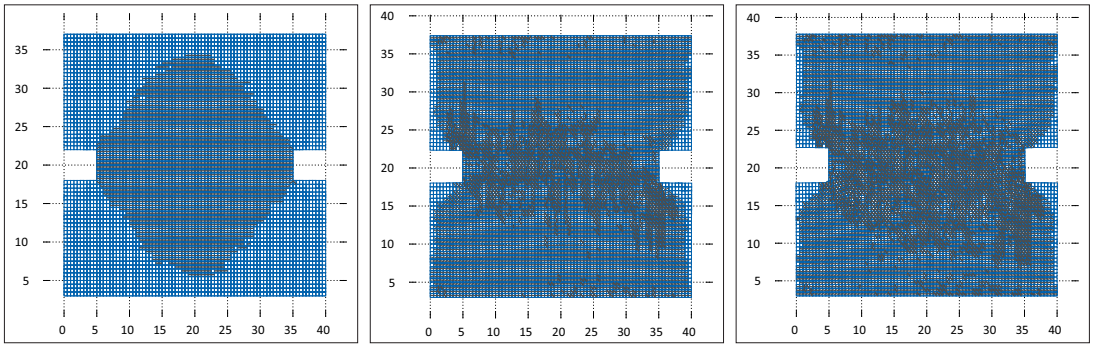

(a) $u = 0.01\,\text{mm}$ (b) $u = 0.38\,\text{mm}$ (c) $u = 0.76\,\text{mm}$

Figure 5.23: Crack pattern results - effect of matrix element size - element size $= 0.5\,\text{mm}$ (displacements scaled by factor 1)

The crack patterns on the deformed mesh geometry for three prescribed displacements are shown in Fig. 5.23. The presented crack pattern in Fig. 5.23(c) for $u = 0.76\,\text{mm}$, corresponds to the peak of total response in reference simulation, Fig. 5.23(b) shows the results in halfway of hardening phase of reference model, $u = 0.38\,\text{mm}$ and Fig. 5.23(a) is related to state shortly after loading is started $u = 0.01\,\text{mm}$.

The crack patterns presented in Fig. 5.23, following the same arrangements as shown in Fig. 5.8. By comparing the crack patterns shown in Fig. 5.12, related to the reference model, with Fig. 5.23, more crack elements are observed in the notched area and both supports in the model with the smaller size of the matrix than the reference model when the applied load is increasing.

Fiber stresses and bond stresses are shown for the enumerated three prescribed displacements in Fig. 5.24. Figs. 5.24(a,b) show the stage shortly after loading is started, small values are computed for stresses in fiber and bond elements. The highest values of stresses belong to the fibers in the center of the notched model, this corresponds the crack pattern shows in Fig. 5.23(a) whereby $u = 0.01\,\text{mm}$. Figs. 5.24(c,d) show the stage corresponding to the halfway of hardening phase in reference model whereby $u = 0.76\,\text{mm}$. In this stage, several fibers in the mid part of the specimen experience stress almost equal to the tensile strength of the fiber, and the stresses in the corresponding bond elements also have high values equal to bond strength. The stress pattern in this stage is also comparable to the crack pattern. Figs. 5.24(e,f) show the stage end of hardening phase whereby $u = 1.56\,\text{mm}$. It is observed that more fibers, which are located in the center of the model, reaching the limited strength compared to the previous level. This stage is shortly after the softening stage is started.

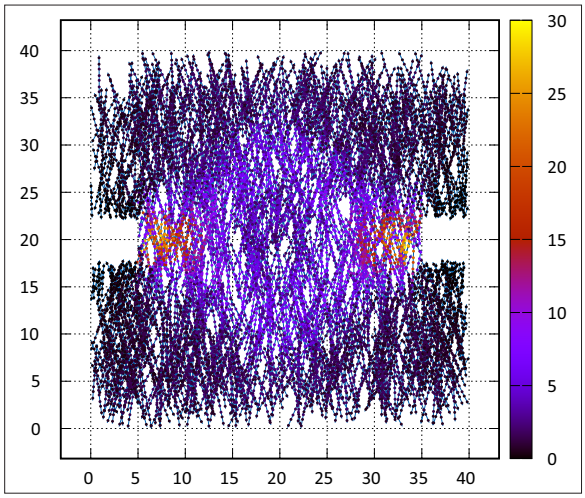

(a) Fiber stress in N/mm^2 , $u = 0.01$ mm

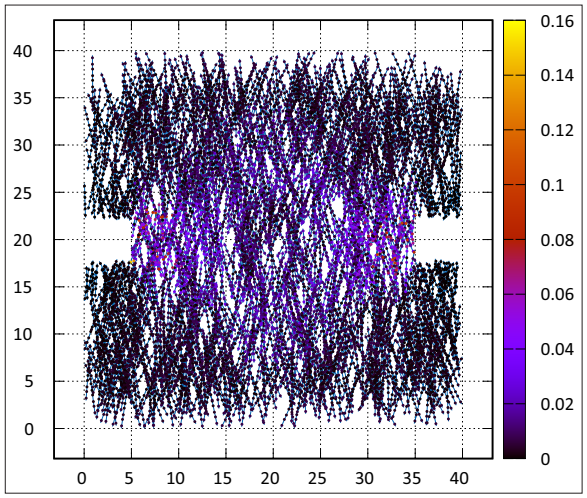

(b) Bond stress in N/mm^2 , $u = 0.01$ mm

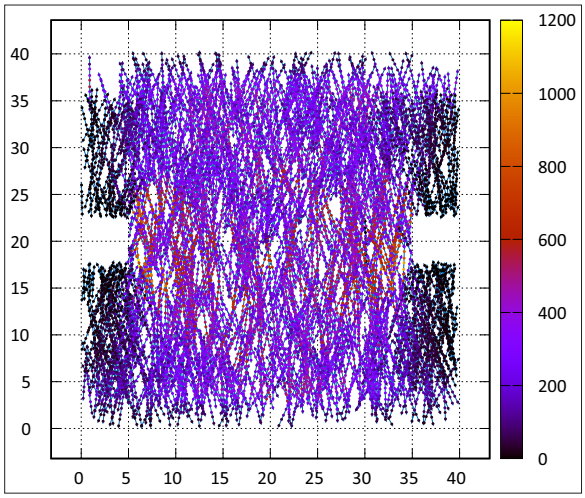

(c) Fiber stress in N/mm^2 , $u = 0.38$ mm

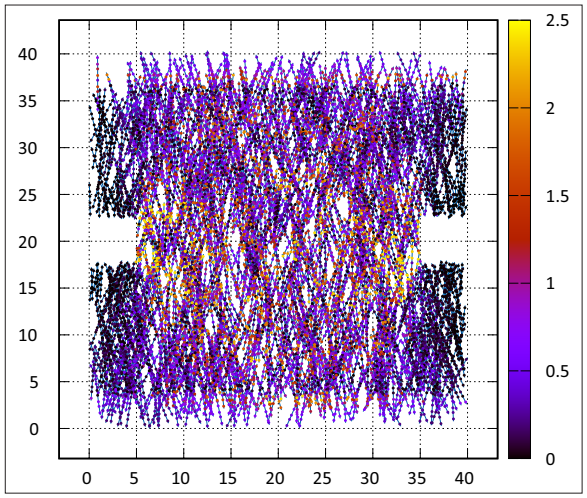

(d) Bond stress in N/mm^2 , $u = 0.38$ mm

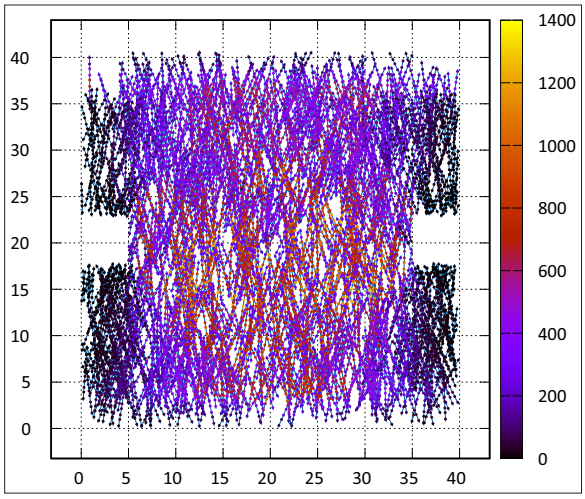

(e) Fiber stress in N/mm^2 , $u = 0.76$ mm

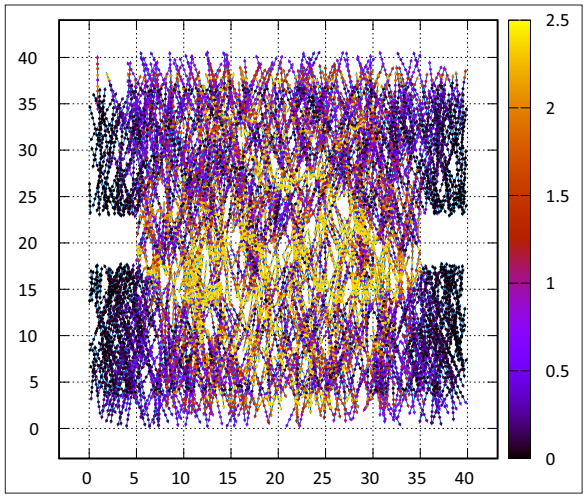

(f) Bond stress in N/mm^2 , $u = 0.76$ mm

Figure 5.24: Fiber stresses and bond stresses - effect of matrix element size - element size $= 0.5$ mm (displacements scaled by factor 1)

5.3.3 The effect of concrete tensile strength

Two new models are used to study the effect of concrete tensile strength. The value of tensile strength, which is assigned to continuum elements in reference simulation, is $f_{ct} = 3.8\,\mathrm{N/mm^2}$, whereas this parameter in the new models is assumed to be 3.0 and $4.6\,\mathrm{N/mm^2}$.

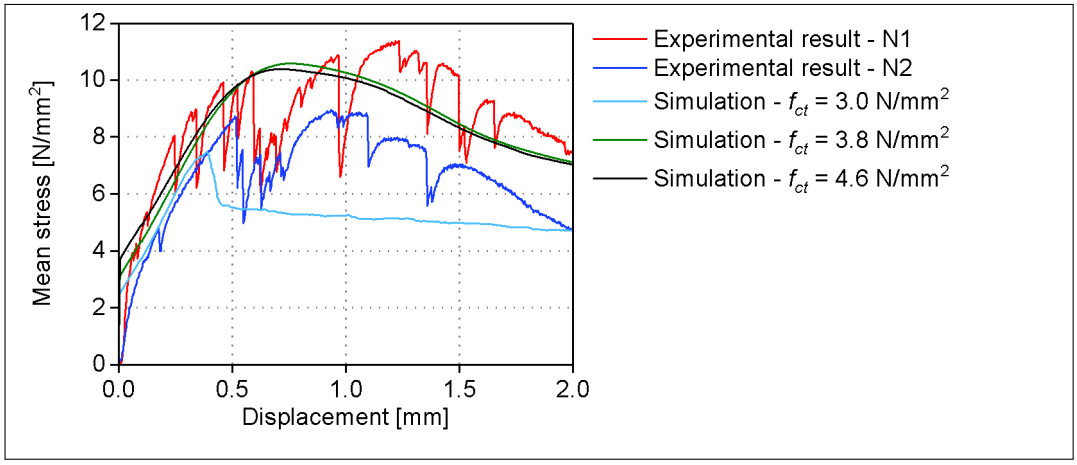

(a) Overall range

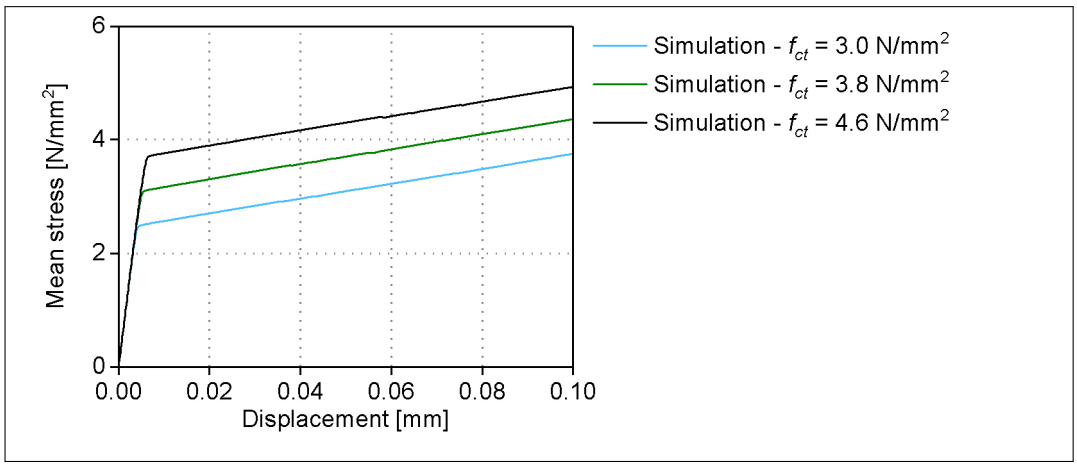

(b) Initial range

Figure 5.25: Mean stress - displacement results - effect of concrete tensile strength; a) overall range, b) initial range

From the results shown in Fig. 5.25(b), it is observed that peak of the response curves in elastic phase is increased by the concrete tensile strength increase, as expected, whereas this peak is still higher than the concrete tensile strength since it is a total response of the inhomogeneous composite. The model with lower concrete tensile strength has a shorter hardening phase compare to the reference model. There is a sharp fall after the peak, which is continued with a slight decrease in the model with the lowest concrete

tensile strength. This sudden drop can be explained by this fact that assigning lower tensile strength leads to cracking of a large number of matrix elements simultaneously with the lower tensile strength limit. Thus, the model is stabilized later with the continuation of applied loading. Thus, the model with higher concrete tensile strength is slightly higher than the reference model in the elastic and hardening phase while the reference model is stiffer in the softening phase, see Fig. 5.25(a). Since this parameter is related to the SDA elements, no significant changes are expected in the softening stage.

5.3.4 The effect of concrete fracture energy

In this section, the effect of concrete fracture energy is studied. The continuum's fracture energy is computed with Eqs. 4.82 and is equal to the area under the loading stage shown in Fig. 4.3. Four new simulations are performed to see this parameter's effect on the total response of specimen under quasi-static tensile loading.

The value of fracture energy which is assigned to the continuum elements in reference simulation is $G_f = 1e^{-}1\,\mathrm{N/mm}$, whereas this value is multiplied by factors : 2, 0.5, 0.05, 0.005 for parameter studies. As it was explained in chapter 2, concrete must develop multiple cracks to perform the desired strain-hardening behavior of SHCC. To this aim, high strength concrete with low crack energy is recommended. However, by considering the curve results for simulation within very low assigned fracture energy, shown in Fig. 5.26, a sudden drop is observed when the crack bridging stage is started, and simulation will be diverged shortly without fulfilling the stain-hardening behavior of SHCC perfectly. It can be explained with the fact that lots of continuum elements are cracked at the same time due to the very low fracture energy, and this leads to an unrealistic behavior, which causes a sudden drop in the start point of the hardening phase.

Thus, the resulting curve for a small value of fracture energy ($G_f = 5e^{-}4\,\mathrm{N/mm}$) does not even reach the tensile strength of concrete in the elastic stage of the total response. The model will be stabilized later on by redistribution of stresses into the overall elements, but the simulations with very low fracture energy diverged at a small hardening phase.

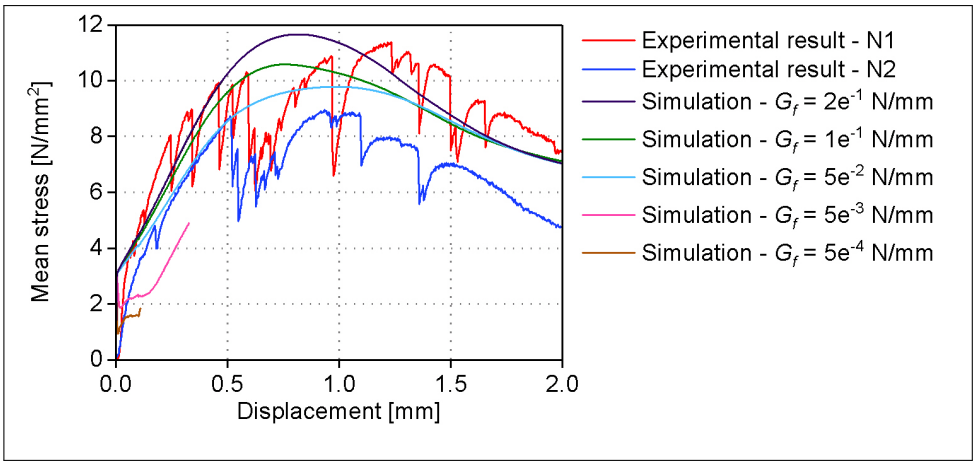

(a) Overall range

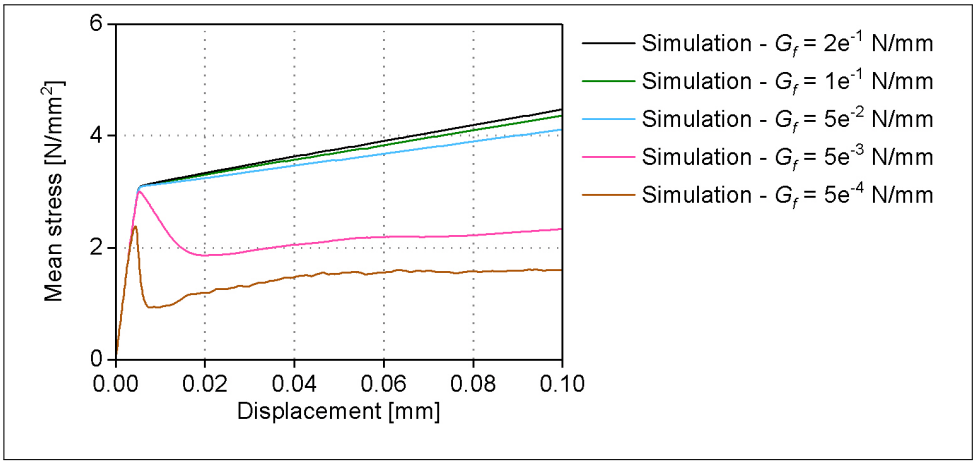

(b) Initial range

Figure 5.26: Mean stress - displacement results - effect of concrete fracture energy; a) overall range, b) initial range

On the other hand, simulations with crack energy equal to ($G_f = 5e^{-}2\,\mathrm{N/mm}$) can pass the whole path of three stages of SHCC behavior, see Fig. 5.26. It is observed that in model with higher crack energy than the reference value, ($G_f = 2e^{-}1\,\mathrm{N/mm}$), the curve has a higher peak point in total response while the corresponding displacement load to this peak is also larger than similar parameter in the reference model. The post-peak path of all three models with higher value than ($G_f = 5e^{-}2\,\mathrm{N/mm}$), will meet each other in same point at the end of simulation displacement $= 2.0\,\mathrm{mm}$. Since this parameter affects crack formation in SDA elements, it does not have a significant effect on the softening path.

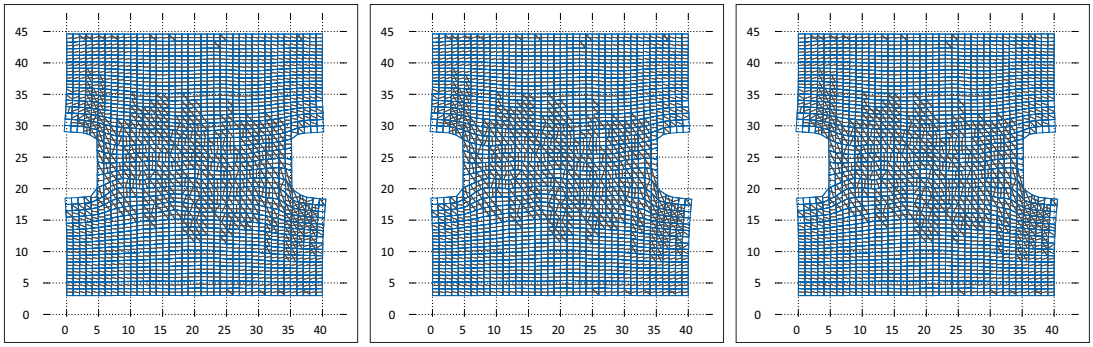

(a) $G_f = 2e^{-}1N/mm$ (b) $G_f = 1e^{-}1N/mm$ (c) $G_f = 5e^{-}2N/mm$

Figure 5.27: Crack pattern results - effect of concrete fracture energy - $u = 0.76\,\text{mm}$(displacements scaled by factor 10)

The crack patterns are shown in Fig. 5.27 following the same arrangements, as shown in Fig. 5.9 whereas the interpretation of this simulation property has also been discussed in Section 4.2.5. Crack patterns for enumerated simulations within three different assigned crack energy, i.e., $G_f = 2e^{-}1{,}1e^{-}1{,}5e^{-}2\,\text{N/mm}$, are mostly the same since the selected load step is the endpoint of hardening phase for all three selected simulations whereas the crack localization begins.

In Fig. 5.28, fiber stresses and bond stresses are shown for each mentioned three simulations within three different assigned fracture energy at the same prescribed displacements loading condition. The fibers and bond elements located in the notched area have reached their maximum values equal to their strength. Moreover, it is observed that the stresses in the fibers and bond elements are mostly the same concerning the distribution and the values of these parameters. Thus, the differences in the total responses shown in Fig. 5.26 can be explained with this fact that by increasing the fracture energy of the matrix elements, the contribution of the matrix will be increased in load-bearing and leads to increase of total response.

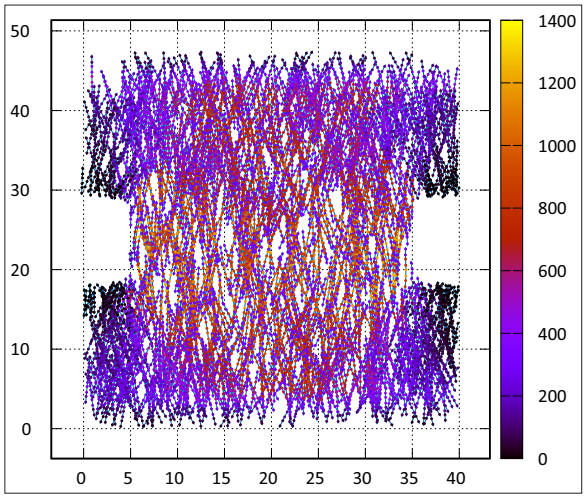

(a) Fiber stress in N/mm^2 , $G_f = 2e^{-}1N/mm$

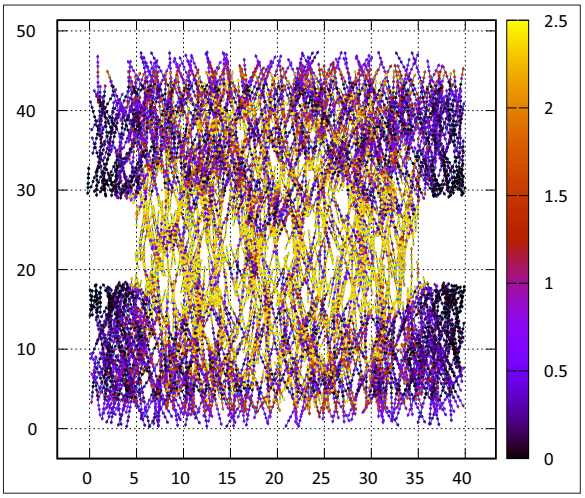

(b) Bond stress in N/mm^2 , $G_f = 2e^{-}1N/mm$

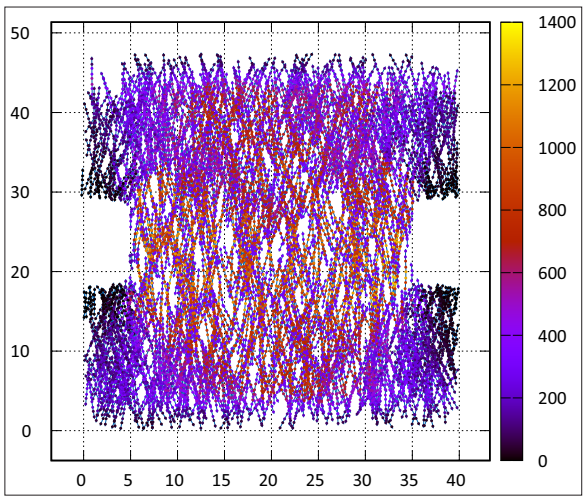

(c) Fiber stress in N/mm^2 , $G_f = 1e^{-}1N/mm$

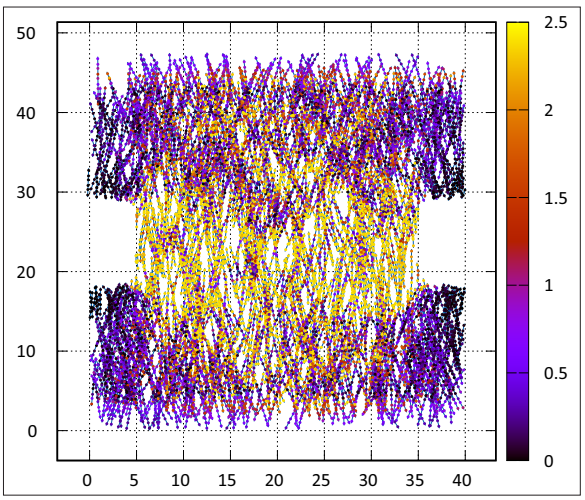

(d) Bond stress in N/mm^2 , $G_f = 1e^{-}1N/mm$

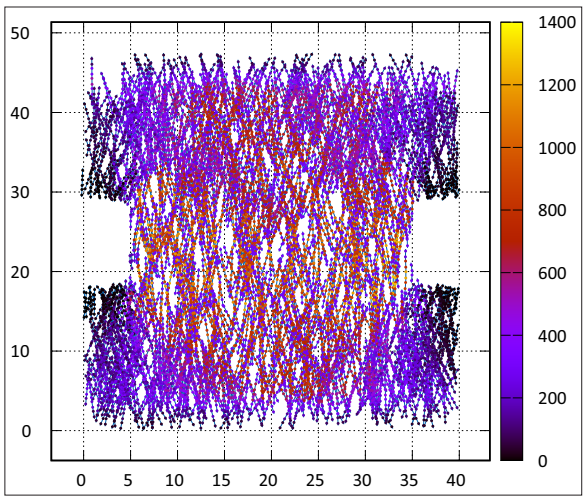

(e) Fiber stress in N/mm^2 , $G_f = 5e^{-}2N/mm$

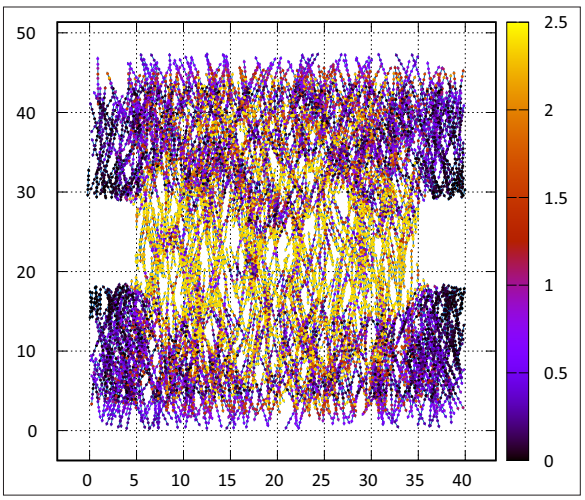

(f) Bond stress in N/mm^2 , $G_f = 5e^{-}2N/mm$

Figure 5.28: Fiber stresses and bond stresses - effect of concrete fracture energy - $u = 0.76\,\text{mm}$ (displacements scaled by factor 10)

5.3.5 The effect of Young's modulus of concrete

Two new simulations are performed to see the influence of Young's modulus of concrete on the total response of specimen under quasi-static tensile loading. The value of Young's modulus of concrete assigned to the continuum elements in reference simulation is $E = 29000\,\mathrm{N/mm^2}$, whereas this value is multiplied by factors: 2, 0.5 for parameter studies.

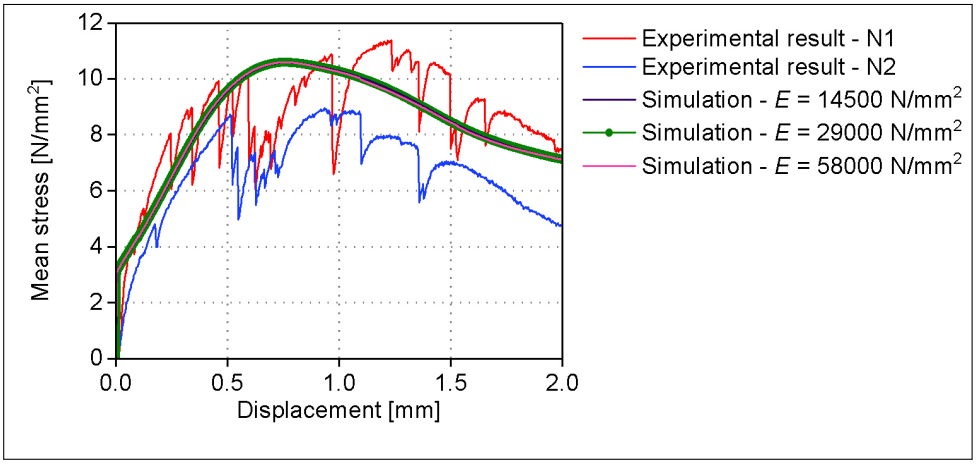

(a) Overall range

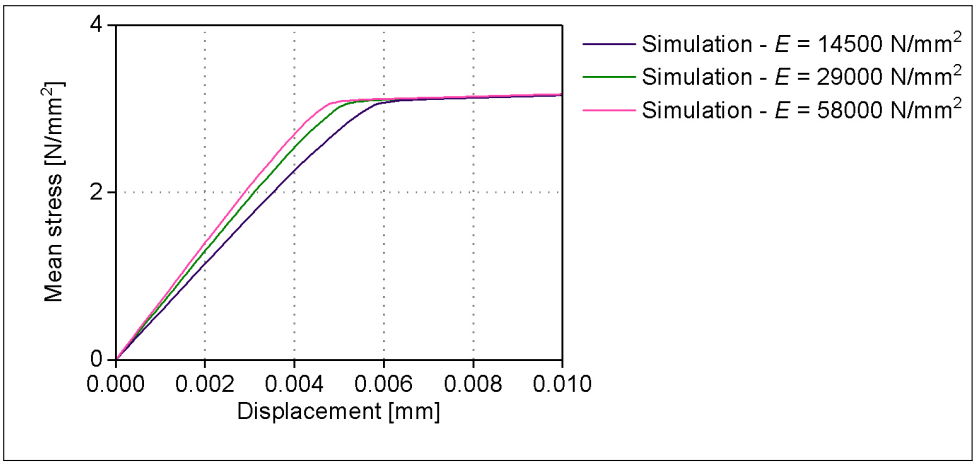

(b) Initial range

Figure 5.29: Mean stress - displacement results - effect of Young's modulus of concrete; a) overall range, b) initial range

From the results shown in Fig. 5.29, it is observed that a high range of variation of this parameter will cause slight changes in the elastic stage of response, whereas the initial slope of the curve is sharper for higher Young's modulus of concrete as expected. Based on the results shown in Fig. 5.29(a), since all graphs reach the same point shortly after

starting the strain-hardening stage and following the same path, it can be said that this parameter does not have a significant effect on the total response of specimen.

5.3.6 The effect of tensile strength of fiber

Two new simulations are performed to study the influence of tensile strength of fiber on the total response of specimen under quasi-static tensile loading. The value of tensile strength of fiber assigned to the fiber elements in reference simulation is $F_f = 1600\,\mathrm{N/mm^2}$, whereas this value is multiplied by factors: 2, 0.5 for parameter studies.

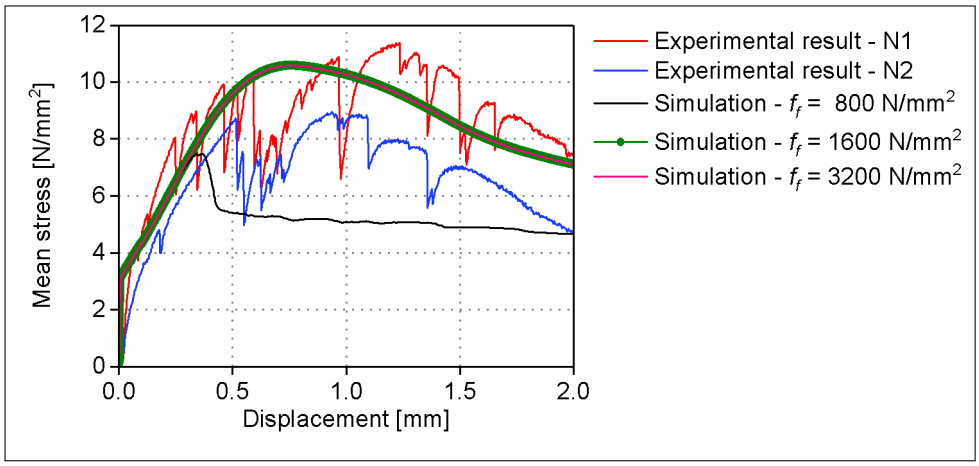

Figure 5.30: Mean stress - displacement results - effect of ultimate fiber strength

From the graph results shown in Fig. 5.30, it is observed that for the higher range of tensile strength of fiber, the total response curve lays on the same path as the reference curve. However, in the case of the smaller tensile strength of fibers, the strain-hardening phase is shorter. This graph has a lower peak while it has the same elastic phase and following the same slope for the hardening phase before the immature softening stage has started. In the developed program, the fiber element will be eliminated from simulation when the truss element's stress exceeds the value corresponding to the fiber tensile strength. In analysis with lower tensile strength for fibers, several fibers will fail simultaneously, and this can explain the short hardening phase and sudden drop in the start point of the softening stage, see Fig. 5.30. Since the full pullout is not modeled in the model, and the bond elements will stay active in the model even in higher deformation conditions, the analysis reaches somewhat the plateau.

5.3.7 The effect of fiber volume fraction

In this section, the influence of fiber volume fraction is investigated by comparing two new models with the reference model. The volume fraction of fiber in reference model is 2%; hence two new models with volume fraction equal to 1% are used to see the effect of this parameter in the total response of specimen under quasi-static tensile loading. Two approaches are common to investigate this parameter effect, i.e., reducing the number of fibers, considering this effect as a factor applies to the fiber section area. Thus, in the first model, fibers have the same cross-section area as the reference model; however, the number of fibers is reduced by the factor of 0.5 compare to the number of fibers in the reference model. In the second model, the number of fibers is kept the same as the reference model, while the fibers section area is decreased by the factor of 0.5 compare to the fibers section area in the reference model. It should be stated that no changes are applied to the bond laws of all three models.

From the graph results shown in Fig. 5.31, it is observed that all three simulations have the same elastic path, and models with lower volume fraction have shorter strain-hardening phases. However, in the first model with fewer fibers, the strain-hardening phase, and the softening stage are mostly scaled with the same reduction factor applied to volume fraction. This means that the total response peak is reduced by the factor of 2 compare to reference simulation graph.

On the other hand, the second model with a reduced section area starts its crack-bridging stage with a sharper slope; however, this model ends this stage with a sudden drop. Later, The model will be stable again, and the analysis reaches the plateau fairly.

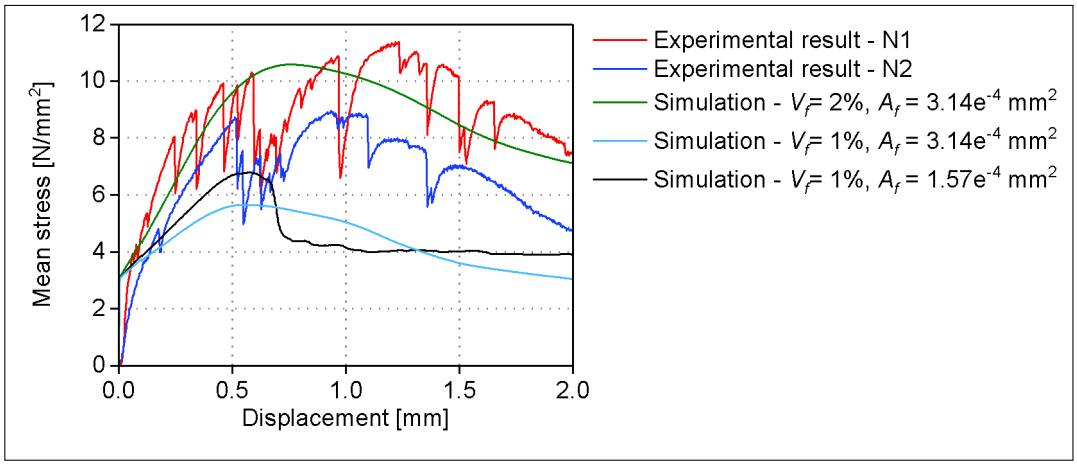

Figure 5.31: Mean stress - displacement results - effect of fiber volume fraction

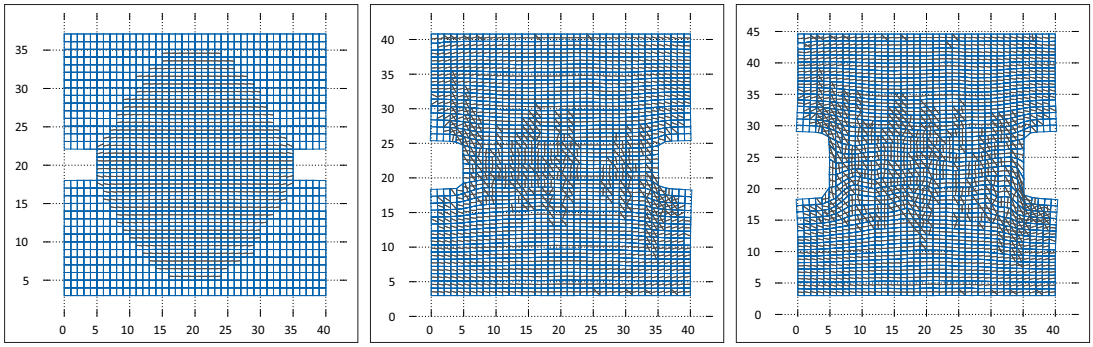

(a) $u = 0.01\,\text{mm}$ (b) $u = 0.38\,\text{mm}$ (c) $u = 0.76\,\text{mm}$

Figure 5.32: Crack pattern results - effect of fiber volume fraction - $V_f = 2\%, A_f = 3.14e^{-}4mm^2$ (displacements scaled by factor 10)

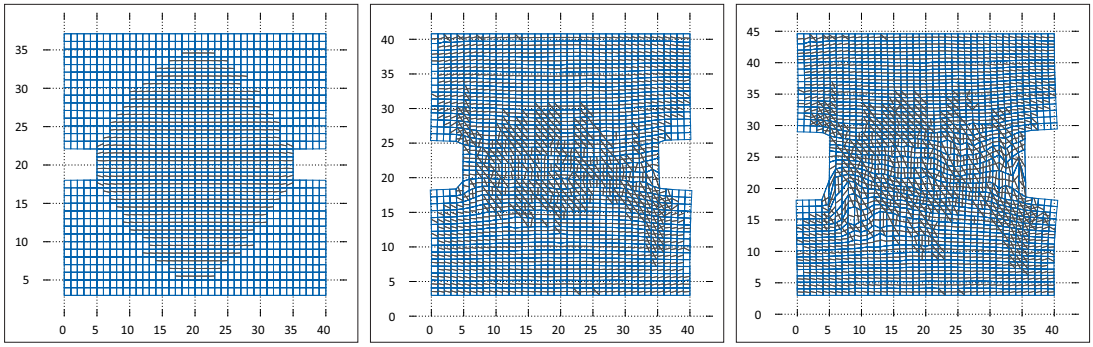

(a) $u = 0.01\,\text{mm}$ (b) $u = 0.38\,\text{mm}$ (c) $u = 0.76\,\text{mm}$

Figure 5.33: Crack pattern results - effect of fiber volume fraction - $V_f = 1\%, A_f = 3.14e^{-}4mm^2$ (displacements scaled by factor 10)

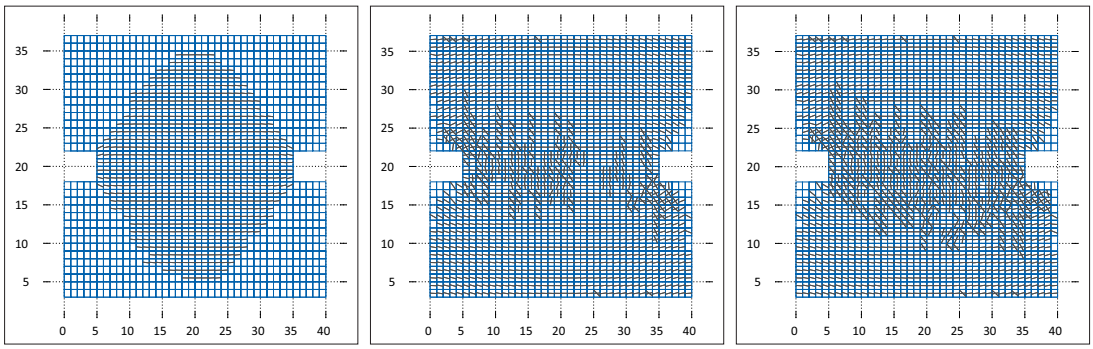

(a) $u = 0.01\,\text{mm}$ (b) $u = 0.38\,\text{mm}$ (c) $u = 0.76\,\text{mm}$

Figure 5.34: Crack pattern results - effect of fiber volume fraction - $V_f = 1\%, A_f = 1.57e^{-}4mm^2$ (displacements scaled by factor 0.1)

The crack patterns for all three models are shown in Figs. 5.32, 5.33 and 5.34 following the same arrangements shown in Fig. 5.9. The interpretation of this simulation property has also been discussed in Section 4.2.5. By comparing these patterns, it is observed that the first model with the fewer number of fibers experienced more crack at the load step ($u = 0.38\,\text{mm}$), so in the conditions of lack of fiber, the contribution of the matrix in load-bearing will increase, and more cracks are formed. On the other hand, models with the same number of fibers and different fiber volume fractions mostly experience the same crack pattern in the hardening phase.

Fiber stresses and bond stresses are shown in Figs. 5.35 5.36 and 5.37 for each mentioned three simulations at the same prescribed displacements loading condition. It is observed that fibers and bond elements located in the notched area have reached their maximum values equal to their strength. The range of fiber stresses and bond stresses in different loading steps for the model with $V_f = 2\%$ is mostly the same with the model with $V_f = 1\%$ and less number of fibers. However, in model with $V_f = 1\%$ and lower fiber section area, stresses in fibers located in the notched area are at the highest value comparing to all other simulations in parameter studies. Thus, the crack localization is visible in the stress contours in this model's fibers and bonds elements, especially in the last load step. It can be explained by this fact that this model is already in the softening phase at the selected load step.

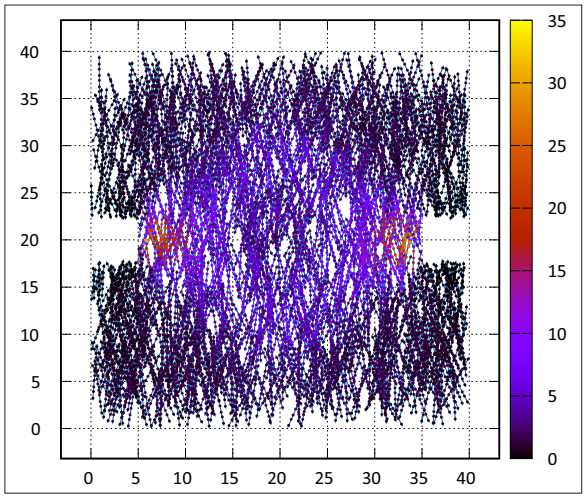

(a) Fiber stress in N/mm^2 , $u = 0.01$ mm

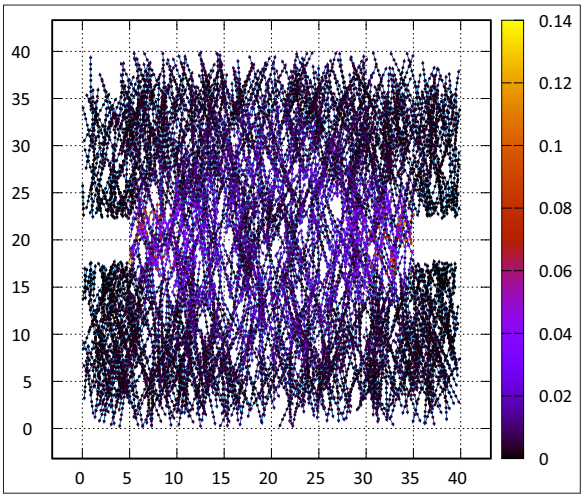

(b) Bond stress in N/mm^2 , $u = 0.01$ mm

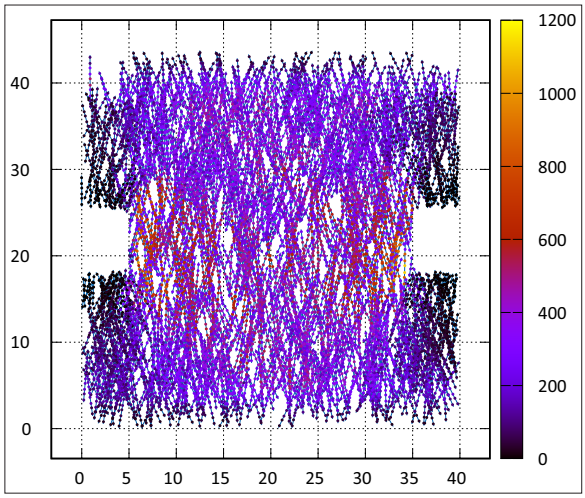

(c) Fiber stress in N/mm^2 , $u = 0.38$ mm

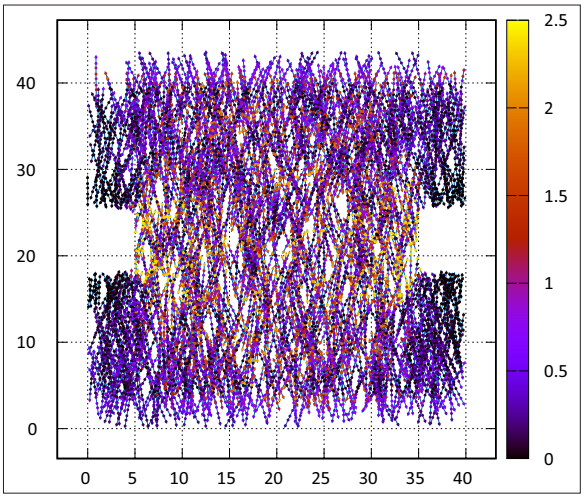

(d) Bond stress in N/mm^2 , $u = 0.38$ mm

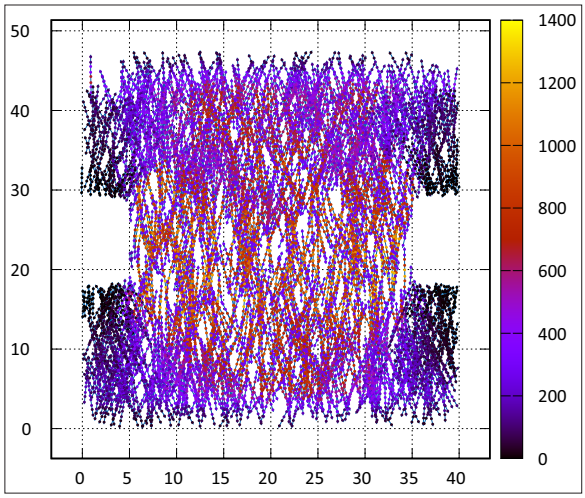

(e) Fiber stress in N/mm^2 , $u = 0.76$ mm

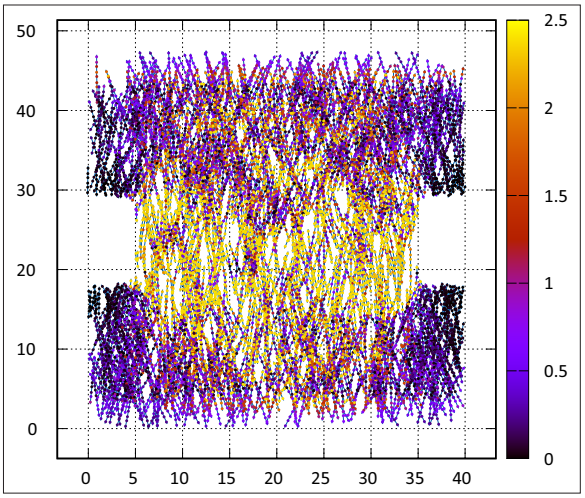

(f) Bond stress in N/mm^2 , $u = 0.76$ mm

Figure 5.35: Fiber stresses and bond stresses - effect of fiber volume fraction - $V_f = 2\%, A_f = 3.14e^{-}4mm^2$ (displacements scaled by factor 10)

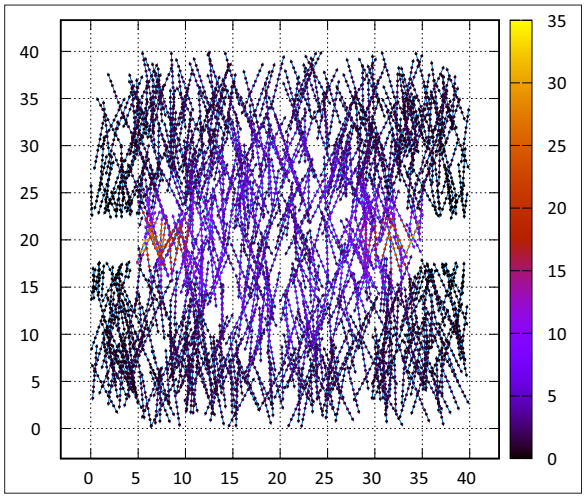

(a) Fiber stress in N/mm^2 , $u = 0.01$ mm

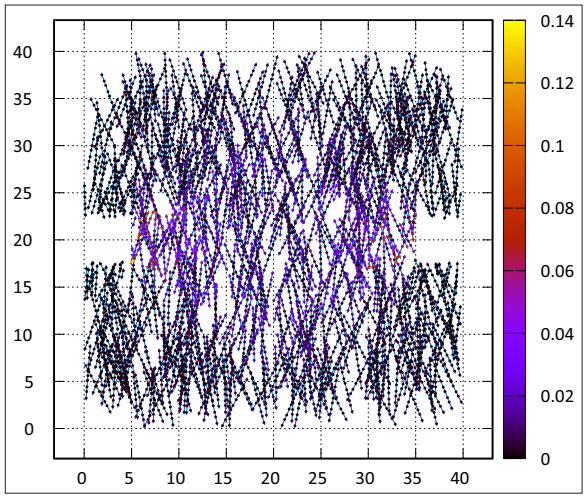

(b) Bond stress in N/mm^2 , $u = 0.01$ mm

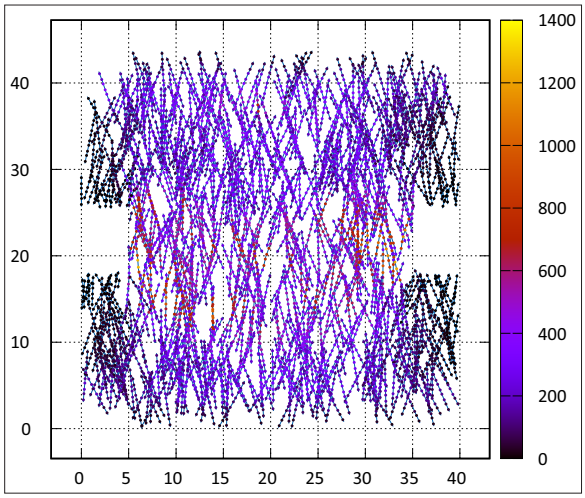

(c) Fiber stress in N/mm^2 , $u = 0.38$ mm

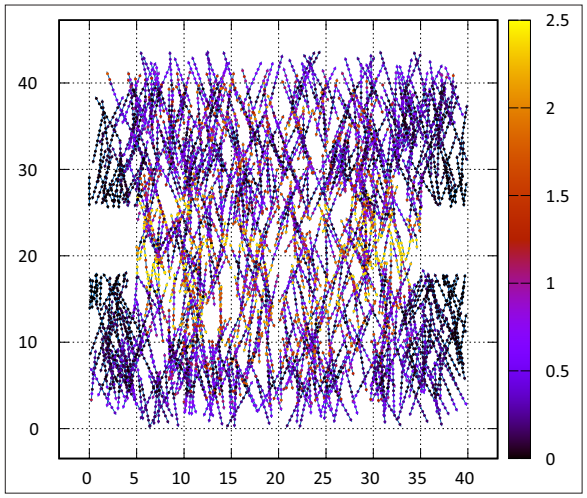

(d) Bond stress in N/mm^2 , $u = 0.38$ mm

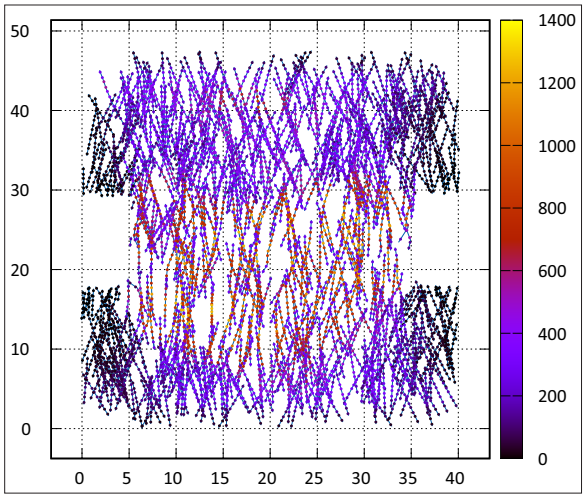

(e) Fiber stress in N/mm^2 , $G_f = 5e^{-}2N/mm$

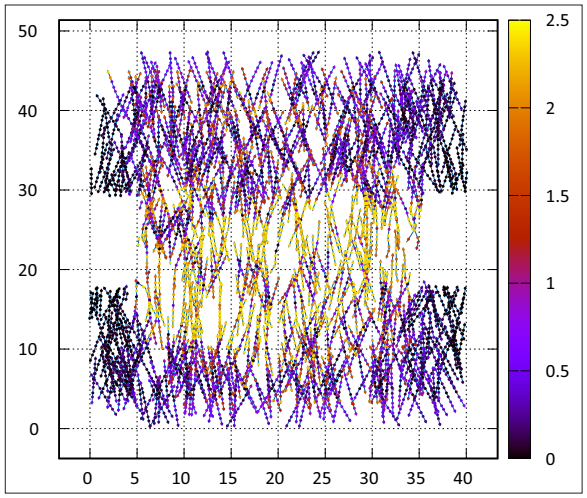

(f) Bond stress in N/mm^2 , $G_f = 5e^{-}2N/mm$

Figure 5.36: Fiber stresses and bond stresses - effect of fiber volume fraction - $V_f = 1\%, A_f = 3.14e^{-}4mm^2$ (displacements scaled by factor 10)

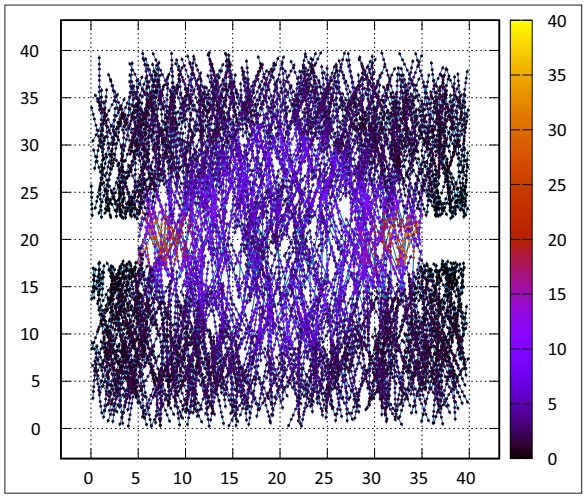

(a) Fiber stress in N/mm^2 , $u = 0.01$ mm

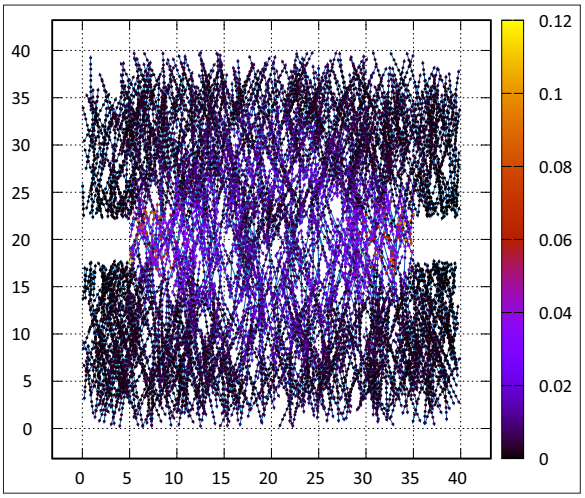

(b) Bond stress in N/mm^2 , $u = 0.01$ mm

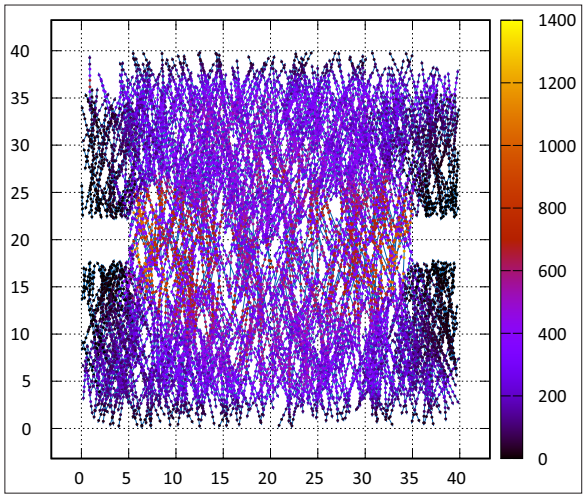

(c) Fiber stress in N/mm^2 , $u = 0.38$ mm

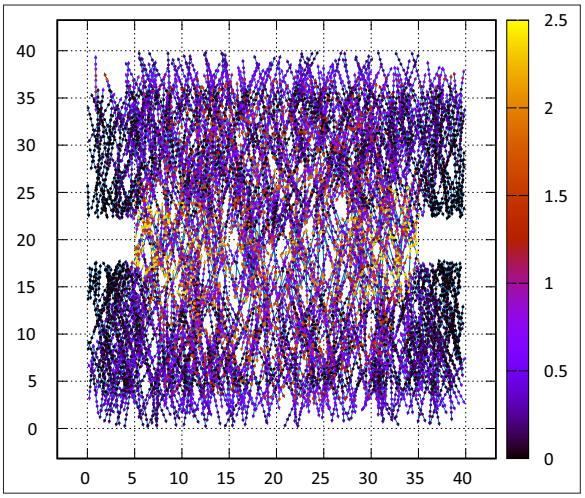

(d) Bond stress in N/mm^2 , $u = 0.38$ mm

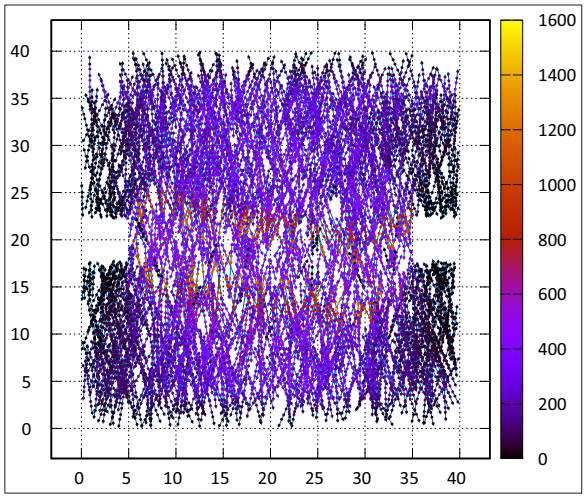

(e) Fiber stress in N/mm^2 , $u = 0.76$ mm

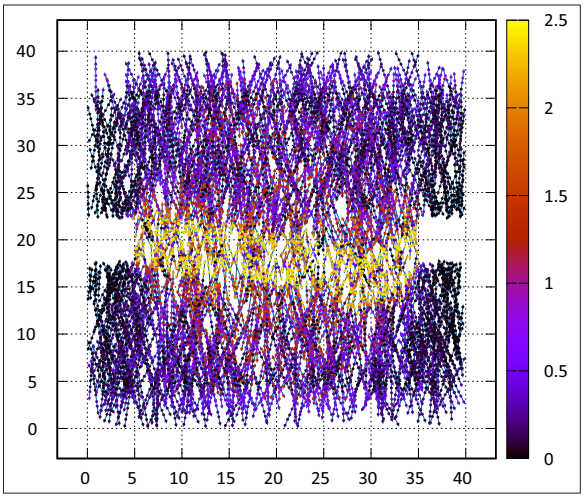

(f) Bond stress in N/mm^2 , $u = 0.76$ mm

Figure 5.37: Fiber stresses and bond stresses - effect of fiber volume fraction - $V_f = 1\%, A_f = 1.57e^{-}4mm^2$ (displacements scaled by factor 0.1)

5.3.8 The effect of considering second crack in matrix elements

In this section, the effect of considering the secondary cracking on the total response of the specimen is studied, as it is explained before, the secondary cracking is constrained by a minimum deviation of 45 degrees compared to primary cracking orientation and expected to form relatively soon. This introduces some bias into a secondary crack orientation, whereas some overall skewness of fiber orientations presumably triggers the overweight with a counterclockwise orientation, see Section 4.2.5. The secondary cracking is not allowed for the new model to investigate the effect on the total response, crack pattern, and distribution of stresses under the same loading condition as the reference model.

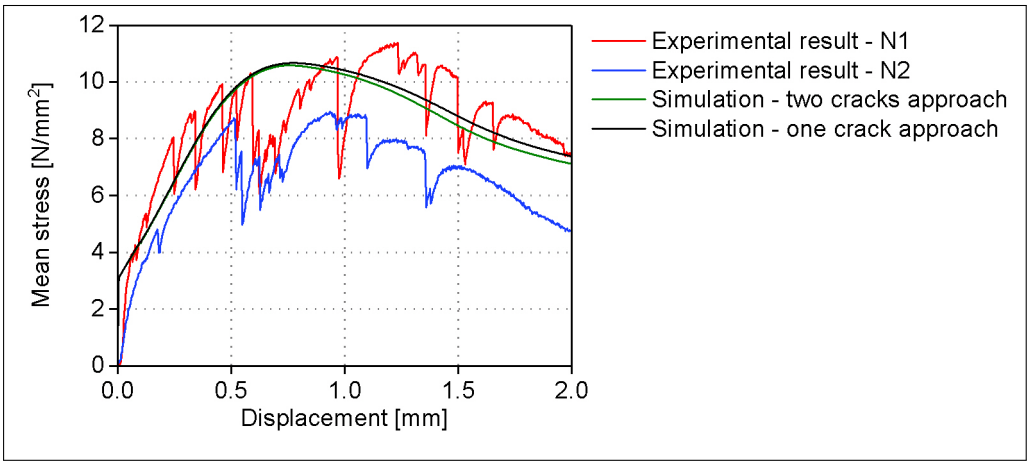

Figure 5.38: Mean stress - displacement results - effect of secondary cracking in matrix elements

From results shown in Fig. 5.38 It is observed that in the model which continuum elements are limited to experience just one crack during the analysis, is slightly stiffer in softening phase and no significant differences in elastic and hardening stages is observed. This can be explained by this fact that the cracks in matrix elements are fixed and stress blocking can occur while the load is increasing. This restriction is visible in crack patterns shown in Fig. 5.40. by comparing these patterns with crack pattern belong to reference model(two cracks are allowed in reference model, see Fig. 5.39), no localization of cracks can be seen in the model crack pattern with one crack in matrix elements, see Fig. 5.40. However, these crack are different concerning the crack width. This can be observed in the fiber and bond stresses presented in Fig. 5.41, which contours show stresses in fibers and bonds elements in notched area reach their

strengh value. By comparing the stress distribution in fiber and bond elements for both models (one/two cracks in matrix element), the contours shown in Fig. 5.13 and Fig. 5.41 are quite similar. This can be explained by this fact that selected load steps belong to elastic and hardening phase and these models show the same behavior in these two phases, see Fig. 5.38.

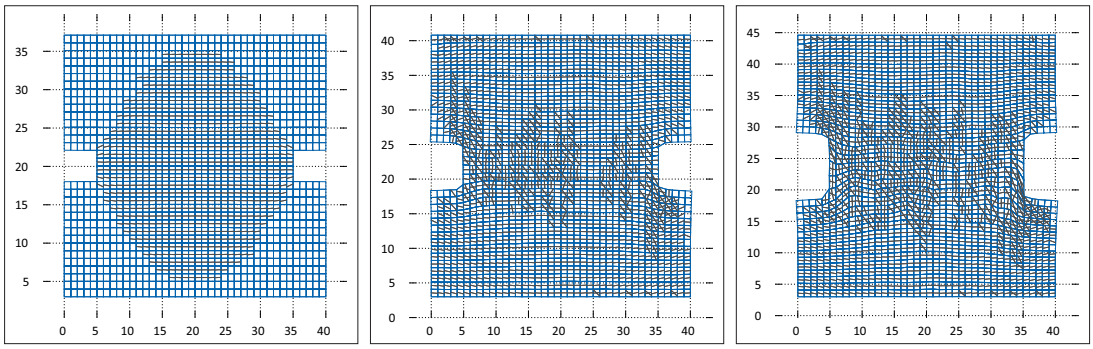

(a) $u = 0.01\,\text{mm}$ (b) $u = 0.38\,\text{mm}$ (c) $u = 0.76\,\text{mm}$

Figure 5.39: Crack pattern results - effect of secondary cracking in matrix elements - two cracks are allowed (displacements scaled by factor 10)

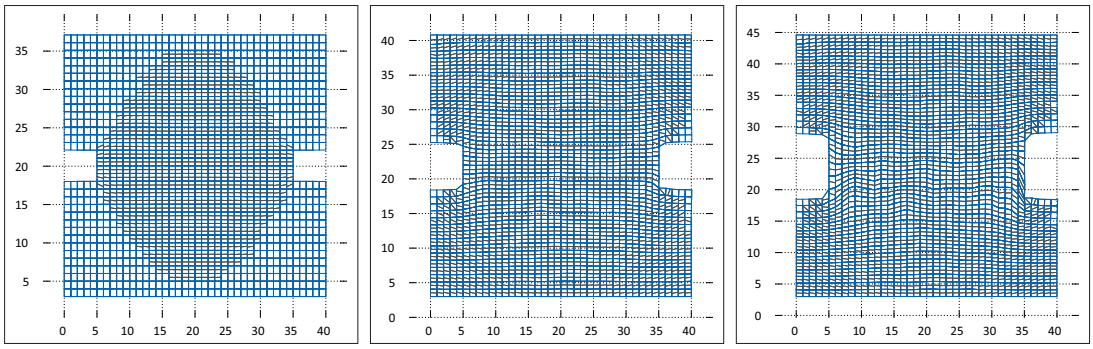

(a) $u = 0.01\,\text{mm}$ (b) $u = 0.38\,\text{mm}$ (c) $u = 0.76\,\text{mm}$

Figure 5.40: Crack pattern results - effect of secondary cracking in matrix elements - one crack is allowed (displacements scaled by factor 10)

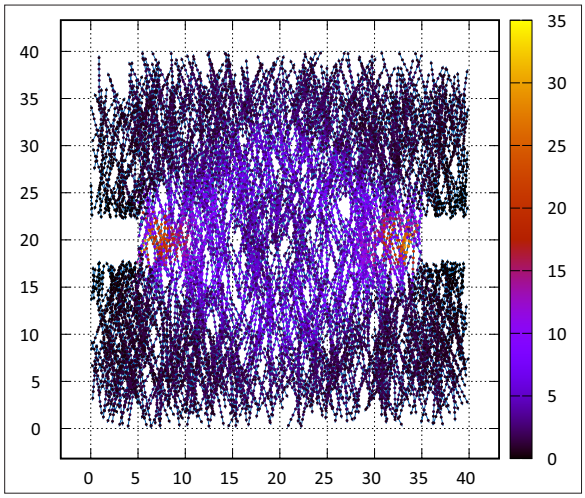

(a) Fiber stress in N/mm^2 , $u = 0.01$ mm

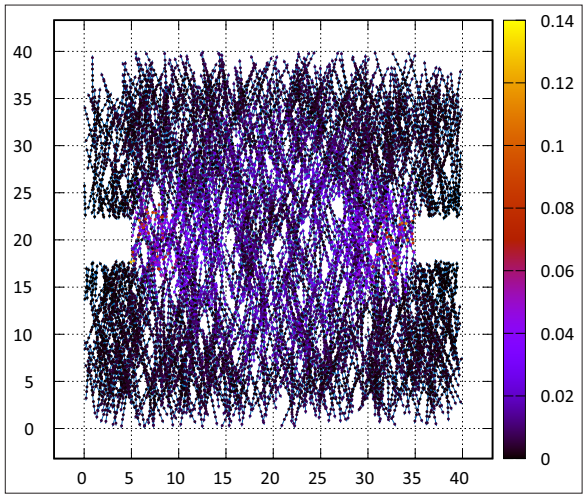

(b) Bond stress in N/mm^2 , $u = 0.01$ mm

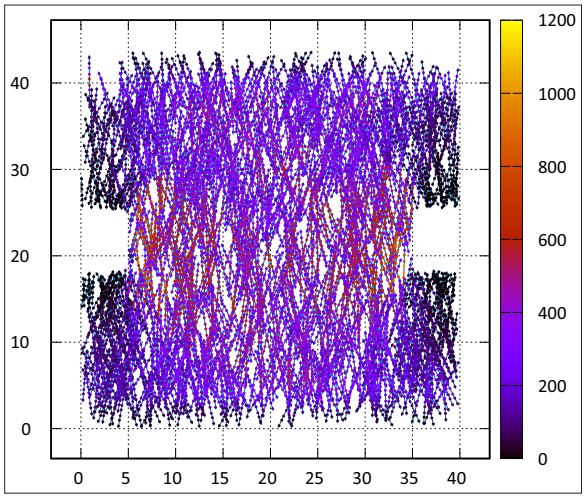

(c) Fiber stress in N/mm^2 , $u = 0.38$ mm

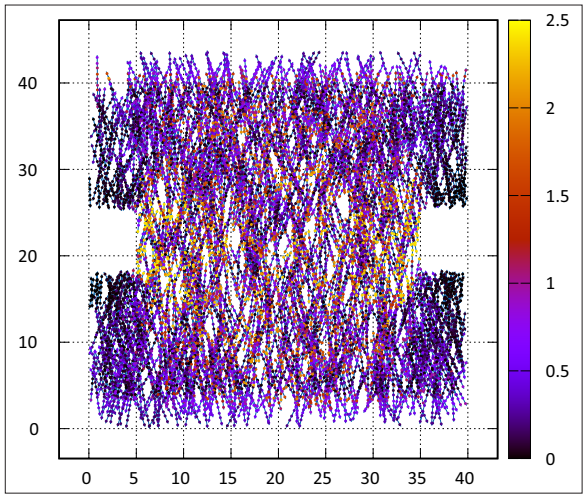

(d) Bond stress in N/mm^2 , $u = 0.38$ mm

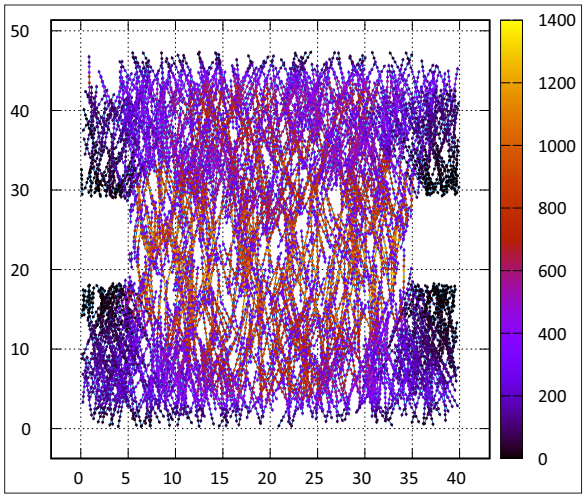

(e) Fiber stress in N/mm^2 , $u = 0.76$ mm

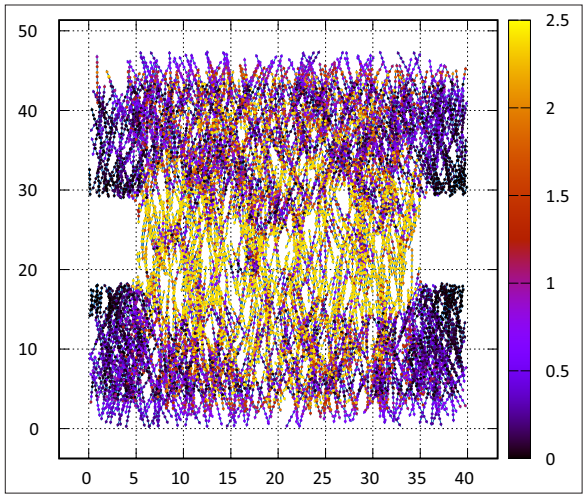

(f) Bond stress in N/mm^2 , $u = 0.76$ mm

Figure 5.41: Fiber stresses and bond stresses - effect of secondary cracking in matrix elements - one crack is allowed (displacements scaled by factor 10)

5.4 CONCLUSION

In this chapter, the simulations of 2D SHCC dumbbell specimens under tensile loading conditions were performed to validate the numerical methods discussed in Chapter 4. The bond law assigned to bond elements was derived from a single-fiber pullout test and explained in detail in Section 2.2.5. Later, it was modified and assigned to the FEM model to provide the desired strain-hardening phase and achieve better agreement with performed experiments published in[114]. This model was used as a reference model, and the total responses of several simulations concerning the effect of different material and structural parameters were investigated.

First, the influence of bond characteristics was studied. It was observed that the total response of large scale specimen is following the shape of bond behavior. Thus, the total response has a steep hardening phase if the initial slope of bond law is sharp. On the other hand, a slight increase in bond strength will cause an increase in the total response simultaneously.

Furthermore, the mesh objectivity of the model was studied, and it was observed that by decreasing the mesh size of matrix element with a factor: 0.5, the time of calculation increased by factor two, and much smaller load steps were needed to provide the convergence in the model. The simulation result of the model with finer mesh shows a mesh dependency effects raised in the strain softening range due to the formation and propagation of cracks in a large area of the specimen, whereas further research is needed.

From the performed sensitivity analyses regarding matrix properties, it was observed that the increase in Young's modulus of concrete and concrete tensile strength would not have significant results on the total response; however, a decrease in concrete tensile strength can cause a sudden drop in the response curve. On the contrary, the changes in concrete fracture energy caused significant changes likewise and were seen as notable shifts in the total response curve.

In contrast, the increase in fiber's tensile strength did not influence the total response, while the decrease caused an immature hardening behavior. Later two analyses, with lower fiber volume fraction compare to reference model, were performed, i.e., 1)the increase in fiber volume fraction was obtained by increasing the number of fibers, 2)

it was achieved by increasing the fiber section area. It was observed that the total response was decreased in both cases, and the localization of crack was more visible in the second model, while the first model response showed smoother hardening and softening phases.

In the end, the effect of considering the secondary cracking was investigated by performing a simulation, whereas just one crack is allowed to perform in each matrix element. It was observed that this model has a stiffer softening path, and crack patterns can not present the localization of cracks.

It should be stated that simulation cracking patterns cannot be directly compared to experimental cracking patterns as the simulation model's current state is deterministic, whereby random material properties influence the experimental specimen behavior. The simulation model seems to describe enumerated SHCC behavior at an acceptable level considering the random field and other simplifying assumptions, nevertheless the research needs to be extended concerning the mesh dependency aspects.

6 CONCLUSION

6.1 RETROSPECTIVE VIEW AND FINDINGS

A numerical method was developed to model reinforced cracked material with an application focus on fiber-reinforced cement composite. With its use, the total response of specimens was investigated, focusing on the effect of mechanical characterization of different components in FRCC, i.e., Matrix, fibers, and bond interfaces.

In the present model, the cement matrix cracking is modeled with the finite element strong discontinuity approach (SDA). In this method, the extension of the uncracked element to the SDA cracked element is ruled by the Rankine criterion, depending on the loading history. Two alternative types of discontinuity consist of the fictitious or cohesive crack concept employed with crack tractions depending on crack width computed explicitly. This approach is recommended due to several significant advantages. First, this approach allows for the reproduction of the fracture energy independent of element size and naturally solves the mesh dependency problem for softening material behavior. Second, it can be used with nonlinear material laws for the continuum, arbitrary cracking criteria, nonlinear crack traction-crack width relations, and multiple cracking with different orientations at a given point. Furthermore, SDA's special formulation is dealing with the discontinuity in element level without explicitly imposing additional degrees of freedom to the system. These advantages make SDA as a good alternative in case of a large number of cracks.

In the developed finite element based model, the fibers are explicitly model with truss elements. The discretization of fibers is independent of the underlying continuum mesh with truss nodes independent from continuum nodes. Thus, an arbitrary fiber position and orientation become possible. Nonlinear material behavior can be assigned to the truss elements, and a newly developed bond element is introduced to couple the truss elements to continuum elements. This bond interface acts as spring collections connecting truss nodes and neighbored continuum nodes. Different bond laws can be

assigned to the bond elements, characterized as nonlinear in the longitudinal direction, and constrained for mutual intersection in the lateral direction by a penalty approach. This particular type of coupling allows for fibers crossing a discontinuity or crack of the underlying continuum without further arrangements.

Single fiber pullout experiment has been modeled with commercial software DIANA to identify the bond law. Since the experimental results characterized by relatively large scatter, the mean values were used for generalization.

First, this newly developed model was calibrated with several simple configurations. Later 2D SHCC dumbbell specimen under tensile loading condition was simulated, and a series of numerical case studies were performed to assess the quality, credibility, and limitations of the numerical model. These thin specimens are exposed to tension and can be modeled in 2D, whereas a high number of fibers are distributed randomly. Fibers are allowed to have different orientations based on the capabilities of the developed numerical method. However, due to unique production techniques, the fibers in these 2D dumbbell specimens were oriented in the direction of applied tensile load. It should be noted that cracking patterns cannot be directly compared to experimental cracking patterns as the simulation model's current state is deterministic by random material properties influence the experimental specimen behavior. Taking the effect of random field and other simplifying assumptions into account, the simulation model seems to describe enumerated SHCC behavior at an acceptable level.

6.2 RECOMMENDATIONS

The current approach assumes small displacements, linear elasticity with limited tensile strength for material behaviors before crack initiation or failure, simple shear retention for cracks, a viscous stabilization for unstable system behazuhhgvior, and a deterministic view with non-scattering system properties.

Further developments and investigations should treat the following items currently exceeding the scope of this research:

- Mesh dependency aspects for strain softening behavior
- Extension for large displacements for improved modeling of fiber pullout.

- Replacing of elastic material behavior with limited tensile strength by damage and/or plasticity in order to describe cement matrix compression behavior.
- Systematic investigation of the influence of type and parameter values for shear retention and viscous stabilization.
- Introduction of stochastic fields implemented with, e.g., Monte-Carlo methods in order to model stochastic properties of FRCC.

Especially regarding the last item, it should be mentioned that the computational effort currently is quite high; thus, further development is necessary. In summary, however, it can be stated that a further base is given for the target-oriented design of FRCC material composition to reach the given objectives of material properties. Besides, the presented concepts and methods can be used for simulation of both short and thin polymer fibers in a random position and steel fibers and structures with long reinforcement in a regular arrangement.

BIBLIOGRAPHY

[1] Discussion, in proceedings of rilem symposium on testing and test methods of fiber cement composites, 1978.

[2] Dyneema® fact sheets, ultra high molecular weight polyethylene fiber form dyneema, eurofibers, 2010.

[3] A. G. Bitencourt, L., Manzoli, O. L., Bittencourt, T. N., and Vecchio, F. J. Numerical modeling of steel fiber reinforced concrete with a discrete and explicit representation of steel fibers. *International Journal of Solids and Structures 159* (2019), 171–190.

[4] Alfaiate, J., Simone, A., and Sluys, L. Non-homogeneous displacement jumps in strong embedded discontinuities. *International Journal of Solids and Structures 40*, 21 (2003), 5799–5817.

[5] Alfaiate, J., and Sluys, L. J. Strong discontinuity formulations: A comparative study. In *Fracture Mechanics of Concrete and Concrete Structures - New Trends in FractureMechanicsof Concrete* (London, 2007), A. Carpinteri, P. Gambarova, G. Ferro, and G. Plizzari, Eds., Taylor and Francis Group, pp. 147–153.

[6] Avenston, J, C. G., and Kelly, A. Single and multiple fracture in the properties of fiber-composites. *Proceedings of the National Physical Laboratory* (1971), 15–26.

[7] Bažant, Z., and Jirásek, M. Non local integral formulations of plasticity and damage: A survey on recent results. *Journal of Engineering Mechanics 128* (2002), 1129–1239.

[8] Barhum, R. *Mechanisms of the interaction between continuous and short fibres in textile-reinforced concrete (TRC).* PhD thesis, Technical University of Dresden, 2014.

[9] Bathe, K. *Finite Element Procedures.* Prentice Hall, Englewood Cliffs, New Jersey, 1996.

[10] Bathe, K. *Finite Element Procedures.* MPrentice Hall, Englewood Cliffs, New Jersey, 1996.

[11] Bazant, Z., and Jirásek, M. Nonlocal integral formulations of plasticity and damage: Survey of progress. *Journal of Engineering Mechanics 128* (2002).

[12] Bažant, Z. P., and Lin, F. B. Nonlocal smeared cracking model for concrete fracture. *Journal of Structural Engineering 114*, 11 (1988), 2493–2510.

[13] Bažant, Z. P., and Oh, B. H. Crack band theory for fracture of concrete. *Matériaux et construction 16*, 3 (1983), 155–177.

[14] Bazilevs, Y. e. Isogeometric analysis using T-splines. *Computer Methods in Applied Mechanics and Engineering 199* (2010), 229–263.

[15] Belytschko, T., L. W., and Moran, B. *Nonlinear Finite Elements for Continua and Structures.* John Wiley Sons, Chichester, 2000.

[16] Belytschko, T., L. Y., and Gu, L. Element-free Galerkin methods. *International Journal for Numerical Methods in Engineering 37* (1994), 229–256.

[17] Belytschko, T., Liu, W., and Moran, B. *Nonlinear Finite Elements for Continua and Structures.* John Wiley and Sons, Chichester, 2000.

[18] Belytschko, T. e. Meshless Methods: An overview and recent developments. *Comput. Methods Appl. Mech. Engrg 139* (1996), 3–46.

[19] Belytschko, T. Lu, Y., and Gu, L. Element-Free Galerkin Methods. *International Journal for Numerical Methods in Engineering 37* (1994), 229–256.

[20] Bentur, A., and Mindess, S. *Fiber reinforced cementitious composites.* Taylor Francis, Canada, 2007.

[21] Berard, A. Artificial stone, 15 1874. U.S. Patent No. 157 903.

[22] Bolander, J. E., and Saito, S. Discrete modeling of short-fiber reinforcement in cementitious composites. *Advanced Cement Based Materials 6*, 3 (1997), 76–86.

[23] Bouchard, P.-O., Bay, F., Chastel, Y., and Tovena, I. Crack propagation modelling using an advanced remeshing technique. *Computer methods in applied mechanics and engineering 189*, 3 (2000), 723–742.

[24] Caner, F.C. Bažant, Z., and Wan-Wendner, R. Microplane model M7f for fiber reinforced concrete. *Engineering Fracture Mechanics 105* (2013), 41–57.

[25] Cottrell, J.A., H. T., and Bazilevs, Y. *Isogeometric analysis: toward integration of CAD and FEA*. John Wiley Sons, Chichester, 2009.

[26] Cunha, V. M. C. F., Barros, J. A. O., and Sena-Cruz, J. M. An integrated approach for modelling the tensile behaviour of steel fibre reinforced self-compacting concrete. *Cement and Concrete Research 41*, 1 (2011), 64–76.

[27] Cunha, V. M. C. F., Barros, J. A. O., and Sena-Cruz, J. M. A finite element model with discrete embedded elements for fibre reinforced composites. *Computers & Structures 94-95* (2012), 22–33.

[28] Curosu, I. *Influence of fiber type and matrix composition on the tensile behavior of strain-hardening cement-based composites (SHCC) under impact loading*. PhD thesis, 2017.

[29] Curosu, I., Liebscher, M., Mechtcherine, V., Bellmann, C., and Michel, S. Tensile behavior of high-strength strain-hardening cement-based composites (hs-shcc) made with high-performance polyethylene, aramid and pbo fibers. *Cement and Concrete Research 98* (2017), 71–81.

[30] Curosu, I., Mechtcherine, V., Forni, D., and Cadoni, E. Performance of various strain-hardening cement-based composites (shcc) subject to uniaxial impact tensile loading. *Cement and Concrete Research 102* (2017), 16–28.

[31] Curosu, I., Mechtcherine, V., and Millon, O. Effect of fiber properties and matrix composition on the tensile behavior of strain-hardening cement-based composites (shccs) subject to impact loading. *Cement and Concrete Research 82* (2016), 23–35.

[32] deVekey, R. C., and Majumdar, A. J. Determining bond strength in fibre-reinforced composites. *Magazine of Concrete Research 20*, 65 (1968), 229–234.

[33] DIANA, F. *Finite Element Analysis User's Manual*. The Netherlands, 2018.

[34] Dias-da Costa, D., Alfaiate, J., Sluys, L., and Júlio, E. A discrete strong discontinuity approach. *Engineering Fracture Mechanics 76*, 9 (2009), 1176–1201.

[35] Dvorkin, E. N., Cuitiño, A. M., and Gioia, G. Finite elements with displacement interpolated embedded localization lines insensitive to mesh size and distortions. *International journal for numerical methods in engineering 30*, 3 (1990), 541–564.

[36] Echter, R., and Bischoff, M. Numerical efficiency, locking and unlocking of NURBS finite elements. *Computer Methods in Applied Mechanics and Engineering 199* (2010), 374–382.

[37] Fischer, G., Stang, H., and Dick-Nielsen, L. Initiation and development of cracking in ECC materials: experimental observations and modeling. 6.

[38] Fleming, M., C. Y., and Belytschko, T. Enriched element-free Galerkin methods for crack tip fields. *Int. J. Numer. Meth. Engng 40* (1997), 1483–1504.

[39] Fries, T.-P., and Belytschko, T. The extended/generalized finite element method: An overview of the method and its applications. *International Journal for Numerical Methods in Engineering 84*, 3 (2010), 253–304.

[40] Gasser, T. C., and Holzapfel, G. A. Geometrically non-linear and consistently linearized embedded strong discontinuity models for 3d problems with an application to the dissection analysis of soft biological tissues. *Computer Methods in Applied Mechanics and Engineering 192*, 47-48 (2003), 5059–5098.

[41] Gopalaratnam, V., and Shah, S. P. Softening response of plain concrete in direct tension. In *Journal Proceedings* (1985), vol. 82, pp. 310–323.

[42] Han, T.-S., Feenstra, P., and Billington, S. Simulation of highly ductile fiber-reinforced cement based composite components under cyclic loading. *ACI Structural Journal 100* (2003).

[43] Hannant, D. *Fiber Cements and Fiber Concretes*. J. Wiley, 1978.

[44] Hartig, J., Häussler-Combe, U., and Schicktanz, K. Influence of bond properties on the tensile behaviour of textile reinforced concrete. *Cement and Concrete Composites 30*, 10 (2008), 898–906.

[45] Häussler-Combe, U. *Computational Methods for Reinforced Concrete Structures*. Ernst Sohn / Wiley, Berlin, 2014.

[46] Häussler-Combe, U., Chihadeh, A., and Shehni, A. Modelling of discrete cracks in reinforced concrete plates with the strong discountinuity approach

(SDA). In *7th International Conference on Structural Engineering, Mechanics and Computation (SEMC 2019)* (2019), pp. 611–616.

[47] Hillerborg, A., Modéer, M., and Petersson, P.-E. Analysis of crack formation and crack growth in concrete by means of fracture mechanics and finite elements. *Cement and concrete research 6*, 6 (1976), 773–781.

[48] Hughes, T.J.R., C. J., and Bazilevs, Y. Isogeometric analysis: CAD, finite elements, NURBS, exact geometry and mesh refinement. *Comput. Methods Appl. Mech. Engrg 194* (2005), 4135–4195.

[49] Häussler-Combe, U. Ein vergleich aktueller numerischer rechenverfahren am beispiel von scheibentragwerken mit rissen. *Bauingenieur 93*, 4 (2018), 131–140.

[50] Häussler-Combe, U., Shehni, A., and Chihadeh, A. Finite element modeling of fiber reinforced cement composites using strong discontinuity approach with explicit representation of fibers. *International Journal of Solids and Structures 200-201* (2020), 213–230.

[51] Jirasek, M. Nonlocal models for damage and fracture: comparison of approaches. *International Journal of Solids and Structures 35* (1998), 4133–4155.

[52] Jirásek, M. Comparative study on finite elements with embedded discontinuities. *Computer methods in applied mechanics and engineering 188*, 1-3 (2000), 307–330.

[53] Jirasek, M. Comparative study on finite elements with embedded discontinuities. *Comput. Methods Appl. Mech. Engrg. 188* (2000), 307–330.

[54] Jirásek, M., and Zimmermann, T. Embedded crack model: I. basic formulation. *International journal for numerical methods in engineering 50*, 6 (2001), 1269–1290.

[55] Kang, J., and Bolander, J. E. Event-based lattice modeling of strain-hardening cementitious composites. *International Journal of Fracture 206*, 2 (2017), 245–261.

[56] Kelly, A. Reinforcement of structural materials by long strong fibres. *Metallurgical Transactions 3*, 9 (1972), 2313–2325.

[57] Kelly, A., and Davies, G. J. The principles of the fibre reinforcement of metals. *Metallurgical Reviews 10*, 1 (1965), 1–77.

[58] Kim, J. *New finite elements with embedded strong discontinuities to model failure of three-dimensional continua.* PhD thesis, UC Berkeley, 2013.

[59] Krenchel, H. *Fiber Reinforcement.* Eng. translation,, 1964.

[60] Kunieda, M., Ogura, H., Ueda, N., and Nakamura, H. Tensile fracture process of strain hardening cementitious composites by means of three-dimensional meso-scale analysis. *Cement and Concrete Composites 33*, 9 (2011), 956–965.

[61] Lankard, D. R. Slurry infiltrated fiber concrete (SIFCON): Properties and applications.

[62] Lankard, D. R., and Newell, J. K. Preparation of highly reinforced steel fiber reinforced concrete composites.

[63] Laranjeira, F. *Design-oriented constitutive model for steel fiber reinforced concrete.* PhD thesis, 2010.

[64] Laranjeira, F., Aguado, A., and Molins, C. Predicting the pullout response of inclined straight steel fibers. *Materials and Structures 43*, 6 (2010), 875–895.

[65] Laranjeira, F., Molins, C., and Aguado, A. Predicting the pullout response of inclined hooked steel fibers. *Cement and Concrete Research 40*, 10 (2010), 1471–1487.

[66] Lee, C., and Zhou, C. On error estimation and adaptive refinement for element free Galerkin method: Part I: stress recovery and a posteriori error estimation. *Computers Structures 82* (2004), 413–428.

[67] Li, V. C. On engineered cementitious composites (ecc). *Journal of advanced concrete technology 1*, 3 (2003), 215–230.

[68] Li, V. C., and Leung, C. K. Steady-state and multiple cracking of short random fiber composites. *Journal of Engineering Mechanics 118*, 11 (1992), 2246–2264.

[69] Li, V. C., Wang, Y., and Backer, S. Effect of inclining angle, bundling and surface treatment on synthetic fibre pull-out from a cement matrix. *Composites 21*, 2 (1990), 132–140.

[70] Li, V. C., Wang, Y., and Backer, S. A micromechanical model of tension-softening and bridging toughening of short random fiber reinforced brittle matrix composites. *Journal of the Mechanics and Physics of Solids 39*, 5 (1991), 607–625.

[71] Li, V. C., and Wu, H.-C. Conditions for pseudo strain-hardening in fiber reinforced brittle matrix composites. 390–398.

[72] Li, V.C., W. S., and Wu, C. Tensile strain-hardening behaviour of polyvinyl alcohol engineered cementitious composite (PVA-ECC). *ACI Materials Journal 98* (2001), 483–492.

[73] Li Victor C., and Leung Christopher K. Y. Steady-state and multiple cracking of short random fiber composites. 2246–2264.

[74] Logan, D. L. *A first course in the finite element method.* Cengage Learning, Stamford, 2012.

[75] López, C. M., Carol, I., and Aguado, A. Meso-structural study of concrete fracture using interface elements. i: numerical model and tensile behavior. *Materials and structures 41*, 3 (2008), 583–599.

[76] Maalej, M. Tensile properties of short fiber composites with fiber strength distribution. *Journal of Materials Science 36* (2001), 2203–2212.

[77] Majumdar, A. J. Glass fiber reinforcement of cement products. *Journal of Glass Technology 9*, 3 (1968), 78–84.

[78] Marshall, D. B., and Cox, B. N. A j-integral method for calculating steady-state matrix cracking stresses in composites. *Mechanics of Materials 7*, 2 (1988), 127–133.

[79] Mechtcherine, V. *Bruchmechanische und fraktologische Untersuchungen zur Rissausbreitung in Beton.* PhD thesis, 2000.

[80] Mihai, I.C. Jefferson, A., and Lyons, P. A plastic-damage constitutive model for the finite element analysis of fiber reinforced concrete. *Engineering Fracture Mechanics 159* (2016), 35–62.

[81] Moës, N., Dolbow, J., and Belytschko, T. A finite element method for crack growth without remeshing. *International journal for numerical methods in engineering 46*, 1 (1999), 131–150.

[82] Naaman, A., Argon, A., and Moavenzadeh, F. A fracture model for fiber reinforced cementitious materials. *Cement and Concrete Research 3*, 4 (1973), 397–411.

[83] Naaman, A., and Reinhardt, H. *Characterization of high performance fiber reinforced cement composites-HPFRCC*. EFN SPON, London, 1996.

[84] Naaman, A. E. *A statistical theory of strength for fiber reinforced concrete*. PhD thesis, Massachusetts Institute of Technology, 1972.

[85] Naaman, A. E. Fracture and multiple cracking of cementitious composites. *Fracture Mechanics Applied to Brittle Materials* (1979).

[86] Naaman, A. E. Advances in high performance fiber reinforced cement based composites. In *Proceedings of the International Symposium on Fiber Reinforced Concrete, V.S. Parameswaran and T.S. Krishnamurti, Editors* (1987), pp. 7.87–7.98.

[87] Naaman, A. E. High performance fiber reinforced cement composites. In *Proceedings of the IABSE Symposium on Concrete Structures for the Future, Paris* (1987), pp. 371–376.

[88] Naaman, A. E. High performance fiber reinforced cement composites: Classification and applications. In *CBM-CI International Workshop, Karachi, Pakistan* (2007).

[89] Naaman, A. E. Tensile strain-hardening FRC composites: Historical evolution since the 1960. 181–202.

[90] Naaman, A. E. *Fiber Reinforced Cement and Concrete Composites*. Techno Press 3000, 2018.

[91] Naaman, A. E., and Homrich, J. R. Tensile stress-strain properties of sifcon. *Materials Journal 86*, 3 (1989), 244–251.

[92] Naaman, A. E., Moavenzadeh, F., and McGarry, F. J. Probabilistic analysis of fiber-reinforced concrete. *Journal of Engineering Mechanics 100*, nm2 (1974).

[93] Naaman, A. E., and Reinhardt, H. W. Characterization of high performance fiber reinforced cements composites hpfrcc, international workshop; 2nd, high performance fiber reinforced cement composites. In *High performance fiber*

reinforced cement composites, RILEM PROCEEDINGS, International workshop; 2nd, High performance fiber reinforced cement composites (1996), no. 31, E & FN Spon, pp. 1–24.

[94] Nagadeepika, S. *Modeling concrete behavior at mesoscopic scale.* PhD thesis, Technische Universität Dresden, 2012.

[95] Neville, A., Testing, I. A. o., Materials, R. L. f., and Structures. *Fibre reinforced cement and concrete.* Ciment Et Béton Renforcés de Fibres. Construction Press, 1975.

[96] Nguyen, V. P. e. Isogeometric analysis: An overview and computer implementation aspects. *Mathematics and Computers in Simulation 117* (2015), 89–116.

[97] Oliver, J., Huespe, A., and Samaniego, E. A study on finite elements for capturing strong discontinuities. *International journal for numerical methods in engineering 56*, 14 (2003), 2135–2161.

[98] Oliver, J., Huespe, A., Samaniego, E., and Chaves, E. Continuum approach to the numerical simulation of material failure in concrete. *International Journal for Numerical and Analytical Methods in Geomechanics 28*, 7-8 (2004), 609–632.

[99] Padmarajaiah, S. K., and Ramaswamy, A. A finite element assessment of flexural strength of prestressed concrete beams with fiber reinforcement. *Cement and Concrete Composites 24*, 2 (2002), 229–241.

[100] Pamin, J., and de Borst, R. Gradient enhanced damage and plasticity models for plain and reinforcedconcrete. In *ECCM 99, European Conference on Computational Mechanics, August 31- September3,1999, Munich, Germany* (1999).

[101] Panteki, E. *Bond of reinforcement in concrete under high loading rates.* PhD thesis, 2018.

[102] Petersson, P.-E. Crack growth and development of fracture zones in plain concrete and similar materials.

[103] Pivonka, P., Ozbolt, J., Lackner, R., and Mang, H. Comparative studies of 3d-constitutive models for concrete: application to mixed mode fracture. *Int. J. Numer. Meth. Engng. 60* (2004), 549–570.

[104] Pros, A., Diez, P., and Molins, C. Modeling steel fiber reinforced concrete: numerical immersed boundary approach and a phenomenological mesomodel for concrete-fiber interaction. *International Journal for Numerical Methods in Engineering 90*, 1 (2012), 65–86.

[105] Radtke, F., Simone, A., and Sluys, L. A partition of unity finite element method for simulating non-linear debonding and matrix failure in thin fibre composites. *International Journal for Numerical Methods in Engineering 86* (2011), 453–476.

[106] Reinhardt, H. W., Cornelissen, H. A., and Hordijk, D. A. Tensile tests and failure analysis of concrete. *Journal of structural engineering 112*, 11 (1986), 2462–2477.

[107] Romualdi, J. Two phase concrete and steel materials, Feb. 25 1969. U.S. Patent No.3,439,094.

[108] Romualdi, J. P., and Mandel, J. A. Tensile strength of concrete affected by uniformly distributed and closely spaced short lengths of wire reinforcement. 657–672.

[109] Ruiz, G. Propagation of a cohesive crack crossing a reinforcement layer. *International Journal of Fracture 111*, 3 (2001), 265–282.

[110] Sancho, J., Planas, J., Fathy, A., Galvez, J., and Cendon, D. Three-dimensional simulation of concrete fracture using embedded crack elements without enforcing crack path continuity. *International Journal for Numerical and Analytical Methods in Geomechanics 31*, 2 (2007), 173–187.

[111] Shah, S. P. Do fibers increase the tensile strength of cement-based matrix? *Materials Journal 88*, 6 (1992), 595–602.

[112] Shah, S. P., and Rangan, B. V. Fiber reinforced concrete properties. In *Journal Proceedings* (1971), vol. 68, pp. 126–137.

[113] Shehni, A., and Häussler-Combe, U. New approach on discretization methods for mesoscopic study of concrete structures. In *6th European Conference on Computational mechanics (ECCM 6) 7th European Conference on Computational Fluid Dynamic (ECFD 7)* (2018), pp. 1223–1233.

[114] Shehni, A., Häussler-Combe, U., Curosu, I., Gong, T., and Mechtcherine, V. Numerical simulation of hs-shcc under quasi-static tensile loading. In *10 th International Conference on Fracture Mechanics of Concrete and Concrete Structures FraMCoS-X* (2019), pp. 23–26.

[115] Simo, J. C., and Rifai, M. S. A class of mixed assumed strain methods and the method of incompatible modes. *International journal for numerical methods in engineering 29*, 8 (1990), 1595–1638.

[116] Smolcic, Z., and Ozbolt, J. Meso scale model for fiber-reinforced-concrete: Microplane based approach. *Computers and Concrete 19* (2017).

[117] Stolarska, M., Chopp, D. L., Moes, N., and Belytschko, T. Modelling crack growth by level sets in the extended finite element method. *Int. J. Numer. Meth. Eng. 51* (2001), 943–960.

[118] Stroeven, P. *Some aspects of the micromechanics of concrete.* PhD thesis, 1973.

[119] Suwada, H., and Fukuyama, H. Nonlinear finite element analysis on shear failure of structural elements using high performance fiber reinforced cement composite. *Journal of Advanced Concrete Technology 4*, 1 (2006), 45–57.

[120] Švec, O., Žirgulis, G., Bolander, J. E., and Stang, H. Influence of formwork surface on the orientation of steel fibres within self-compacting concrete and on the mechanical properties of cast structural elements. *Cement and Concrete Composites 50* (2014), 60–72.

[121] Willam, K., Pramono, E., and Sture, S. Fundamental issues of smeared crack models. In *Fracture of Concrete and Rock*, S. P. Shah and S. E. Swartz, Eds. Springer, 1989, pp. 142–157.

[122] Wittman, F., and van Zijl, G. *Durability of strain-hardening fiber-reinforced cement-based composite(SHCC).* Springer, Berlin, 2011.

[123] Wittmann, F. Structure of concrete and crack formation. 1987, pp. 309–340.

[124] Wu, C. *Micromechanical tailoring of PVA-ECC for structural applications.* phdthesis, 2001.

[125] Yao, J., and Leung, C. K. A new physical model for empirical fiber snubbing effect in cementitious composites based on large deflection beam theory. 238–251.

[126] Zaitsev, Y. B., Wittmann, F. H., and Govindjee, S. Simulation of crack propagation and failure of concrete. *Materials and Construction 14* (1981), 357–365.

[127] Zhang, Y., Lackner, R., Zeiml, M., and Mang, H. A. Strong discontinuity embedded approach with standard sos formulation: Element formulation, energy-based crack-tracking strategy, and validations. *Computer Methods in Applied Mechanics and Engineering 287* (2015), 335–366.

[128] Zienkiewicz, O., and Taylor, R. *The finite element method.* Mc-Graw Hill, London, 1989.

[129] Zienkiewiczand O.C.and Taylor, R. *The Finite Element Method.* McGraw Hill, 1989.